SYNTHESIS, STRUCTURAL AND OPTICAL STUDIES OF COPPER SULFIDE AND SILVER SULFIDE NANOPARTICLES FROM Cu(II) AND Ag(I) DITHIOCARBAMATE SINGLE SOURCE PRECURSORS

Nandipha Loveness Botha

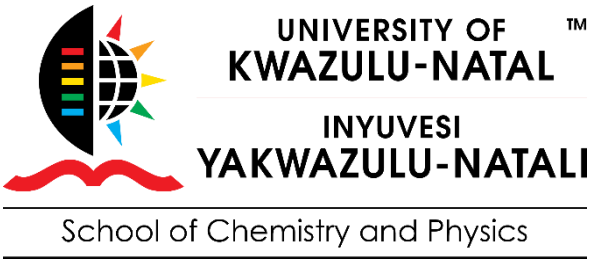

December 2018

SYNTHESIS, STRUCTURAL AND OPTICAL STUDIES OF COPPER SULFIDE AND SILVER SULFIDE NANOPARTICLES FROM Cu(II) AND Ag(I) DITHIOCARBAMATE SINGLE SOURCE PRECURSORS

By

NANDIPHA LOVENESS BOTHA (217075510)

B. Sc., B. Sc. (Honours), MSc Chemistry (UFH)

Being a thesis submitted to the College of Agriculture, Engineering and Science in fulfilment of the requirements for the award of the degree of

Doctor of Philosophy in Chemistry

of the

University of KwaZulu-Natal

Supervisor: Professor P. A. Ajibade

December 2018

DECLARATION BY CANDIDATE ON PLAGIARISM

I, Nandipha Botha, declare that:

1. The research in this thesis, except where otherwise indicated, is my original research.
2. This thesis has not been submitted for any degree or examination at other university.
3. This thesis does not contain any other person data unless specifically acknowledged as being sourced from them.
4. This thesis does not contain any other persons' writing, unless specifically acknowledged as being sourced from other researchers. Where other written sources have been quoted, then:
    a. Their words have been re-written, but the general information attributed to them has been properly referenced.
    b. In all instances where the exact words of other authors have been used, then their writing has been placed in italics and inside a quotation marks and referenced.
5. This thesis does not contain text or graphics from the internet copied and pasted, unless specifically acknowledged, and the source being detailed in the dissertation/thesis and in the references section.

10/09/2019 

Date **Nandipha L. Botha**

CERTIFICATION

This is to certify that this research is a record of original work carried out by Nandipha Loveness Botha under my supervision in the Inorganic Materials Research laboratory of the School of Physics and Chemistry, University of Kwa Zulu Natal in fulfilments of the requirements for the award of Doctor of Philosophy in Chemistry.

_____ _____

Date Supervisor

P. A. Ajibade

Professor of Inorganic Materials Chemistry

B. Sc (Hons), MSc (Ibadan);

PhD (UniZul); MRSC (London)

DEDICATION

I wholeheartedly dedicate this work to my lovely mother, Nombulelo Mgijima, who is my source of inspiration and support, and all my friends who held my hand through this journey.

ACKNOWLEDGEMENT

First and foremost, with deep gratitude I would like to acknowledge the Almighty God for his never-ending love, unmeasurable mercy and grace, for his protection and guidance most of all for the wisdom and knowledge. Throughout this journey He gave me strength and hope. This work would not have been a success without him. I would also like to thank my supervisor Prof Ajibade for supervision.

I also would like to extend my appreciation to:

- The University of Kwa Zulu Natal, School of Physics and Chemistry for the opportunity and the fee remission.
- Technical staff members for their assistance with the instrument operation
- Colleagues
- Nation Research foundation for NRF innovation PhD scholarship award
- Family and friends for their love and support
- SASOL and NRF for funding the research

TABLE OF CONTENT

LIST OF FIGURES

LIST OF SCHEMES

LIST OF TABLES

ABBREVIATIONS AND SYMBOLS

NIR	-	Near Infrared
JCPDS	-	Joint Committee on Powder Diffraction Standards
a.u	-	Arbitrary Unit
ORTEP	-	Oak Ridge Thermal Ellipsoid Plot
et. al	-	Et alia
LMCT	-	Ligand to Metal Charge Transfer
NP	-	Nanoparticles
DTC	-	Dithiocarbamate
FTIR	-	Fourier-transform infrared spectroscopy
NMR	-	Nuclear magnetic resonance spectroscopy
UV-Vis	-	Ultra Violet-Visible
SC-XRD	-	single crystal X-ray diffraction
P-XRD	-	powder X-ray diffraction
SEM	-	Scanning electron microscope
TEM	-	Transmission electron microscopy
EDX	-	Energy-dispersive X-ray spectroscopy

RESEARCH OUTPUTS

- **Nandipha L. Botha and Peter A. Ajibade**

  Copper(II) piperidine dithiocarbamate and silver(I) N-ethyl aniline dithiocarbamate complexes: Synthesis, crystal structure and their use as precursor for metal sulphide nanoparticles (To be submitted).

- **Nandipha L. Botha and Peter A. Ajibade**

  Synthesis and optical studies of Silver Sulphide Nanoparticles via single molecule precursor method (To be submitted)

- **Nandipha L. Botha and Peter A. Ajibade**

  Synthesis and optical studies of oleic acid capped silver sulphide nanoparticles (To be submitted)

- **Nandipha L. Botha and Peter A. Ajibade**

  Synthesis, structural and optical studies of copper sulphide nanoparticles prepared from bis(dithiocarbamato) single source precursors (To be submitted)

- **Nandipha L. Botha and Peter A. Ajibade**

  X-ray crystal structures of Cu(II) and Ag(I) dibenzyl amine dithiocarbamate complexes and their use as single source precursors for metal sulphide nanoparticles (To be submitted)

ABSTRACT

Eight dithiocarbamate ligands were synthesized from butylamine, diallylamine, N-ethyl aniline, N-methyl benzyl amine, piperidine, morpholine, dibenzyl amine and phenyl piperizine. Eight copper(II) dithiocarbamate complexes and Eight silver(I) dithiocarbamate complexes were synthesized. Spectroscopy techniques were used to characterise the obtained compounds. The structure of the synthesized dithiocarbamate ligands was confirmed using NMR spectroscopy. Proton NMR showed all the expected peaks and showed the ligands to be pure with no extra peaks for contaminations. ^{13}C NMR showed the peak corresponding to the carbon in the carbon disulphide resonation at around 200 to 220 ppm in all the ligands confirming their formation.

FTIR was carried out for all the compounds, ligands and their corresponding metal complexes. In the ligands the C – S, C = S and C – N vibrations were observed corresponding to the dithio-moiety. In the copper complexes the C – S and C = S frequency merged and gave one vibration which confirmed the coordination of the metal to the ligands. UV-Visible was also used to confirm the geometry of the complexes. The ligands gave the bands corresponding to $\pi - \pi^*$ and $n - \pi^*$ due to N–C=S and S–C=S groups. The copper complexes showed the intra-ligand transitions and two extra bands in the visible region corresponding to the *d-d* transition of the square planar geometry of copper(II) complexes. Crystal structures of four complexes were isolated, two copper(II)complexes which confirmed the square planar geometry given by the UV-Vis data and two Silver(I) complexes. However, it turned out that silver complexes obtained are the metal clusters. The sixteen metal dithiocarbamate complexes were used as single source precursors to synthesize thirty-two metal sulphide nanoparticles.

Four single source precursors, from each metal ion were thermolyzed at 220°C to study the effect of the precursor on the nanoparticle structural and optical properties. The other four precursors for each metal ion were further thermolyzed at three different temperatures, 220°C, 180°C and 120°C, to study the influence of the temperature on the structural and optical properties of the nanoparticles. The obtained nanoparticles were further studied using p-XRD. The X-ray data showed the copper sulphide nanoparticles to have $Cu_{1.8}S$ digenite phase. Silver sulphide nanoparticles have α-Ag_2S phase that is usually obtained at lower temperature. The shape and crystallite sizes of the nanoparticles were determined using TEM/HRTEM.

TEM images showed the silver nanoparticles synthesized at 220°C all adapted the same spherical shape that are monodispersed. Their size ranged from 8 nm to 78 nm. When the thermolysis was done at 180°C the sizes ranged from 5 to 71 nm and 2-23 nm when thermolyzed at 120°C. For the copper sulphide nanoparticles synthesized at 220°C the size ranged from 5 to 125 nm. 180°C and 120°C gave size ranges of 10 to 55 nm and 4 to 40 nm respectively. The copper sulphide nanoparticles showed some effect of agglomeration and a mixture of shapes from spherical to hexagonal shapes. Their surface morphology was examined with SEM and they changed with different temperature and precursors. EDX was used to confirm the metals and sulphur present in the particles. The interaction of the capping agents and nanoparticles was studied by FTIR. Their optical properties were studied using photoluminescence and UV-Visible spectroscopy. The nanoparticles were found to be quantum confined as the estimated band gap energies showed blue shift when compared to that of the bulk.

CHAPTER ONE

1.1. Introduction

Nanotechnology is the field of science that is about synthesis and development of various nanomaterials. These materials have acquired the prominence in technological advancements all because of their tuneable physical, chemical and biological properties with improved performance compared to their bulk counterparts [1]. They are categorized according to their different sizes, compositions, shapes, and where they originate [1]. Some of the known categories are: Organic nanomaterials synthesized mostly from different organic matter [2 - 4], Inorganic nanomaterials based on different metals including metal oxides, metal sulphides among others [5, 6], Composite based nanomaterials [7 - 11] and carbon based nanomaterials usually in tube morphologies [12 - 15].

Nanoscale materials or nanomaterials according to the International Organization for Standardization (ISO), are defined as the materials that fall under the nanoscale or with internal structure or surface structure within the nanoscale [16]. These nanomaterials exhibit enhanced properties such as reactivity, greater sensing capability and increased mechanical strength [17]. Nanoscale materials have unique optical properties which were found to be due to effect of their quantum size caused by the electron confinement within particles of their smaller dimensions [18]. More interestingly, the optical properties of such materials can be finely tailored by controlling the crystal dimensions and the chemistry of their surfaces [19]. These nanomaterials can be classified in different categories which are dendrimers, carbon material, metallic nanoparticles, quantum dots, composites etc. with different applications [20].

1.1.1. Dendrimers

Dendrimers are nano-sized, radially symmetric molecules with well-defined, homogeneous, and monodisperse structure consisting of tree-like arms or branches. They are nearly monodispersed macromolecules that contain symmetric branching units built around a small molecule or a linear polymer core [21]. Linear macromolecules sometimes contain some shorter or longer branches. Recently it was discovered that the properties of highly branched macromolecules are not the same as the properties of conventional polymers as the structure of these materials has a huge influence on their applications [22]. Dendrimer is only an architectural motif and not a compound. Poly ionic dendrimers do not have a persistent shape and may undergo changes in size, shape, and flexibility as a function of increasing generations [23].

1.1.2. Carbon nanotubes

There are two types of carbon nanotubes; single walled carbon nanotubes and multi-walled carbon nanotubes. They are 1 nm in diameter and 100 nm in length with a layer of graphite of a cylinder shape. These materials are unique because of their small dimensions and their remarkable physical, mechanical and electrical properties [24]. The nanotubes may consist of one up to tens and hundreds of concentric shells of carbons with adjacent shells separation of approximately 0.34 nm [25]. They are known for their higher tensile strength that is due to the sp^2 bonds between the individual carbon atoms and their elasticity as under high force and when exposed to great compressive forces, carbon nanotubes can twist, bend, kink and buckle without damaging the nanotube, and can still go back to the original structure [26].

1.1.3. Quantum dots

Quantum dots are nanometre scale semiconductor crystals composed of groups II to VI or III to V elements and are defined as particles with physical dimensions smaller than the exciton Bohr radius [28]. Semiconductor quantum dots are brightly luminescent colloidal semiconductor nanocrystals with dimensions between 1 and 10 nm range [29]. Quantum dots have dimensions and numbers of atoms between the atomic-molecular level and bulk material with a band-gap that depends upon different factors that include the type and strength of bond with their closest neighbours [30]. Because of their ability to vary their band gap energy with size, and the quantized energy states that result, these nanoscale device structures have potential in numerous applications [31].

1.1.4. Metallic Nanoparticles

ISO defines nanoparticles as nano-objects that has all the three external dimensions within the nanoscale as the nanoscale is the size ranging from 1–100 nm [16]. Since this small sized molecules and atoms work differently resulting from the different components of the material, they behave as a whole unit in terms of its properties and, provide a numerous advantage when used as a transport in drug delivery [32]. Nanoparticle have unusual properties including their exceptionally high surface area to volume ratio due to their small size and this surface area means that the surface is the most important component of the nanomaterials [33]. Surface and interface properties play a significant role in determining materials behaviour [34]. Thus, high surface area materials open a new dimension in material design for a multitude of technologically important areas, such as the conversion and storage of energy and catalysis to name a few. Beyond morphology, the properties of high surface area materials can be further fine-tuned [35].

When the nanoparticles are synthesized to be small enough in a nano range, they tend to experience the Quantum confinement effect due to the confinement of the movement of electrons. This effect however leads to the limitation of the energies at which electrons and holes can exist in the particles [36]. Because of this, artificial structure with desired properties not the same with those of the corresponding bulk materials are created. The structure of the material has an influence on the interaction of materials with optical waves and photons, therefore, the structure can then be used to control light field distribution and light propagation [37]. Since energy is related to wavelength of the resulting photon, this means that the optical properties of the particle can be finely tuned depending on its size and shape.

Optical properties are one of the most fascinating and useful aspects of the nanoparticles. Nanoparticles due to their small particle sizes show enhanced optical emission as well as nonlinear optical properties resulting from the quantum confinement effect [38]. However, there are often complicating factors in understanding the nanoparticle optical properties, including the presence of a supporting substrate, a solvent layer on top of the particles, and particles that are close enough together that their electromagnetic coupling changes the spectra [39]. Nanostructured semiconductors show the same pattern of change in band structure for electronic and optical properties when the size is reduced [40]. The Quantum confinement also influences the band gap of matrix lattice, as it increases when the particle size is minimized to nanoscale, as demonstrated in Figure 1.1 [41]. The energy gap between valence and conduction band is of fundamental importance for the properties of a solid material. Some activities of the materials depend on the energy gap of materials including intrinsic conductivity, optical

transitions, or electronic transitions. Therefore, any change of the gap may significantly alter the material's physics and chemistry [42].

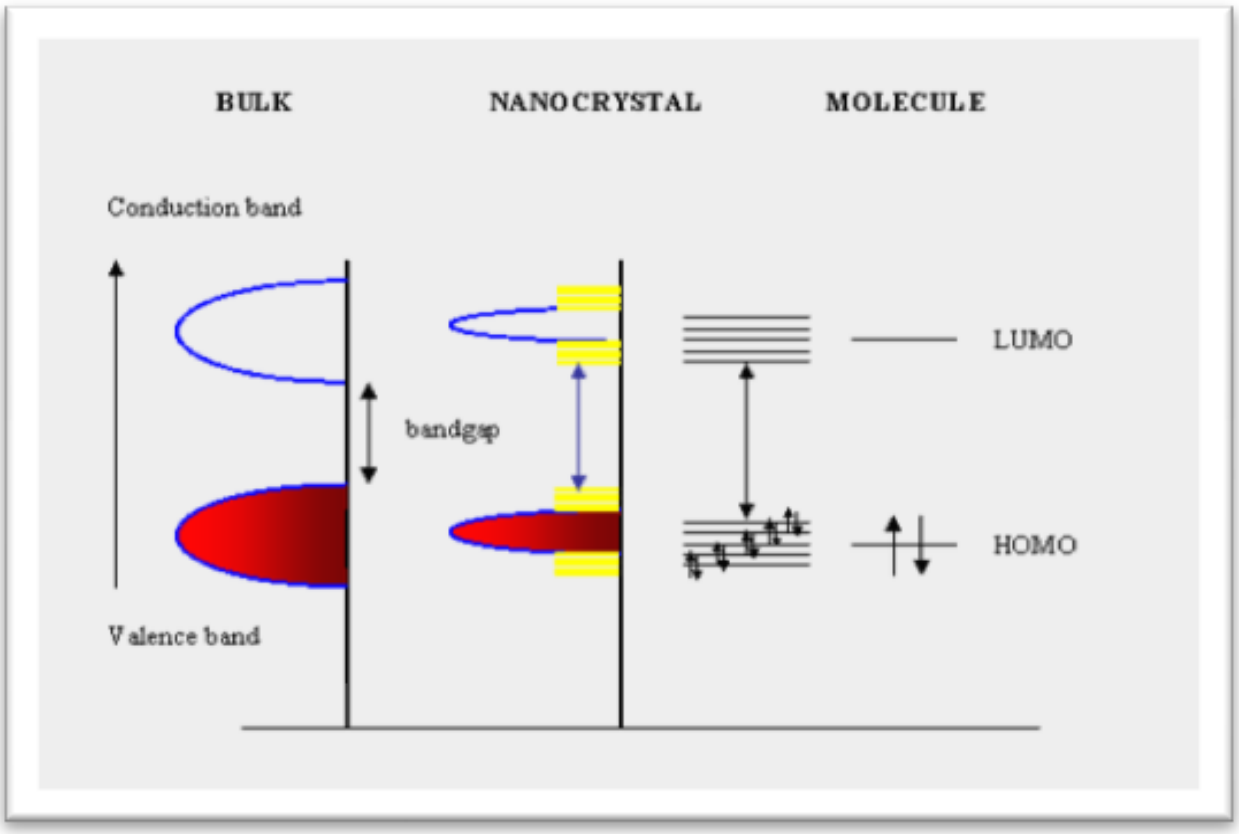

Figure 1. 1. The Energy band gap of the materials [41].

1.1.5. The applications of nanomaterials

Nanoparticles have shown potential in various applications due to their fine-tune able properties and their small size. The quantum phenomena in the nanoparticles lead to their surface reactivity making them unpredictable as their surface can be improved with different reactants, therefore, increasing the ability of the surface to bind, adsorb and carry other compounds such as drugs, probes and proteins [16]. Natural and synthetic nanoparticles have practical applications in various fields from environmental remediation to an emerging multidisciplinary areas bringing chemistry, engineering, physics, biology, and medicine

together [43]. Figure 1.2 shows the different fields in which nanotechnology has impacted in medicine, pharmacy and diagnostics.

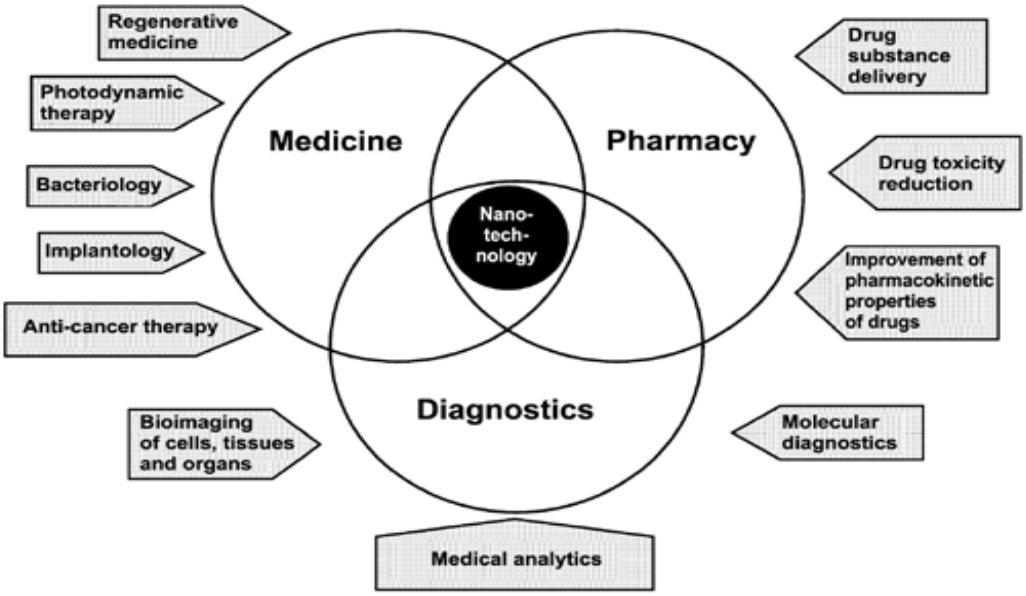

Figure 1. 2. The scope of nanotechnology's impact on medical sciences [43].

Nanoparticles have received an abundance of attention for potential use in therapeutic drug development [16]. In the last few years, they have been found to have promising carrier abilities for targeted drug delivery and imaging probes [20]. The interaction of nanomaterials with biomolecules and cells highly depends on their properties including size, shape, chemical composition, surface structure and charge, aggregation and agglomeration, and solubility [17]. Nanoparticles are also used in electronic applications that includes computing, flash memory chips for iPod nanos, antimicrobial and antibacterial coatings on the mouse, the keyboard, and the cell phone castings [45, 46]. Nanoparticles have also gained attention in the dye synthesized solar cells research replacing the molecular and they are very promising due to their low-temperature solution processing, excellent tuneable bandgap properties with quantum confinement effect, multiple exciton generation, and higher absorption coefficients [47].

Currently nanostructured materials are being studied for their potential applications in photovoltaic. Nano-structured layers in thin film solar cells provides significant advantages [48]. These materials give hope to the development of photovoltaics, be it in inorganic or organic solar cells. They have potential in emerging energy applications due to their wide bandgap [49]. Researchers believe that nanoparticles can also be used in the paint and coatings industry as they can improve the hardening, ultra violet light absorption and biocide properties to a very great extent [50]. Currently nanotechnology is investigated in transportation field specifically in nano-filters, anti-glare coatings, carbon black in tyres, Giant magnetoresistance (GMR) sensors, fuel additives, dirt protection, nano-catalysts to name a few [51].

Nanotechnology is now being used in agriculture for plant protection (protecting the food and agriculture from bacteria, fungal and viral agents [52]), processing, packaging transportation of the products, as to limit the pathogenic growth on packaged foods. It has been shown that agriculture can be more efficient by using nano-sensors and nano-agricultural chemicals [53]. Nanoparticles exhibit a broad-spectrum antipathogenic activity against possible pathogens that are the reason for food borne diseases. The antimicrobial mechanism of action of nanoparticles is typically considered as of few prototypes such as oxidative stress and cell damage, metal ion release, or non-oxidative mechanisms [54].

1.1.6. Synthesis of nanoparticles

There are various ways to synthesize nanoparticles including physical, chemical and biological methods. However, these methods show several advantages as well as some limitations [55]. At this point, the aim of all researchers is to synthesize nanomaterials with specific properties that will suit certain applications. Synthesis of nanomaterials can be broken down into physical

and chemical synthesis. The physical methods are based on subdivision of bulk materials and that includes mechanical crushing or breaking the materials. The chemical methods are about reducing the metal ions or decomposition of specific precursors to form atoms. Chemical methods tend to give nanoparticles with narrow size distribution [56].

There are two major approaches to prepare nanomaterials, the top down and bottom up approach (Figure 1.3). The top down approach is where the nanoparticles are synthesized by breaking down the bulk materials into smaller sizes creating the desired nanostructured materials. Physical methods are usually used to break down the materials such as mechanical milling [57], thermal ablation and some chemical treatments such as chemical etching. The bottom up approach is the inverse of the top down. In this approach, the nanoparticles are synthesized by building them up atom by atom. These atoms or molecules are assembled together by certain forces building up to larger and more organised system [58 - 60].

There are many methods that have been developed to synthesize nanoparticles under this big umbrella of bottom up and top down approaches. These methods can be divided into three categories; Chemical method, physical methods and the bio-assisted methods as demonstrated in Figure 1.4 [62]. Chemical methods include Condensation, Vacuum Deposition and Vaporization, Chemical Vapour Deposition (CVD) and Chemical Vapour Condensation (CVC), Mechanical Attrition, Chemical Precipitation, Sol-Gel Techniques, Electrodeposition [63].

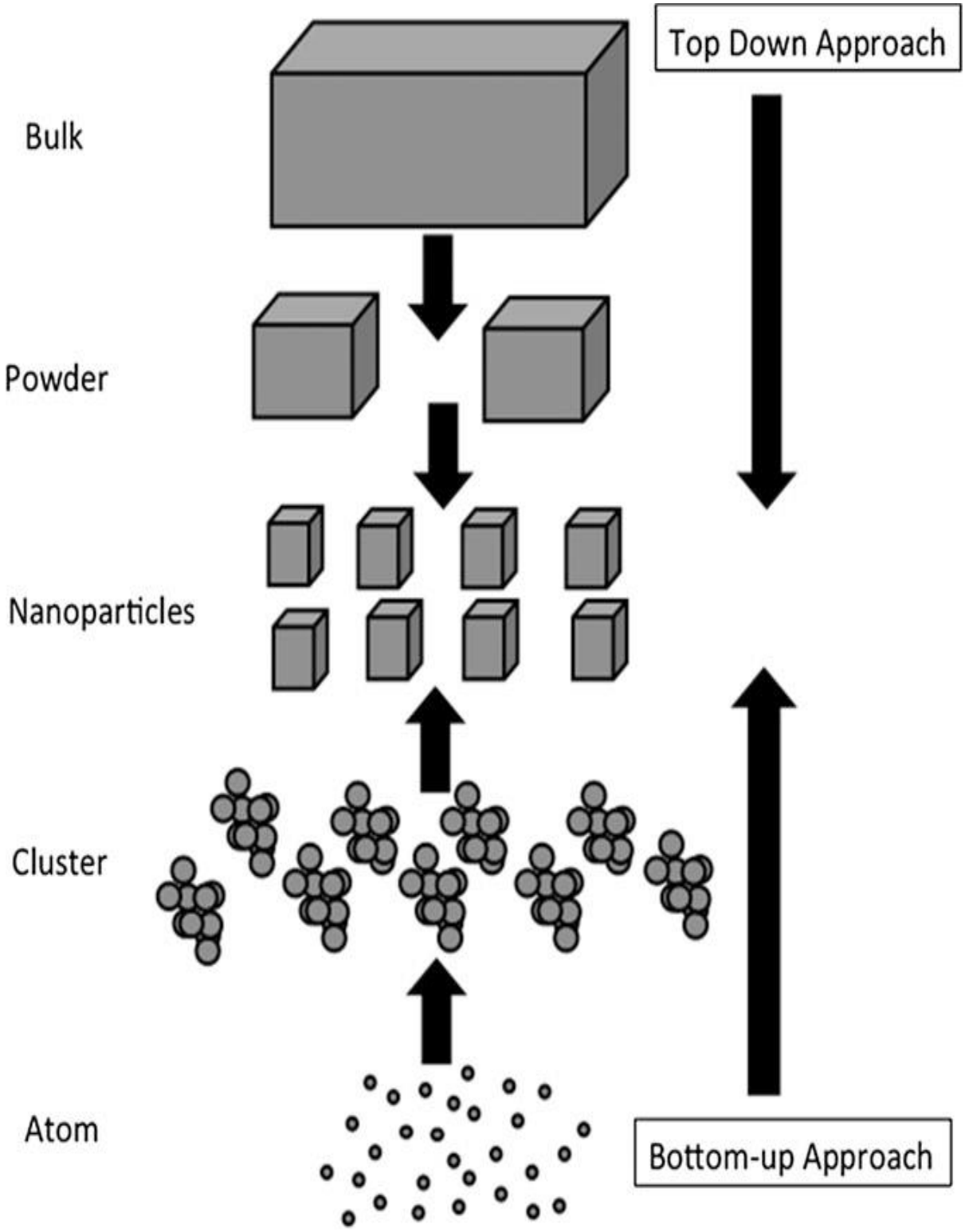

Figure 1. 3 Bottom up and top down approaches for nanoparticle synthesis [61].

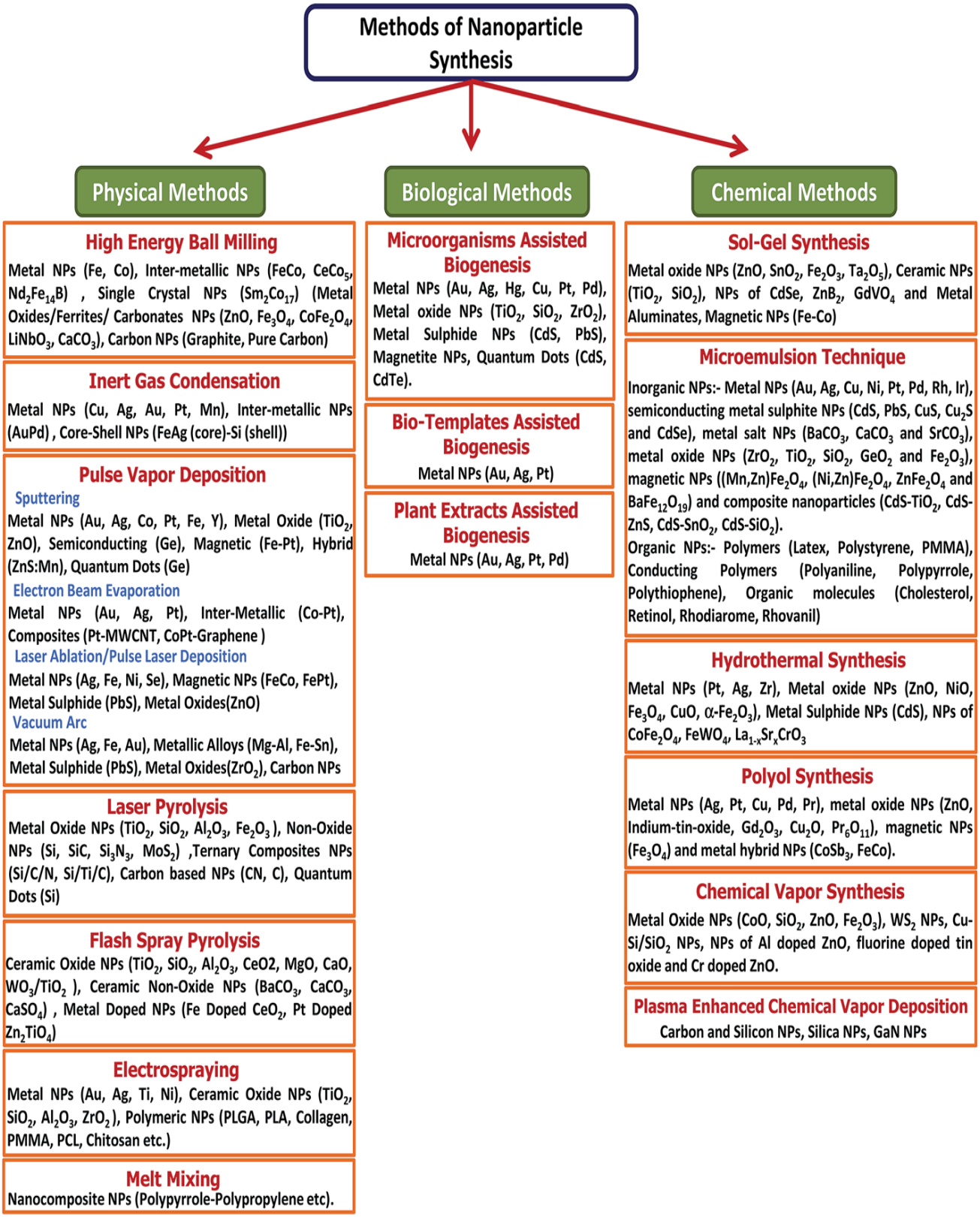

Figure 1. 4. Different methods for nanoparticle synthesis [62].

1.1.7. Single source precursor method

A lot have been done to develop methods to synthesize nanoscale particles. The single source molecular precursor method is one of those methods, it is proven to be an effective method to yield high quality well monodispersed crystalline nanoparticles [63]. In many other methods two different highly volatile starting materials are used in elevated temperatures to motivate the decomposition and nucleation [64]. Lately the use of the single source precursor route has gained tremendous attention because of its advantage of adopting a single-pot procedure under controllable conditions usually produce nanoparticles with higher surface area and less defects with improved stoichiometry [65, 66].

The single source precursor method has been used widely to synthesize metal sulphide nanoparticles [67-69]. In recent years, this method has been used to make various metal sulphide nanoparticles with different shapes and sizes [70-75]. It has been discovered that the structural and optical properties and the stability of the nanoparticles synthesized completely depends on conditions of the experiment and specific method of preparation furthermore it is known that in the synthesis of nanoparticles, it is of paramount importance to control not only the size but also the particle shape and morphology [76]. Therefore, the single source precursor has been used to study the effect of different temperatures on the shapes, morphologies and size of the nanoparticles [77]. It is also known that a particular single source precursor will give different morphologies when synthesized at different temperatures [78]. This method has also been used to study the effect of different capping agents on the properties of nanoparticles synthesized using different precursors. In this study metal dithiocarbamate complexes will be used as single source precursors.

1.1.8. Dithiocarbamates

Dithiocarbamate ligands are unsaturated bidentate ligands that can stabilize a variety of oxidation states and coordination geometries and form dithiolene complexes [79]. These ligands are widely active in transition metal chemistry, and the willingness of sulphur as a ligand in transition metal chemistry has been identified, their structural chemistry is extraordinarily diverse and has imperative advantages as compared to other organic ligands [80]. A developing interest in all dithiolate chemistry is all because of the functionalization of the dithio group which adds a rise to more intriguing architectures and modified physical properties. The molecular electrical conductivities make the sulphur rich planar complexes more interesting in these ligands shown in Figure 1.5. The cyclic substituents on the C-CS2 backbone may enhance conjugation with some degree of delocalization of negative charge over the cyclic skeleton and they are able to give greater electron delocalisation through C–S and C–C bonds [81].

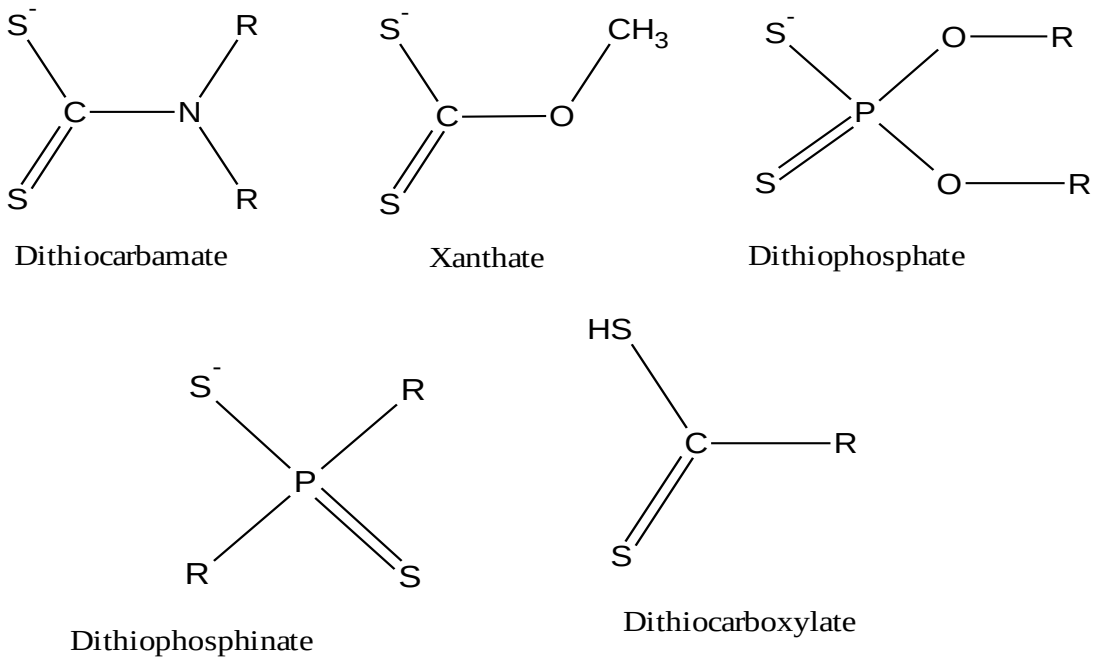

Figure 1. 5 Chemical structures of some 1,1-dithiolate [79].

In this study dithiocarbamate (DTC) will be used as ligands. DTC ligands freely make chelates with all transition metal ions through the two sulphur donor atoms. They are also known as molecules that selectively and strongly bind to different metal ions [82]. They are lipophilic and not hard to prepare, they can be synthesized from primary or secondary amines and tend to be soluble in water depending on the nature of the cation [83]. Dithiocarbamate and thiocarbamate anions when complexed with transition metal seem to possess a strong ability to hinder the growth of tumours of different tissues [84]. Dithiocarbamates are very interesting because of their metal binding property and their chelates vital role in biological systems [85].

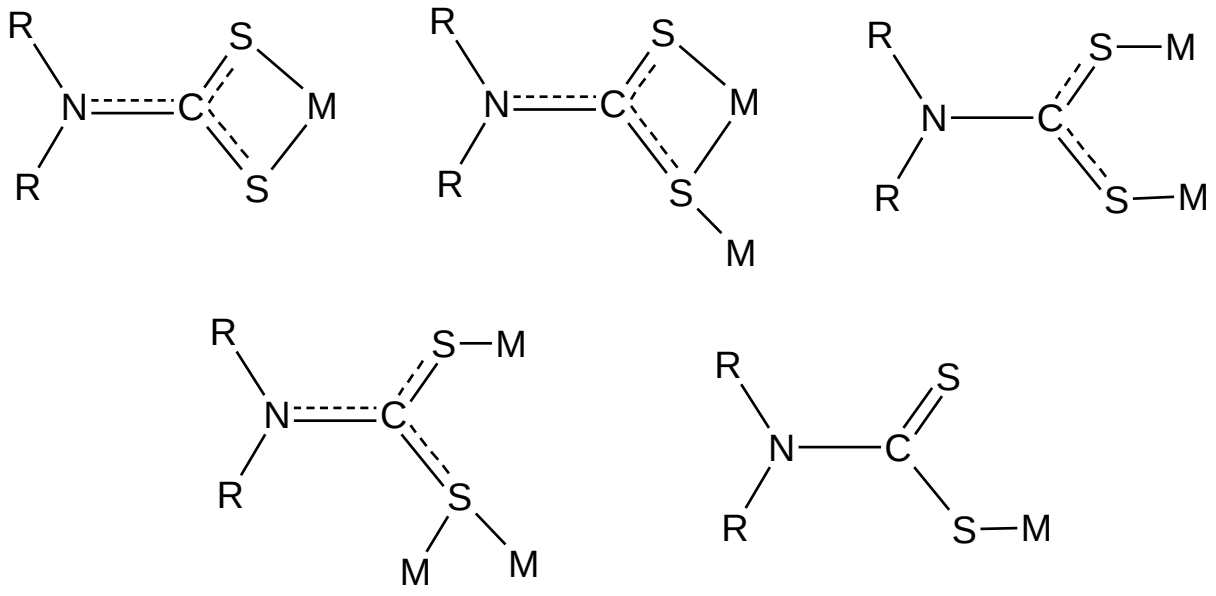

Figure 1. 6 The different binding modes of dithiocarbamates [86].

1.1.9. Problem statement of the study

Nanomaterials are getting immense attention in various fields. However, the smaller the particle size the more useful the materials. In drug delivery. It has been noted that the efficiency of the drug delivery system highly depends on the nanoparticle sizes [87]. In nanocatalysis; the smaller the nanoparticles the faster the reaction rate [88]. All this is due to the large surface area of the smaller sized particles. The focus now in nanotechnology research is to further reduce the size of particles and control the morphology and facet orientation of the nanoparticles, while synthesizing stable nanoparticles without affecting their activity [89].

Factors affecting the properties of these materials such as are agglomeration, are still a challenge. When the nanoparticles are agglomerated their size increases and that reduces their surface area which is one of the important properties of the nanoparticles and that calls for the synthesis of well dispersed nanomaterials. Therefore, the aim is now to overcome the attractive forces that lead to the agglomeration between the nanoparticles without disturbing the structural properties [90, 91]. Currently stabilizers, surfactants and capping agents are used to minimize the agglomeration effect. However, sometimes their effect is not the desired one. Their presence can block the accessibility of the active sites and can at times increase the size of the particles [92]. Another general challenge is to replace noble and critical metals by other abundant base transition metals depending on the applications [89].

1.1.10. Motivation of the study

The near Infrared light absorption of CuS nanoparticles that is attributed to the *d-d* transition of Cu^{2+} ions makes the copper sulphides to be beneficiary to various applications in different ways. Copper sulphides are found to be important base materials as absorber coating and are extensively utilised in photovoltaic and photodetectors applications because of their different near solar control characteristics. It is also a moderate conductor of electricity and has its potential use in catalysis [93]. These materials have also attracted a growing attention from biomedical researchers worldwide, because of their known intriguing properties [94].

Silver metal is known of its ability to adsorb and penetrate the bacterial wall while disturbing the cellular respiration and damaging compounds that contains sulphide and/or phosphorous like DNA and proteins, because of this, silver-based nanoparticles were found to be suitable material for different biological application as they are less toxic [95]. Silver sulphide semiconductor nanoparticles exhibit a potential in photoelectric and thermoelectric application and have been employed in optical and electronic devices, such as photovoltaic cells, photoconductors, IR detectors and as superionic conductors [96].

In this study oleylamine was chosen because of its ability to offer a strong reductive environment in the synthesis of nanoparticles. Oleylamine can act as an alternative reducing agent, which is inexpensive and even stronger when compared to other reducing agents and also act as a capping agent [97]. On the other side Oleic acid has been used and found to be able to control the size and monodispersity of the nanoparticles [98]. Oleic acid is an organic

species with high affinity due to its carboxylic group, and attributed to that, oleic acid is often used as a surfactant to improve the surface passivation of nanoparticles [99].

1.2. Literature review

1.2.1. Copper sulphide nanoparticles

Copper transition metal has interesting chemical and physical properties. Copper based materials are able to undergo different reactions because of their various oxidation states 0, +1, +2, and +3. Due to those unique characteristics and properties, the copper-based nanomaterials have gained attention in many nanotechnology applications [100]. Copper has been discovered to be one of the safe inorganic materials because of its non-toxicity with antifungal activity, and remarkable potential in a wide range of biological, catalytic and other applications especially in the form of nanoparticles [101]. Therefore, because of the high conductivity, high melting points and low electrochemical migration behaviour of these materials, copper nanoparticles are being investigated [102].

In all the copper chalcogenides, copper sulphides have attracted a lot of attention from researchers. Copper sulphide is a *p*-type semiconductor with different crystal structures and optical properties. Their possible air and thermal stable phases are: Cu_2S, $Cu_{31}S_{16}$ or $Cu_{1.96}S$, Cu_9S_5 or $Cu_{1.8S}$, Cu_7S_4 or $Cu_{1.75}S$, Cu_9S_8 or $Cu_{1.12}S$ and CuS. Covellite (CuS) contains the more concentration of free carriers compared to others with the lowest Cu: S ratio. However, the chalcocite, Cu_2S, contains the highest Cu:S ratio owing to the free holes due to the copper deficiency. This phase has lesser carriers and can change to djurleite, $Cu_{1.97}S$, phase when exposed to air. $Cu_{1.97}S$ has more carriers and due to that this phase can have near infrared Localised Surface Plasmon Resonance (NIR LSPR) band [103-107]. The bandgap energy of

copper sulphide that ranges from 1.2 to 2.53 eV is beneficial for light absorption under sunlight illumination [108].

Copper sulphide nanoparticles have been synthesized from different methods as described in Figure 1.4. Using some of these methods, the shape of the copper sulphide nanoparticles has been controlled to different shapes such as; nanorods that have been achieved with the solvent-free thermolysis of copper thiolate precursors and can now be synthesized with other methods and be stable [109, 110], nanodisk that were at first mistaken for nanorods when standing vertically on the substrate [111, 112] and nanofibers [113-115]. These materials have been investigated in different applications as presented in Figure 1.7.

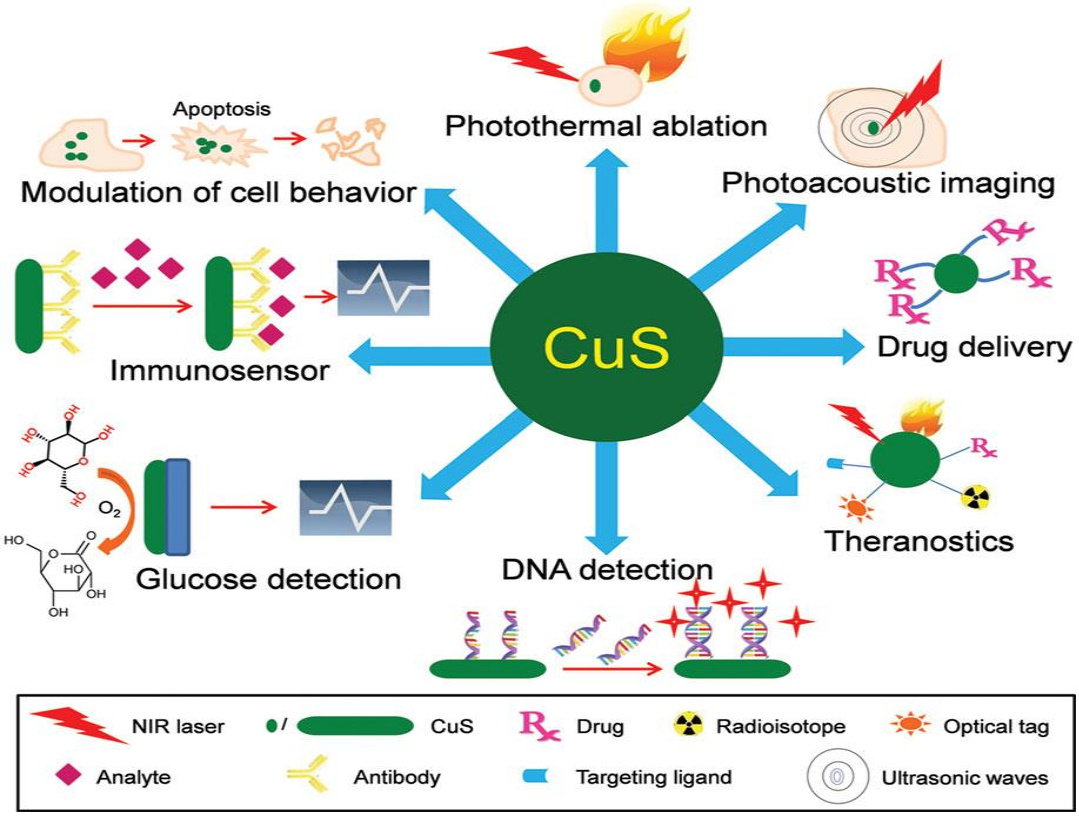

Figure 1. 7. Some copper sulphide nanoparticles biomedical applications [116].

Copper sulphide nanoparticles have gained an increasing consideration from biomedical researchers, they have been studied at preclinical level, molecular imaging with different techniques, cancer therapy based on the copper sulphide photothermal properties, and also in drug delivery and theranostic applications [117]. The effect of various surface morphologies, structures, and shapes (nanowires, nanospheres, nanotubes, nanoplates, and nanorods) have also been studied in both photoacoustic imaging and cancer therapy [118]. Although the found evidence from all the studies about metallic sulphide shows that these nanoparticles have a promising potential, there are still many different challenges to be investigated and cleared before they can be utilised in biomedicine [119].

1.2.2. Silver sulphide nanoparticles

Silver and some silver complexes have been widely used to treat bacterial and wound infections more especially in the treatment of burns. After the emergence of nanotechnology as the metals were reduced to nano sized materials silver nanoparticles were found to have antimicrobial activity [120]. Silver nanoparticles are currently used as antimicrobial agents to dress wounds and as coats for surgical instruments. They have been found to have different ways in which they penetrate the human body and accumulate in various tissues [121]. The applications of silver nanoparticles are now expanding to various fields that includes medical, food, health care, consumer, and industrial purposes, this is all due to their unique physical and chemical properties [122].

As a result of certain shortcomings of the silver nanoparticles against some microbials, interest in stabilizing these materials, using inorganic and other materials have been studied [123]. Silver nanoparticles has been noticed to always go through sulfidation, which is the

transformation of silver nanoparticles to more stable silver sulphide nanoparticles [124]. Through this sulfidation the silver nanoparticles toxicity is reduced and that lead to the investigation of silver sulphide nanoparticle [124].

Ag_2S is a direct narrow band gap semiconductor with special properties. Ag_2S nanostructures have been widely researched in chemistry and biochemistry fields because of their unusual optical, electrical, and mechanical properties [125]. Silver sulphide nanoparticles have also been synthesized via single source precursor method [126-128]. It was observed that when making these materials, they have a tendency of giving final products as a mixture of silver sulphide and metallic silver crystallites when the precursor molecule is injected at a lower temperature [129].

Silver sulphides were proven to possess high ion conductivity when compared to other metal and that attracted special attention as they can be used in resistive switches and non-volatile memory devices [130]. Silver sulphide nanoparticles are currently being further investigated as infrared active nanomaterials that can provide environmentally stable alternatives to heavy metals [131]. Silver nanoparticles are being given an attention because of their more desirable antimicrobial effects towards a wide range of microorganisms as well as multi drug resistant and yeast pathogen, they are now investigated for their anticancer activity [132].

According to the study by Venkatesan *et al.* silver nanoparticles are showing effective anticancer property against breast cancer cells [133]. After silver nanoparticles were tested against breast cancer, leukaemia, hepatocellular carcinoma, skin and lung carcinoma, cell lines Wei *et al*. confirmed that they can serve as therapeutic platforms in many biomedical

applications, but their effectiveness needs to be fully understood before they can be widely employed [134]. Silver sulphide nanoparticles have also been found as attractive nano-agents with near-infrared fluorescence for biological imaging [135]. As a result, they are now being investigated for possible applications in various optoelectronics, electronics and industrial applications [136].

1.2.3. Aims and Objectives of the study

1.2.3.1. Aim:

The main aim of the study is to synthesize, characterize copper(II) and silver(I) dithiocarbamate complexes and use them as single source precursors to synthesize metal sulphide nanoparticles and study their structural and optical properties.

1.2.3.2. Objectives:

- Synthesis and characterization of eight dithiocarbamate ligands.
- Synthesis and characterization of copper(II) dithiocarbamate complexes.
- Synthesis and characterization silver(I) dithiocarbamate complexes.
- Synthesis of copper sulphide and silver sulphide nanoparticles.
- Structural studies of the synthesized metal sulphide nanoparticles using p-XRD, TEM, ERTEM, SEM, EDX and FTIR.
- Optical studies of the metal sulphide nanoparticles using UV-Vis and PL spectroscopy

1.3. References

[1] Jeevanandam, J.; Barhoum, A.; Chan, Y. S.; Dufresne, A.; Danquah, M. K. Review on nanoparticles and nanostructured materials: History, sources, toxicity and regulations. *Beilstein J. Nanotechnol*. **2018**, 9, 1050–1074.

[2] Ng, K. K.; Zheng, G. Molecular interactions in organic nanoparticles for phototheranostic applications. *Chem. Rev*. **2015**, 115, 11012−11042.

[3] Kumar, R.; Lal, S. Synthesis of organic nanoparticles and their applications in drug delivery and food nanotechnology: A review. *Nanomater. Mol. Nanotechnol.* 3:4, 1-11.

[4] Virlan, M. J. R.; Miricescu, D.; Radulescu, R.; Sabliov, C. M.; Totan, A.; Calenic, B.; Greabu, M. Organic nanomaterials and their applications in the treatment of oral diseases. *Molecules*, **2016**, 21, 207, 1-23.

[5] Rao, C. N. R.; Govindaraj, A.; Vivekchand, S. R. C. Inorganic nanomaterials: Current status and future prospects. *Ann. Rep. Prog. Chem. Sect. A*, **2006**, 102, 20–45.

[6] Rao, C. N. R.; Vivekchand, S. R. C.; Biswasa, K.; Govindaraja, A. Synthesis of inorganic nanomaterials. *Dalton Trans*. **2007**, 3728–3749.

[7] Dhand, V.; Rhee, K. Y.; Kim, H. J.; Jung, D. H. A comprehensive review of graphene nanocomposites: Research Status and Trends. *J. Nanomater.* **2013**, 2013, 1-14.

[8] Hussain, F.; Hojjati. M. Review article: Polymer-matrix nanocomposites, processing, manufacturing, and application: An Overview. *J. Composite Mater*. **2006**, 40, 17, 1511-1517.

[9] Rahul Sahay, Venugopal Jayarama Reddy and Seeram Ramakrishna. Synthesis and applications of multifunctional composite nanomaterials. *Inter. J. Mechanical Mater. Eng.* **2014**, 9, 25, 1- 13.

[10] Bogue, R. Nanocomposites: A review of technology and applications. *Assembly Autom.* **2011**, 31/2, 106–112.

[11] Liu, H.; Feng, Y.; Chen, D.; Li, C.; Cuia, P.; Yang, J. Noble metal-based composite nanomaterials fabricated via solution-based approaches. *J. Mater. Chem. A*, **2015**, 3, 3182–3223.

[12] Raunika, A.; Raj, S. A.; Jayakrishna, K.; Sultan, M. T. H. Carbon nanotube: A review on its mechanical properties and application in aerospace industry. *IOP Conf. Ser.: Mater. Sci. Eng*. **2017**, 270 012027, 1-7.

[13] Thines, R. K.; Mubarak, N. M.; Nizamuddin, S.; Sahu, J. N.; Abdullah, E. C.; Ganesan, P. Application potential of carbon nanomaterials in water and wastewater treatment: A review. *J. Taiwan Institute Chem. Eng.* **2017**, 72, 116 –133.

[14] Casais-Molina, M. L.; Cab, C.; Canto, G.; Medina, J.; Tapia, A. Carbon nanomaterials for breast cancer treatment. *J. Nanomater*. **2018**, 2018, 1-9.

[15] Manawi, Y. M.; Ihsanullah, I. D.; Samara, A.; Al-Ansari, T.; Atieh, M. A.; A review of carbon nanomaterials' synthesis via the chemical vapor deposition (CVD) method. *Materials*, **2018**, 11, 822. 1-36.

[16] Abhilash, M. Potential applications of nanoparticles. *Int. J. Pharma Bio Sci.* 1, 1, **2010**, 1-12.

[17] Dong, L.; Craig, M. M.; Khang, D.; Chen, C. Applications of nanomaterials in biology and medicine. *J. Nanotech*. **2012**. 1-2.

[18] Zhang, Q. X.; Xu, X.; Bertrand, N.; Pridgen, E.; Swamia, A.; Farokhzada, O. C. Interactions of nanomaterials and biological systems: Implications to personalized nanomedicine. *Adv. Drug Deliv. Rev*. **2012**, 64, 13, 1363–1384.

[19] Dahman, Y. Chapter 9 - Electronic and Electro-Optic Nanotechnology. *Nanotechnol. Functional Mater. Eng. Micro Nano Technol.* **2017**, 191-206.

[20] Tan, J.; Shah, S.; Thomas, A.; Ou-Yang, H.; Liu, Y. The influence of size, shape and vessel geometry on nanoparticle distribution. *Micrifluid nanofluid*. **2012**, 14(1-2), 77–87.

[21] Sherje, A. P.; Jadhav, M.; Dravyakar, B. R.; Kadam, D. Dendrimers: A versatile nanocarrier for drug delivery and targeting. *Int. J. Pharm*. **2018** 5;548, 1, 707-720.

[22] Klajnert, B.; Bryszewska, M. Dendrimers: Properties and applications. *Acta Biochim. Polonica*, **2001**, 48, 1, 199-208.

[23] Balogh, L. P.; Redmond, S. M.; Balogh, P.; Tang, H.; Martin, D. C.; Rand, C. Self assembly and optical properties of dendrimer nanocomposite multilayers. *Macromol. Biosci.* **2007**, 7, 1032–1046.

[24] Pal, S. L.; Jana, U.; Manna, P. K.; Mohanta, G. P.; Manavalan, R. Nanoparticle: An overview of preparation and characterization. *J. Appl. Pharmac. Sci*. **2011**, 01, 06, 228-234.

[25] Popov, V. N. Carbon nanotubes: Properties and application. *Mater. Sci. Eng.* **2004**, 43, 3, 61-102.

[26] Eatemadi, A.; Daraee, H.; Karimkhanloo, H.; Kouhi, M.; Zarghami, N.; Akbarzadeh, A.; Abasi, M.; Hanifehpour, Y.; Joo, S. W. Carbon nanotubes: Properties, synthesis, purification, and medical applications. *Nanoscale Res. Lett*. **2014**, 9, 1- 13.

[27] Abbasi, E.; Aval, S. F.; Akbarzadeh, A.; Milani, M.; Nasrabadi, H. T; Joo, S. W.; Hanifehpour, Y.; Nejati-Koshki, K.; Pashaei-Asl, R. Dendrimers: Synthesis, applications, and properties. *Nanoscale Res. Lett*. **2014**, 9, 1, 247 - 250.

[28] Valizadeh, A.; Mikaeili, H.; Samiei, M.; Farkhani, S. M.; Zarghami, N.; kouhi, M.; Akbarzadeh, A.; Davaran, S. Quantum dots: Synthesis, bioapplications, and toxicity. *Nanoscale Res. Lett*. **2012**, 7, 480. 1-14.

[29] Petryayeva, E.; Algar, W. R.; Medintz, I. L. Quantum dots in bioanalysis: A Review of applications across various platforms for fluorescence spectroscopy and imaging. *Focal Point Rev*. **2013**, 67, 3, 215-252.

[30] Bera, D.; Qian, L.; Teng-Kuan, T.; Holloway, P. H. Quantum dots and their multimodal applications: A Review. *Materials*, **2010**, 3, 2260-2345.

[31] Bukowski, T. J.; Simmons, J. H. Quantum dot research: Current state and future prospects. *Crit. Rev. Solid State Mater. Sci*. **2002**, 7, 119–142.

[32] Tiruwa, R. A review on nanoparticles – preparation and evaluation parameters. *Indian J. Pharm. Biol. Res*. **2015**; 4, 27-31.

[33] Von der Kammer, P. C. F.; Hofmann, M. B. T. Nanoparticles: Structure, properties, preparation and behaviour in environmental media. *Ecotoxicology*, **2008**, 17, 326-343.

[34] Baer, D. R. Surface Characterization of Nanoparticles: Critical needs and significant challenges. *J. Surface Analysis*, **2011**, 17, 3, 163-169.

[35] Biener, J.; Wittstock, A.; Baumann, T. F.; Weissmüller, J.; Bäumer, M.; Hamza, A. V. Surface chemistry in nanoscale materials. *Materials*, **2009**, 2, 2404-2428.

[36] Ashrafi, A. Quantum confinement: An ultimate physics of nanostructures. *Encyclopedia Semicond. Nanotech*. **2011**, 5, 1–67.

[37] Flory, F.; Escoubas, L.; Berginc, G. Optical properties of nanostructured materials: A review. *J. Nanophot.* **2011**, 5, 052502-1 – 052502-20.

[38] Kumbhakar, P.; Ray, S. S.; Stepanov, A. L. Optical properties of nanoparticles and nanocomposites. *J. Nanomater*. **2014**, 1-2.

[39] Kelly, K. L.; Coronado, E.; Zhao, L. L.; Schatz, G. C. The optical properties of metal nanoparticles: The influence of size, shape, and dielectric environment. *J. Phys. Chem*. B **2003**, 107, 668-677.

[40] Sun, C. Q.; Chen, T. P.; Tay, B. K.; Li, S.; Huang, H.; Zhang, Y. B.; Pan, L. K.; Lau, S. P.; Sun, X. W. An extended 'quantum confinement' theory: surface-coordination imperfection modifies the entire band structure of a nanosolid. *J. Phys. D: Appl. Phys*. **2001**, 34, 3470–3479.

[41] Duan, X.; Yi, L.; Zhang, X.; Huang, S. Size-dependent optical properties of nanoscale and bulk long persistent phosphor SrAl2O4:$Eu^{2+,}$ Dy^{3+}. *J. Nanomater*. **2015**, 1-7.

[42] Sattler, K.; The energy gap of clusters nanoparticles, and quantum dots. *Nanomater. Magn. Thin Films*. **2002,** 5, 61-97.

[43] Bhatia S. (**2016**) Nanoparticles Types, Classification, Characterization, Fabrication Methods and Drug Delivery Applications. In: Natural Polymer Drug Delivery Systems. Springer, Cham.

[44] Zaman, M.; Ahmad, E.; Qadeer, A.; Rabbani, G.; Khan, R. H. Nanoparticles in relation to peptide and protein aggregation. *Int. J. Nanomed*. **2014**, 9, 899–912.

[45] Guo, D.; Xie, G.; Luo, J. Mechanical properties of nanoparticles: Basics and applications. *J. Phys. D: Appl. Phys*. **2014**, 47, 1-26.

[46] Rae, A. Real life applications of nanotechnology in electronics. *Microsyst. Special Report Nanosyst*. **2005**, 36-39

[47] Kumar, S.; Nehra, M.; Deep, A.; Kedia, D.; Dilbaghi, N.; Kim, K. Quantum-sized nanomaterials for solar cell applications. *Renew. Sustain. Energy Rev*. **2017**, 73, 821–839.

[48] Nabhani, N.; Emami, M. Nanotechnology and its Applications in Solar Cells. *ICMIE,* **2013**. 88 – 91.

[49] Tala-Ighil, R. Nanomaterials in Solar Cells. *Nanoelectrochem*. **2015**, 1-18.

[50] Cuffari, B. Nanotechnology in the Paint Industry. **2017**, https://www.azonano.com/article.aspx?ArticleID=4710 05\01\2019

[51] Mathew, J.; Joy, J.; Geaorge, C. S. Potential applications of nanotechnology in transportation: A review. *J. King Saud University – Scienc,* **2018**, doi:10.1016/j.jksus.

[52] Singh, S.; Singh, B. K.; Yadav, S. M.; Gupta, A. K. applications of nanotechnology in agricultural and their role in disease management. *Res. J. Nanosci. Nanotech.* **2015**, 5, 1, 1-5.

[53] Yogesh Bhagat, K. Gangadhara, Chidanand Rabinal, Gaurav Chaudhari and Padmabhushan Ugale. Nanotechnology in Agriculture: A Review. *J. Pure Appl. Microbio.* **2015**, 9, 1-12.

[54] Thakur, S.; Thakur, S.; Kumar, R. Bio-Nanotechnology and its Role in agriculture and food industry. *J. Mol. Genet. Med*. **2018**, 12, 1-5.

[55] Vikram; P.; Arpit, B.; Rinki, G.; Navin, J.; Jitendra, P. Synthesis and Applications of Noble Metal Nanoparticles: A Review. *Eng. Med.* **2017**, 7, 8, 527-544(18).

[56] Tavakoli, A.; Sohrabi, M.; Kargari, A. A Review of methods for synthesis of nanostructured metals with emphasis on iron compounds. *Chem. Pap.* **2007**, 61, 151—170.

[57] Yadav, T. P.; Yadav, R. M.; Singh, D. P. Mechanical Milling: A top down approach for the synthesis of nanomaterials and nanocomposites. *Nanosci. Nanotech*. **2012**, 2(3), 22-48.

[58] Wang, Y.; Xia, Y. Bottom-up and top-down approaches to the synthesis of monodispersed spherical colloids of low melting-point metals. *Nano Letters.* **2004**, 4, 10 2047-2050.

[59] Wang, C.; Gao, X.; Chen, Z.; Chen, Y.; Chen, H. preparation, characterization and application of polysaccharide-based metallic nanoparticles: A review. *Polymers*, **2017**, 9, 689. 1-34.

[60] Arole, V. M.; Munde, S. V. Fabrication of nanomaterials by top-down and bottom-up approaches –An overview. *Mater. Sci.* (Special Issue), **2014**, 1, 89-93.

[61] Su, S. S.; Chang, I. Review of production routes of nanomaterials. *Commer. Nanotechnolog. A Case Study Approach*. **2018**, 15-28.

[62] Dhand, C.; Dwivedi, N.; Loh, X. J.; Ying, A. N. J.; Verma, N. K.; Beuerman, R. W.; Lakshminarayanan, R.; Ramakrishna, S. Methods and strategies for the synthesis of diverse nanoparticles and their applications: A comprehensive overview. *RSC Adv*. **2015**, 5, 105003–105037

[63] Malik, M. A.; Revaprasadu, N.; O'Brien, P. Air-stable single-source precursors for the synthesis of chalcogenide semiconductor nanoparticles. *Chem. Mater*. **2001**, 13, 913-920.

[64] Green, M.; O'Brien, P. A novel synthesis of cadmium phosphide nanoparticles using the single-source precursor $[MeCdPtBu_2]_3$. *Adv. Mater*. **1998**, 10, 7, 527-528.

[65] Maneeprakorn, W.; Malik, M. A.; O'Brien, P. The preparation of cobalt phosphide and cobalt chalcogenide (CoX, X ¼ S, Se) nanoparticles from single source precursors. *J. Mater. Chem*. **2010**, 20, 2329–2335.

[66] Majia, S. K.; Dutta, A. K.; Dutta, S.; Srivastava, D. N.; Paul, P.; Mondala, A.; Adhikarya, B. Single-source precursor approach for the preparation of CdS nanoparticles and their photocatalytic and intrinsic peroxidase like activity. *Appl. Catal. B: Environ*. **2012**, 126, 265–274.

[67] Deng, M.; Shen, S.; Zhang, Y.; Xuc, H.; Wang, Q. A generalized strategy for controlled synthesis of ternary metal sulfide nanocrystals. *New J. Chem*. **2014**, 38, 77—83.

[68] Akhtar, M.; Akhter, J.; Malik, M. A.; O'Brien, P.; Tuna, F.; Raftery, J.; Helliwell, M. Deposition of iron sulfide nanocrystals from single source precursors. *J. Mater. Chem*. **2011**, 21, 9737–9745.

[69] Shen, S; Zhang, Y.; Peng, L.; Xu, B.; Du, Y.; Deng, M.; Xub, H.; Wang, Q. Generalized synthesis of metal sulfide nanocrystals from single-source precursors: Size, shape and chemical composition control and their properties. *Cryst. Eng. Comm*. **2011**, 13, 4572–4579.

[70] Fartisincha, P. A.; Ajibade, P. A. Metal complexes of alkyl-aryl dithiocarbamates: Structural studies, anticancer potentials and applications as precursors for semiconductor nanocrystals. *J. Mol. Struct*. **2018**, 1155, 843-855.

[71] Sun, J.; Buhro, W. E. The use of single-source precursors for the solution–liquid–solid growth of metal sulfide semiconductor nanowires. *Angew. Chem*. **2008**, 120, 3259 –3262.

[72] Ajibade, P. A.; Botha, N. L. Synthesis and structural studies of copper sulfide nanocrystals. *Results in Physics*. **2016**, 6, 581-589.

[73] Mbese, J. Z.; Ajibade, P. A. Synthesis, structural and optical properties of ZnS, CdS and HgS nanoparticles from dithiocarbamato single molecule precursors, *J. Sulfur Chem*. **2014**, 35(4), 438–449.

[74] Nqombolo, A; Ajibade. P. A. Synthesis and spectral studies of Ni(II) dithiocarbamate complexes and their use as precursors for nickel sulphide nanocrystals. *J. Chem.* **2016,** 2016. 1-9.

[75] Chintso, T.; Ajibade, P. A. Synthesis and structural studies of hexadecylamine capped lead sulphide nanoparticles from dithiocarbamate complexes single source precursors. *Matt. Lett*. **2015**, 141, 1-6.

[76] Neena, D.; Devraj, K. M.; Bhagat, A. P. Role of capping agent in the synthesis of silver nanoparticles. *J. Pharmacy Reseach*. **2012**, 5, 4710-4712.

[77] Botha, N. L.; Ajibade, P. A. Effect of temperature on crystallite sizes of copper sulfide nanocrystals prepared from copper(II) dithiocarbamate single source precursor. *Mat. Sci. Semicond. Process*. **2016**, 43, 149–154.

[78] Mubiayi, K. P.; Revaprasadu, N.; Garje, S. S.; Moloto, M. J. Designing the morphology of PbS nanoparticles through a single source precursor method. *J. Saudi Chem. Soc*. **2017**, 21, 593–598.

[79] Tiekink, E. R. T. Aggregation patterns in the crystal structures of organometallic group XV 1,1-dithiolates: The influence of the Lewis acidity of the central atom, metal- and ligand bound steric bulk, and coordination potential of the 1,1-dithiolate ligands upon supramolecular architecture. *Cryst. Eng. Comm*, **2006**, 8, 104–118.

[80] Singh, M. K.; Sutradhar, S.; Paul, B.; Adhikari, S.; Laskar, F.; Butcher, R. J. Acharya, S.; Das, A. A new cadmium(II) complex with bridging dithiolate ligand: Synthesis, crystal structure and antifungal activity study. *J. Mol. Struc.* **2017**, 1139, 395 - 399.

[81] Gupta, A. N.; Kumar, V.; Singh, V.; Manar, K. K.; Singh, A. K.; Drew, M. G. B. Singh, N. Synthesis, crystal structures and conducting properties of heteroleptic nickel(II) 1,1-dithiolate-bpy/dppe ligand complexes. *Polyhedron*, **2015**, 101, 251–256.

[82] Nabipour, H.; Ghammamy, S.; Ashuri, S.; Aghbolagh, Z. S. Synthesis of a new dithiocarbamate compound and study of its biological Properties. *Org. Chem. J.* **2010**, 2, 75-80.

[83] Hogarth, G. Metal-dithiocarbamate complexes: Chemistry and biological activity. *Mini Rev. Med. Chem*. **2012**, 12, 12, 1202-15.

[84] Kennedy, T. P.; Method of treating cancer using dithiocarbamate derivatives. *United States Patent*. **2003**, US 6,548,540 B2.

[85] Ramesh, P. B.; Venkatesh, P.; Jabbar, A. A. Influence of dithiocarbamate on metal complex and thin film depositions. *Int. J. Innov. Res. Sci. Eng. Technol*. **2014**. 3, 15301-15309.

[86] Ajibade, P. A; Onwidiwe, D. C. Synthesis and characterization of group 12 complexes of N, N-methyl phenyl-N, N-butyl phenyl dithiocarbamate. *J. Coord. Chem*. **2011**, 64, 2963-2973.

[87] Rizvi, S. A. A.; Saleh, A. M. Applications of nanoparticle systems in drug delivery technology. *Saudi Pharmaceut. J*. **2018**, 26, 64–70.

[88] Suchomel, P.; Kvitek, L.; Prucek, R.; Panacek, A.; Halder, A.; Vajda, S.; Zboril, R. Simple size-controlled synthesis of Au nanoparticles and their sizedependent catalytic activity. *Scient. Reports*. **2018**, 8, 4589, 1-12.

[89] Navalón, S.; García, H. Nanoparticles for Catalysis. *Nanomaterials,* **2016**, 6, 123;

[90] Ashraf, M. A.; Peng, W.; Zare, Y.; Rhee, K. Y. Effects of size and aggregation/ agglomeration of nanoparticles on the interfacial/interphase properties and tensile strength of polymer nanocomposites. *Nanoscale Res. Lett*. **2018**, 13, 214, 1-7.

[91] Engelmann, U.; Buhl, E. M.; Baumann, M.; Schmitz-Rode, T.; Slabu, L. Agglomeration of magnetic nanoparticles and its effects on magnetic hyperthermia. *Curr. Directions Biomed. Eng*. **2017**, 3, 2, 457–460.

[92] Campisi, S.; Schiavoni, M.; Chan-Thaw, C. E.; Villa, A. Untangling the role of the capping agent in nanocatalysis: Recent advances and perspectives. *Catalysts*, **2016**, 6, 185, 1-22.

[93] Riyaz, S.; Parveen, A; Azam, A. Microstructural and optical properties of CuS nanoparticles prepared by sol—gelroute. *Perspectives Sci*. **2016**, 8, 632—635.

[94] Goel, S.; Chen, F.; Cai, W. Synthesis and biomedical applications of copper sulfide nanoparticles: From sensors to theranostics. *Small*, **2014**, 10, 4, 631–645.

[95] Sibiya, P. N.; Moloto, M. J. Synthesis, characterisation and antimicrobial effect of starch capped silver sulphide nanoparticles against *Escherichia coli* and *Staphylococcus aureus*. *Int. J. Nanotechnol*. **2017**, 14, 385-398.

[96] Emadi, H.; Salavati-Niasari, M.; F. Davar, F. Synthesis and characterisation of silver sulphide nanoparticles by ultrasonic method. *Micro Nano Lett.* **2011**, 6, 909–913.

[97] Xu, Z.; Shen, C.; Hou, Y.; Gao, H.; Sun, S. Oleylamine as both reducing agent and stabilizer in a facile synthesis of magnetite nanoparticles. *Chem. Mater*. **2009**, 21, 1778–1780.

[98] Guardiaa, P; Batlle-Brugala, B.; Rocab, A. G.; Iglesiasa, O.; Moralesb, M. P.; Sernab, C. J.; Labarta, A.; Batllea, X. Surfactant effects in monodisperse magnetite nanoparticles of controlled size. *J. Magnet. Magnet. Mater*. **2007**, 316, 1-2.

[99] Lobato, N. C. C.; Mansur, M. B.; de Mello Ferreira, A. Characterization and chemical stability of hydrophilic and hydrophobic magnetic nanoparticles. *Mater. Res*. **2017**, 20, 3, 736-746.

[100] Gawande, M. B.; Goswami, A.; François-Xavier Felpin, F.; Asefa, T.; Huang, X.; Silva, R.; Zou, X.; Zboril, R.; Varma, R. S. Cu and Cu-based nanoparticles: Synthesis and applications in catalysis. *Chem. Rev*. **2016**, 116, 3722−3811.

[101] Rafique, M.; Shaikh, A. J.; Tahir, M. B.; Rasheed, R. A review on synthesis, characterization and applications of copper nanoparticles using green method. *Nano Brief Reports Rev*. **2017**, 12, 1750043-1 - 1750043-23.

[102] Tamilvanan, A.; Balamurugan, K.; Ponappa, K.; Kumar, M. Copper nanoparticles: Synthetic strategies, properties and multifunctional applications. *Int. J. Nanosci*. **2014**, 13, 2, 1430001-1 – 1430001-23.

[103] Liu, Y.; Liu, M.; Swihart, M. T. Plasmonic Copper Sulfide-Based Materials: A brief introduction to their synthesis, doping, alloying, and applications. *J. Phys. Chem*. C, **2017**, 121, 13435−13447.

[104] Shen, S.; Wang, Q. Rational tuning the optical properties of metal sulfide nanocrystals and their applications. *Chem. Mater*. **2013**, 25, 1166−1178.

[105] Kristl, M.; Hojnik, N.; Gyergyek, S.; Drofenik, M. Sonochemical preparation of copper sulfides with different phases in aqueous solutions. *Mater. Res. Bull*. **2013**, 48, 1184-1188.

[106] Khan, M. D.; Akhtar, J.; Malik, M. A.; Revaprasadu. N. Tuning the phase and shape of copper sulfide nanostructures using mixed solvent systems. *Chem. Select*. **2016**, 1, 5982-5989.

[107] Lim, W. P.; Wong, C. T.; Ang, S. L.; Low, H. Y.; Chin, W. S. Phase-selective synthesis of copper sulfide nanocrystals. *Chem. Mater*. **2006**, 18, 6170-617.

[108] Isac, L.; Popovici, I.; Enesca, A.; Duta, A. Copper sulfide (CuxS) thin films as possible *p*-type absorbers in 3D solar cells. *Energy Procedia*. **2010**, 2, 71–78.

[109] Kruszynska, M.; Borchert, H.; Bachmatiuk, A.; Rummeli, M. H.; Buchner, B.; Parisi, J.; Kolny-Olesiak, J. Size and shape control of colloidal copper(I) sulfide nanorods. *ACS Nano*, **2012**, 6, 7, 5889–5896.

[110] Fang, J.; Zhang, P.; Zhou, G. Hydrothermal synthesis of highly stable copper sulfide nanorods for efficient photo-thermal conversion. *Mater. Lett*. **2018**, 217, 71–74.

[111] Wang, J.; Su-Wen, H.; Tao, A. R.; Jokerst, J. V. Copper sulfide nanodisk as photoacoustic contrast agent for ovarian tumor detection. *Proc. of SPIE,* **2017**, 10064, 100642D-1- 100642D5.

[112] Zhang.; Gao, L. Copper sulfide flakes and nanodisks. *J. Mater. Chem*. **2003**, 13, 2007–2010.

[113] Chen, J.; Deng, S. Z.; Xua, N. S.; Wang, S.; Wen, X.; Yanga, S.; Yang, C.; Wang, J.; Ge, W. Field emission from crystalline copper sulphide nanowire arrays. *Appl. Phys. Lett*. **2002**, 80, 19, 3620 – 3623.

[114] Foley, S.; Geaney, H.; Bree, G.; Stokes, K.; Connolly, S.; Zaworotko, M. J.; Ryan, K. M. Copper sulphide (CuxS) nanowire-in-carbon composites formed from direct sulfurization of the metal-organic framework hkust-1 and their use as Li-ion battery cathodes. *Adv. Funct. Mater*. **2018**, 28, 1 – 8.

[115] Hsua, K. K.; Chenb, Y C.; Linc, Y. G. Synthesis of copper sulfide nanowire arrays for high-performance supercapacitors. *Electrochim. Acta.* **2014**, 139, 401–407.

[116] Gross, S.; Vittadini, A.; Dengo, N. Functionalisation of colloidal transition metal sulphides nanocrystals: A fascinating and challenging playground for the chemist. *Crystals,* **2017**, 7, 1 – 40.

[117] Li, Y.; Lu, W.; Huang, Q.; Huang, M.; Li, C.; Chen, W. Copper sulfide nanoparticles for photothermal ablation of tumor cells. *Nanomedicine,* **2010**, 5, 1161–1171

[118] Wang, L. Synthetic methods of CuS nanoparticles and their applications for imaging and cancer therapy. *RSC Adv*. **2016**, 6, 82596-82615.

[119] Argueta-Figueroa, L.; Martínez-Alvarez, O.; Santos-Cruz, J.; Garcia-Contreras, R.; Acosta-Torres, L. S.; de la Fuente-Hernández, J.; Arenas-Arrocena, M. C. Nanomaterials made of non-toxic metallic sulfides: A systematic review of their potential biomedical applications. *Mat. Sci. Engineer*. **2017**, 76, 1305–1315.

[120] Khatoon, N.; Mazumder, J. A.; Sardar, M. biotechnological applications of green synthesized silver nanoparticles. *J. Nanosci. Curr. Res*. **2017**, 2, 1 - 10

[121] Ciucă, A. G.; Grecu, C. I.; Rotărescu, P; Gheorghe, I.; Bolocan, A.; Grumezescu, A. M.; Holban, A. M.; Andronescu, E. Chapter 30 - Nanostructures for drug delivery: Pharmacokinetic and toxicological aspects. *Micro. Nano. Technol*. **2017**, 941-957.

[122] Zhang, X. F.; Liu, Z. G.; Shen, W.; Gurunathan, S. Silver nanoparticles: Synthesis, characterization, properties, applications, and therapeutic approaches. *Int. J. Mol. Sci*. **2016**, 17, 1534, 1-34.

[123] Burdus, A. C.; Gherasim, O.; Grumezescu, A. M.; Mogoanta, L.; Ficai, A.; Andronescu, E. Biomedical applications of silver nanoparticles: An up-to-date overview. *Nanomaterials*, **2018**, 8, 681.

[124] Li, L.; Zhou, Q.; Geng, F.; Wang, Y.; Jiang, G. Formation of nanosilver from silver sulfide nanoparticles in natural waters by photoinduced Fe(II, III) redox cycling. *Environ. Sci. Technol*. **2016**, 50, 13342-13350.

[125] Cui, C.; Li, X.; Liu, J.; Hou, Y.; Zhao, Y.; Zhong, G. Synthesis and functions of Ag_2S nanostructures. *Nano. Res. Lett.* **2015**, 10:431.

[126] Jayanthi, K.; Kannaiyan, P. Synthesis of silver nanoparticles doped bismuth sulphide using single source precursor and its electrocatalytic activity on oxidation of hydrazine. *Asian J. Chem*. **2013**, 25, S91 – S94.

[127] Adner, D.; Noll, J.; Schulze, S.; Hietschold, M.; Lang, H. Asperical silver nanoparticles by thermal decomposition of a single-source-precursor. *Inorg. Chim. Acta*. **2016**, 446, 19–23.

[128] Lin, X. Z.; Teng, X.; Yang, H. Direct synthesis of narrowly dispersed silver nanoparticles using a single-source precursor. *Langmuir*, **2003**, 19, 10081-10085.

[129] Tang, Q.; Yoon, S. M.; Yang, H. J.; Lee, Y.; Song, H. J.; Byon, H. R.; Choi, H. C. Selective degradation of chemical bonds: From single-source molecular precursors to metallic Ag and semiconducting Ag_2S nanocrystals via instant thermal activation. *Langmuir*, **2006**, 22, 2802-2805.

[130] Sadovnikov, S. I.; Gusev, A. I. Structure and properties of Ag_2S/Ag semiconductor/metal hetero-nanostructure. *J. Nanotech. Mater. Sci.* **2016**, 3, 27 – 36.

[131] Kang, M. H.; Kim, S. H.; Jang, S.; Lim, J. E.; Chang, H.; Ki-jeong, K.; Myung, S.; Park, J. K. Synthesis of silver sulfide nanoparticles and their photodetector applications. *RSC Adv*. **2018**, 8, 28447–28452.

[132] Ramachandran, R.; Krishnaraj, C.; Sivakumar, A. S.; Prasannakumar, P.; Kumar, V. K. A.; Shimc, K. S.; Chul-Gyu, S.; Yun, S. Anticancer activity of biologically synthesized silver and gold nanoparticles on mouse myoblast cancer cells and their toxicity against embryonic zebrafish. *Mat. Sci. Eng*. **2017**, 73, 674–683.

[133] Venkatesan, J.; Lee, J. Y.; Kang, D. S; Anil, S.; Kim, S. K.; Shim, M. S.; Kim, D. G. Antimicrobial and anticancer activities of porous chitosan-alginate biosynthesized silver nanoparticles. *Int. J. Biol. Macromol*. **2017**. 98, 515-525

[134] Wei, L.; Lu, J.; Xu, H.; Patel, A.; Chen, Z.; Chen, G. Silver nanoparticles: synthesis, properties, and therapeutic applications. *Drug Discov. Today*, **2015**, 20, 595–601.

[135] Ma, L.; Li, L.; Li, X.; Deng, L.; Zheng, H. Silver sulfide nanoparticles as photothermal transducing agents for cancer treatment. *J. Nanomater. Mol. Nanotechnol*. **2016**, 5:2.

[136] Nwofe, P. A.; Prospects and challenges of silver sulphide thin films: A review. *Euro. J. Appl. Eng. Sci. Res.* **2015**, 4, 20-27

CHAPTER TWO

EXPERIMENTAL

2.1. Physical measurements

2.1.1. Conductivity measurements

The conductivity values were measured using 5410 conductivity meter. The ligands were dissolved in water and the copper complexes were dissolved in dimethyl sulfoxide.

2.1.2. FTIR spectroscopy

The FTIR spectra were scanned using Perkin Elmer FTIR spectrometer (FTIR-100). The spectra were recorded from 400 to 4000 cm^{-1}. They were all collected at room temperature.

2.1.3. UV-Visible spectroscopy

The electronic spectra of the ligands and complexes in solution were recorded using the Cary 100 UV-Vis spectrophotometer (Agilent technologies). The ligands were dissolved in water and complexes in DMSO or chloroform, quartz cuvette which is 10 mm in length was used.

2.1.4. NMR spectroscopy

The NMR spectra of the ligands and complexes were recorded using NMR Bruker 400Hz. The ligands were dissolved in water and the complexes in DMSO and chloroform.

2.1.5. Thermal Gravimetric Analysis

The thermal gravimetric analysis was studied using Perkin Elmer thermogravimetric analyser at a temperature range of 50 to 900°C under nitrogen. The thermal studies of the complexes were studied using Perkin Elmer thermogravimetric analyser 4000.

2.2. Chemicals

Sodium hydroxide, carborn disulphide, piperidine, morpholine, diallyl amine, N- methyl benzyl amine, phenyl piperizine, N- Ethyl aniline, dibenzyl amine, butyl amine, copper chloride, silver nitrate, diethyl ether, acetone, methanol, acetonitrile, dichloromethane and chloroform were purchased from Sigma Aldrich and they were used without any further purifications.

2.3. Synthesis of sodium dithiocarbamate ligands

2.3.1. Synthesis of sodium N-Methyl benzyl amine dithiocarbamate, NMB DTC.

A method from the literature was used [1]. Scheme 2.1 shows the schematic representation of this synthesis. Sodium hydroxide (2 g, 0.05 mol) was dissolved in minimum amount of distilled water and allowed to attain an ice temperature, cold carbon disulphide (3 mL, 0.05 mol) was added to the solution. This was then followed by the addition of an N-methyl benzyl amine (6.6 mL, 0.05 mol). The mixture was stirred for 2-3 h while keeping the temperature below 4°C. A white solid product was filtered and washed with diethyl ether and dried in a desiccator [1]. Yield = 83%, Selected IR (Solid state, cm^{-1}): ν(C-N) =1392, νs(C-S) = 950, νas(C-S) = 972. ^{1}H NMR (400 MHz, D_2O, ppm): 7.4 (d,2H); 7.5 (t, 1H); 7.6 (t, 2H). 5.4 (s, 2H); 3.4 (s, 2H). ^{13}C NMR (400 MHz, D_2O, ppm): 210 (CS); 139, 129, 128, 128 (C_6H_5); 60 (CH_3N), 49 (CH_2)

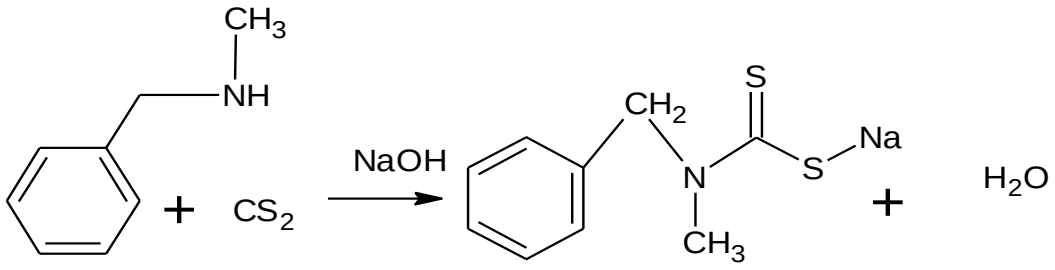

Scheme 2. 1. Synthesis of sodium N-methyl benzyl amine dithiocarbamate

2.3.2. Synthesis of sodium Phenyl Piperizine dithiocarbamate, PP DTC.

A method from the literature [1] was used. The reaction was carried as demonstrated in scheme 2.2. Sodium hydroxide (2 g, 0.05 mol) was dissolved in minimum amount of distilled water and allowed to attain an ice temperature, cold carbon disulphide (3 mL, 0.05 mol) was added to the solution. Then 1-phenyl piperazine amine (7.6 mL, 0.05 mol) was added dropwise. The mixture was stirred for 2-3 h while keeping the temperature below 4°C. A white solid product formed was filtered and washed with ether and dried in a desiccator. Yield = 77%, Selected IR (Solid state, cm^{-1}): V(C-N) =1462, Vs(C-S) = 1011, Vas(C-S) = 1050. ^{1}H NMR (400 MHz, D_2O, ppm): 7.1 (t,1H); 7.2 (t, 2H); 7.3 (t, 2H). 4.6 (t, 4H); 3.2 (t, 4H). ^{13}C NMR (400 MHz, D_2O, ppm): 210 (CS); 119, 121, 138, 150 (C_6H_5); 50, 52 ($C_4H_8N_2$).

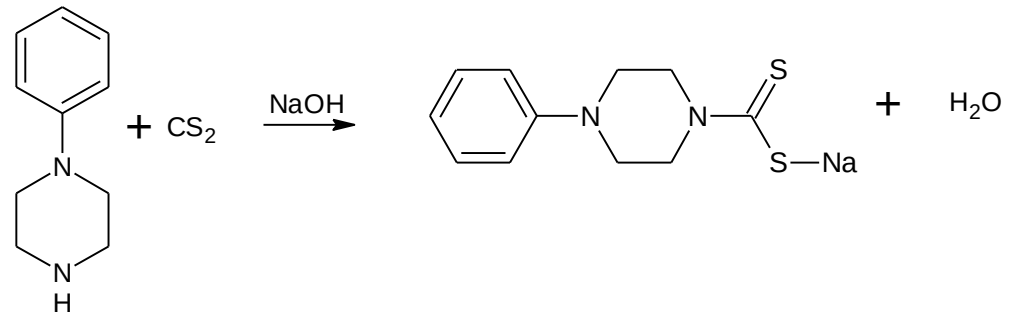

Scheme 2. 2. Synthesis of Sodium 1-phenyl piperizine dithiocarbamate

2.3.3. Synthesis of sodium diallylamine dithiocarbamate, DA DTC

A modified general method was used. Cold carbon disulphide (3mL, 0.05 mol) was added to cold diallylamine (6.2 mL, 0.05 mol) as described in scheme 2.3. This was stirred for 30 minutes until it solidified to a yellow product then the solution of (2 g, 0.05 mol) sodium hydroxide was added in drops very slowly while stirring. The reaction was carried out at a temperature less than 4°C for 4 hr. A white product formed was washed with ether and dried in a desiccator. It was then recrystallized with methanol and white product was obtained. Yield = 63%, Selected IR (Solid state, cm^{-1}): V(C-N) =1410, Vs(C-S) = 967, Vas(C-S) = 1021. ^{1}H NMR (400 MHz, D_2O, ppm): 5.9 (m, 2H); 6.2 (d, 2H); 6.3 (d, 2H); 4.2 (d, 4H). ^{13}C NMR (400 MHz, D_2O, ppm): 210 (CS); 55, 115, 130, (CH_2CHCH_2N).

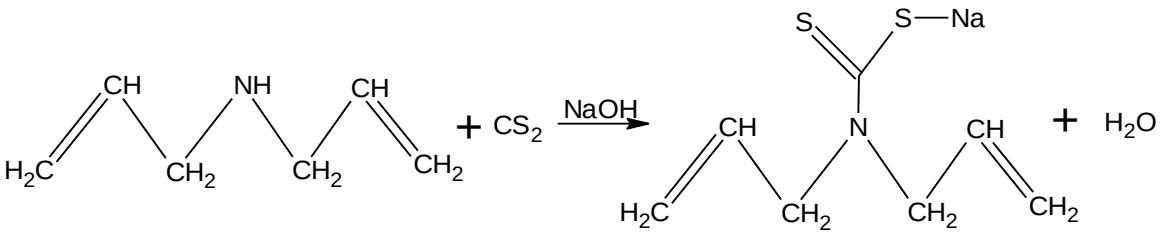

Scheme 2. 3. Synthesis of sodium diallylamine dithiocarbamate

2.3.4. Synthesis of sodium morpholine dithiocarbamate, Morph DTC.

Scheme 2.4 shows the synthesis of morpholine DTC ligand. In an ice cold (3 mL, 0.05 mol) carbon disulphide (2 g, 0.05 mol) cold solution of sodium hydroxide was added, while stirring (4.4 mL, 0.05 mol) cold morpholine was added drop wise. The mixture formed a solid immediately then 15 mL of diethyl ether was added, and the mixture was stirred for 4 h. the reaction was carried out at room temperature. A pure white solid product was then filtered, washed with diethyl ether and dried in a desiccator [3,4]. Yield = 88%, Selected IR (Solid state, cm^{-1}): V(C-N) =1444, Vs(C-S) = 967, Va(C-S) = 1010. ^{1}H NMR (400 MHz, D_2O, ppm): 2.82 (t, 4H); 4.42 (t, 4H); ^{13}C NMR (400 MHz, D_2O, ppm): 210 (CS); 50, 65 (OC_4H_8N).

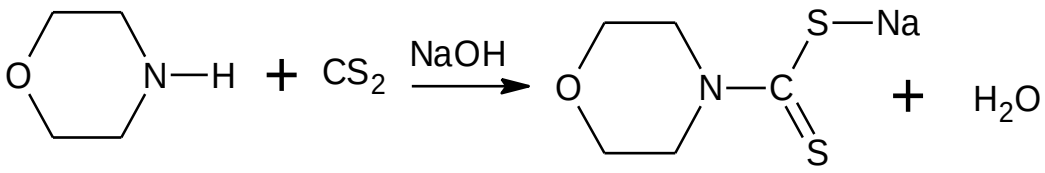

Scheme 2. 4. Synthesis of sodium morpholine dithiocarbamate

2.3.5. Synthesis of sodium piperidine dithiocarbamate, Piper DTC.

Sodium piperidine dihtiocarbamate ligand was synthesized with a reaction shown in Scheme 2.5. An ice cold 3 mL, 0.05 mol of carbon disulphide was added to 2 g, 0.05 mol of cold solution of sodium hydroxide, while stirring 0.05 mol of cold piperidine was added drop wise. The mixture formed a solid immediately then 15 mL of diethyl ether was added, and the mixture was stirred for 4 h. the reaction was carried out at room temperature. A white solid product was then filtered and washed with diethyl ether and dried in a desiccator [3,4]. Yield = 79%, Selected IR (Solid state, cm^{-1}): V(C-N) =1426, Vs(C-S) = 957, Vas(C-S) = 1000. ^{1}H

NMR (400 MHz, D_2O, ppm): 4.3 (t, 4H); 1.7 (q, 4H); 1.8 (q, 2H). ^{13}C NMR (400 MHz, D_2O, ppm): 205 (CS); 24, 26, 52 ($C_5H_{10}N$).

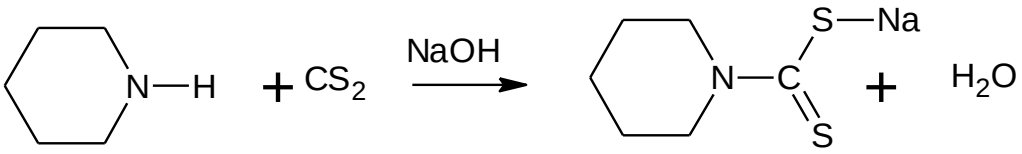

Scheme 2. 5 Synthesis of sodium piperidine dithiocarbamate

2.3.6. Synthesis of sodium N-ethyl aniline dithiocarbamate, NEA DTC.

A method from the literature [1] was used to synthesize N-ethyl aniline DTC ligand as described in Scheme 2.6. Sodium hydroxide (2 g, 0.05 mol) was dissolved in minimum amount of distilled water and allowed to attain an ice temperature, in this cold solution (6.4 mL, 0.05 mol) of N-ethyl aniline was added. Then (3 mL, 0.05 mol) of carbon disulphide was added to the solution. This mixture was then stirred for 2-3 h under the temperature below 4°C. A yellow solid product was then filtered and washed with ether and dried in a desiccator [1,4]. Yield = 52%, Selected IR (Solid state, cm^{-1}): V(C-N) =1444, Vs(C-S) = 997, Va(C-S) = 1021. ^1H NMR (400 MHz, D_2O, ppm): 7.2 (d,2H); 7.4 (t, 1H); 7.5 (t, 2H). 4.4 (q, 2H); 1.2 (t, 3H). ^{13}C NMR (400 MHz, D_2O, ppm): 210 (CS); 149, 139, 127, 128 (C_6H_5); 52 (CH_2N), 12 (CH_3).

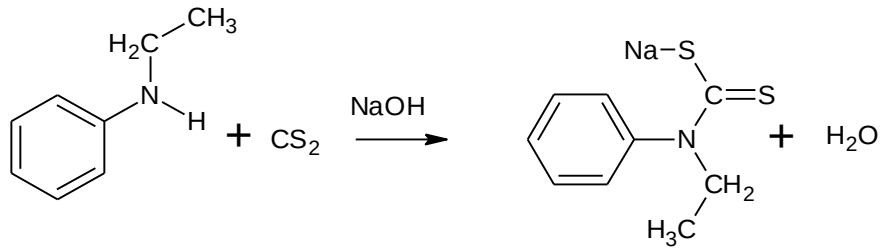

Scheme 2. 6. Synthesis of sodium ethyl aniline dithiocarbamate

2.3.7. Synthesis of sodium butyl amine dithiocarbamate, BA DTC.

The method used for the synthesis of butyl amine dithiocarbamates is presented in Scheme 2.7. Cold 5 mL, 0.05 mol of butyl amine was added to 2 g, 0.05 mol of sodium hydroxide dissolved in minimum amount of distilled water. While stirring 3 mL, 0.05 mol of carbon disulphide in 10 mL of methanol was added to the solution. This mixture was then stirred for 2-3 h at temperature below 4°C. A white solid product was then filtered and washed with diethyl ether and dried in a desiccator [1]. Yield = 77%, Selected IR (Solid state, cm^{-1}): V(N-H) = 3365, V(C-N) =1498, Vs(C-S) = 905, Vas(C-S) = 970. ^{1}H NMR (400 MHz, D_2O, ppm): 1 (t, 3H); 1.5 (m, 2H); 1.7 (q, 2H). 3.6 (t, 2H). ^{13}C NMR (400 MHz, D_2O, ppm): 210 (CS); 10, 20, 30, 49 ($CH_3CH_2CH_2CH_2N$).

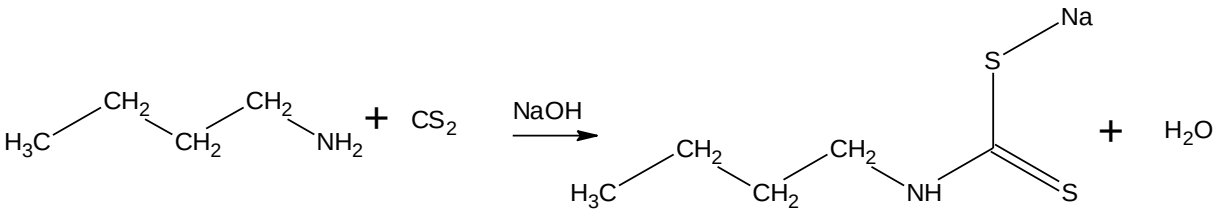

Scheme 2.7. Synthesis of sodium butyl amine dithiocarbamate

2.3.8. Synthesis of sodium dibenzyl amine dithiocarbamate, DBA DTC.

A modified literature method was used as shown in Scheme 2.8. In cold dibenzyl amine (9 mL, 0.05 mol) sodium hydroxide (2 g, 0.05 mol) dissolved in minimum amount of distilled water was added. The mixture was allowed to attain an ice temperature, after which cold carbon disulphide (3 mL, 0.05 mol) was added to the solution dropwisely. This mixture was then stirred for 2-3 h at temperature below 4°C. A white solid product was then filtered and washed with ether and dried in a desiccator [1]. Yield = 76%, Selected IR (Solid state, cm^{-1}): V(C-N) =1448, Vs(C-S) = 972, Va(C-S) = 1032. ^{1}H NMR (400 MHz, D_2O, ppm): 7.3 (d, 4H); 7.4 (t, 2H); 7.5 (t, 4H). 5.4 (s, 4H); ^{13}C NMR (400 MHz, D_2O, ppm): 210 (CS); 139, 129, 128, 128 (C_6H_5); 58 (CH_2N).

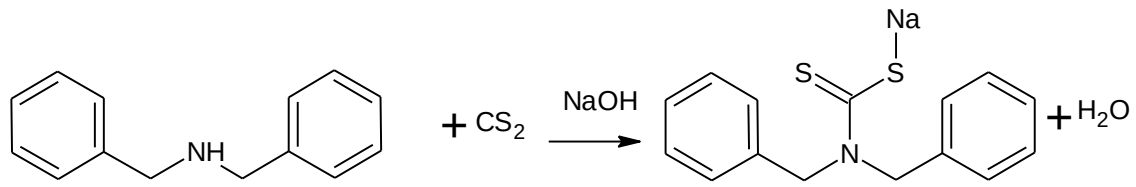

Scheme 2.8. Synthesis of sodium dibenzyl amine dithiocarbamate

2.4. Synthesis of copper(II) dithiocarbamate complexes

2.4.1. Synthesis of copper(II) N-methyl benzyl amine dithiocarbamate complex, [Cu(NMB)$_2$]

About 20 mL solution of the $CuCl_2$ (0.85 g, 0.005 mol), was added to 20 mL solution of NMB DTC ligand (2.19 g, 0.01 mol) as shown in Scheme 2.9. The brown precipitate which immediately formed was stirred for about 2 hours to ensure complete reaction. The solid precipitate was filtered off, rinsed with distilled water and dried at ambient temperature [5]. Yield = 62%, Selected IR (Solid state, cm^{-1}): V(C-N) =1390, V(C-S) = 933. Colour: brown.

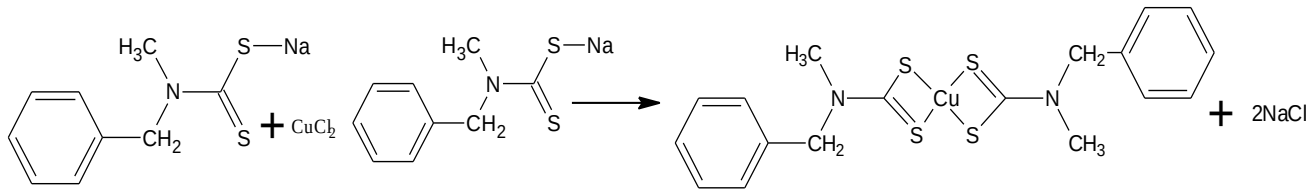

Scheme 2.9. Synthesis of copper(II) N-methyl benzyl amine dithiocarbamate complex

2.4.2. Synthesis of copper(II) phenyl piperizine dithiocarbamate complex, [Cu(PP)$_2$].

Scheme 2.10 shows the synthetic procedure for the reaction. 20 mL solution of the $CuCl_2$ (0.005 mol, 0.85 g), was added to 20 mL solution of PP DTC ligand (0.01 mol, 2.60 g). A brown precipitate formed immediately. The solution was stirred for about 2 h to ensure complete reaction. The solid precipitate formed was filtered off, rinsed with distilled water and dried at ambient temperature. Yield = 70%, Selected IR (Solid state, cm^{-1}): V(C-N) =1477, V(C-S) = 1013. Colour: brown.

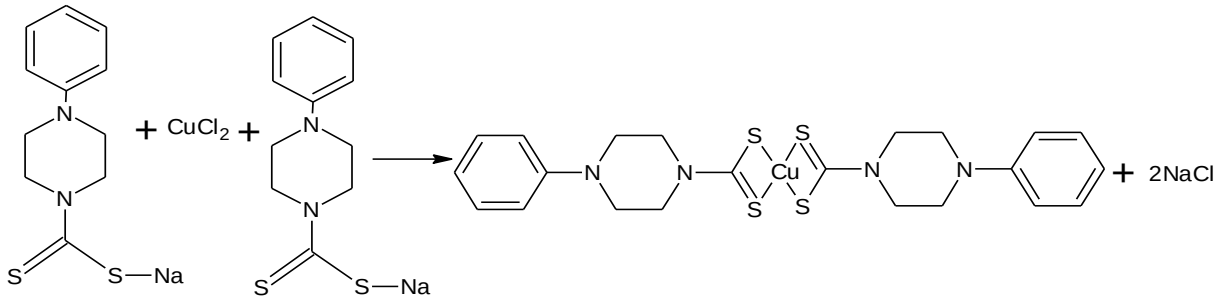

Scheme 2.10. Synthesis of copper(II) phenyl piperidine dithiocarbamate complex

2.4.3. Synthesis of copper(II) diallyl amine dithiocarbamate complex, [Cu(DA)$_2$].

A solution of the $CuCl_2$ (0.0025 mol, 0.43 g) was added to the solution of sodium diallyl amine dithiocarbamate ligand (0.005mol, 0.98 g) at room temperature, A brown to black precipitate was formed immediately but the reaction continued to stir for about 2 h to ensure complete reaction. The solid precipitate was filtered off, rinsed with distilled water and dried at ambient temperature. The synthetic poceedure is demonstrated in scheme 2.11. Yield = 48%, Selected IR (Solid state, cm^{-1}): V(C-N) =1401, V(C-S) = 987. Colour: brown.

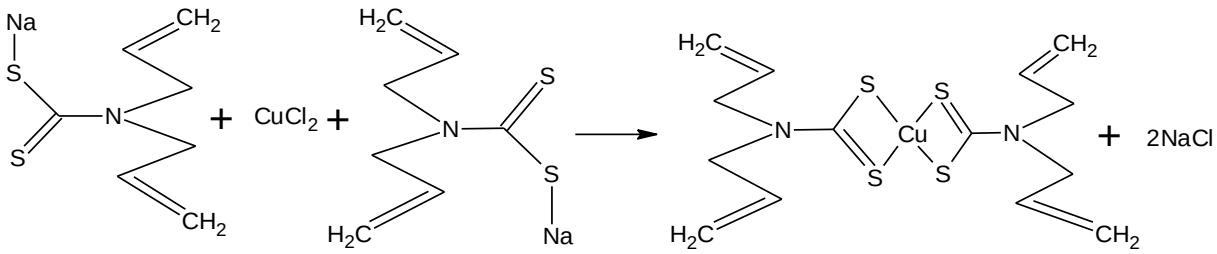

Scheme 2.11. Synthesis of copper(II) diallyl amine dithiocarbamate complex

2.4.4. Synthesis of copper(II) morpholine dithiocarbamate complex, [Cu(Morph)$_2$].

Copper(II) morpholine dithiocarbamate complex was synthesized according to the reaction in Scheme 2.12 by the addition of 20 mL solution of the $CuCl_2$ (0.005mol, 0.85 g) to 20 mL solution of sodium morpholine dithiocarbamate ligand (0.01 mol, 1.85 g). The experiment was carried out at room temperature. The brown precipitate which immediately formed was stirred

for about 2 h to ensure complete reaction. The solid precipitate was filtered off, rinsed with distilled water and dried at ambient temperature [4]. Yield = 72%, Selected IR (Solid state, cm^{-1}): V(C-N) =1477, V(C-S) = 1006. Colour: brown.

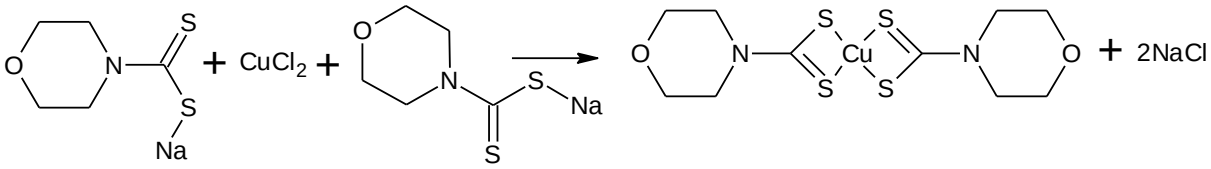

Scheme 2.12. Synthesis of copper(II) morpholine dithiocarbamte complex

2.4.5. Synthesis of copper(II) piperidine dithiocarbamate complex, [Cu(Piper)$_2$]

The same method was employed also for this complex. Scheme 2.13 shows the reaction of the synthesis of copper(II)piperidine dithiocarbamate. The reaction was carried out at room temperature. About 20 mL solution of the $CuCl_2$ (0.005 mol, 0.85 g), was added to 20 mL solution of piperidine dithiocarbamate ligand (0.01 mol, 1.83 g), the brown precipitate which immediately formed was stirred for about 2 h. Then the solid precipitate was filtered off, rinsed with distilled water and dried at ambient temperature. Yield = 73%, Selected IR (Solid state, cm^{-1}): V(C-N) =1435, V(C-S) = 993. Colour: brown.

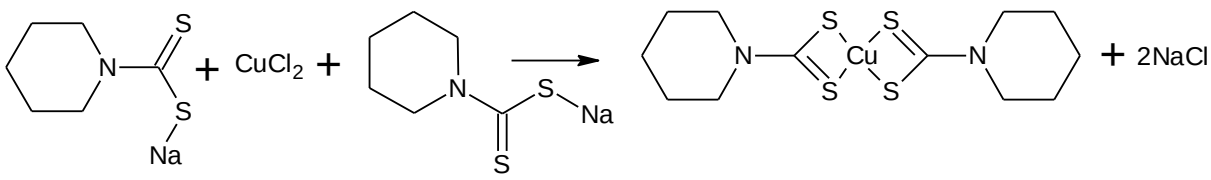

Scheme 2.13. Synthesis of copper(II) piperidine dithiocarbamate complex

2.4.6. Synthesis of copper(II) N-ethyl aniline dithiocarbamate complex, [Cu(NEA)$_2$].

The synthesis of Cu(II) N-ethyl aniline dithiocarbamate complex (Scheme 2.14) was carried out at room temperature. The metal salt, $CuCl_2$ (0.0025 mol, 0.43 g) was dissolved in 20 mL of distilled water and also sodium N-ethyl aniline dithiocarbamate ligand (0.005 mol, 1.09 g) was dissolved in 20 mL of water in a separate beaker. The two solutions were then mixed stirred for about 2 h to ensure complete reaction. The solid precipitate was filtered off, rinsed with distilled water and dried at ambient temperature [4]. Yield = 56%, Selected IR (Solid state, cm^{-1}): V(C-N) =1456, V(C-S) = 960. Colour: brown.

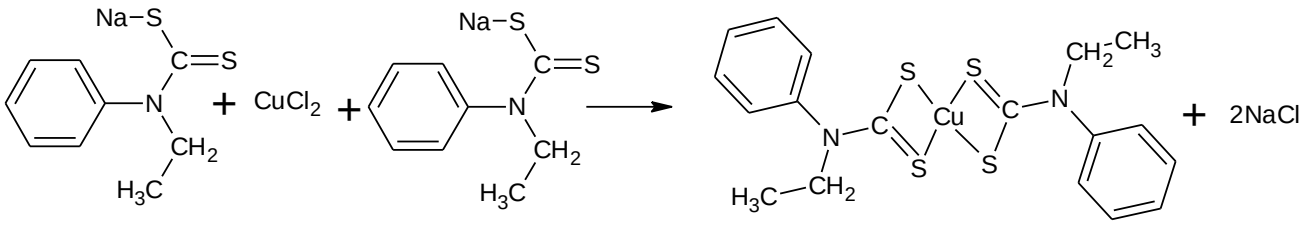

Scheme 2.14. Synthesis of copper(II) N-ethyl anilline dithiocarbamate complex

2.4.7. Synthesis of copper(II) butyl amine dithiocarbamate complex, [Cu(BA)$_2$].

At room temperature 20 mL solution of the $CuCl_2$ (0.005 mol, 0.85 g) was added to 20 mL solution of sodium butyl amine dithiocarbamate ligand (0.01 mol, 1.71 g), immediately a yellow precipitate formed. The reaction was then stirred for 2 h. The yellow solid precipitate was filtered off, rinsed with distilled water and dried at ambient temperature. The reaction is

shown in scheme 2.15. Yield = 62%, Selected IR (Solid state, cm^{-1}): V(N-H) = 3119, V(C-N) =1503, V(C-S) = 907. Colour: Yellow.

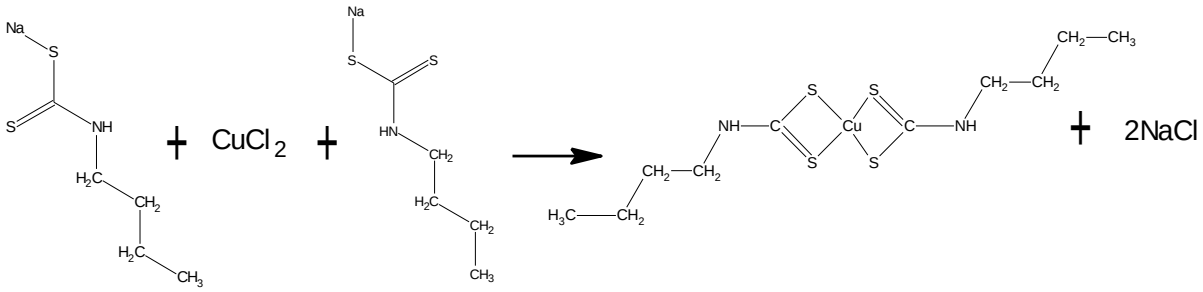

Scheme 2.15. Synthesis of copper(II) butyl amine dithiocarbamate complex

2.4.8. Synthesis of copper(II) dibenzyl amine dithiocarbamate complex, [Cu(DBA)$_2$].

This reaction was carried out at room temperature. About 20 mL solution of the $CuCl_2$ (0.005 mol, 0.85 g) was added to 20 mL solution of sodium butyl amine dithiocarbamate ligand (0.01 mol, 2.9 g). The brown precipitate which immediately formed was stirred for about 2 h to ensure complete reaction. The solid precipitate was filtered off, rinsed with distilled water and dried at ambient temperature (Scheme 2.16). Yield = 70%, Selected IR (Solid state, cm^{-1}): V(C-N) =1479, V(C-S) = 985. Colour: Yellow.

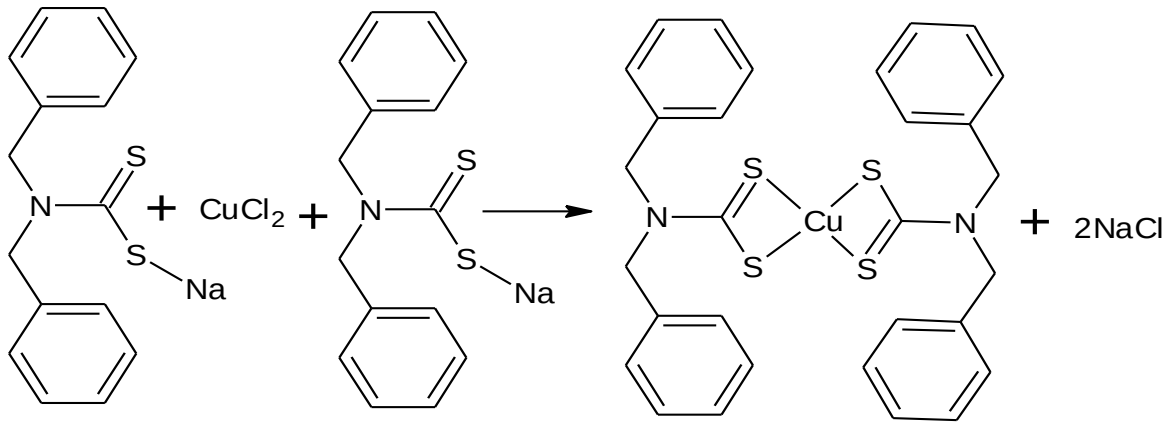

Scheme 2.16. Synthesis of copper(II) dibenzyl amine dithiocarbamate complex

2.5. Synthesis of silver(I) dithiocarbamate complexes

2.5.1. Synthesis of silver(I) N-methyl benzyl amine dithiocarbamate complex, [Ag(NMB)]

All the silver complexes were synthesized using the same method used to synthesize copper dithiocarbamate complexes. They were prepared at room temperature. 0.005 mol, 0.84 g of $AgNO_3$ was dissolved in 20 mL of water while the 0.005 mol, 1.09 g of sodium N-ethyl aniline dithiocarbamate was also dissolved in 20 mL of water separately, the two solutions were then mixed together and stirred for 4 h. The yellow precipitated product was filtered off, rinsed with distilled water and dried at ambient temperature [4]. Scheme 2.17 shows the schematic reaction. Yield = 66%, Selected IR (Solid state, cm^{-1}): V(C-N) =1375, V(C-S) = 941. Colour: Yellow.

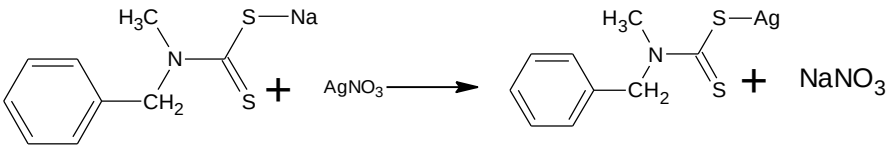

Scheme 2.17. Synthesis of silver(I) N-methyl benzyl amine dithiocarbamate complex

2.5.2. Synthesis of silver(I) phenylpiperazyl dithiocarbamate complex, [Ag(PP)].

All silver dithiocarbamate complexes were synthesized using the same method. Scheme 2.18 shows the synthesis of silver(I)phenyl piperazyl DTC complex. Where (0.005 mol, 0.84 g) of $AgNO_3$ in 20 mL of water followed by the addition (0.005 mol, 0.30 g) of sodium phenyl piperizine in 20 mL of water. The two solutions were then added together and stirred for 4 h. The yellow solid precipitate was filtered off, rinsed with distilled water and dried at ambient temperature. Yield = 68%, Selected IR (Solid state, cm^{-1}): V(C-N) =1418, V(C-S) = 1002. Colour: Yellow.

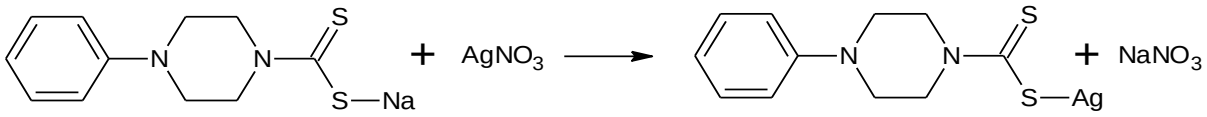

Scheme 2.18. Synthesis of silver(I) phenylpiperazine dithiocarbamate complex

2.5.3. Synthesis of silver(I) diallyl dithiocarbamate complex, [Ag(DA)].

Silver(I) diallyl amine dithiocarbamate complex was also synthesized while (0.005 mol, 0.8494 g) of $AgNO_3$ in 20 mL of water while dissolving (0.005 mol, 0.9764 g) of sodium diallyl amine dithiocarbamate salt was also dissolved in 20 mL of water both solutions were mixed and the reaction was left to carry on for four hours stirring at room temperature. The yellow solid that precipitated was filtered off, rinsed with distilled water and dried in a desiccator. The reaction is shown in scheme 2.19. Yield = 44%, Selected IR (Solid state, cm^{-1}): V(C-N) =1394, V(C-S) = 985. Colour: Grey.

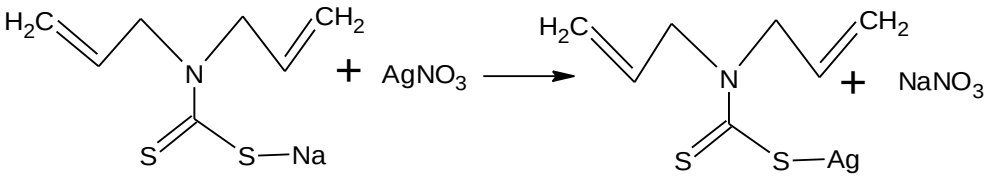

Scheme 2.19. Synthesis of silver(I) diallyl dithiocarbamate complex

2.5.4. Synthesis of silver(I) morpholine dithiocarbamate complex, [Ag(morph)].

Silver(I)morpholine dithiocarbamate complex was synthesized as presented in Scheme 2.20. The silver salt, $AgNO_3$ (0.005 mol, 0.8494 g), was dissolved in a beaker in 20 mL of water and the sodium morpholine DTC ligand (0.005 mol, 0.9262 g) dissolved in 20 mL of water in a separate beaker, the two solutions were then added together and stirred for 4 h. The yellow solid precipitate was filtered off, rinsed with distilled water and dried at ambient temperature Yield = 69%, Selected IR (Solid state, cm^{-1}): V(C-N) =1418, V(C-S) = 991. Colour: Yellow.

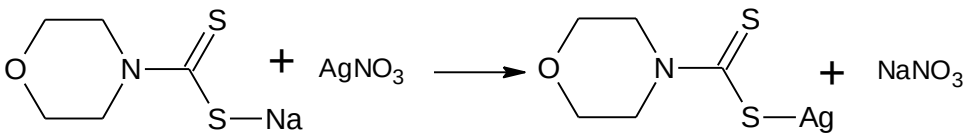

Scheme 2.20. Synthesis of silver(I) morpholine dithiocarbamte complex

2.5.5. Synthesis of silver(I) piperidine dithiocarbamate complex, [Ag(piper)].

Silver(I)piperidine dithiocarbamate complex was synthesized by adding the silver salt solution, $AgNO_3$ (20 mL, 0.8494 g), to a sodium piperidine dithiocarbamate solution (20 mL, 0.9186 g). This mixture was stired for 4 h and the yellow precipitate was filtered off, rinsed with distilled water and dried at ambient temperature. Scheme 2.21 shows the synthesis of silver(I)piperidine

DTC. Yield = 71%, Selected IR (Solid state, cm^{-1}): V(C-N) =1449, V(C-S) = 994. Colour: Yellow.

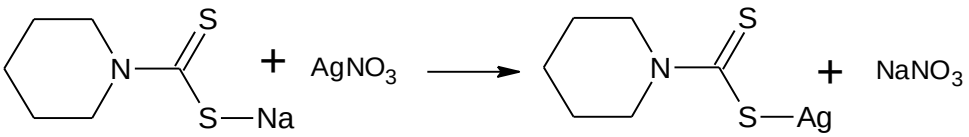

Scheme 2.21. Synthesis of silver(I) piperidine dithiocarbamate complex

2.5.6. Synthesis of silver(I) N-ethyl aniline dithiocarbamate complex, [Ag(NEA)].

Silver(I)N-ethyl aniline dithiocarbamate complex was synthesized as shown in Scheme 2.22 by the addition $AgNO_3$ (0.005 mol, 0.8494 g) dissolved in 20 mL of water to the solution of N-ethyl aniline DTC ligand (0.005 mol, 1.096 g), the mixture was stirred for 4 h. The yellow solid precipitate was filtered off, rinsed with distilled water and dried at ambient temperature. Yield = 61%, Selected IR (Solid state, cm^{-1}): V(C-N) =1438, V(C-S) = 987. Colour: Yellow.

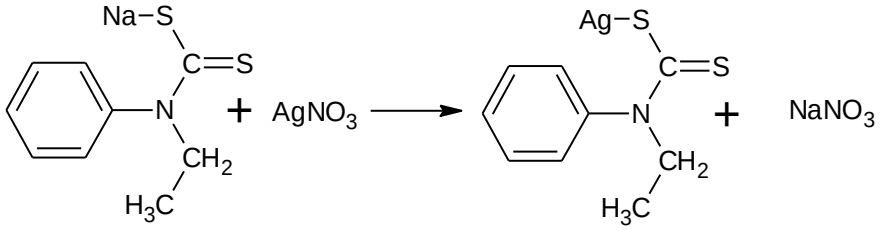

Scheme 2.22. Synthesis of silver(I) N-ethyl aniline dithiocarbamate complex

2.5.7. Synthesis of silver(I) butylamine dithiocarbamate complex. [Ag(BA)].

To synthesize Silver(I)butyl amine dithiocarbamate complex. 20 mL solution of $AgNO_3$ (0.005 mol, 0.8494 g) was added to 20 mL of sodium butyl amine DTC (0.005 mol, 0.8563 g) solution. A yellow solid precipitate formed immediately and the reaction was stirred for 4 h. The yellow solid was filtered off, rinsed with distilled water and dried in a desiccator. The synthesis is shown in Scheme 2.23. Yield = 62%, Selected IR (Solid state, cm^{-1}): V(N-H) = 3244, V(C-N) =1485, V(C-S) = 928. Colour: Yellow.

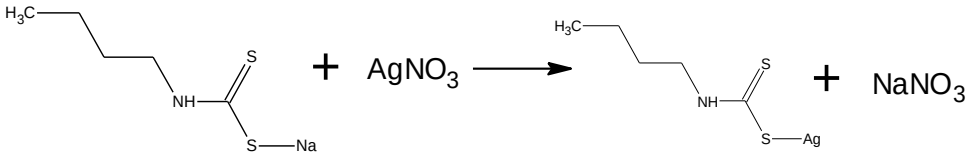

Scheme 2. 23. Synthesis of silver(I) butyl amine dithiocarbamate complex

2.5.8. Synthesis of silver(I) dibenzyl dithiocarbamate complex, [Ag(DBA)].

Silver(I) dibenzyl dithiocarbamate complex (Scheme 2.24) was synthesized at room temperature. The silver salt, $AgNO_3$ (0.005 mol, 0.8494 g), dissolved in a beaker in 20 mL of water was added to sodium dibenzyl amine dithiocarbamate ligand (0.005 mol, 0.1.4770 g) also dissolved in 20 mL of water in a beaker while stirring. The reaction continued for 4 h. A yellow solid precipitated and it was filtered off, rinsed with distilled water and dried in desiccator. Yield = 66%, Selected IR (Solid state, cm^{-1}): V(C-N) =1478, V(C-S) = 976. Colour: Yellow.

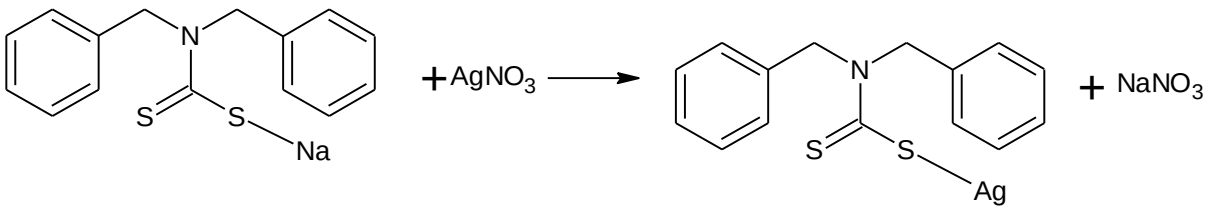

Scheme 2.24. Synthesis of silver(I) dibenzyl dithiocarbammate complex

2.6. References

[1] Onwudiwe, D.C.; Ajibade, P.A. Synthesis and crystal structure of bis(N-alkyl-N-phenyl dithiocarbamato)mercury(II). *J. Chem. Crystallogr*. **2011**, 41, 980-985.

[2] Segovia, N.; Crovetto, G.; Lardelli, P.; Espigares, M. In vitro toxicity of several dithiocarbamates and structure–activity relationships. *J. Appl. Toxicol*. **2002**, 22, 353–357.

[3] Sharma, M.; Sharma, A.; Sachar, R. Synthesis and characterization of the adducts of morpholine dithioccarbamate complexes of oxovanadium(IV), nickel(II), and copper(II) with piperidine and morpholine. *J. Chem*. **2012**, 9(4), 1929-1940.

[4] Botha, N. L.; Copper dithiocarbamate complexes and copper sulfide nanoparticles: Synthesis, characterization and antifungal studies. MSc dissertation, **2015**, 33-41.

[5] Onwudiwe, D.C.; Ajibade, P.A. Synthesis and characterization of metal complexes of N-alkyl-N-phenyl dithiocarbamates. *Polyhedron*, **2010**, 29, 1431-1436.

CHAPTER THREE

SPECTROSCOPIC CHARACTERIZATION OF THE DITHIOCARBAMATE LIGANDS AND COPPER(II) AND SILVER(I) COMPLEXES

3.1. Introduction

Dithiocarbamates are well known for their ability to form stable complexes with metal ions in wide ranges of oxidation states [1, 2]. Even though these compounds possess s-donor and n-back-donation, their compounds have interesting features associated with an additional n-electron flowing from nitrogen to sulphur via a planar delocalised π-orbital system, see Figure 3.1.The different resonance are the reason for the strong electron donation and a high electron density on the metal which leads to the higher oxidation state [3, 4]. The anti-oxidant properties of these compounds make them even more valuable compounds. They are now used in different applications in fields like agriculture and medicine [5].

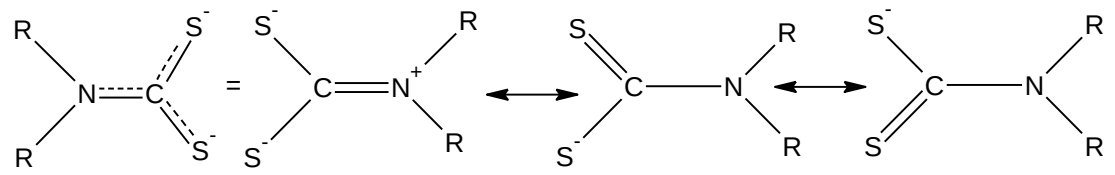

Figure 3. 1. Different resonance forms of dithiocarbamic moiety

Dithiocarbamates received attention because of their rich coordination chemistry, especially with transition metal ions as they readily form chelates with all transition metal ions through the two sulphur donor atoms forming water insoluble sulphates [6, 7]. Figure 3.2 shows the possible binding modes of dithiocarbamate ligands to metal ions [8]. Some abilities of the dithiocarbamates are owed to their strong metal-binding capacity, which enables them to act as inhibitors of enzymes with a profound effect on biological systems [9]. Dithiocarbamate metal complexes have found a wide range of applications in different fields [10]. Metal

complexes of dithiocarbamates are synthesized and investigated for many applications, because they possess various biological properties [11, 12] such as antibacterial activity [13]. Recently the complexes of dithiocarbamates are being studied for their anti-bacterial, antifungal, anti-malarial, anti-viral, anti-HIV, anti-estrogenic, anti progestational, anti-osteoporosis, anti-diabetic, anti-obesity, anti-helminthes, activities [14]. They also show very promising antitumor activities [15]. Modifications of the R groups attached to nitrogen atom of the dithiocarbamate fragment can have effect on both the structure and chemical properties, mainly due to a change in the acid–base nature of the dithiocarbamate fragment [16].

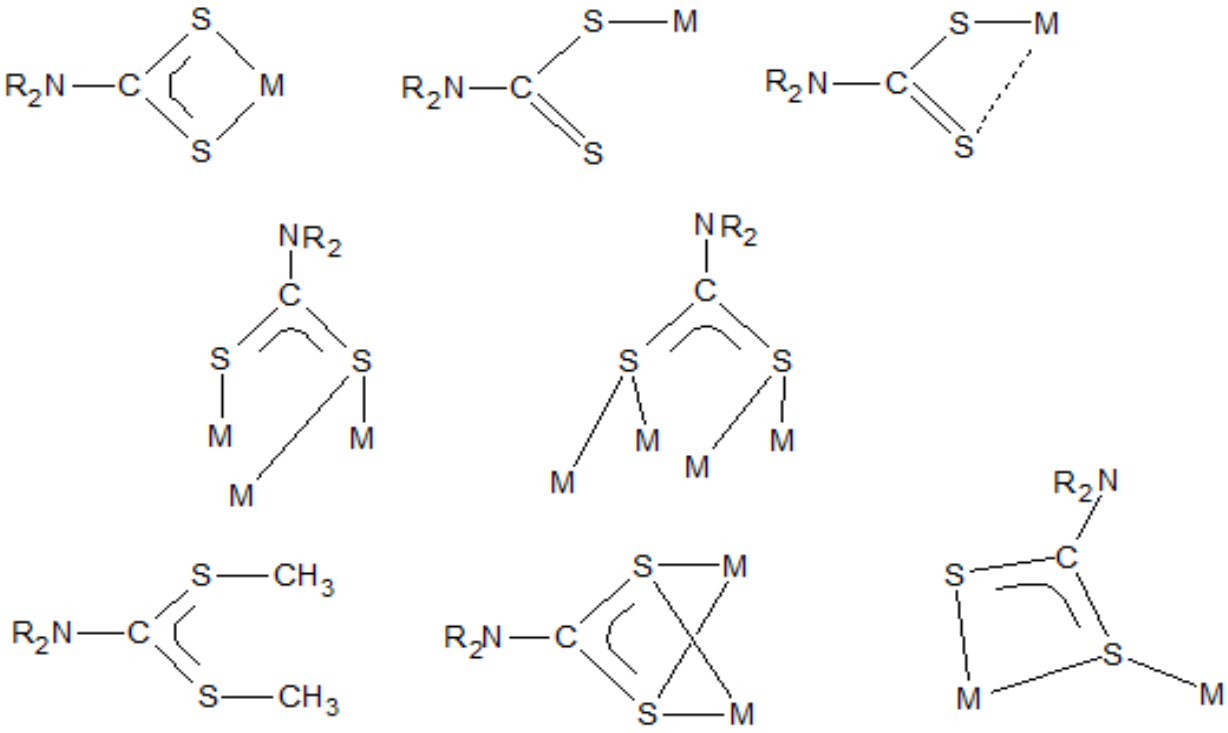

Figure 3. 2. Possible coordination modes of dithiocarbamates [8].

3.1.1. Synthesis

There are many methods for the synthesis of dithiocarbamates derivatives that have been reported. They include the synthesis of dithiocarbamates using thiophosgene chlorothioformate and isothiocyanate which are costly and toxic reagents [23]. They are also synthesized using markovnikov addition reaction which gives excellent yields for secondary amines but poor yields for hindered secondary amine [24]. Their synthesis by only reacting amines with carbon disulphide and alkyl halide in the presence of strong base like NaOH or KOH using the toxic solvents such as DMF or DMSO in the presence of catalyst has also been reported [25].

Even though it is known that solvents play an important role for mixing the ingredients in an organic reaction making the molecular interactions easier but carrying out organic reactions without using toxic organic solvents is now of great interest in green organic synthesis [26]. In this study the dithiocarbamates were synthesized without the use of solvents. They were synthesized by just adding carbon disulphide in to the cold amine in the presence of the base at low temperatures as shown in Scheme 3.1. In this study the dithiocarbamate ligands were synthesized using the exothermic reaction between carbon disulphide and a primary/secondary amine in the presence of sodium hydroxide. Scheme 3.1 shows the general synthesis from the primary amines. Scheme 3.2 shows the synthesis of the dithiocarbamate complexes, whereby, a simple direct addition method was used, and water was used to dissolve the starting materials the reaction was carried out at room temperature [27].

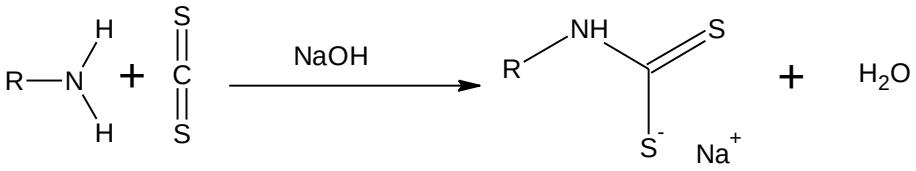

Scheme 3. 1. General synthesis of dithiocarbamates

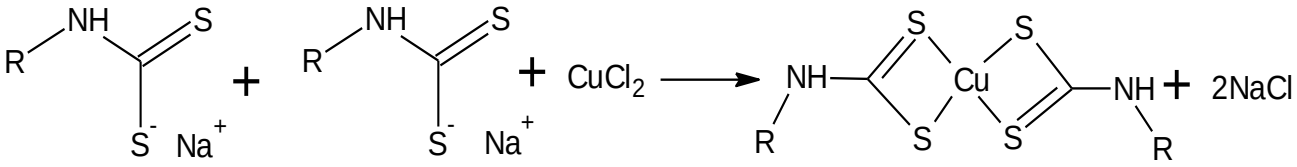

Or

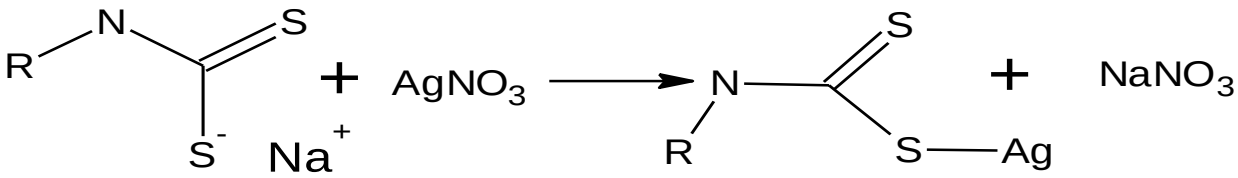

Scheme 3. 2 Synthesis of metal complexes from dithiocarbamate ligands

3.2. Physicochemical properties

The metal complexes synthesized from dibenzyl amine (DBA), N-methyl benzyl amine (NMB), piperidine (Piper), Morpholine (morph), N-ethyl aniline (NEA), phenyl piperazine (PP), diallyl amine (DA) and butyl amine (BA) dithiocarbamates (DTC), are labelled as $[M(DBA)_n]$, $[M(DA)_n]$, $[M(BA)_n]$, $[M(PP)_n]$, $[M(NMB)_n]$, $[M(NEA)_n]$, $[M(Piper)_n]$ and $[M(morph)_n]$, where M is either Cu(II) or Ag(I) and n is 1 in the Ag complexes or 2 in the Cu complexes. All the ligands gave white products and the copper(II) complexes gave brown powder while yellow powder was obtained for silver(I) complexes as shown in Table 3.1.

The conductivity measurements were taken to test the molecular ions liberated by the compounds in solution. The higher the molar conductance the higher the number of ions the compound liberates in solution [28]. Because of the Na^+ ions in the dithiocarbamate ligands their molar conductivity is expected to be high and it is expected to be low for the complexes. The conductivity values of the ligands and copper complexes were measured using the 4510-conductivity meter. The ligands were dissolved in water and the copper complexes were dissolved in Dimethyl sulfoxide.

The molar conductance measured for the ligand ranged from 24 to 387 µS which are higher when compared to the molar conductance values measured from the copper complexes which ranged from -1.07 to 0.08 µS. This difference between these values confirms the formation of the complexes by the absence of Na^+ ions in the complexes limiting the number of ions that liberates in the solution. The conductivity of the silver complexes could not be tested due to the insolubility of the complexes.

Table 3.1. Physical measurements of synthesized DTC complexes

Compound	Molar mass (g/mol)	Conductance (µS)	Colour
DBA DTC	295.398	387	White
$[Cu(DBA)_2]$	608.363	-1.04	Yellow
[Ag(DBA)]	380.276	-	Yellow
BA DTC	171.259	24	White
$[Cu(BA)_2]$	360.084	-1.07	Brown
[Ag(BA)]	256.138	-	Grey
NMB DTC	219.302	216	White
$[Cu(NMB)_2]$	456.186	0.04	Brown
[Ag(NMB)]	304.180	-	Yellow
Morph DTC	185.243	75.0	White
$[Cu(morph)_2]$	388.052	0.05	Brown
[Ag(morph)]	270.121	-	Yellow
Piper DTC	178.229	67.0	White
$[Cu(piper)_2]$	374.026	0.08	Brown
[Ag(piper)]	268.48	-	Yellow
NEA DTC	219.302	48.0	Off White
$[Cu(NEA)_2]$	456.171	0.13	Brown
[Ag(NEA)]	304.186	-	Yellow
PP DTC	206.354	38.0	White
$[Cu(PP)_2]$	538.275	0.10	Brown
[Ag(PP)]	345.233	-	Yellow

DA DTC	195.280	87.4	White
$[Cu(DA)_2]$	410.145	0.03	Brown
[Ag(DA)]	280.159	-	Yellow

3.3. Fourier-transform infrared spectroscopy studies

The infrared spectra studies of the dithiocarbamate compounds complexes are important as they show the coordination modes of DTC ligands, and also their M–S bonds in their complexes. The region from 1520 to 1528 cm^{-1} is associated to the ($N–CS_2$) vibration mode. The position of this band in the IR spectrum in general is found in between a single and a double C–N bond. The band in the range of 978–987 cm^{-1}, asy(C–S), contributes to determining the coordination mode of the dithiocarbamate ligand. In the case of bidentate binding, a single absorption band is observed in this region while in the case of asymmetric bonding, asy(C–S) appears as a duplicated band. Finally, in monodentate coordination the duplicated band separates further [29, 30]

Table 3.2. FTIR results of DTC complexes

Serial numbers	**Compounds**	**νN—H (cm^{-1})**	**νC—N (cm^{-1})**	**νC—S (cm^{-1})**	**νC==S (cm^{-1})**
1.	*DBA DTC*	-	1448	972	1032
	[Cu(DBA)$_2$]	-	1479	985	-
	[Ag(DBA)]		1478	976	-
2.	*BA DTC*	3365	1498	905	970
	[Cu(BA)$_2$]	3119	1503	928	-
	[Ag(BA)]	3244	14931485	981	-

3.	*NMB DTC*	-	1392	950	972
	[Cu(NMB)$_2$]	-	1390	933	-
	[Ag(NMB)]	-	1375	997741	-
4.	*Morph DTC*	-	1444	967	1010
	[Cu(morph)$_2$]	-	1477	1006	-
	[Ag(morph)]	-	1418	991	-
5.	*Piper DTC*	-	1426	957	1000
	[Cu(piper)$_2$]	-	1435	993	-
	[Ag(piper)]	-	1449	994	-
6.	*NEA DTC*	-	1444	997	1021
	[Cu(NEA)$_2$]	-	1418	987	
	[Ag(NEA)]	-	1438	987	-
7.	*PP DTC*	-	1462	1011	1050
	[Cu(PP)$_2$]	-	1479	1013	-
	[Ag(PP)]	-	1418	1002	-
8.	*DA DTC*	-	1410	967	1030
	[Cu(DA)$_2$]	-	1401	987	-
	[Ag(DA)]	-	1394	985	-

3.3.1. FTIR spectra of N-methyl benzyl DTC and it's copper(II) and silver(I) complexes.

Figure 3.3 shows the overlay spectra of N-methyl benzyl dithiocarbamate ligand and copper(II) dithiocarbamate and silver(I) dithiocarbamate complex. The spectrum showed all the three important vibrations of the dithio-moiety. The free ligand spectra showed two ν(C-S) vibrations from the dithio group at 950 cm^{-1} and 972 cm^{-1}. The frequencies shifted to lower wavenumbers in the complexes while merging into a single peak at 933 cm^{-1} and 941 cm^{-1} for the copper(II) and silver(I) complexes respectively. This is due to the binding of the sulphur atoms in the ligand to the metal centres in a bidentate chelation mode.

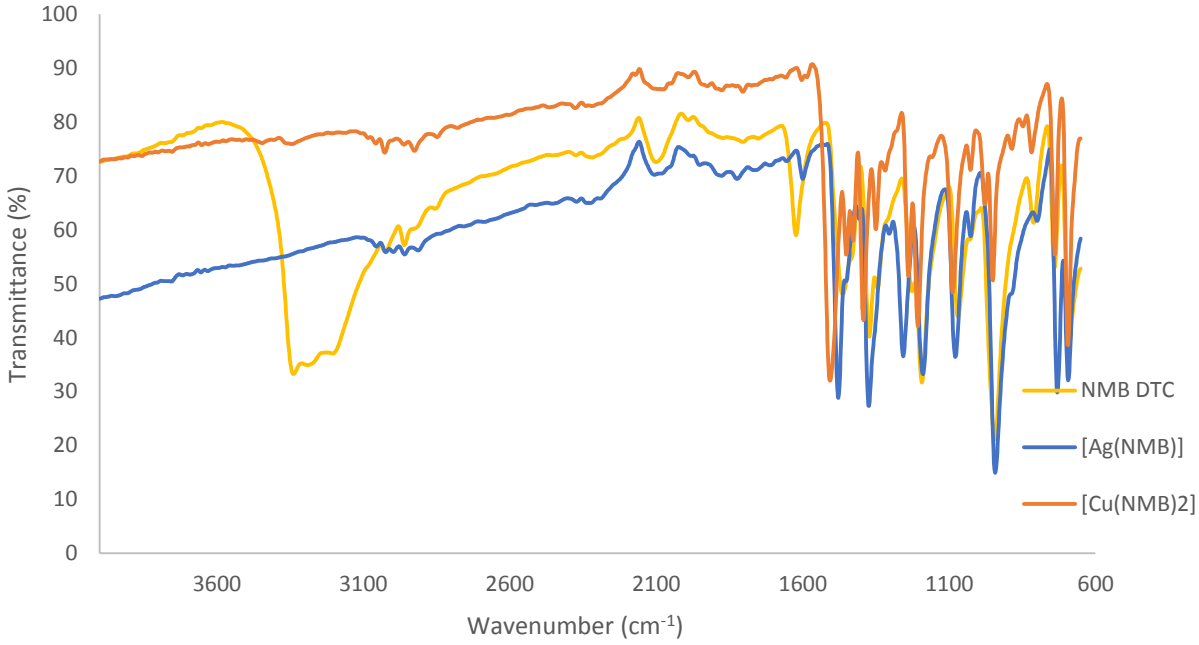

Figure 3. 3 Overlay FTIR spectra of N-methyl benzyl amine DTC and it's copper(II) and silver(I) complexes

3.3.2. FTIR spectra of phenylpiperazine DTC and it's copper(II) and silver(I) complexes.

Figure 3.4 shows the FTIR spectra of the phenylpiperazine dithiocarbamate ligand and it's copper(II) dithiocarbamate and silver(I) dithiocarbamate complexes. The free ligand spectrum showed the C-N vibrations from the NCSS moiety of the dithiocarbamate at 1462 cm^{-1}. This peak was observed at different wavenumbers in the complexes as the copper complex spectrum showed the vibration at 1479 cm^{-1} and 1418 cm^{-1} for the silver(I) complex. This shift is as a result of the coordination of the ligand to the metal centres changing the single bond between the carbon and the nitrogen forming a partial double bond. The free ligand spectrum also showed the ν(C-S) symmetric and asymmetric vibrations at 1011 cm^{-1} and 1050 cm^{-1}. However, these vibrations merged into a single peak in the complexes at 1013 and 1002 cm^{-1} for the copper and the silver(I) complexes respectively. This is due to the sulphur bonding to the metals confirming the bidentate coordination of the ligand to the copper(II) complex.

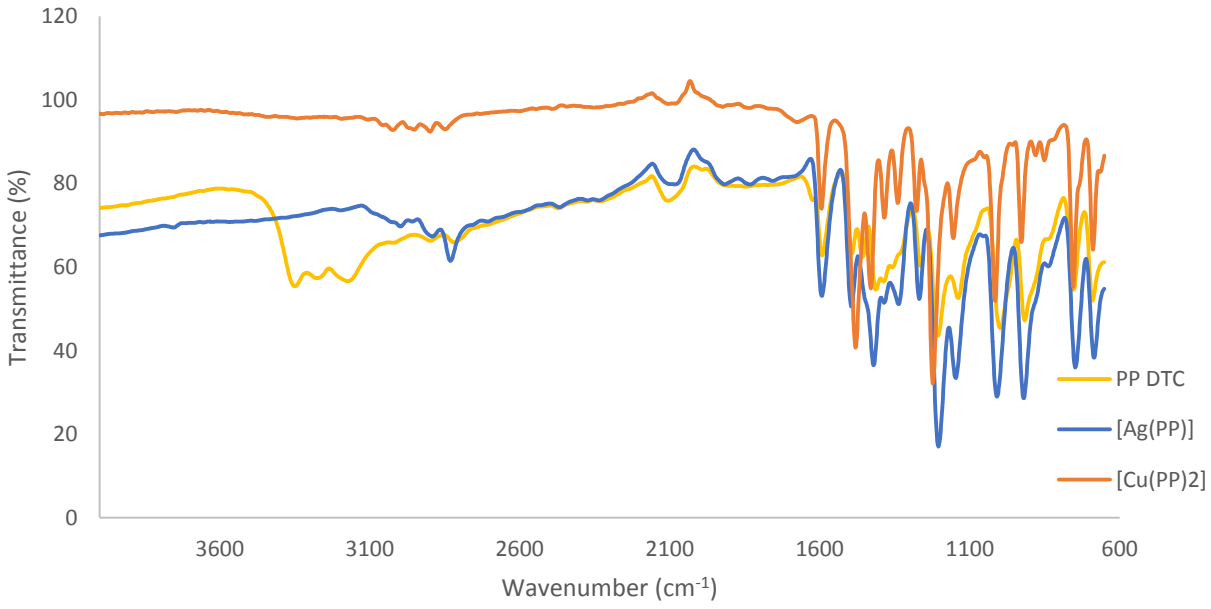

Figure 3. 4. Overlay FTIR spectra of phenylpiperazine DTC and it's copper(II) and silver(I) complexes

3.3.3. FTIR spectra of diallyl amine DTC and it's copper(II) and silver(I) complexes.

Figure 3.5 shows the FTIR spectra of diallyl amine dithiocarbamate ligand and its copper(II) and silver(I) dithiocarbamate complexes. The expected dithio moiety were observed in all the three FTIR spectra. The ν(C-N) vibration from the NCSS moiety was observed in the spectrum of the ligand at 1410 cm^{-1}. The shift of this stretching vibration was observed in the complexes spectra. The ν(C-N) vibration was observed at 1401cm^{-1} and 1394 cm^{-1} for copper(II) complex and silver(I) complex respectively. The free ligand spectrum showed the ν(C-S) vibration mode split into two peaks at 967 cm^{-1} and 1021 cm^{-1} and they were ascribed to the symmetric and asymmetric vibrations. In the complexes, the ν(C-S) vibration appeared in a single peak at 987 cm^{-1} and 985 cm^{-1} for copper(II) complex and silver(I) complex respectively. This confirmed the binding of the ligand to the metal centre forming bidentate coordination in the copper(II) complex and metal cluster for silver(I) complex.

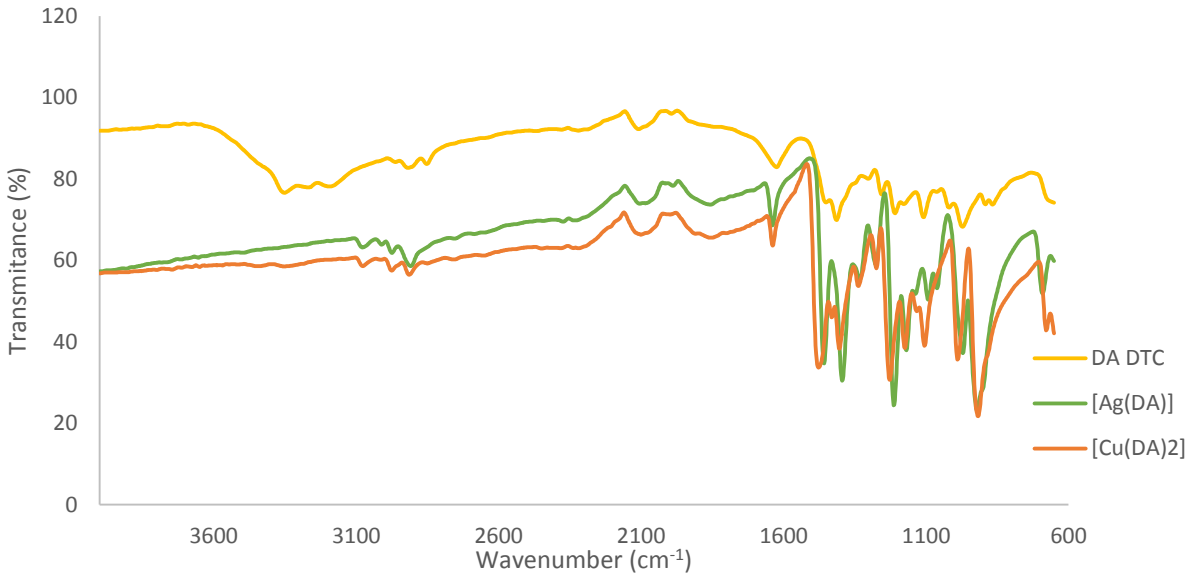

Figure 3. 5. Overlay FTIR spectra of diallylamine DTC and it's copper(II) and silver(I) complexes

3.3.4. FTIR spectra of morpholine DTC and it's copper(II) and silver(I) complexes.

Figure 3.6 shows the overlay spectra of mophorline dithicarbamate ligand the copper(II) and silver(I) complexes. The free ligand spectrum shows the ν(C-N) stretching vibration at 1444 cm^{-1} which shifted to 1477 cm^{-1} and 1418 cm^{-1} in copper(II) and silver(I) complexes due to the binding of the ligand to the metal centre. The ligand and the silver complex showed two vibrations at 967 and 1010 cm^{-1} for the ligand and 991 and 1010 cm^{-1} for the silver complex attributed to the symmetric and asymmetric ν(C-S) vibrations. This peak merged to one peak at 1006 cm^{-1} in the spectrum of copper(II) complex confirming the bidentate coordination of the ligand to the metal ion.

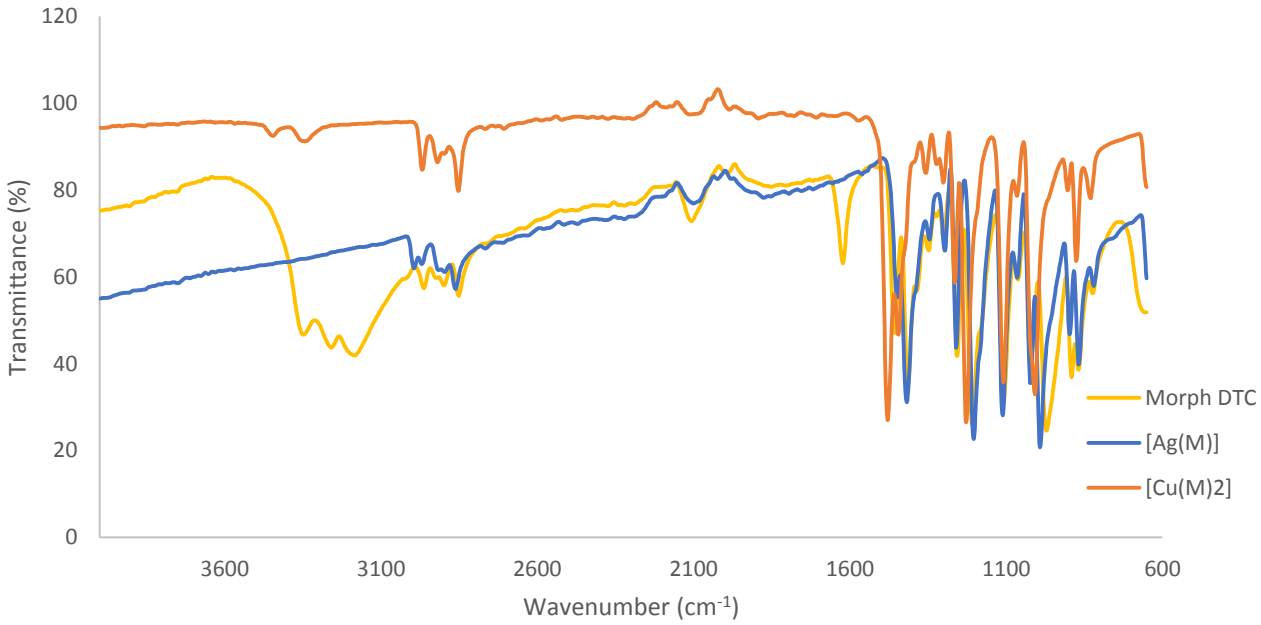

Figure 3. 6. Overlay FTIR spectra of morphiline DTC and it's copper(II) and silver(I) complexes

3.3.5. FTIR spectra of piperidine DTC and it's copper(II) and silver(I) complexes.

Figure 3.7 displays the FTIR spectra of piperidine dithiocarbamate, copper(II) piperidine DTC complex and siver(I) piperidine DTC complex overlay. The N-CSS moiety ν(C-N) vibration was observed at 142 cm^{-1} in the free ligand spectrum. This vibration shifted to higher wavenumber in the complexes, at 1435 and 1449 cm^{-1} for copper(II) complex and silver(I) complex. The C-S symmetric and asymmetric vibration were observed at 957 and 1000 cm^{-1} in the ligand. In the complexes, this C-S vibration became a single band at 993 cm^{-1} and 994 cm^{-1} in copper(II) and silver(I) complex respectively. This single band observed in the complexes shows that both the sulphur atoms have bonded to the metal ion in the complexes.

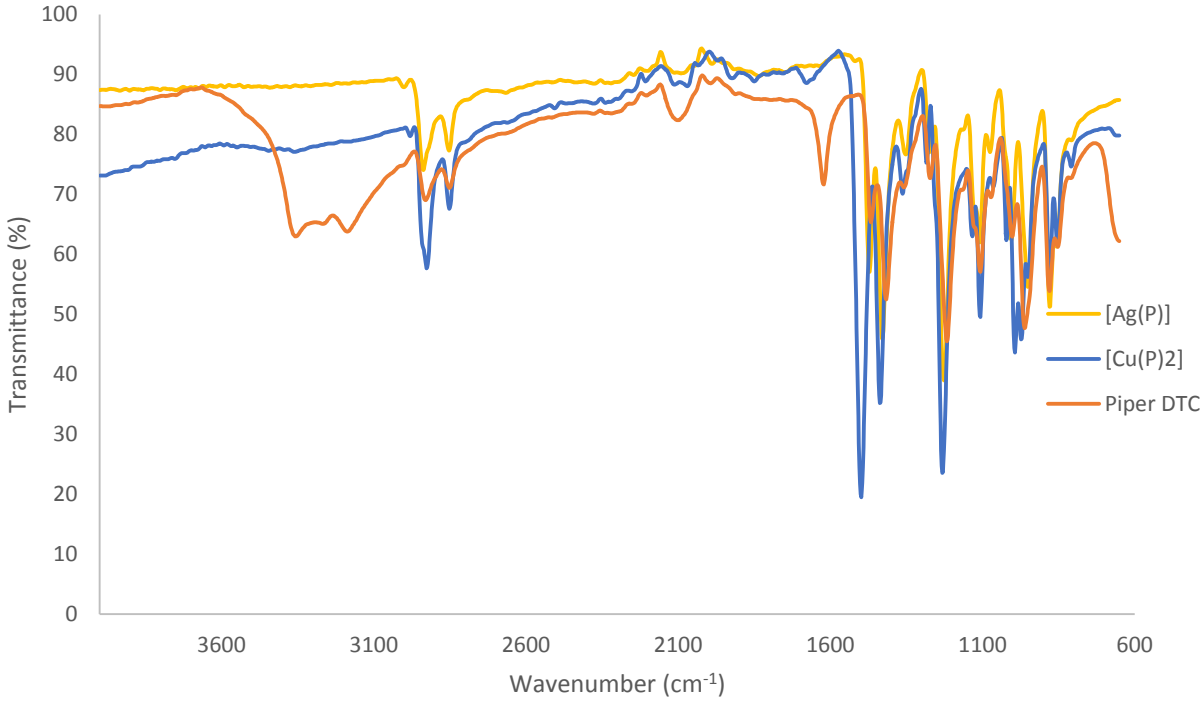

Figure 3. 7. Overlay FTIR spectra of piperidine DTC and it's copper(II) and silver(I) complexes

3.3.6. FTIR spectra of butylamine DTC and it's copper(II) and silver(I) complexes.

The FTIR spectra of butylamine, copper(II) and silver(I) butyl amine dithiocarbamate complexes are shown in Figure 3.8. The important vibrations were observed. The free ligand spectrum showed the ν(C-S) symmetric and asymmetric vibration modes at 905 and 970 cm^{-1} respectively. These vibration modes made a single vibration in the spectra of the complexes, at 907 (Cu(II)) and 928 cm^{-1} (Ag(I)) due to the sulphur atoms bonding to the metal centre and forming the bidentate coordination in the copper(II) complex. ν(C-N) stretching vibration was observed at 1498 cm^{-1} in the spectrum of the ligand and shifted to 1503 cm^{-1} in copper(II) complex spectrum and 1485 cm^{-1} in the silver(I) complex spectrum. The shifts are due to the bonding of the ligand to the metal centres. The ν(N-H) stretching mode was observed in all the spectra at 3365, 3119 and 3244 cm^{-1} for the butylamine DTC ligand, copper(II)DTC complex and silver(I) DTC complex respectively.

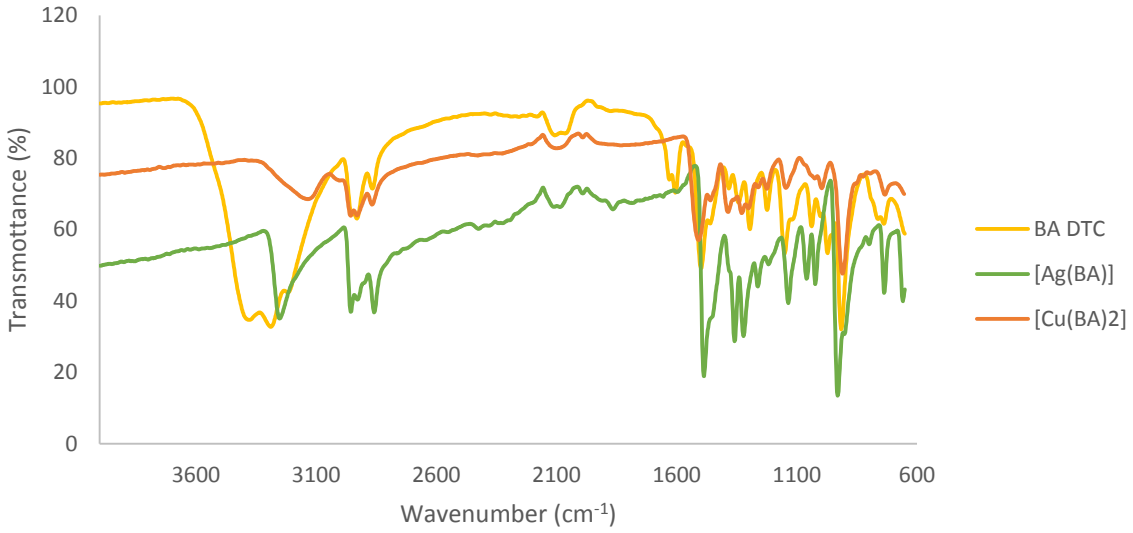

Figure 3. 8. Overlay FTIR spectra of butylamine DTC and it's copper(II) and silver(I) complexes

3.3.7. FTIR spectra of N-ethyl aniline DTC and it's copper(II) and silver(I) complexes.

N-ethyl aniline dithiocarbamate ligand, copper (II) dithiocarbamate complex and silver(I) dithiocarbamate complex FTIR spectra are shown in Figure 3.9. Important vibrations of the dithiocarbamate moiety are observed in all the spectra. The ligand showed the ν(C-N) stretching vibration at 1444 cm^{-1} which shifted to 1418 cm^{-1} and 1438 cm^{-1} in copper(II) and silver(I) complex respectively, due to the coordination of the ligand to the metal ions. The vibrations observed at 997 cm^{-1} and 1021 cm^{-1} in the spectrum of the ligand are ascribed to the symmetric and asymmetric ν(C-S) vibrations. The complexes showed a single peak at 987 cm^{-1}. This is due to the bidentate coordination in the copper(II) complex, and the sulphur atoms in the ligand to the silver ion forming a metal cluster complex. The C-H from the ethyl group of the ligand and C=C stretching vibrations from the ring were observed in all the spectra around 2900 cm^{-1} and 1500 cm^{-1} respectively showing the coordination of the ligand in the complexes.

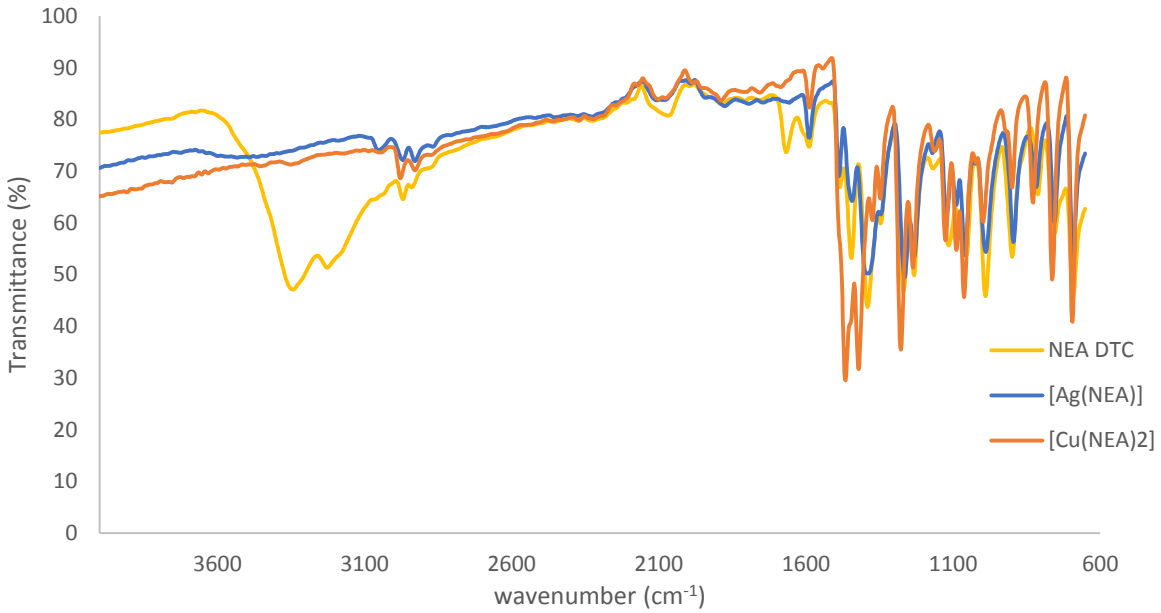

Figure 3. 9. Overlay FTIR spectra of N-ethyl aniline DTC and it's copper(II) and silver(I) complexes

3.3.8. FTIR spectra of dibenzylamine DTC and it's copper(II) and silver(I) complexes.

The overlay FTIR spectra of dibenzylamine DTC ligand, copper(II) dibenzyl amine DTC complex and silver(I) dibenzylamine DTC complex are displayed in Figure 3.10. Two peaks in the range 950 - 1050 cm^{-1} were observed in the FTIR spectrum of the ligand at 972 cm^{-1} and 1032 cm^{-1} and were assigned to C-S symmetric and asymmetric vibrations of the dithio moiety respectively. These vibrations were replaced by one vibration in the complexes observed at 976 cm^{-1} (Cu(II)) and 985 cm^{-1} (Ag(I)) due to the absence of C=S with only C-S bond available in the complexes. The C-N vibration was observed in the ligand at 1448 cm^{-1} which shifted to higher wavenumbers in the complexes, 1478 (Cu(II)) and 1479 cm^{-1} (Ag(I)) due to the partial double bond formation after the coordination of the ligand to the metal centres.

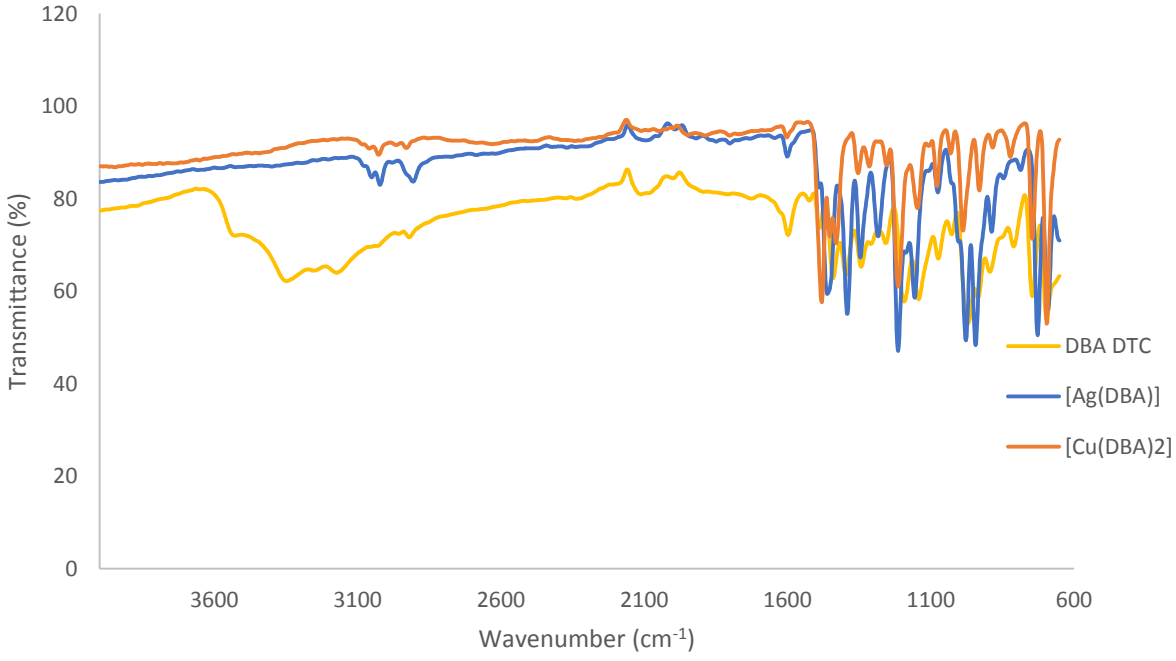

Figure 3. 10. Overlay FTIR spectra of Morphiline DTC and it's copper(II) and silver(I) complexes

3.4. NMR spectra Studies

The NMR spectra of the ligands were recorded in deuterated water (D_2O) as the solvent, so all the proton NMR spectra of the ligands are expected to show a solvent peak at around 4.79 ppm [31]. From the proton NMR, there are no specific shifts expected. The ^{1}H NMR spectra were recorded to predict the structures. The Carbon NMR spectra were recorded to confirm the formation of the dithiocarbamate by looking at the chemical shift of the carbon atom in NCS_2 fragment of the dithiocarbamate ligands expected in the range 185 to 220 ppm downfield [32]. These chemical shifts differ with the coordinated group and also with the molecular framework [32]. They come with very weak intensity which is the characteristic of the quaternary carbon signals [33].

3.4.1. NMR spectra of N-methyl benzyl amine dithiocarbamate ligand

The proton NMR spectrum (Figure 3.11 B) showed all the expected chemical shifts. In the upper field three expected resonances were observed, the two triplets and the doublet assigned to the protons from the aromatic ring in the range between 7 - 7.6 ppm. The two singlets that appear at 5.45 ppm and 3.45 ppm were assigned to the protons from the methyl groups attached to the nitrogen. The ^{13}C NMR spectrum, Figure 3.11 A, shows the presence of carbons in seven different chemical environments in the structure. The carbons in the ring gave signals from 40 ppm to 150 ppm. The signal for the δ ($N^{13}CS_2$) of NCS2 moiety resonated at 210 ppm, confirming the formation of the ligands.

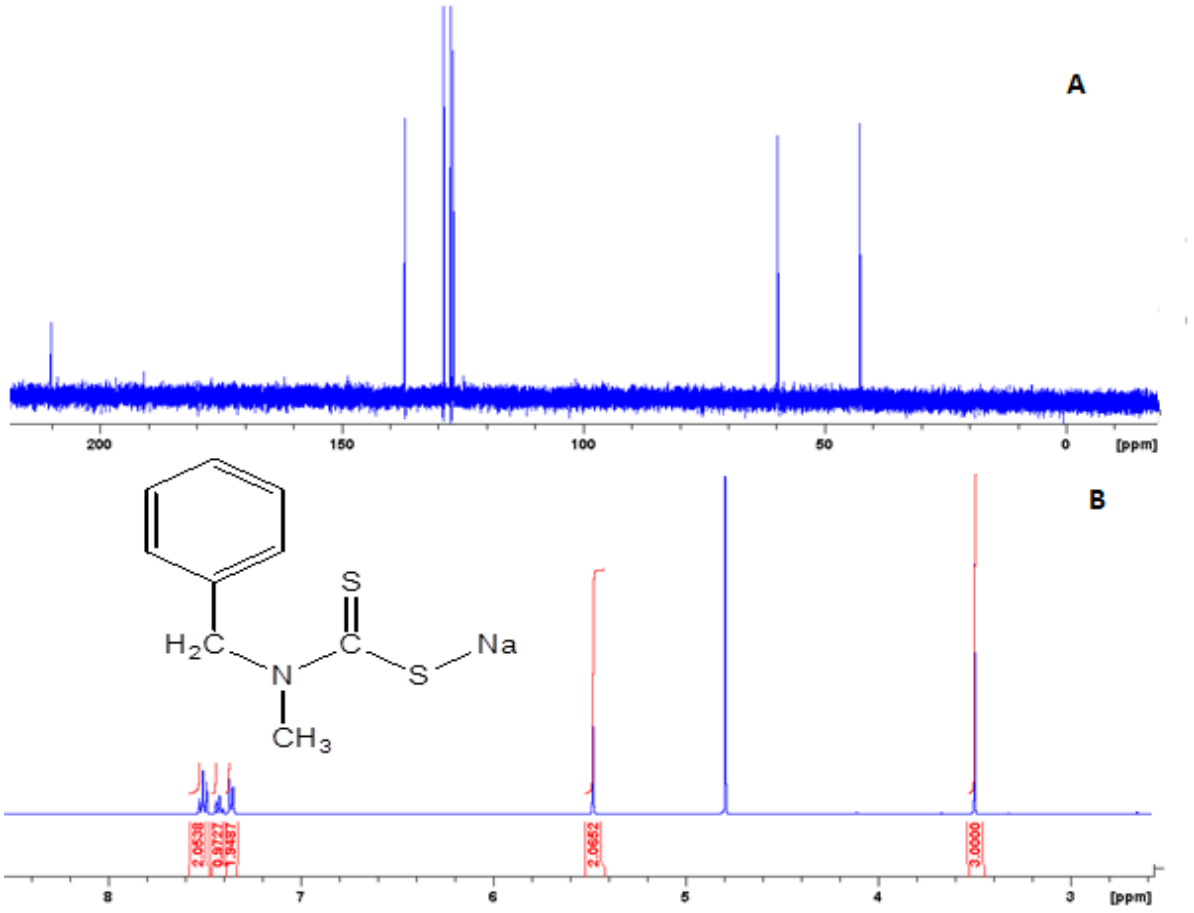

Figure 3. 11 Sodium N-methyl benzyl amine dithiocarbamate ligands NMR spectra. A. ^{13}C NMR and B. ^{1}H NMR

3.4.2. NMR spectra of sodium phenyl piperizine dithiocarbamate

In the proton NMR spectrum, Figure 3.12B, three resonances around 7 ppm appeared and they are assigned to the protons from the aromatic ring. Two triplet chemical shifts showed in the range between 2 - 5 ppm and they correspond to the four protons in the piperizine ring. The ^{13}C NMR spectrum (Figure 3.12A) showed the signals corresponding to the carbons in the piperizine ring at around 50 ppm. Four signals were observed in the range 120 ppm - 150 ppm and they are assigned to the carbons in the aromatic ring. The last signal observed at 210 ppm is ascribed to the δ ($N^{13}CS_2$) of NCS_2 moiety.

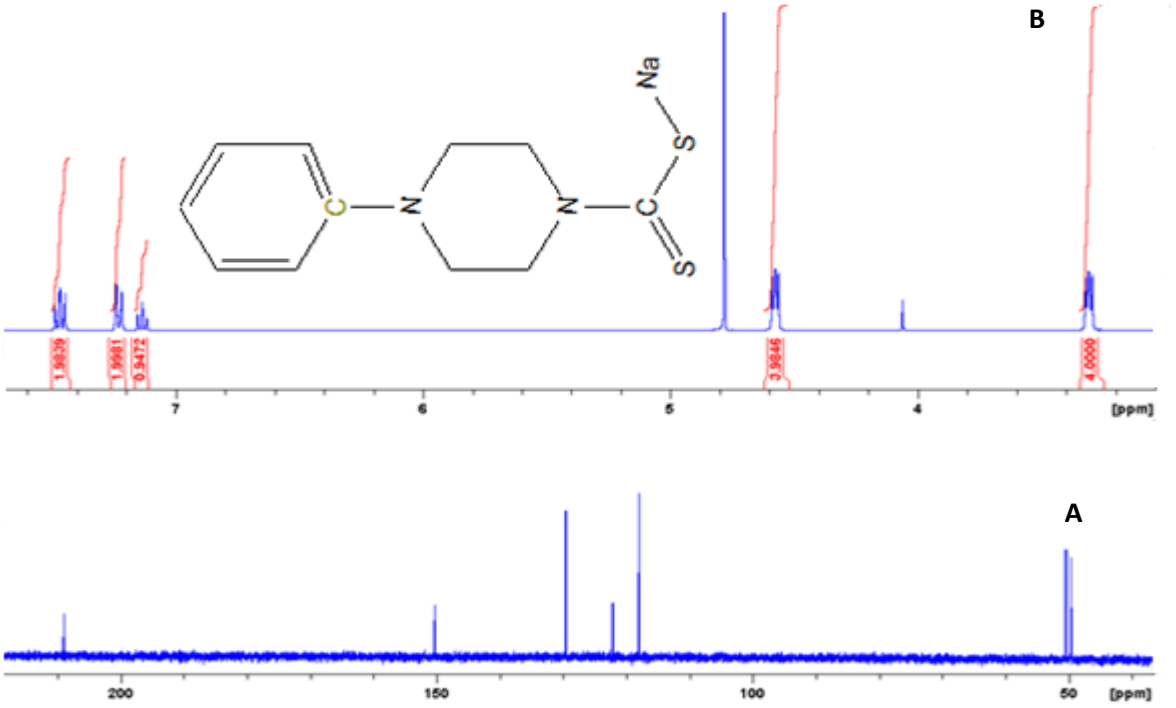

Figure 3. 12 A. ^{13}C NMR and B. ^{1} H NMR spectra of Sodium phenyl piperizine dithiocarbamate ligand

3.4.3. Sodium diallyl amine dithiocarbamate NMR spectra

In the proton NMR spectrum, a doublet of a doublet (dd) is exhibited at a region from 5.15 ppm to 5.35 ppm corresponding to the two protons bonded to the carbons with double bonds which are *cis* to the protons bonded to the second carbon with a double bond (Figure 3.13B). The reason being the two terminal protons are anisotropic. Around 5.8 ppm, there is a multiplet peak that corresponds to the protons of the second carbon atom with a double bond. The multiplet arises because the terminal protons split the protons differently and the vicinal methylene protons are also split further. The doublet that appeared between 4.8 ppm is for the protons bonded to the methyl amine groups. The ^{13}C NMR spectrum (Figure 3.13 A) showed all the expected peaks corresponding to the carbons in three different chemical environments and also the peak that is due to the thiocarbonyl group was observed at 210 ppm.

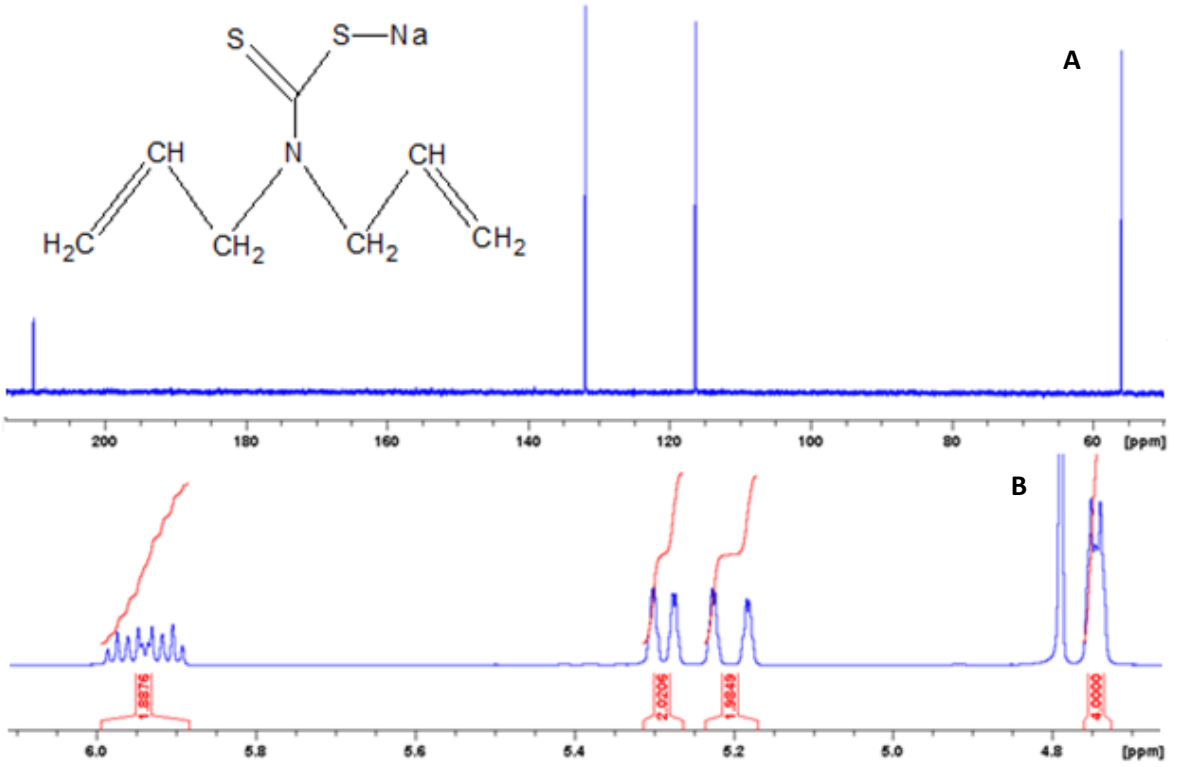

Figure 3. 13 A. ^{13}C NMR and B. ^{1}H NMR spectra of sodium diallyl amine dithiocarbamate ligand

3.4.4. Sodium morpholine dithiocarbamate NMR spectra

The proton NMR spectrum (Figure 3.6 B) exhibit two triplet peaks. The one at 5.8 ppm corresponds to the four protons in the dimethyl ether group in the ring and the one at the region 2 to 3 ppm corresponds to the four protons in the dimethyl amine group. The ^{13}C NMR spectrum showed the two peaks resonating at the region between 50 to 70 ppm corresponding to the four carbons in two different chemical environments in the ring. The last important peak for δ ($N^{13}CS_2$) of NCS_2 moiety was observed at 210 ppm with a very low intensity.

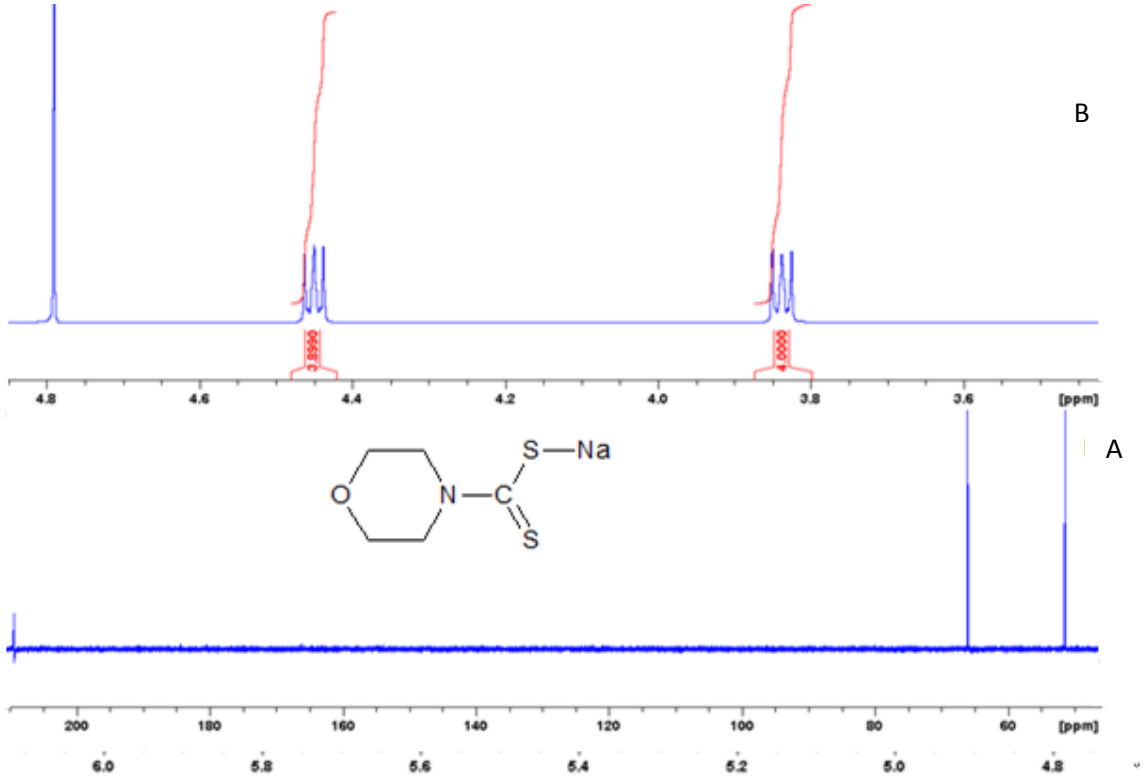

Figure 3. 14. A. ^{13}C NMR and B. ^{1}H NMR spectra of sodium morpholine dithiocarbamate ligand

3.4.5. Sodium piperidine dithiocarbamate NMR spectra

The proton NMR spectrum (Figure 3.15 B) showed two multiplets at a region from 1.4 ppm to 1.8 ppm. These peaks are attributed to the protons in the ring. The triplet that appeared at 4.2 ppm is attributed to the protons in the ring from the carbons bonded to the nitrogen atom. The carbon NMR spectrum (Figure 3.15 A) showed all expected signals. One signal corresponding to the δ ($N^{13}CS_2$) of NCS_2 moiety appeared around 200 ppm as expected. In the range from 20 ppm to 50 ppm three signals appeared corresponding to the carbons in three different environments of the ring.

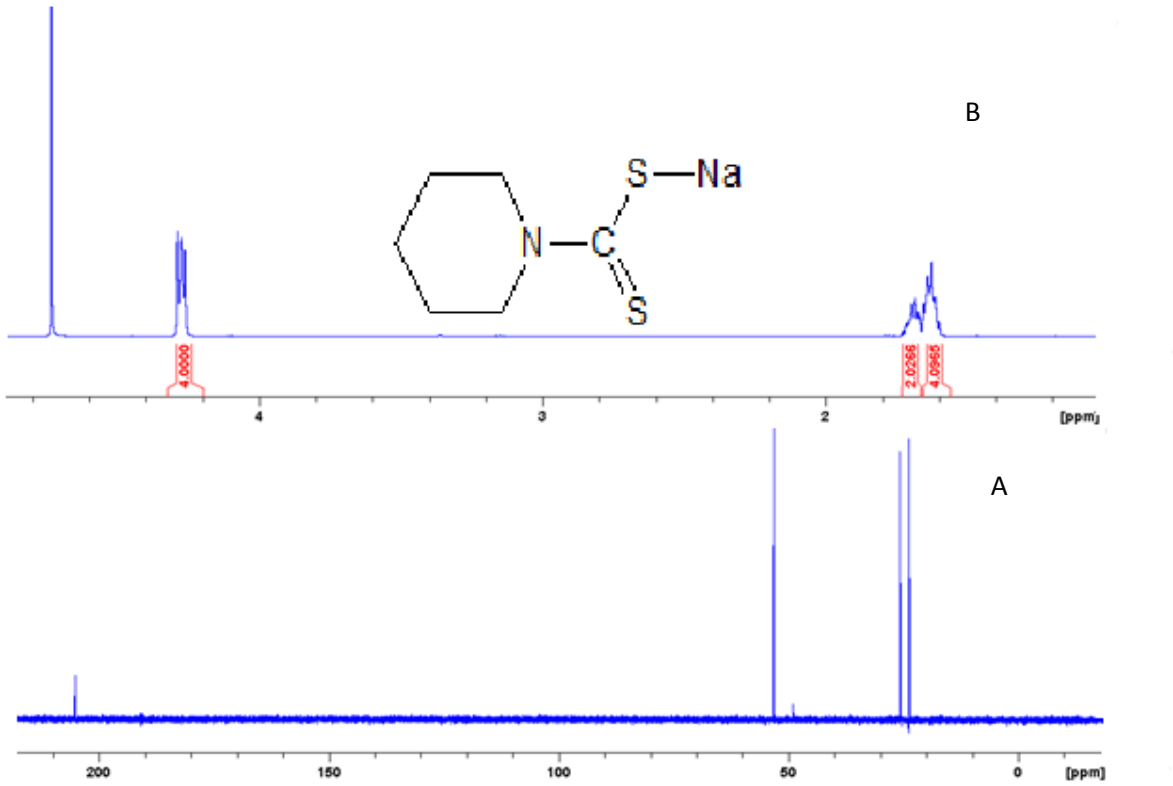

Figure 3. 15. A. ^{13}C NMR and B. ^{1}H NMR spectra of sodium piperidine dithiocarbamate ligand

3.4.6. Sodium butyl amine dithiocarbamate ligand NMR spectra

The protons from the Alkyl groups expected in the range between 0 - 3 ppm in the proton NMR spectrum were observed. The triplet corresponding to the protons in carbon A resonated at 0.99 ppm. The sextet corresponding to the protons in carbon B and the quintet that corresponds to the proton in carbon C were observed (Figure 3.16 B) at 1.4 ppm and 2.7 ppm respectively. The triplet expected for the protons in the amine group resonated at 3.6 ppm. The carbon 13 spectrum (Figure 3.16 A) showed the peaks for all the five carbon in the structure, the first four in the range 10 to 50 ppm as they are all in different environments. The signal for the δ ($N^{13}CS_2$) of NCS_2 moiety at exactly 210 ppm confirmed the presence of carbon disulphide.

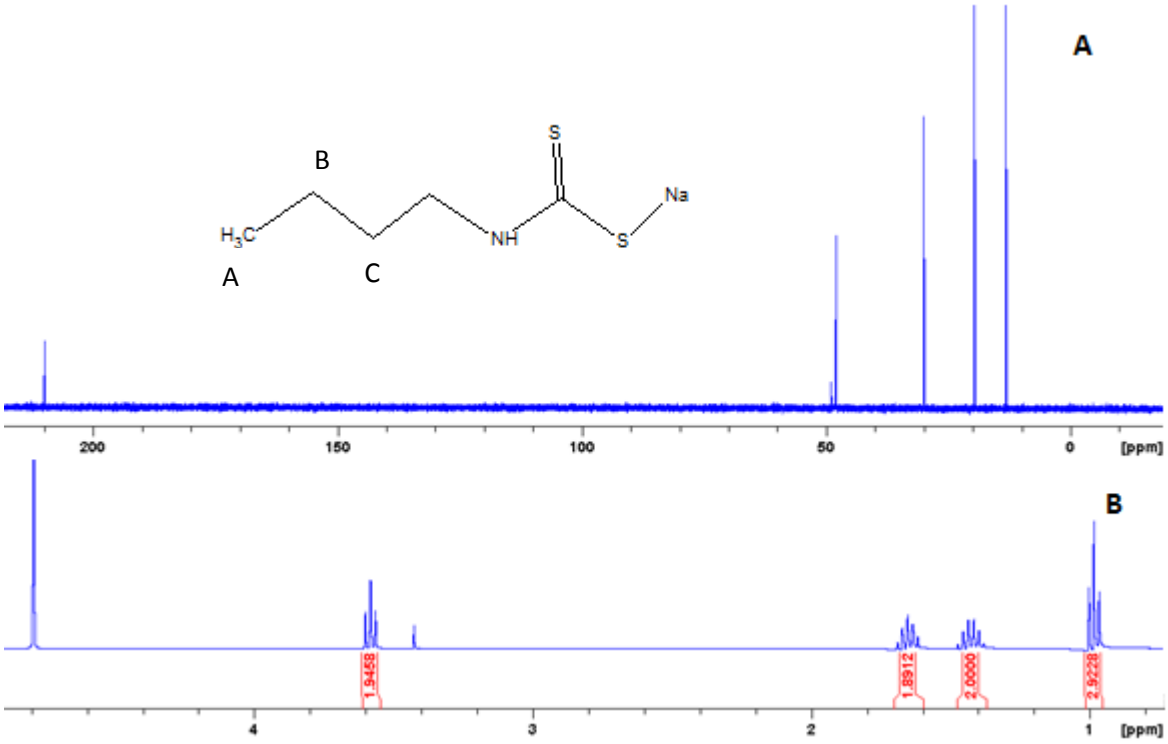

Figure 3. 16. A. ^{13}C NMR and B. ^{1}H NMR spectra of sodium butyl amine dithiocarbamate ligand

3.4.7. Sodium N-ethyl aniline dithiocarbamate ligand NMR spectra

Figure 3.17 shows the sodium-ethyl aniline dithiocarbamate ligand spectra for carbon 13 NMR (A) and proton NMR (B). Spectra A showed all the expected proton peaks. Two chemical shifts at around 1 ppm and 4.5 ppm were observed and assigned to the protons from the ethyl group as a quintet and a triplet respectively. Three chemical shifts appeared above 7 ppm and were attributed to the ring protons. No impurities or unknown peaks were observed. The ^{13}C NMR spectrum (A) showed six peaks for carbons resonating at six different chemical environments. The peak that confirmed the carbon atom bonded to the sulphur atom was also observed at 210 ppm.

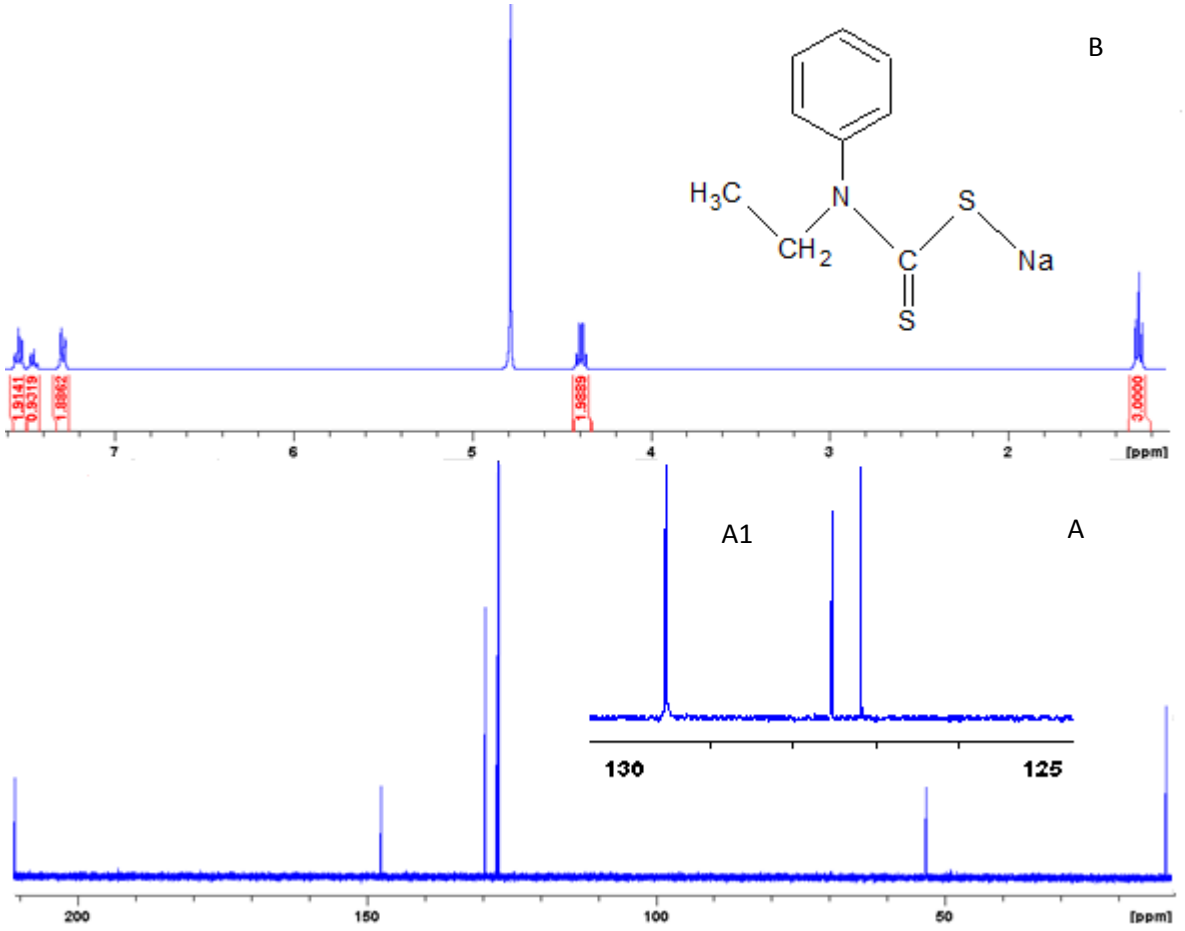

Figure 3. 17. A. ^{13}C NMR and B. ^{1}H NMR spectra of sodium N-ethyl aniline dithiocarbamate ligand

3.4.8. Sodium dibenzyl amine dithiocarbamate ligand NMR spectra

Figure 3.18 shows the proton and ^{13}C NMR spectra of sodium dibenzyl amine dithiocarbamate ligand. The proton NMR spectrum shows the solvent peak calibrated to 4.79 ppm. Followed by the singlet for the four protons in the two methylene groups of the compound at 6.4 ppm. The three peaks corresponding to the ring resonated between 7.3 and 7.6 ppm. The spectrum showed no impurities. The ^{13}C NMR spectrum also showed the expected peaks for carbons in different environments and confirmed the formation of the ligand.

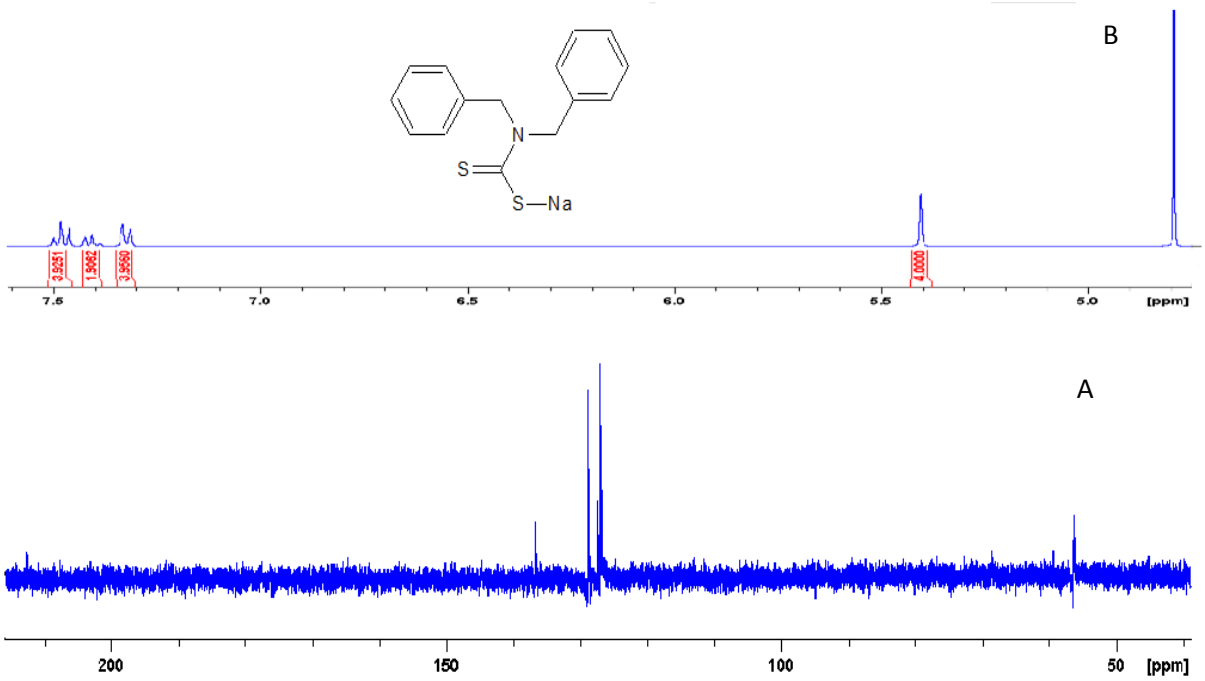

Figure 3. 18. A. ^{13}C NMR and B. ^{1}H NMR spectra of dibenzyl amine dithiocarbamate NMR spectra

3.5. Electronic spectra studies of the copper(II) complexes

The electronic spectra measurements in this study were carried out to assign the stereochemistries of the metal ions in the complexes based on the position and number of the *d-d* transition bands. In the dithiocarbamates, two bands are expected below 380 nm and they are usually attributed to the $\pi-\pi^*$ and $n-\pi^*$ transitions due to N–C=S and S–C=S groups [34]. The shift of these intraligand transition bands in the complexes to the lower or higher wavelength is expected due to the coordination of sulphur atoms to the metal [35]. The visible spectrum of copper(II) complexes is usually difficult to analyse because of the unsymmetrical band which may arise due to the *Jahn-Teller* distortions resulting from a number of overlapping bands [36].

For the tetrahedral geometry of the copper(II) complexes, one band is expected in the visible region below 600 nm, this band is assumed to suggest a $^2T_{2g} \rightarrow {}^2E_g$ transition which is for Cu(II) complexes with tetragonal distortion due to the *Jahn-Teller* effect [37, 38]. For the octahedral geometry of Copper(II) complexes two transitions are expected in the visible and near the Infrared region but also one broad band which may be ascribed to the $^2E \rightarrow {}^2T_2$ [39], is expected due to Jahn Teller distortion [40]. For the square planar geometry two bands at around 600 and 400 nm are expected, these bands are due to $d_{xy} \rightarrow d_z^2$ and $d_{xy} \rightarrow d_{xz}$ transitions [41].

3.5.1. Electronic spectra of N-methyl benzyl amine dithiocarbamate ligand and its copper(II) complex

Electronic spectra of sodium N-methyl benzyl amine dithiocarbamate ligand and its copper(II) complex are presented in Figure 3.19. From the spectra, the ligand shows two bands at 260 and 290 nm. These two bands are attributed to π–π*and n–π* transitions which are due to N–C=S and S–C=S groups. The two bands appeared again in the complex confirming the presence of the ligand in the complex. They are still in the intra-ligand region but have shifted to higher wavelength. In the visible region, the complex spectrum displays two bands at 440 and 643 nm which are expected for Cu(II) ion in square planar geometry.

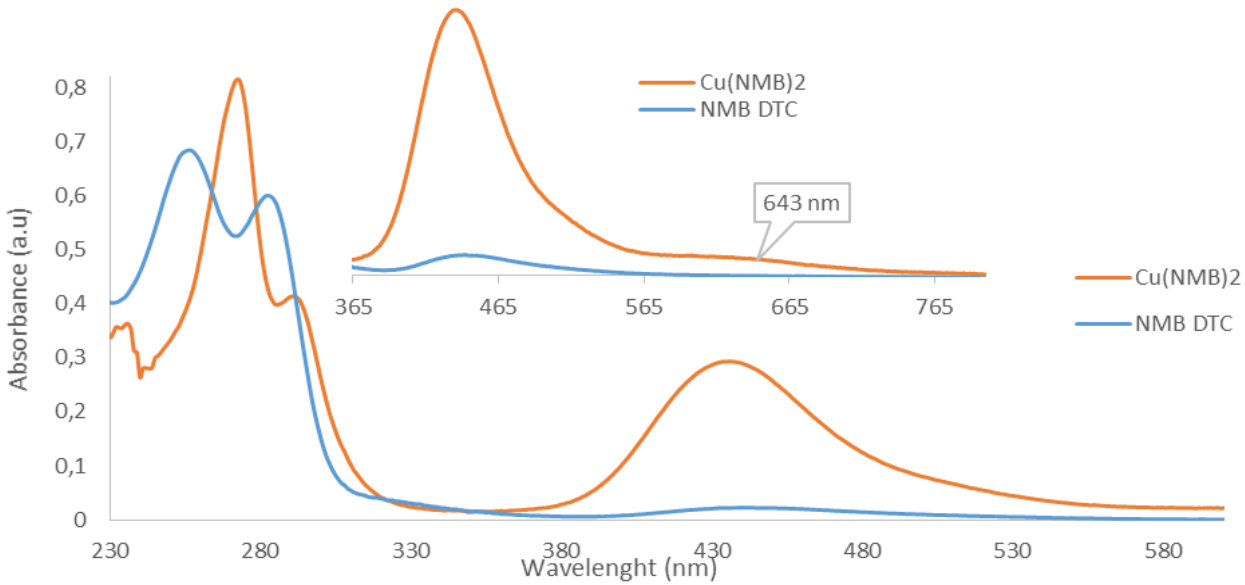

Figure 3. 19. Overlay UV-Vis spectra of N-methyl benzyl amine dithiocarbamate and copper(II) N-methyl benzyl amine dithiocarbamate complex

3.5.2. Electronic spectra of phenyl piperizine dithiocarbamate ligands and its copper(II) complex

Figure 3.20 shows the overlay spectra of the sodium phenyl piperizine dithiocarbamate ligand and its complex. The ligand spectrum show the two expected bands in the ultraviolet region. The first one is at 260 nm and the second which appeared as a shoulder at 290 nm are assigned to π–π*and n–π* transitions which are due to N–C=S and S–C=S moiety. The complex shows the intra-ligand transitions however, at higher wavelengths which is due to the coordination of the ligand to the metal ion. The *d-d* transitions were observed at 450 nm and also at 638 nm which confirmed the square planar geometry for the complex.

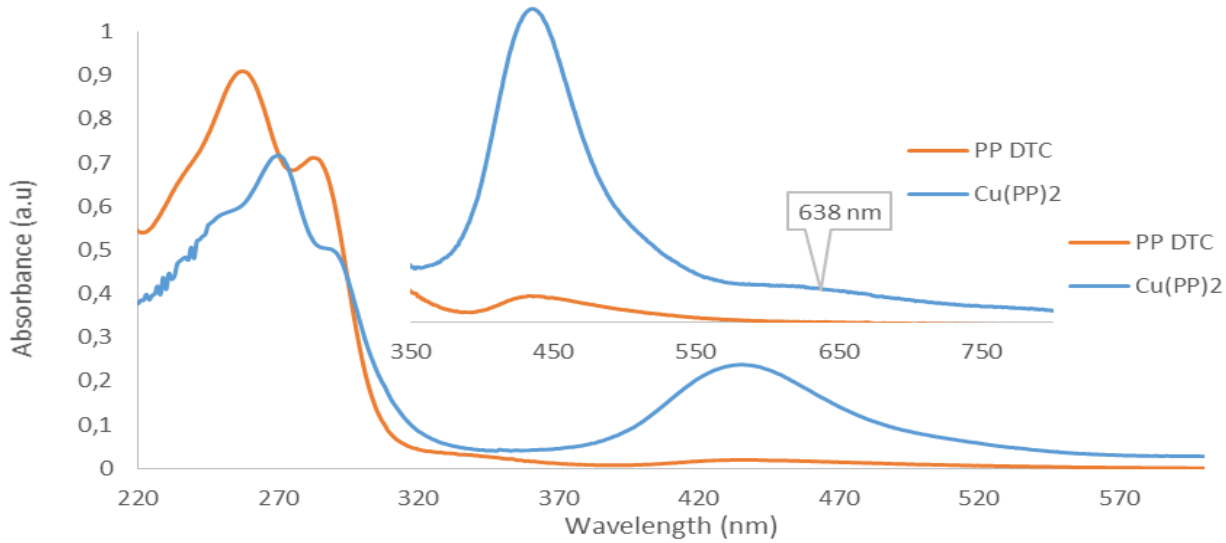

Figure 3.20. Overlay UV-Vis spectra of phenyl piperizine dithiocarbamate and copper(II) phenyl piperizine dithiocarbamate complex

3.5.3. Electronic spectra of diallyamine dithiocarbamate ligand its Copper(II) complex

Electronic spectra of the ligand and the complex are shown in Figure 3.21. The two bands expected in the UV-Vis spectrum of the dithiocarbamate were observed at 261 nm which corresponds to π−π* transition due to the N–C=S moiety, and at 287 nm for n−π* transition due to S–C=S moiety. The spectra of the complex also showed these bands in this region but at higher wavelengths. These bands confirmed the coordination of the ligand to the metal ion. The complex exhibit two bands in the visible region. The first one at 441 nm and another broad one at around 641 nm. These bands are attributed to the d-d transitions that corresponds with the square planar geometry for the metal ion.

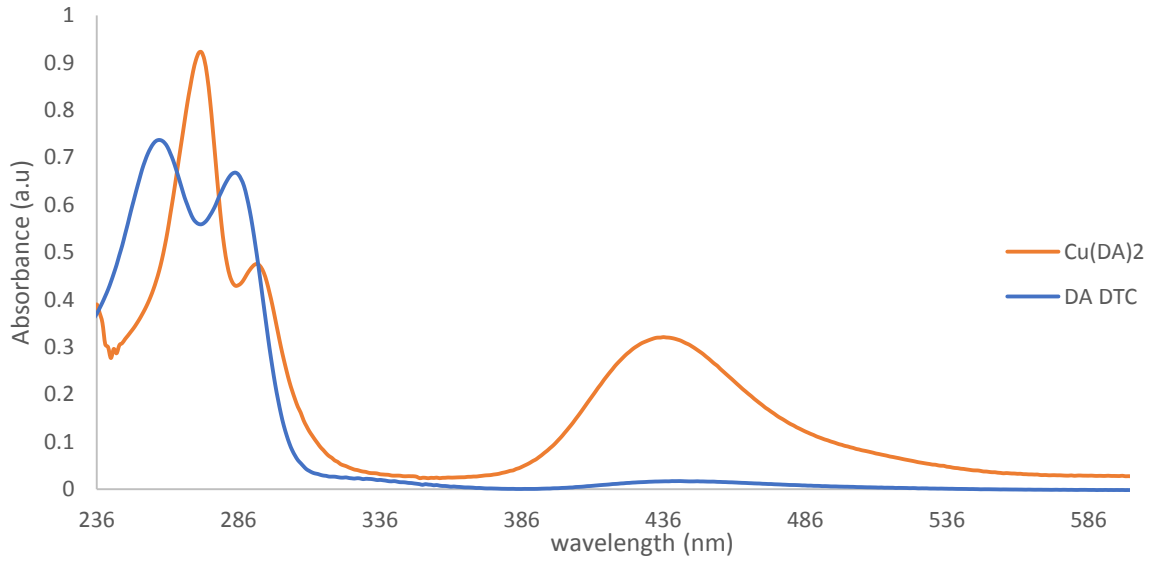

Figure 3.21. Overlay UV-Vis spectra of diallylamine dithiocarbamate and copper(II) diallylamine dithiocarbamate complex

.

3.5.4. Electronic spectra of morpholine dithiocarbamate ligand and its Copper(II) complex

Morpholine dithiocarbamate ligand and the copper(II) complex electronic spectra are shown in Figure 3.22. The ligand showed all the transitions expected. Two bands were observed at 265 and 286 nm which are due to the N–C=S and S–C=S moiety respectively from the ligand structure. These bands were observed in the spectrum of the complex but shifted to higher wavelengths, 276 and 288 nm respectively. The complex showed only one band as the *d-d* transition which may be due to the overlapping of the bands (*Jahn Teller* distortion).

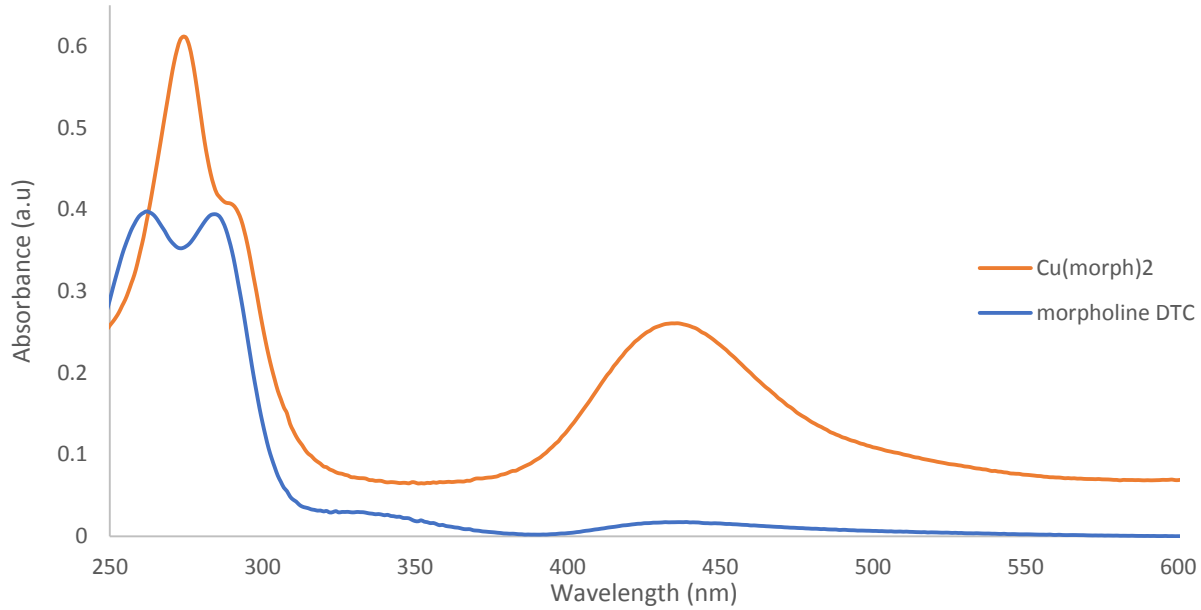

Figure 3.22. Overlay UV-Vis spectra of morpholine dithiocarbamate and copper(II) morpholine dithiocarbamate complex

3.5.5. Electronic spectra of piperidine dithiocarbamate ligand and its Copper(II) complex

The piperidine dithiocarbamate ligand UV spectrum (Figure 3.23) showed two bands in the UV region and they were assigned to π−π*and n−π* transitions of the N–C=S and S–C=S moiety. These bands also appeared in the complex spectrum though at the higher wavelengths. This could be ascribed to the coordination of the metal ion to the ligand. The complex showed two bands at the visible region as the *d-d* transitions. The first band at 440 nm and a very week band at 637 nm are assigned to dxy → dz^2 and dxy → dxz transitions responding to Cu(II) ion in square planar geometry.

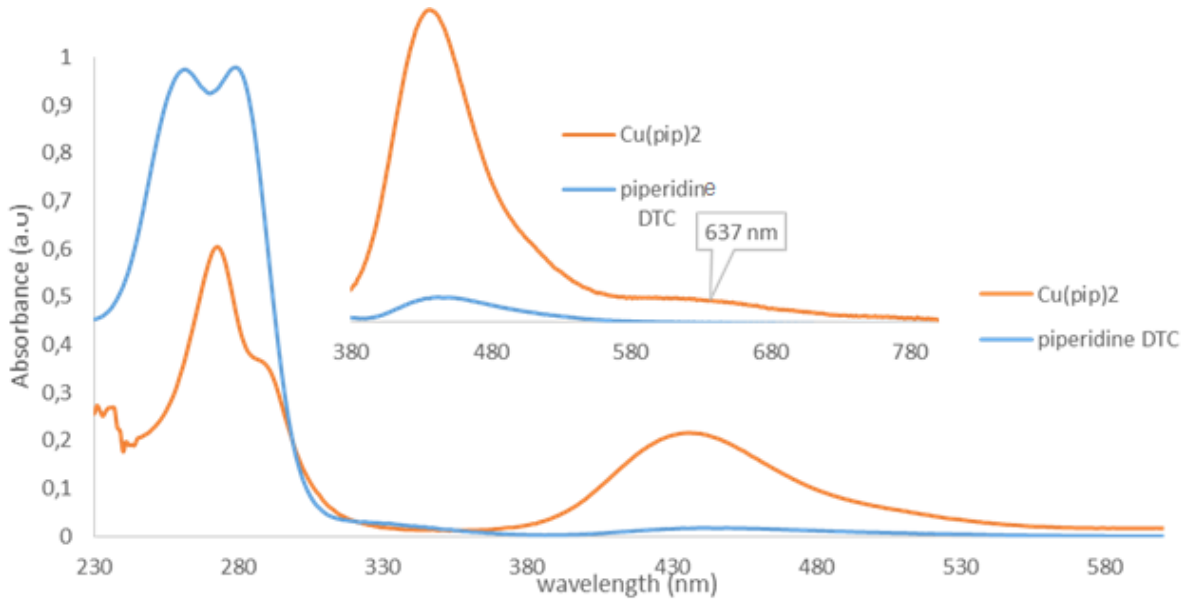

Figure 3. 23. Overlay UV-Vis spectra of piperidine dithiocarbamate and copper(II) piperidine dithiocarbamate complex

3.5.6. Electronic spectra of butyl amine dithiocarbamate ligand and its copper(II) complex

The spectra of butyl amine dithiocarbamate ligand and it's copper(II) complex are displayed in Figure 3.24. In the spectrum of the ligand two bands were observed as expected. These bands appeared at 260 and 287 nm attributed to π–π*and n–π* transitions due to N–C=S and S–C=S from the dithiocarbamate moiety. They were also observed as expected in the spectrum of the complex at higher wavelengths. The complex also showed two d-d transitions assigned to dxy → dz^2 and dxy → dxz transitions corresponding to Cu(II) ion in a square planar geometry.

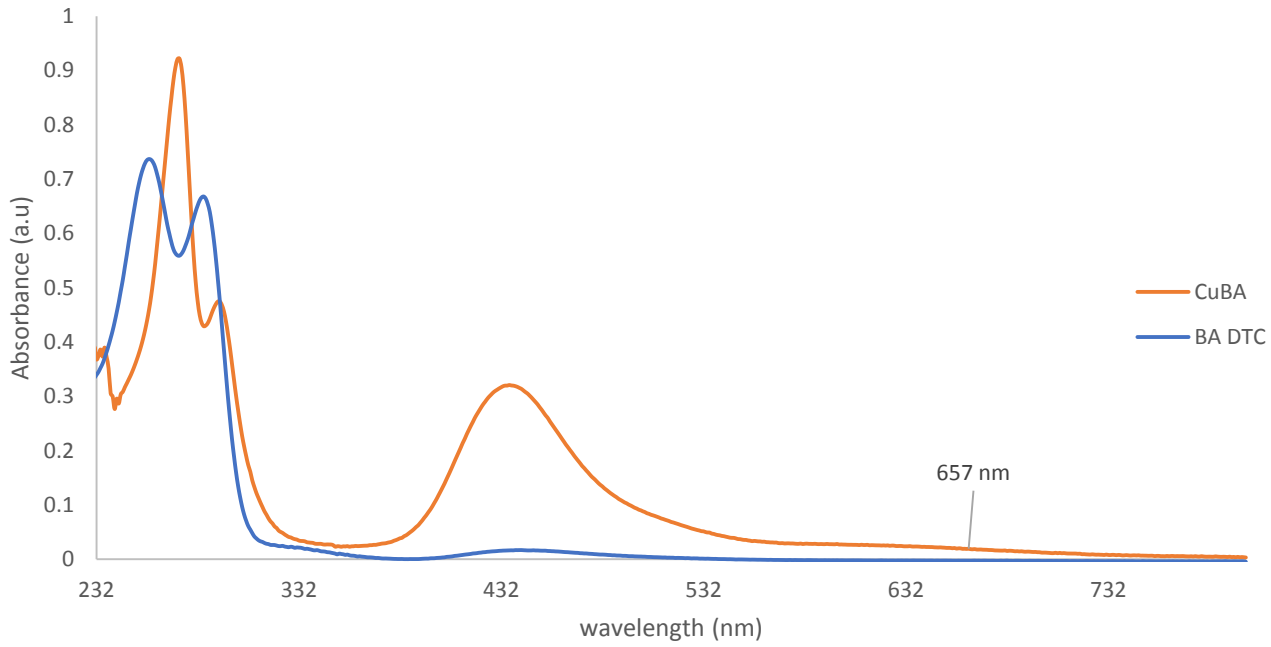

Figure 3.24. Overlay UV-Vis spectra of butyl amine dithiocarbamate and copper(II)butyl amine dithiocarbamate complex

3.5.7. Electronic spectra of N-ethyl aniline dithiocarbamate ligand and its Copper(II) complex

The spectra in Figure 3.25 shows the overlay of N-ethyl aniline dithiocarbamate ligand spectrum and copper(II) N-ethyl aniline dithiocarbamate complex spectrum. In the spectrum of the ligand, two bands were observed in the UV region. These bands appeared at 265 and 295 nm assigned to π–π*and n–π* transitions due to N–C=S and S–C=S moiety. The spectrum of the complex also showed these bands shifted to higher wavelengths. The shifts of these bands may be due to their coordination to the copper(II) ion. The spectrum of the complex also showed two bands at the visible region at around 445 nm and a very weak band at 648 nm, as indicated in the zoomed spectrum, These bands are assigned to dxy → dz^2 and dxy → dxz transitions confirming square planar geometry for the Cu(II) ion in the complex.

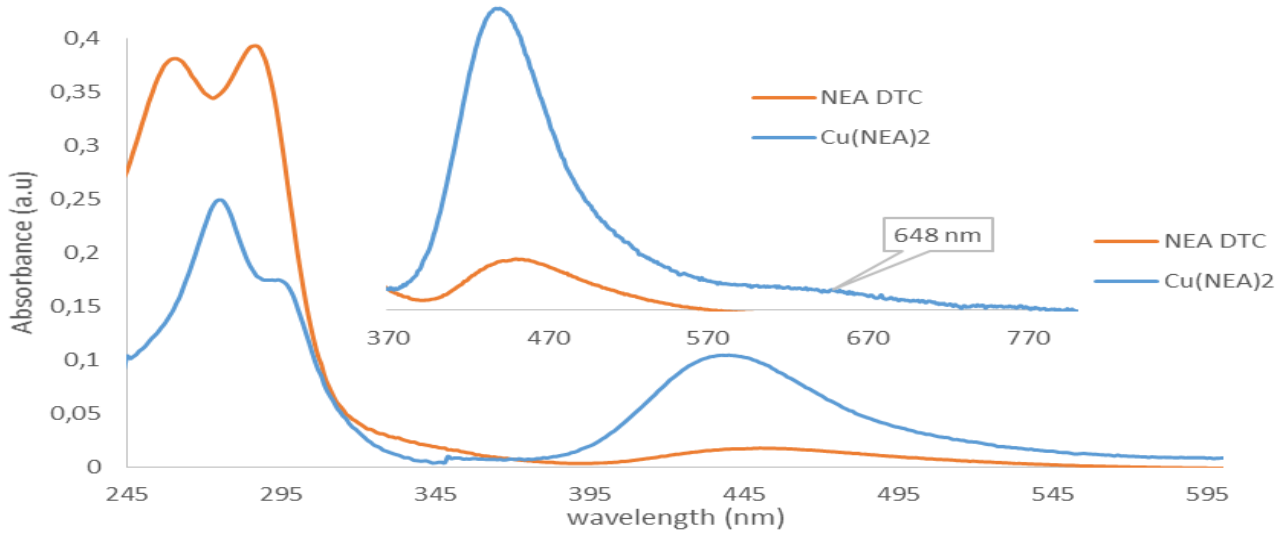

Figure 3.25. Overlay UV-Vis spectra of N-ethyl aniline dithiocarbamate and copper(II) dithiocarbamate complex

3.6. Thermal studies of the metal complexes

3.6.1. Thermal studies of copper dithiocarbamate complexes

The TGA curves of the synthesized metal (Cu/Ag) dithiocarbamate complexes were recorded under nitrogen flow from 55 to 900°C and are presented in Figure 3.26. The thermogram of the metal complexes of the same ligand are overlaid in one graph. The thermogram indicate the decomposition temperature of the complexes and also the percentage of the compound decomposed. All the complexes with dibenzyl amine, N-methyl benzyl amine, piperidine, morpholine ligands (Figure 3.26) showed the same thermal behaviour as they showed one step decomposition. Ag(I) dibenzyl amine DTC and Cu(II) dibenzyl amine DTC complexes showed the decomposition starting at 280°C to 437°C losing 67% and 57% of the compounds respectively. However for Ag(I) N-methyl benzyl amine DTC and Cu(II) N-methyl benzyl amine DTC complexes 60% and 82% weight loss was observed respectively. The decomposition of these complexes started at 220°C, 297°C and continued to 367°C and 377°C for copper or silver complex respectively.

Silver(I) piperidine DTC complex was more stable than copper(II) piperidine DTC complex as it started to decompose at 322°C to 371°C losing weight of 53% while the copper complex started decomposing at 270°C to 340°C with weight loss of 76% of the complex mass. The morpholine ligand complexes also followed the same behaviour as they started decomposing at 344°C to 366°C and 293°C to 399°C for the silver and copper complex respectively.

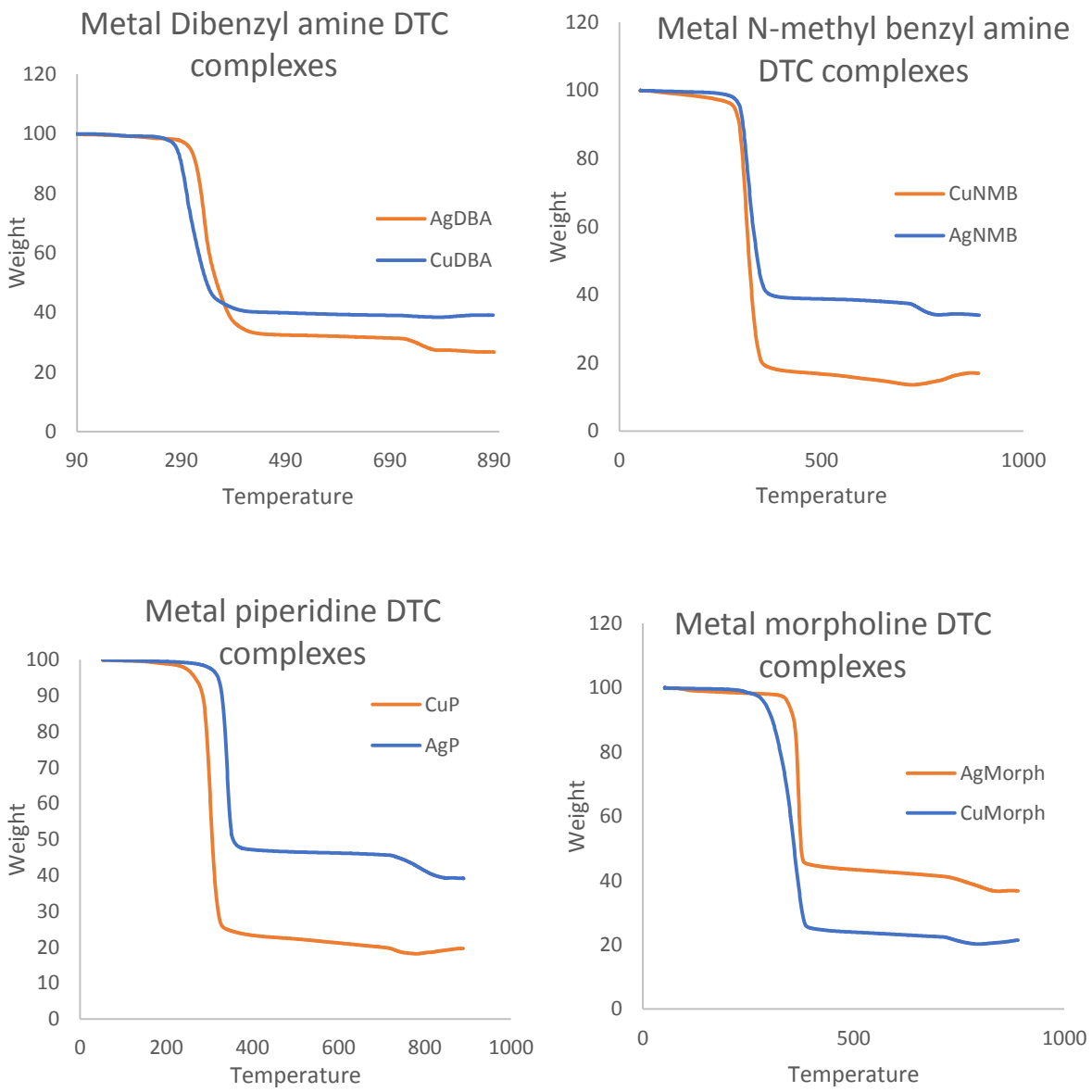

Figure 3. 26 Overlay TGA curves of some synthesized metal dithiocarbamate complexes

The copper complexes of phenyl piperazine and N-ethyl aniline ligands also followed the one step decomposition as they decomposition happened at 262 to 351°C and 276 to 368°C with the weight loss of 5% and 38% respectively. The silver complexes of phenyl piperazine, butyl amine and N-ethyl aniline dithiocarbamate ligands and copper(II) Butyl amine DTC complex however showed different mechanism as they decomposed in two steps.

The first degradation that happened at 174 - 256°C, 129 - 189°C, 57 - 230°C, and 173 - 233°C respectively are ascribed to the extrusion of the entrapped solvent. Otherwise the decomposition of the complexes started at around 200°C for all of them and carried on to around 300°C. After these major decompositions the complexes were stable up to 900°C and showed that there was no more decomposition as the remained material was stable [42]. After the decomposition when the residue remained stable the left material corresponds to the metal sulphides [43].

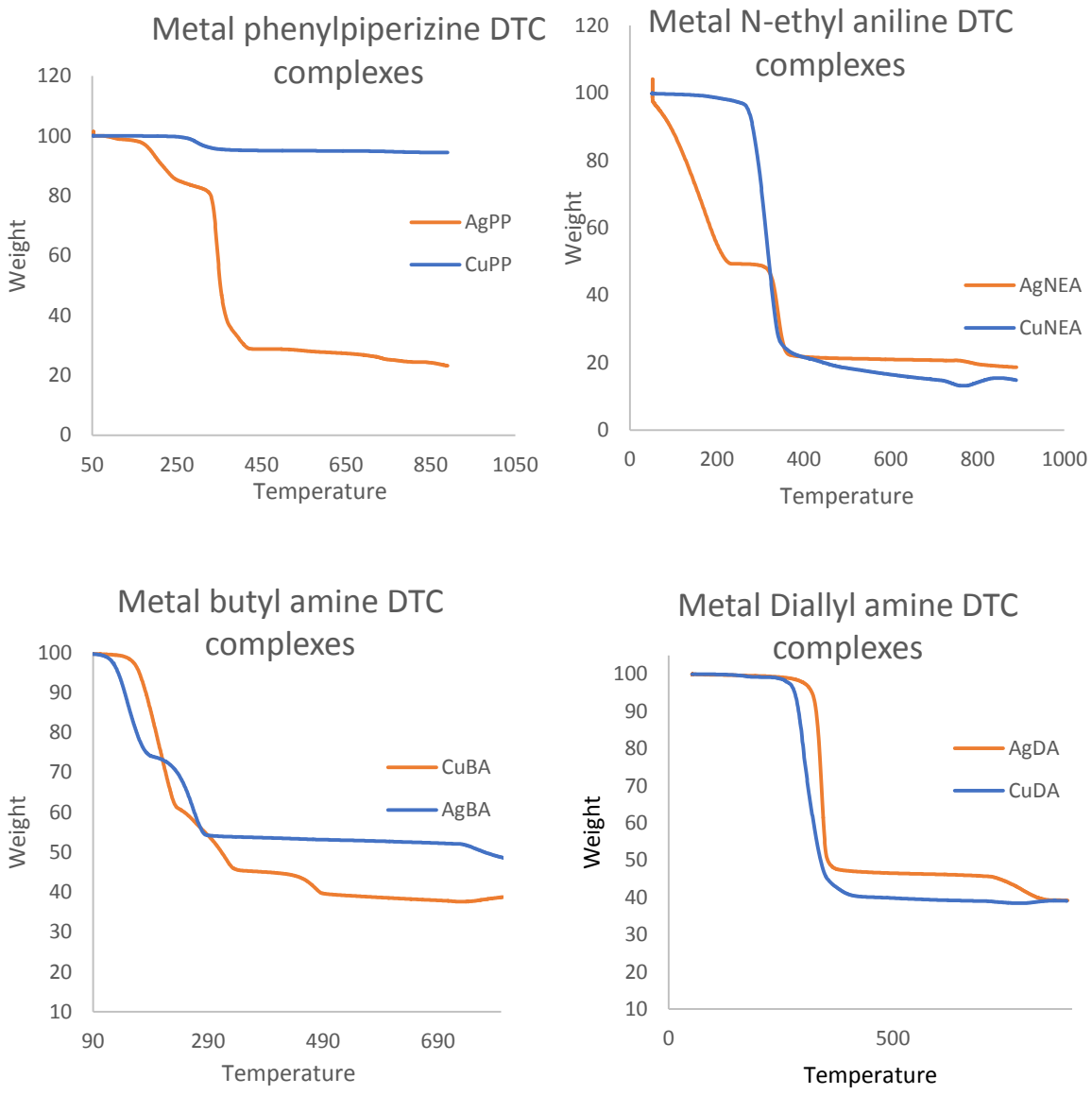

Figure 3. 27. Overlay TGA curves of the metal dithiocarbamate complexes

3.7. Single crystal X-ray analysis

3.7.1. Single crystal X-ray crystallography of [Cu(piper)$_2$] and [Ag$_4$(NEA)$_4$] X-ray crystallography

The crystal structures of the complexes [Cu(piper)$_2$] and [Ag$_4$(NEA)$_4$] complexes are depicted in Figure 3.28 and Figure 3.31. Single green block-shaped crystals of [Cu(piper)$_2$] complex and single yellow block-shaped crystals of [Ag$_4$(NEA)$_4$] were recrystallized from dichloromethane by slow evaporation. A suitable crystal (0.31×0.17×0.12) mm^3 for [Ag$_4$(NEA)$_4$] and (0.33×0.19×0.13) mm^3 for [Cu(piper)$_2$] was selected and mounted on a mitigen holder in paratone oil on a Bruker APEX-II CCD diffractometer at 100(2) K temperature. The structure was solved with the ShelXS-2013 structure solution program, using the direct solution method. The model was refined with version 2016/6 of ShelXL using Least Squares minimisation.

3.7.2. Molecular structures of [Cu(piper)$_2$] and [Ag$_4$(NEA)$_4$]

Crystal data and structural refinements are presented in Table 3.3. Selected bonds lengths for [Cu(piper)$_2$] and [Ag$_4$(NEA)$_4$] are listed in Tables 3.4. The molecular structures and packing diagrams for [Cu(piper)$_2$] are shown in Figures 3.28 and 3.29 and those for [Ag$_4$(NEA)$_4$] are presented in Figures 3.30 and 3.31. [Cu(piper)$_2$] crystallised in the P$_{12/c}$ space group. The compound contains a Cu(II) ion bonded to two molecules of piperidine dithiocarbamate ligand forming a distorted square planar geometry around the copper centre. The bond angle of the S—Cu—S from the two piperidine dithiocarbamate molecule is the same, 77.83(2)°. The two Cu—S bond lengths in each of the ligand are similar and slightly different from each other.

The bond lengths for Cu—S1 and Cu—S1[1] is 2.2894(6) Å while those of Cu—S2 and Cu—S2[2] is 2.3105(6) Å. These bond lengths are similar to those reported for Cu—S in copper(II) dithiocarbamate complexes [17]. In the molecular structure of the copper complex, the N(1)—C(1) bond length of 1.312(3) Å is closer to the C—N double bond (1.28Å) than the C—N single bond (1.47Å) and that shows that the Cu—S bond in the molecule possess strong covalent character. The packing diagram of the copper complex display five asymmetric units in the crystal packing (Figure 3.29). Four of them are at the corner of a rectangle and the fifth molecule is sandwiched at the centre of the other four complexes within the crystal packing. The asymmetric structure at the centre of molecular packing linked each of the other four structures through two H···π intermolecular interactions between the H atom on the piperidine molecule and the S atom, as shown by the blue dashed lines in Figure 3.29.

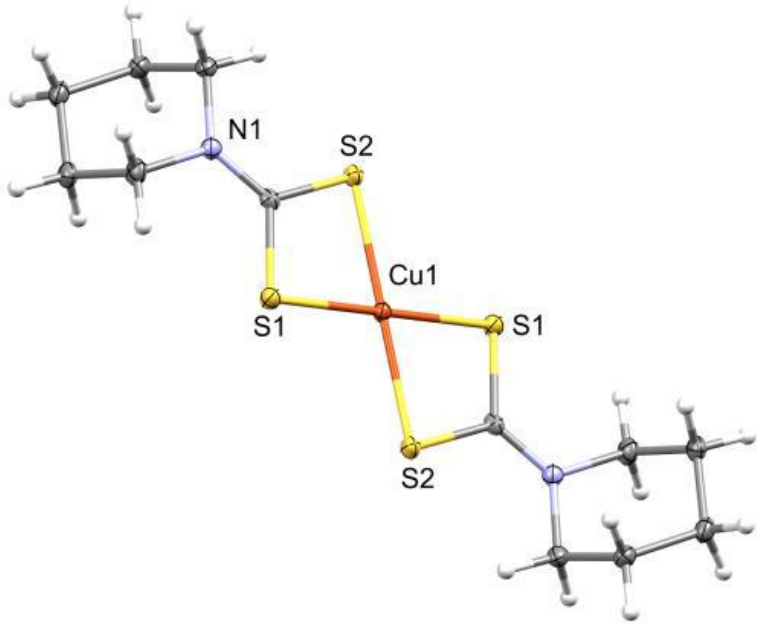

Figure 3. 28: Molecular structure of [Cu(piper)$_2$]. The thermal ellipsoids are shown at 50 % probability level.

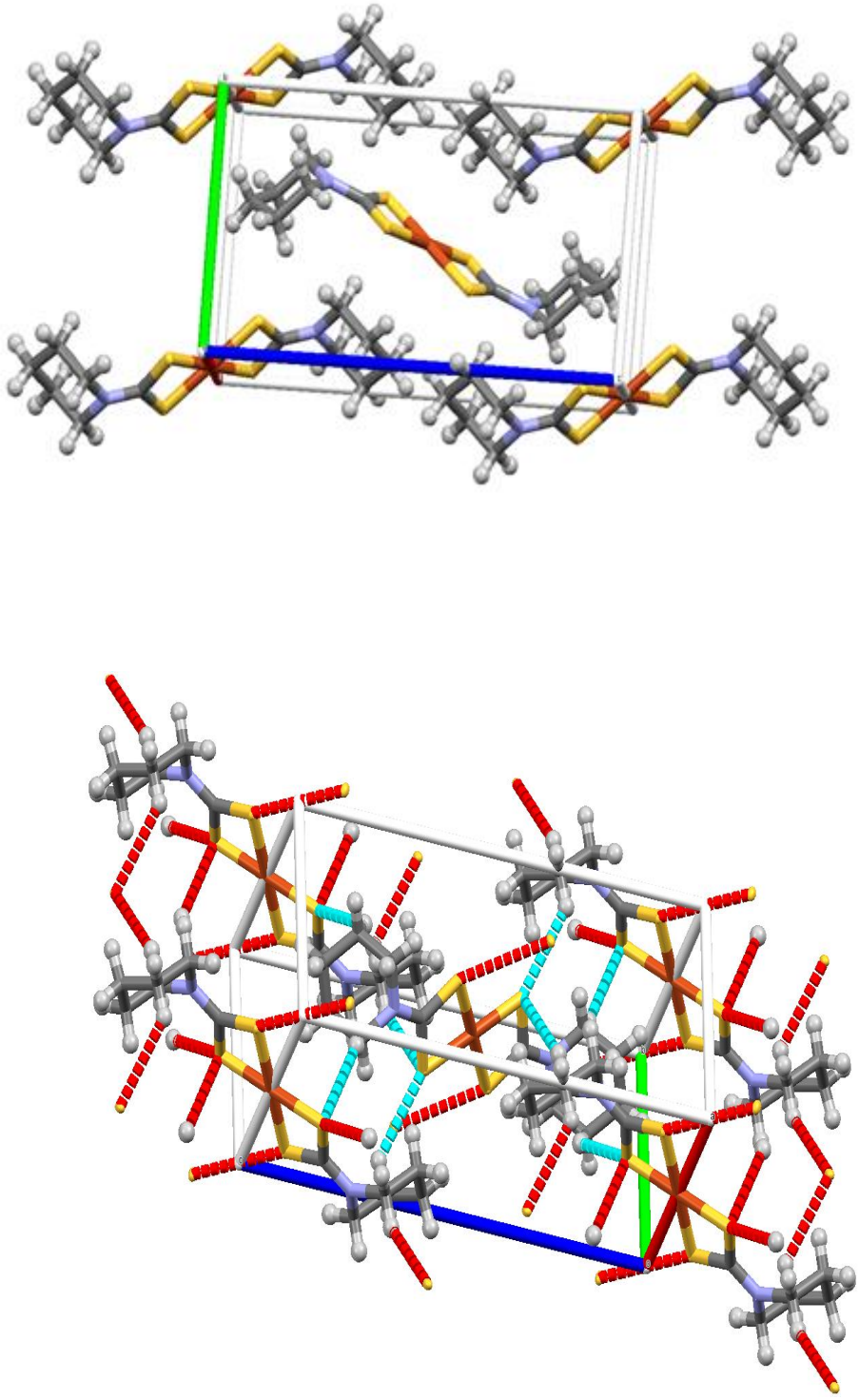

Figure 3. 29: Packing diagram of [Cu(piper)$_2$] as viewed down the crystallographic *b* axis (A). Packing diagram of [Cu(piper)$_2$] as viewed down the crystallographic *b* axis showing C—H···π intermolecular interactions

The silver complex, $[Ag_4(NEA)_4]$ consist of cluster unit with four Ag(I) ions and four molecules of N-ethyl aniline dithiocarbamate ligand in the asymmetric unit. Each dithiocarbamate ligand in the crystal structure is bonded to three Ag(I) ions (Figure 3.30). One sulphur atom of each dithiocarbamate ligand is coordinated to one Ag(I) and the other sulphur atom acts as bridging donor atom between two Ag(I) ions within the cluster and each Ag(I) is linked to the other three Ag(I) ions with Ag-Ag metallic bond distance of 2.9115(3)Å and 3.0376(4)Å. These distances are comparable to the known short Ag….Ag distances. This clearly confirmed the closed shell d^{10}-d^{10} argentophilic interactions within the cluster unit. The three bonds on each S-Ag(I) forms a triangle and the Ag(I) is linked to the other three Ag(I) through another triangle while the six coordinated geometry around each Ag(I) can be described as trigonal prismatic structure (Figure 3.30 and 3.31). In the packing diagram of $[Ag_4(NEA)_4]$ as shown in Figure 3.32, there are six $[Ag_4(NEA)_4]$ unit within the crystal lattice in a pair of two and each one of them is linked to the neighbouring molecule through intermolecular hydrogen bond as shown in Figure 3.33.

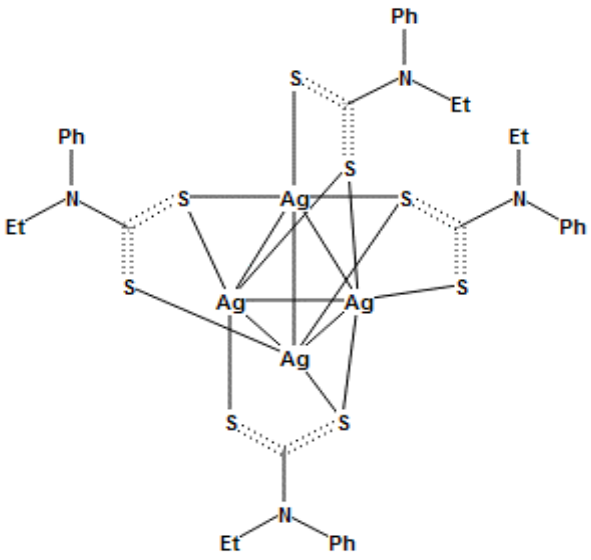

Figure 3. 30: Structure of $[Ag_4(NEA)_4]$

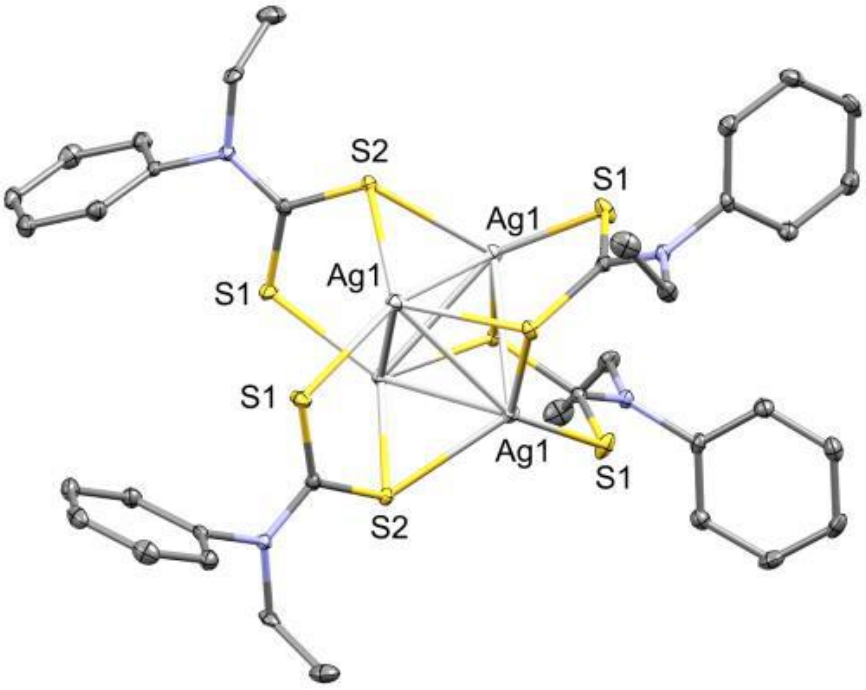

Figure 3. 31. Molecular structure of [$Ag_4(NEA)_4$]. The thermal ellipsoids are shown at 50 % probability level.

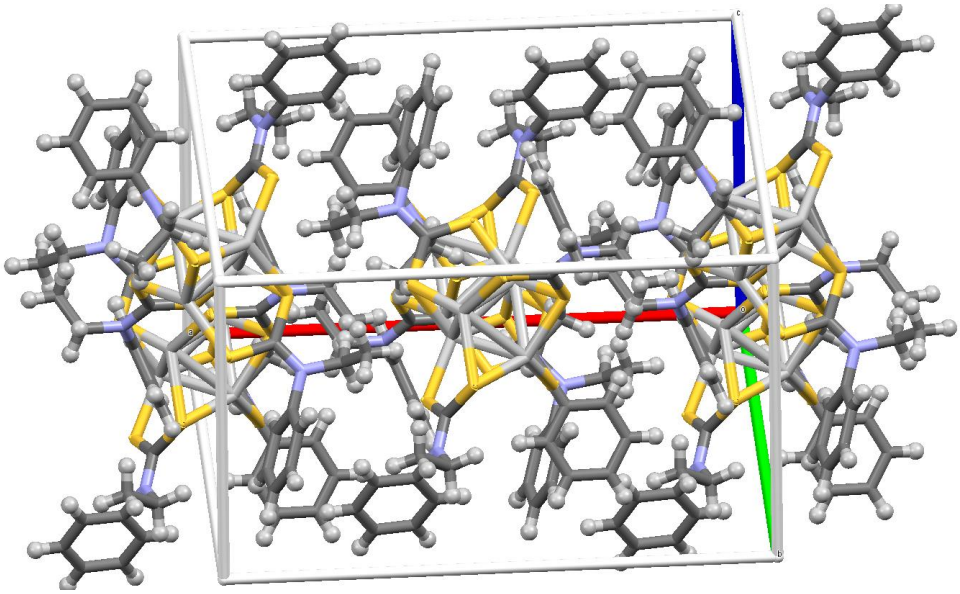

Figure 3. 32. Packing diagram of [$Ag_4(NEA)_4$] as viewed down the crystallographic b axis.

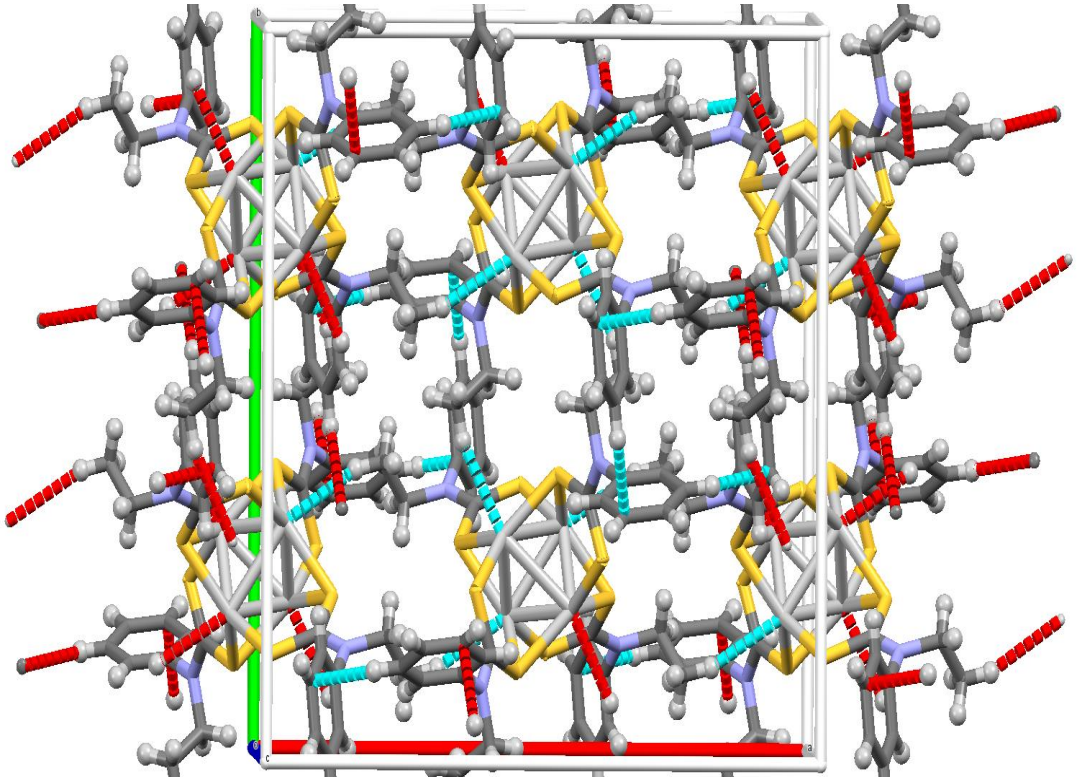

Figure 3. 33. Packing diagram of [$Ag_4(NEA)_4$] as viewed down the crystallographic b axis showing C—H···π intermolecular interactions.

Table 3.3. Structure refinements and crystal data of $[Ag_4(NEA)_4]$ and $[Cu(piper)_2]$

Compound	**$[Ag_4(NEA)_4]$**	**$[Cu(piper)_2]$**
Formula	$C_{36}H_{40}Ag_4N_4S_8$	$C_{12}H_{20}CuN_2S_4$
***Dcalc.*/ g cm^{-3}**	1.993	1.645
***m*/mm^{-1}**	2.349	1.933
Formula Weight	1216.68	384.08
Colour	yellow	green
Shape	block	block
Size/mm^3	0.31×0.17×0.12	0.33×0.19×0.13
***T*/K**	100(2)	100(2)
Crystal System	tetragonal	monoclinic
Space Group	I41/a	P21/c
***a*/Å**	18.9394(7)	6.0792(4)
***b*/Å**	18.9394(7)	8.4270(6)
***c*/Å**	11.3026(5)	15.2231(10)
***a*/°**	90	90
***b*/°**	90	95.995(3)
***g*/°**	90	90
V/Å^3	4054.3(3)	775.61(9)
Z	4	2
Z'	0.25	0.5
Wavelength/Å	0.71073	0.71073
Radiation type	Mo*Ka*	Mo*Ka*

***Qmin*/°**	2.098	2.691
***Qmax*/°**	27.441	27.432
Measured Refl.	32065	12560
Independent Refl.	2319	1752
Reflections Used	2305	1675
Rint	0.0328	0.0294
Parameters	119	88
Restraints	0	0
Largest Peak	1.043	0.442
Deepest Hole	-0.352	-0.283
GooF	1.263	1.233
***wR2* (all data)**	0.0511	0.0617
wR2	0.0509	0.0611
***R1* (all data)**	0.0234	0.0293
R1	0.0231	0.0277

Table 3.4. Selected bond lengths of $[Ag_4(NEA)_4]$ and $[Cu(piper)_2]$

$[Ag_4(NEA)_4]$		**$[Cu(piper)_2]$**	
Atom	**Length/Å**	**Atom**	**Length/Å**
Ag1 — Ag1^1	2.9115(3)	Cu1—S1	2.2894(6)
Ag1 — Ag1^2	2.9115(3)	Cu1 — S1^1	2.2894(6)
Ag1 — Ag1^3	3.0376(4)	Cu1 —S2^1	2.3105(6)
Ag1 — S1^3	2.4490(7)	Cu1 — S2	2.3105(6)
Ag1 — S2	2.4962(7)	S1 — C1	1.737(2)
Ag1 — S2^2	2.5732(7)	S2 — C1	1.731(2)
S1 — C9	1.700(3)	C1 — N1	1.312(3)
S2 — C9	1.758(3)	N1 — C2	1.479(3)
C9 — N1	1.341(3)	N1 — C6	1.480(8)
N1— C1	1.449(3)	C2 — C3	1.526(3)
N1 — C8	1.483(3)	C3— C4	1.533(3)
C4 — C3	1.369(4)	C4 — C5	1.529(3)
C4 — C5	1.395(4)	C5 — C6	1.522(3)
C1 — C2	1.385(4)		
C1 — C6	1.386(4)		
C2 — C3	1.393(4)		
C5 — C6	1.386(4)		
C8 — C7	1.514(4)		

3.7.3. Single crystal X-ray structures of Cu(II) and Ag(I) dibenzyl dithiocarbamate complexes

Ag(I) complexes with dialkyldithiocarbamates have been shown to possibly exist in a variety of coordination configurations and can be monomeric, dimeric, hexameric and even polymeric. $[Ag_6(DBA)_6]$ was crystallised from a solution of chloroform by slow evaporation to give green blocks. Crystals of the two compounds were selected and glued on to the tip of glass fibres. The crystals were then mounted in a stream of cold nitrogen at 100(1) K and centered in the X-ray beam by using a video camera. Crystal evaluation and data collection were performed on a Bruker Smart APEXII diffractometer with Mo Ka radiation ($\lambda = 0.71073$ Å). We obtained the initial cell matrix from three series of scans at different starting angles. Each series consisted of 12 frames collected at intervals of 0.5° in a 6° range with an exposure time of 10 s per frame. Successful indexing of the reflections was done by an automated routine built in the *APEX*II program suite [44] the final cell constants were calculated from a set of 6460 strong reflections from the actual data collection. Data collection method involved v scans of width 0.5°. The program *SAINT* plus [44]. was used for data reduction and structure solved by direct methods using *SHELXS* [44] and refined using *SHELXL* [44]. All structures were checked for solvent-accessible cavities using *PLATON* [45] and the graphics were performed with the *DIAMOND* [46, 47] visual crystal structure information system software as well as *MERCURY*. Non-H atoms were first refined isotropically and then by anisotropic refinement with full matrix least-squares calculations based on *F*2 using *SHELXS*. We positioned all H atoms geometrically and allowed to ride on their respective parent atoms and refined isotropically. Absorption corrections were based on fitting a function to the empirical transmission surface as sampled by multiple equivalent measurements [46]. Crystal data and structure refinement information for $[Ag_6(DBA)_6]$ are summarized in Table 3.5.

Table 3.5: Structure refinement and Crystal data of $[Ag_6(DBA)_6]$ and $[Cu(DBA)_2]$ complexes

Compound	**$[Ag_6(DBA)_6]$**	**$[Cu(DBA)_2]$**
Empirical Formula	$C_{92}H_{86}Ag_6Cl_6N_6S_{12}$	$C_{30}H_{28}CuN_2S_4$
$D_{calc.}$/ g cm^{-3}	1.778	1.464
μ/mm^{-1}	1.709	1.117
Formula Weight	2520.30	608.32
Crystal Size/mm^3	0.310×0.230×0.140	0.340×0.230×0.110
Temperature	100(2)	100(2)
Crystal System	triclinic	triclinic
Space Group	P-1	P-1
Unit cell imensions	11.0126(6)	13.7098(9)
	14.4254(8)	14.3201(10)
	16.2955(10)	16.2979(11)
	78.343(3)	64.916(4)
	73.321(2)	72.302(3)
	73.2140(10)	82.774(2)
V/$Å^3$	2354.0(2)	2760.8(3)
Z	1	4
Theta range for data collection/°	1.316 to 26.500	1.437 to 27.597
Reflections collected	35157	39434
Independent Reflection	9209	11444
Reflections with I > 2(I)	7745	7950

R_{int}	0.0326	0.0485
Parameters	550	667
Restraints	0	0
Largest diff. Peak and hole	1.717 and -1.023	0.558 and -0.956
Goodness of fit on F^2	1.044	1.070
wR_2	0.0502, 0.1006	0.0774, 0.1034
Final R indices[I>2sigma(I)] R_1	0.0388, 0.0937	0.0446, 0.0914

The asymmetric unit of $[Ag_6(DBA)_6]$ consists of half a molecule of $[Ag_6(DBA)_6]$ (the other half generated by an inversion centre) and a molecule of chloroform. The complex is hexameric and has a core consisting of two distorted hexagonal Ag_3S_3 rings (indicated by bold black bonds) from which S—C—S—Ag paddles protrude giving a distorted hexagonal paddle wheel. Two Ag…Ag interactions (dashed red bonds) with distances of 2.9198(5) and 3.0374(5) Å further support the two Ag_3S_3 rings (Figure 3.30A). In this arrangement, two Ag atoms are coordinated by three S atoms and a Ag---Ag interaction completing a distorted tetrahedral coordination geometry around the Ag atom. The third Ag centre in the asymmetric unit is coordinated by three S atoms and two Ag---Ag interactions resulting in a distorted five-coordinate Ag center. In both cases the AgS3 bit is essentially trigonal planar with S—Ag—S bond angles of 135.35(4), 129.72(4) and 91.95(3) for first Ag(I) centre, 117.67(4), 114.64(4) and 113.79(4) for the second Ag(I) centre and 137.30(4), 114.29(4) and 104.99(4) for the third Ag(I) centre, close to ideal trigonal planar arrangement. The Ag---Ag interactions point out of this plane and are not orthogonal. The other two Ag---Ag distances are long and are only

interactions (3.3210(5) and 3.3465(5) Å. The Ag—S distances range between 2.4421(11) to 2.5476(12) Å (figure 3.34C) and are comparable to those of related structures [47 - 49].

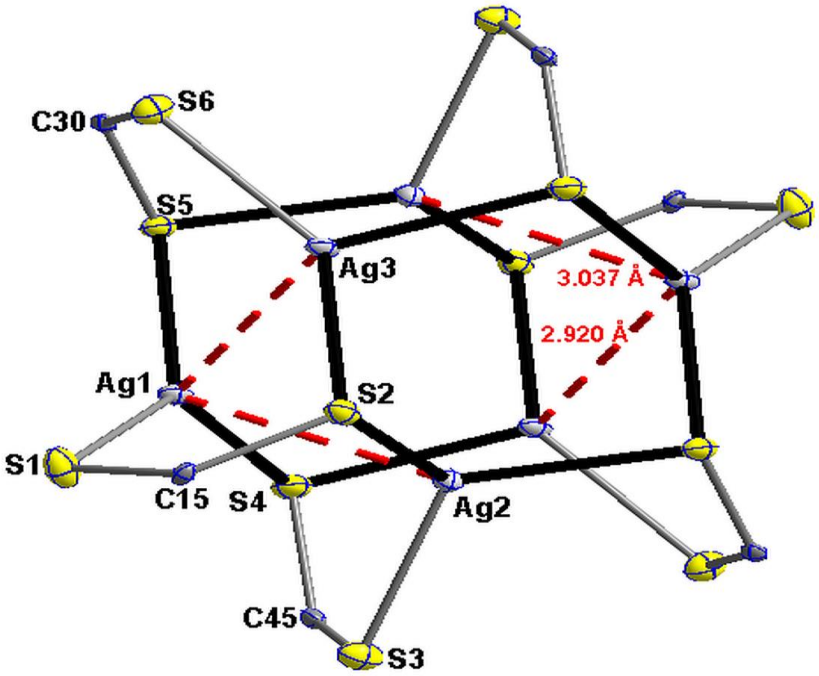

(A)

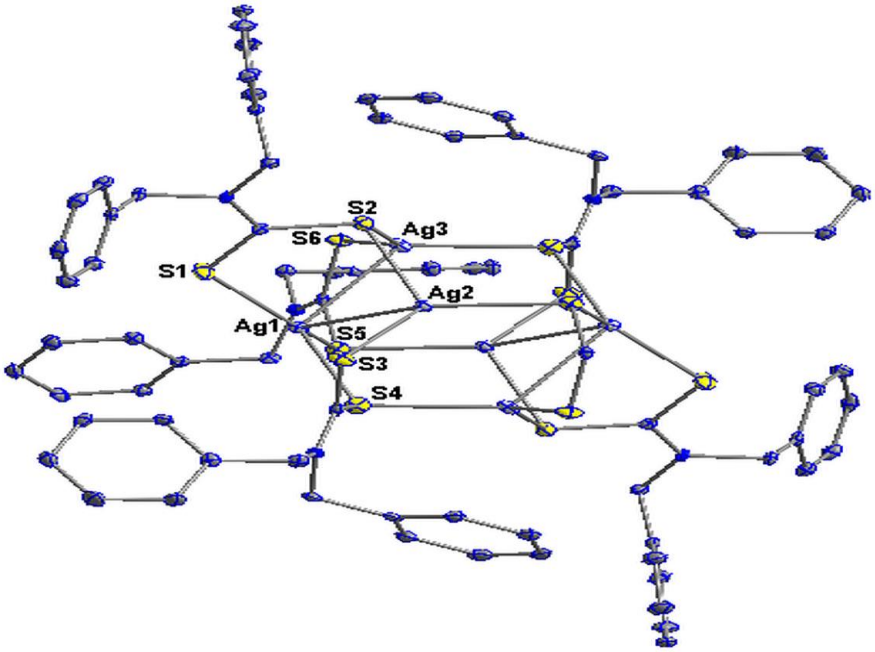

(B)

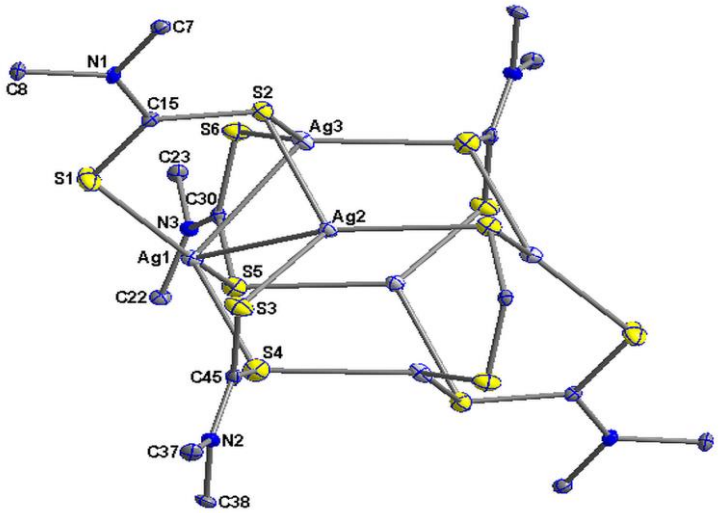

(c)

Figure 3. 34: (a) The hexagonal core consisting of $Ag_3(CS_2)_3$. Other parts of the molecule have been omitted for clarity. (b) Asymmetric unit and (c) full molecular structure

Table 3.6: Important bond distances and angles

Parameter	**$[Ag_6(DBA)_6]$**
Ag—S ranges	2.2602(6) – 2.2708(5)
C—S ranges	1.710(2) – 1.714(2)
S—Ag—S ranges	
Chelate ring	76.72(2) – 76.73(2)
Angle* between chelate rings	93.884(19) – 96.88(3)
S—C—S ranges	110.41(12)

The bimolecular crystal structure of the copper dibenzyl amine dithiocarbamate complex (Figure 3.35) shows that the metal ion is bonded to two molecules of the ligand through their Sulphur atoms forming a distorted square planar geometry. The bond angle between the Cu-ion and the sulphur atoms of each ligands are 77.84(3) and 78.02(3) degrees which are almost similar. Both the molecules showed the same bond angles between the metal and the two sulphur atoms of each ligand. The lengths of the bonds are different with no major difference for each sulphur. The first molecule showed the bond lengths for Cu – S of Cu1 – S1, Cu1 – S2, Cu1 – S 3 and Cu1 – S4 to be 2.297(9), 2.2969 (8), 2.3036 (8) and 2.2924 (9) respectively. The second molecule gave different bond lengths which are slightly the same as those measured for the first molecule. These lengths for Cu2 – S5, Cu2 – S6, Cu2 – S7 and Cu2 – S8 are 2.2733(9), 2.3123 (8), 2.2968 (10) and 2.3231(8) respectively (Figure 3.36). These bond lengths are comparable with the lengths of the crystals in the literature [17].

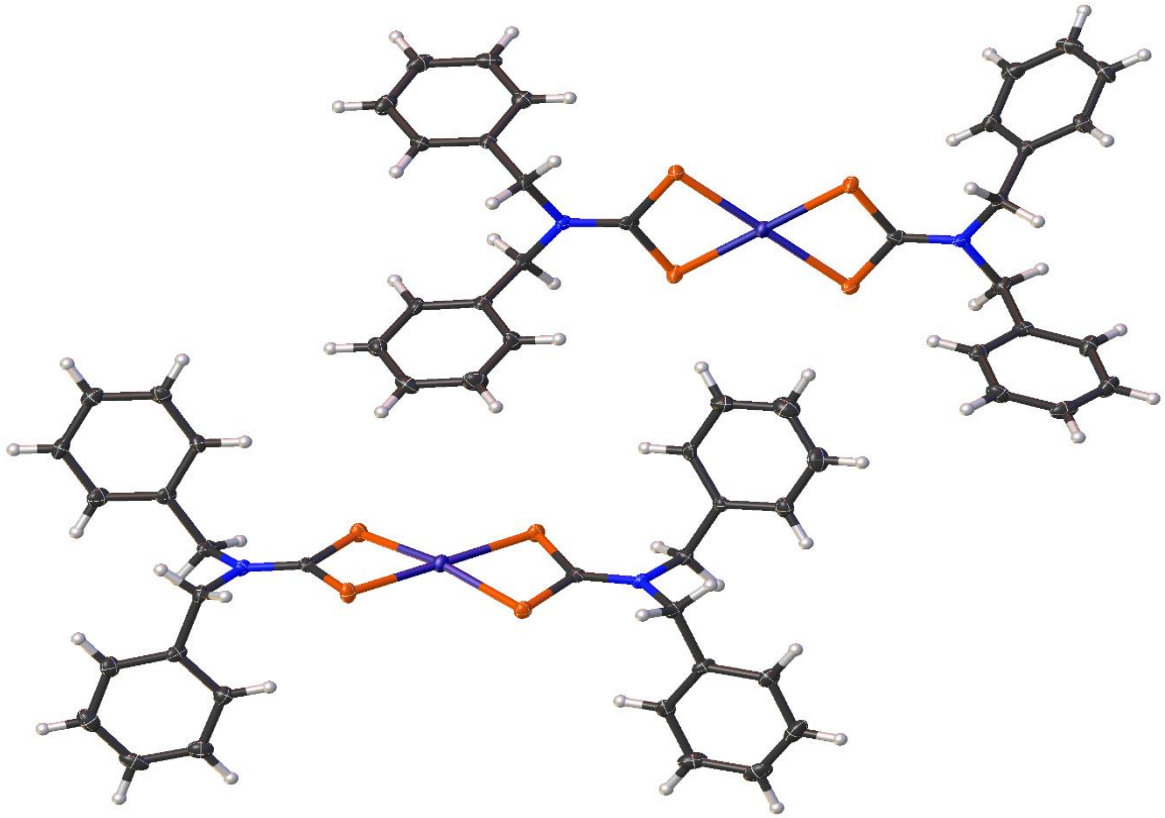

Figure 3. 35. Molecular structure of [Cu(DBA-DTC)$_2$]

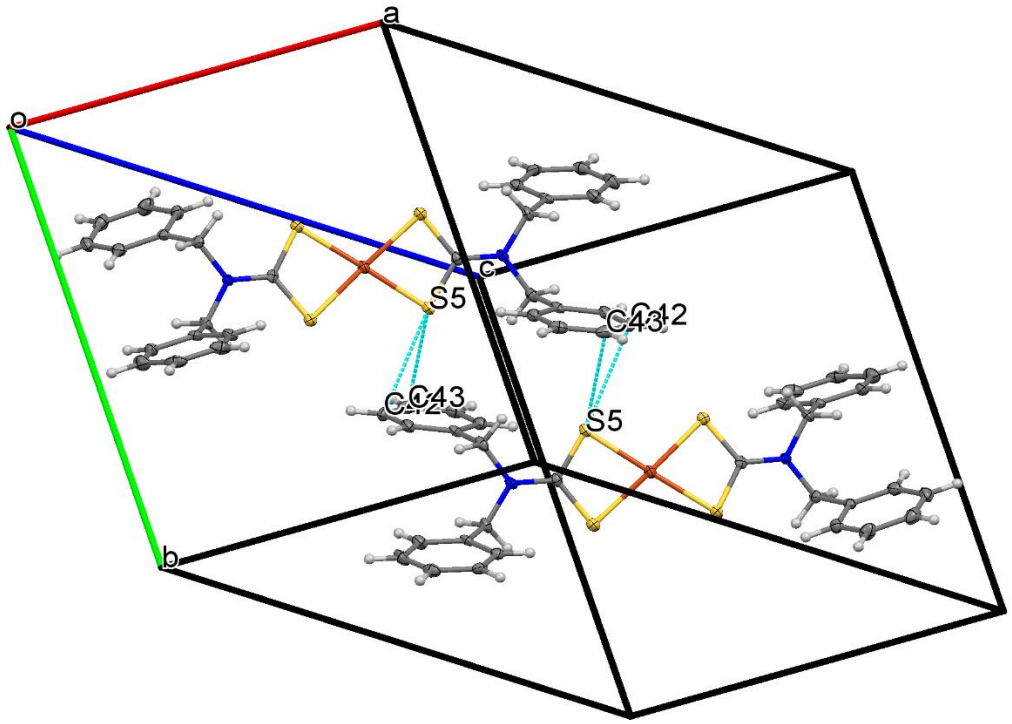

Figure 3. 36: Packing diagram of [Cu(DBA)$_2$]

3.8. References

[1] Graeme, H. Metal-dithiocarbamate complexes: Chemistry and biological activity. *Mini-Rev. Med. Chem*. **2012**, 12(12), 1202 – 1215.

[2] Kanchi, S.; Singh, P.; Bisetty, K. Dithiocarbamates as hazardous remediation agent: A critical review on progress in environmental chemistry for inorganic species studies of 20th century. *Arabian J. Chem*. **2014**, 7, 11–25.

[3] Nabipour, H.; Ghammamy, S.; Ashuri, S.; Aghbolagh, Z. S. Synthesis of a new dithiocarbamate compound and study of its biological properties. *Org. Chem. J.* **2010**, 2, 75-80.

[4] Ajibade, P. A.; Onwudiwe, D. C. Synthesis and characterization of group 12 complexes of N, N-methyl phenyl-N, N-butyl phenyl dithiocarbamate. *J. Coord. Chem*. **2011**, 17, 2963-2973.

[5] Van Boxtel, A. L.; Pieterse, B.; Cenijin, P.; Kamstra, J. H.; Brouwer, A.; Van Wieringen, W.; de Boer, J.; Legler, J. Dithiocarbamate induce craniofacialabnomalities and downregulate sox9a during zebrafish development. *Toxicol. Sci.* **2010**, 117, 209-217.

[7] Hulanicki, A. Complexation reactions of dithiocarbamates. *Talanta*. **1967**, 14, 1371 - 1392.

[8] Karlin, K. D.; Hogarth, G. Transition metal dithiocarbamates 1978-2003. *Progress in inorganic chemistry*. **2005**, 53. 1-10.

[10] Weissmahr, K. W.; Houghton, C. L.; Sedlak, D. L. Analysis of the dithiocarbamate fungicides Ziram, Maneb, and Zineb and the flotation agent ethylxanthogenate by ion-pair reversed-phase HPLC. *Anal. Chem*., **1998**, 70, 4800–4804.

[11] Alya, A. A.; Brown, A, B.; Bedair, T. M. I.; Ishak, E. A. Dithiocarbamate salts: Biological activity, preparation, and utility in organic synthesis. *J. Sulfur Chem*. **2012**, 33, 605–617.

[12] Qing-Han, L.; Ding, Y.; Neng-Wang H. Synthesis and biological activities of dithiocarbamates containing 1, 2, 3-triazoles group. *Chinese Chem. Lett*. **2014**, 25 1469–1472.

[13] Nami, S. A. A.; Ullah, I.; Alam, M.; Dong-Ung, L.; Sarikavakli, N. Synthesis, characterization, molecular docking and biological studies of self-assembled transition metal dithiocarbamates of substituted pyrrole-2-carboxaldehyde. *J. Photochem. Photobiol. B: Biol.* **2016**, 160, 392–399.

[14] Chaturvedi, D.; Zaidi, S. Role of organic dithiocarbamates in drug discovery research. *Res. Rev. J. Chem*. **2016**, 5(2), 10-12.

[15] Andrew, F. P.; Ajibade, P. A. Metal complexes of alkyl-aryl dithiocarbamates: Structural studies, anticancer potentials and applications as precursors for semiconductor nanocrystals. *J. Mol. Struct*. **2018**, 1155, 843-855.

[16] Gurumoorthy, G.; Thirinaron, S.; Ciattini, S. Synthesis and characterization of copper(II) dithiocarbamate complexes involving pyrrole and ferrocenyl moieties and their utility for sensing anions and preparation of copper sulphide and copper–iron sulphide nanoparticles. *Appl. Organometal. Chem.* **2018**; 32: e4363.

[17] Krajciova, D.; Melnik, M.; Havranek, E.; Forgacsova, A.; Mikus, P. Copper compounds in nuclear medicine and oncology. *J. Coord. Chem*. **2014**, 67, (9), 1493-1519.

[18] Festa, R. A.; Thiele, D. J. Copper: An essential metal in biology. *Curr. Biol.* **2011**, 21(21), R877-R883.

[19] Tisato, F.; Marzano, C.; Porchia, M.; Pellei, M.; Santini, C. Copper in diseases and treatments, and copper-based anticancer strategies. *Medicinal Res. Rev*. **2010**, 30(4), 708-749.

[20] Edwards-Jones, V. The benefits of silver in hygiene, personal care and Healthcare. *Lett. Appl.Microbiol*. **2009**, 49, 147–152.

[21] Kalinowska-Lis, U.; Felczak, A.; Checinska, L.; Szabłowska-Gadomska, I.; Patyna, E.; Małecki, M.; Lisowska, K.; Ochocki, J. Antibacterial Activity and Cytotoxicity of Silver(I) Complexes of Pyridine and (Benz)Imidazole Derivatives. X-ray Crystal Structure of [Ag(2,6-di(CH_2OH)py)$_2$]NO_3. *Molecules*. **2016**, 21, 87, 1 -14.

[22] Jamaludin, N. S.; Halim, S. N. A.; Tieklin, E. R. T. Bis(phospane) copper(I) and silver(I) dithiocarbamates: Crystallography and antimicrobial essay. Z. *Kristallogr*. **2016**, 237(6); 341 – 349.

[23] Zaidi, S.; Chaturvedi, A. K.; Singh, N.; Chaturvedi, D. Triton-B catalyzed, efficient and solvent-free approach for the synthesis of dithiocarbamates. *Current Chem. Lett*. **2017**, 6, 143–150.

[24] Halimehjani, A. Z.; Marjani, K.; Ashouri, A. Synthesis of dithiocarbamate by Markovnikov addition reaction in aqueous medium. *Green Chem*. **2010**, 12, 1306–1310.

[25] Hassan, E. A.; Zayed, S. E. Dithiocarbamates as precursors in organic chemistry: Synthesis and uses. *phosphorus, sulphur, and silicon*, **2014**, 189:300–323.

[26] Halimehjani, A. Z.; Dadras, A.; Ramezani, M.; Shamiri, E. V.; Hooshmanda, S. E.; Hashemib, M. M. Synthesis of dithiocarbamates by markovnikov addition reaction in PEG and their application in amido-alkylation of naphthols and indoles. *J. Braz. Chem. Soc*. **2015**, 26, 1500-1508.

[27] Rajarajan, M. Synthesis, characterization and biological evaluation of Hg(II), Cu(II), Ni(II), Co(II), and Zn(II) dithiocarbamate complexes. *Novus Int. J. Chem*. **2013**, 2, 1-6.

[28] Refat, M. S.; El-Deen, I. M.; Zein, M. A.; Adam, A. M. A.; Kobeasy, M. I. Spectroscopic, structural and electrical conductivity studies of Co(II), Ni(II) and Cu(II) complexes derived from 4-acetylpyridine with thiosemicarbazide. *Int. J. Electrochem. Sci*. **2013**, 8, 9894 – 9917.

[29] Ferreira, I. P.; de Lima, G. M.; Paniago, E. B.; Takahashi, J. A.; Pinheiro, C. B. Synthesis, characterization and antifungal activity of new dithiocarbamate-based complexes of Ni(II), Pd(II) and Pt(II). *Inorg. Chim. Acta*. **2014**, 423, 443–449.

[30] Altaf, M.; Monim-ul-Mehboob, M.; Kawde, A. N.; Corona, G.; Larcher, R.; Ogasawara, M.; Casagrande, N.; Celegato, M.; Borghese, C.; Siddik, Z. H.; Aldinucci, D.; Isab, A. A. New bipyridine gold(III) dithiocarbamate-containing complexes exerted a potent anticancer activity against cisplatin-resistant cancer cells independent of p53 status. *Oncotarge*t, **2017**, 8(1), 490-505.

[31] Gottlieb, H. E.; Kotlyar, V.; Nudelman, A. NMR chemical shift of common laboratory solvents as trace impurities. *J. Org. Chem*. **1997**. 62, 7512-7515.

[32] Van Gaal, H. L. M.; Diesveld, J. W.; Pijpers, F. W.; Van der Linden, J. G. M. ^{13}C NMR spectra of dithiocarbamates. chemical shifts, carbon-nitrogen stretching vibration frequencies, and p bonding in the NCS_2 fragment. *Inorg. Chem.* **1979**, 18(11), 3251-3260.

[33] Prakasam, K. B. A.; Ramalingam, U.; Baskaran, R.; Bocelli, G.; Cantoni, A. Synthesis, NMR spectral and single crystal X-ray structural studies on Ni(II) dithiocarbamates with NiS_2PN, NiS_2PC, NiS_2P_2 chromophores: Crystal structures of (4-methylpiperazinecarbodithioato)(thiocyanato-N) (triphenylphosphine) nickel(II) and bis(triphenylphosphine) (4 methylpiperazinecarbodithioato)nickel(II) perchlorate monohydrate. *Polyhedron*, **2007**, 26, 1133–1138.

[34] Srinivasan, N.; Valarmathi, P.; Thirumaran, S.; Ciattini, S. Synthesis and spectral studies on NiS_4, NiS_2PN, NiS_2P_2 chromophores: Single-crystal X-ray structure of $[Ni(dbpdtc)_2]$. (dbpdtc 5 benzyl(4-(benzylamino)phenyl)dithiocarbamate. *Transition Met. Chem*. **2010**, 35:815–819.

[35] Gudasi, K. B.; Patil, S. A.; Vadavi, R. S.; Shenoy, R. V.; Patil, M. S. Synthesis and spectral studies of Cu(II), Ni(II), Co(II), Mn(II), Zn(II) and Cd(II) complexes of a new macroacyclic

ligand N,N'-bis(2-benzothiazolyl)-2,6-pyridinedicarboxamide. *J. Serb. Chem. Soc*. **2006**, 71(5), 529–542.

[36] Halcrow, M. A. Jahn–Teller distortions in transition metal compounds, and their importance in functional molecular and inorganic materials. *Chem. Soc. Rev*., **2013**, 42, 1784—1795.

[37] Marcu, A.; Stanila, A.; Rusu, D.; Rusu, M.; Cozar, O.; David, L. Spectroscopic studies of copper (II) complexes with some amino acids. *J. Optoelectronics. Adv. Mater*. **2007**, 9(3), 741 – 746.

[38] Maria, H.; Hauer, I.; Muller, C.; Rusu, D.; Botond, K.; David, L. Spectroscopic studies of copper(ii) complexes with some amino acid as ligand. *Seria. Fizzica.* **2011**, 77 – 85.

[39] Ekennia, A. C.; Onwudiwe, D. C.; Olasunkanmi, L. O.; Osowole, A. A.; Ebenso, E. E. Synthesis, DFT calculation, and antimicrobial studies of novel Zn(II), Co(II), Cu(II), and Mn(II) heteroleptic complexes containing benzoylacetone and dithiocarbamate. *Bioinorg. Chem*. *Appl*. **2015**, 1-12.

[40] El-Bindary, A. A.; El-Sonbati, A. Z. Synthesis and properties of complexes of copper(II) Nickel(II) , Cobalt(II) and uranyl ions with 3-(p-tolysulphonamido) rhodamine . *Polish J. Chem*. **2000**, 74, 615-620.

[41] Trifunovic, S. R.; Markovic, Z.; Sladic, D.; Andjelkovic, K.; Sabo, T.; Minic, D. The synthesis and characterization of nickel(II) and copper(II) complexes with the polydentate dialkyl dithiocarbamic acid ligand 3-dithiocarboxy-3-aza-5-aminopentanoate. *J. Serb. Shem. Soc*. **2002**, 67(2), 115–122.

[42] Ekennia, A. C.; Onwudiwe, D. C.; Ume, C.; Ebenso, E. E. Mixed ligand complexes of n-methyl-n-phenyl dithiocarbamate: Synthesis, characterisation, antifungal activity, and solvent extraction studies of the ligand. *Bioinorg. Chem. and Appl*. **2015**. 1-10.

[43] Madhusudanan, P. M.; Mohammed Yusuff, K. K.; Ramachandran Nair, G. C. Thermal decomposition kinetics of diethyl dithiocarbamate complexes of copper(II) and nickel(II). *J. Thermal Anal*. **1975**, 8, 31—43.

[44] Sheldrick, G.M., A short history of ShelX. *Acta. Cryst.* **2008**, A64, 339-341.

[45] Dolomanov, O. V.; Bourhis, L. J.; Gildea, R. J.; Howard, J. A K.; Puschmann, H. Olex2: A complete structure solution, refinement and analysis program, *J. Appl. Cryst.* **2009**, 42, 339-341.

[46] Sheldrick, G. M. Crystal structure refinement with ShelX. *Acta Cryst.* **2015**, **C27**, 3-8.

[47] Zhang, Q.; Cao, R.; Hong, M.; Su, W.; Liu, H. Polynuclear silver compound formed from aggregation of Se^{2-} and Ag(I)-tholate complex. *Inorg. Chim. Acta*. **1998**, 277, 171-176.

[48] Huang, Z.; Lei, X.; Hong, M.; Liu, H. Synergism in a transition metal cluster compound. Crystal and molecular structure of a polysilver cluster molecule with an unusual bridging sulfur atom, $Ag_{11}S(Et_2dtc)_9$. *Inorg. Chem*. **1992**, 31, 2990-2991.

[49] Su, W; Hong, M.; Jiang, F.; Liu, H.; Zhou, Z.; Wu, D.; Mak, T. C. W. A cleavage of the SC bond in 2-aminothiophenal. *Polyhedron*, **1996**, 15, 4047- 4051.

CHAPTER FOUR

SYNTHESIS AND CHARACTERIZATION OF METAL SULFIDE NANOPARTICLES

4.1. Introduction

In the past decades the single source molecular precursor method has been used to make different metal sulphide nanoparticles with different shapes and sizes [1-6]. The effect of temperature and the amount of the precursor used when using this method have been studied [7]. The inherent problems associated with the use of toxic and volatile compounds such as metal alkyls at elevated temperatures led to the development of alternative chemical routes to nanoparticles. The use of single-molecule precursors in which the metal-chalcogenide bond is available has proven to be a very efficient route to high-quality nanoparticles [8]. In this study nanoparticles are synthesized from Cu(II) and Ag(I) single source precursor method at different temperatures using oleyl amine and oleic acid as capping agents. The effect of temperature on structural and optical properties of the nanoparticles were studied.

The temperature that is used in the thermolysis when synthesizing nanoparticles is one of the important factors that plays a significant role on the shape, size and the phase of the nanoparticle. It has been noticed that the higher the temperature the larger the particle size when using the single source precursor method. The particles size distribution is also affected by the temperature as it becomes broader at a higher reaction temperature [9]. The competition between kinetic and thermodynamic regime when the particles are growing is the reason why the shape of nanoparticles is also affected by temperature [10].

4.2. Experimental

4.2.1. Materials

Oleylamine, Oleic acid, ethanol, toluene and hexane were used in the synthesis and characterization of the nanoparticles without being further purified. The copper(II) dithiocarbamate complexes and silver(I) dithiocarbamate complexes were synthesized and characterized (Chapters 2 and 3). Table 4.1 shows the complexes and the nanoparticles synthesized from the corresponding metal complex codes.

Table 4.1. Codes of complexes and nanoparticles synthesized

Copper complexes	**CuS Nanoparticles**	**Silver complexes**	**AgS nanoparticles**
$[Cu(DA)_2]$	CuS-(DA)NP	[Ag(DA)]	AgS-(DA)NP
$[Cu(BA)_2]$	CuS-(BA)NP	[Ag(BA)]	AgS-(BA)NP
$[Cu(DBA)_2]$	CuS-(DBA)NP	[Ag(DBA)]	AgS-(DBA)NP
$[Cu(NMB)_2]$	CuS-(NMB)NP	[Ag(NMB)]	AgS-(NMB)NP
$[Cu(PP)_2]$	CuS-(PP)NP	[Ag(PP)]	AgS-(PP)NP
$[Cu(NEA)_2]$	CuS-(NEA)NP	[Ag(NEA)]	AgS-(NEA)NP
$[Cu(Morph)_2]$	CuS-(M)NP	[Ag(Morph)	AgS-(M)NP
$[Cu(Piper)_2]$	CuS-(P)NP	[Ag(Piper)]	AgS-(P)NP

4.2.2. Characterization Techniques

4.2.2.1. Optical studies

The optical properties of the material were studied using Cary 100 UV-Vis spectrophotometer (Agilent technologies) and the florescence L545 Perkin Elmer with FL win lab software. The nanoparticles were dissolved in toluene. A cuvette of 10 mm path length was used.

4.2.2.2. Structural property studies

The structural properties were studied using Perkin Elmer spectrum 100 (FTIR), the shape and size were characterized using Joel jem-1400 Transmission Electron Microscope (TEM) with Gatan Microscopy suite software, SEM images and Energy Dispersive X-ray (EDX) data were obtained using the Zeiss EVO LS 15 Scanning electron microscope with EDX INCA software analysis. The nanoparticle phases were identified with a PANalytical AERIS diffractometer with PIXcel detector and fixed slits with Fe filtered Co-Kα radiation X-ray diffraction.

4.2.3. Synthesis of metal sulphide nanoparticles

A method from the literature was used [13]. 0.2 mmol of each precursor was added into a mixture of (6.9 mL, 20 mmol) oleylamine and (6.7 mL, 20 mmol) of oleic acid in a three-necked flask at room temperature. Then, the mixture was heated to 120°C to remove water and oxygen with vigorous magnetic stirring under vacuum for 30 mins. The solution was then heated to 220°C under N_2 atmosphere. The reaction was allowed to cool down to room temperature after an hour. An excess amount of ethanol was added into the solution, the resulting mixture was centrifugally separated, and the product was collected and dried at room temperature [13].

RESULTS and DISCUSSION

4.3. Structural and optical studies of copper sulphide nanoparticles

4.3.1. Structural and Optical studies of CuS-(P)

4.3.1.1. Powder X-Ray Diffraction patterns of CuS-P nanoparticles

The powder X-ray diffraction patterns of the copper sulphide nanoparticles synthesized from copper(II)piperidine DTC complexes at three different temperatures are displayed in Figure 4.1. JCPDS (95-005-3331) card was used to determine the crystalline phase of the particles to be $Cu_{1.8}S$ digenite. The CuS-P nanoparticles synthesized at 120°C showed diffraction peaks at 2θ = 32°, 34°, 37°, 54° corresponding to 1010, 1013, 0114 and 1112 while the ones at 180°C revealed peaks at 2θ = 32°, 34°,35°, 42°,47° and 54° indexes to 1010, 1013, 105, 0117, 110, and 1112 respectively. For the particles thermolyzed at 220°C. peaks 2θ = 32°, 34°, 35°, 42°, 47°, 54°, 56° indexed to 1010, 1013, 105, 0117, 110, 1112 and 1115 respectively were brevealed. The peaks of these nanoparticles were indexed with reference to JCPDS (47-1748) in the literature [14].

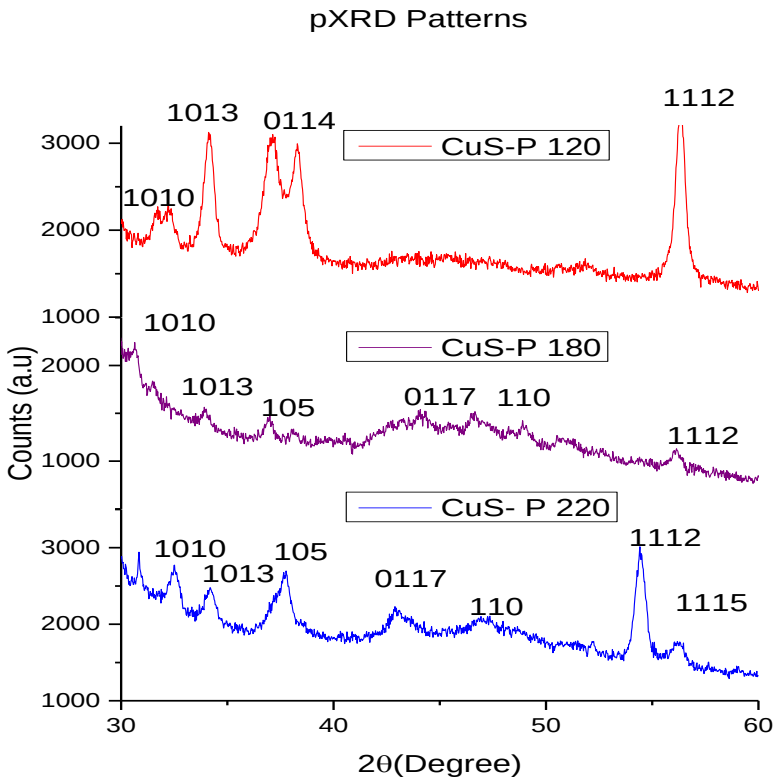

Figure 4. 1 P-XRD patterns of CuS-P nanoparticles synthesized at 120°C, 180°C and 220°C

4.3.1.2. Transmission electron microscopy studies of CuS-P nanoparticles

The TEM images of CuS-P nanoparticles synthesized at 220°C and 180°C showed some degree of agglomeration as shown in Figure 4.2. The nanoparticles are semi-spherical in shape and the particle size increased as the temperatures increases. CuS-P prepared at 220°C gave particles within the size range of 74.36 to 125.42 nm, while the size of CuS-P obtained at 180°C ranges between 31.28 to 43.98 nm. However, CuS-P synthesized at 120°C have three different shapes, hexagonal, triangular and spherical with no agglomeration. The crystallite size of the nanoparticles is in the range 4.94 - 51.38 nm. This clearly means that the shape and size of the nanoparticles synthesized from this precursor are highly affected by the temperature at which

the thermolysis was carried out. According to the selected area electron diffraction patterns of the nanoparticles synthesized at 220°C from the copper(II)piperidine dithiocarbamate complex, the nanoparticles are crystalline as the image is showing bright spots. However, the image also shows that the particles are not well monodispersed as the spots are scattered and not arranged in discrete pattern. The distance between the lattice fringes were also measured in different selected areas, and they were all 0.33 nm which matches the distance of a digenite copper sulphide phase in the literature [15].

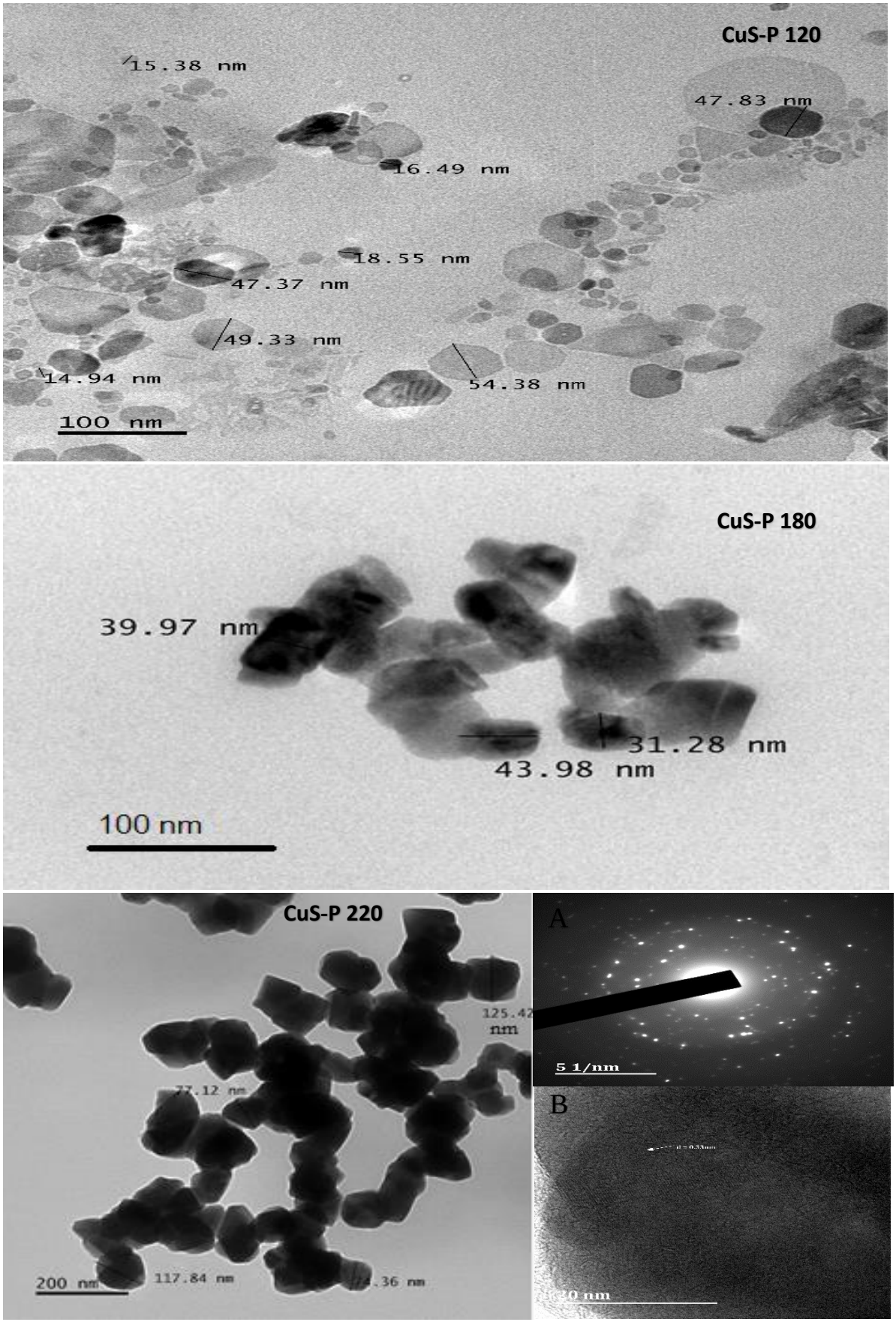

Figure 4. 2 TEM images of CuS-P nanoparticles synthesized at 120°C, 180°C and 220°C and A. SAED and B. lattice fringes of CuS-P 220.

4.3.1.3. Scanning electron microscope studies of CuS-P nanoparticles

Figure 4.3. shows the SEM micrographs of CuS-P nanoparticles synthesized at different temperatures with their corresponding EDX spectra. The images displayed different morphologies when nanoparticles are prepared at different temperatures. The micrographs show packed fibres, rough surface and a surface with disorientated layers when the nanoparticles prepared at 220°C, 180°C and 120°C respectively. The EDX spectra confirmed the presence of copper and sulphur in the particles. Carbon and oxygen peaks observed resulting from the capping agent used for the preparation of the nanoparticles.

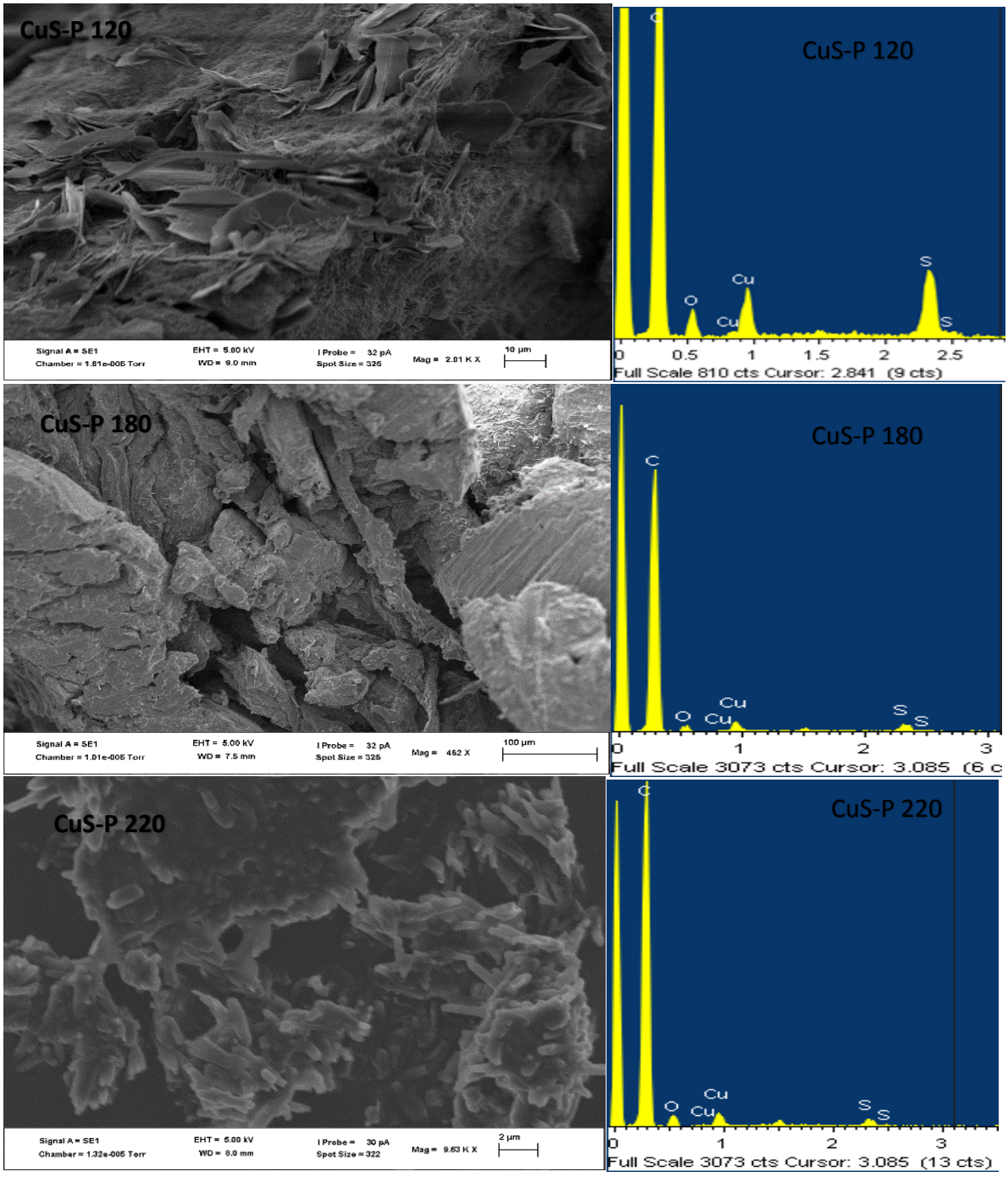

Figure 4. 3 SEM micrographs and EDX spectra of CuS-Pnanoparticles synthesized at 120°C, 180°C and 220°C

4.3.1.4. Fourier-transform infrared spectroscopy studies of CuS-P nanoparticles

The comparison of the FTIR spectra of the synthesized copper sulphide nanoparticles and the surfactant agents used in the synthesis are presented in Figure 4.4. From the Figure it can clearly be seen that the bands of the pure oleic acid are present also in the spectra of the nanoparticles. A little shift to a lower wavelength of the C=O stretching mode was observed, from 1750 cm^{-1} in the oleic acid spectra to 1650 cm^{-1} in the spectra of all the nanoparticles while the carboxylate stretching mode was observed at 1550 cm^{-1} for all the nanoparticles and the oleic acid. The OH stretching mode appeared at 2950 cm^{-1} in all the spectra [16]. The presence of these bands on the nanoparticle spectra confirmed the presence of only oleic acid on the surface of the copper sulphide nanoparticles as the N-H wagging vibration of the oleylamine did not appear in any of the nanoparticle's spectrum.

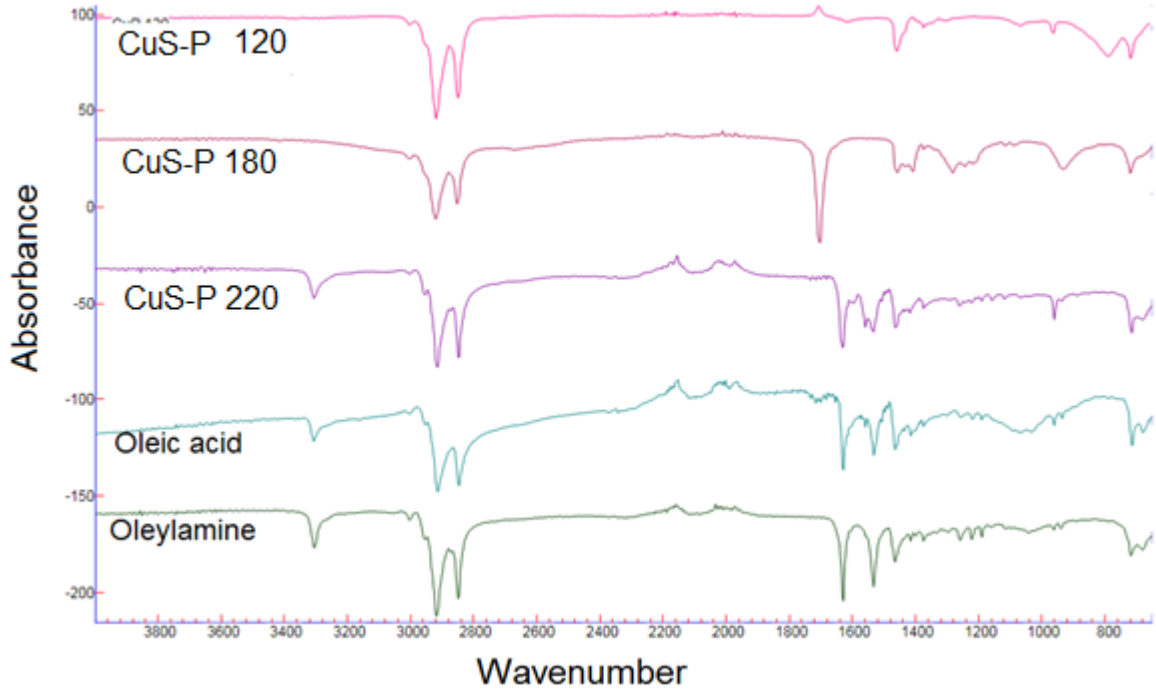

Figure 4. 4 Overlay FTIR spectra of CuS-P nanoparticles synthesized 120°C, 180°C and 220°C

4.3.1.5. Absorption studies of CuS-P nanoparticles

Figure 4.5 shows the overlay absorption spectra for the CuS-P nanoparticles prepared at three different temperatures and their corresponding Tauc plots. UV-Visible spectrophometer was used to determine the optical absorption spectra of the synthesized copper sulphide nanoparticles. The absorption spectra were used directly to calculate the band energy (eV) using the Tauc's equation 1.

$$(\alpha h\nu)^2 = B(h\nu - E_{cb}) \quad \text{.....1}$$

Where α is the absorption coefficient, hv is the photon energy, E_{cb} is the conduction band energy, and B is a constant [11,12]. The band energy was then determined by plotting $(\alpha h\nu)^2$ against (hv) and extrapolation of the linear part of the curve to the energy axis. The estimated band gap energy from the Tauc plots are 2.93eV, 3.73eV and 3.47eV for CuS-P synthesized at 120°C, 180°C and 220°C respectively. It is observed that the estimated band gap energy values are greater than the reported 1.2eV band gap of the bulk [17]. This increase of the band gap energy is mainly because of the decrease in the size of the nanoparticles which is due to the quantum confinement of the particles [18].

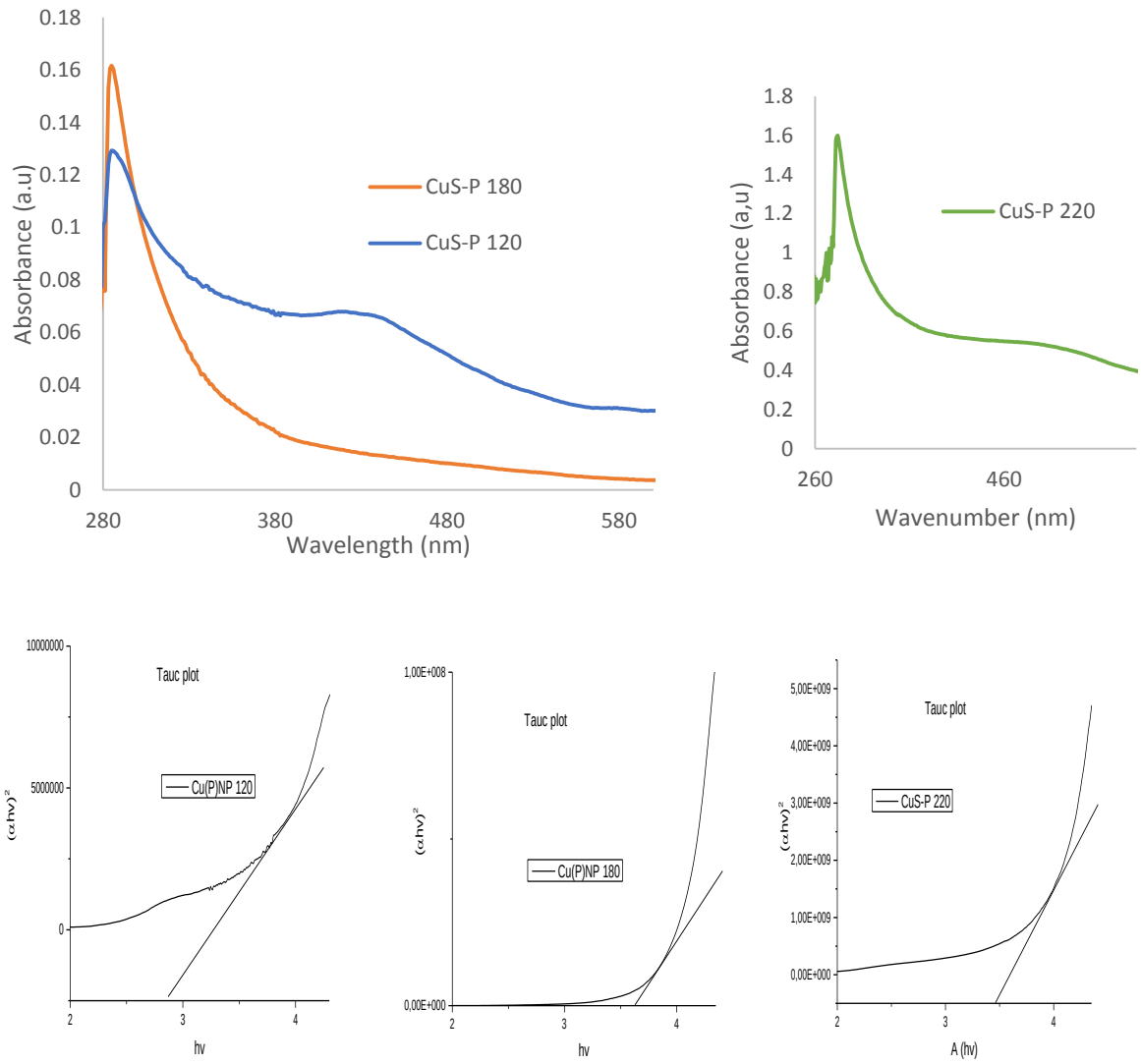

Figure 4. 5 Overlay UV-Vis spectra and Tauc plot of CuS-P synthesized at 120°C, 180°C and 220°C

4.3.1.6. Emission studies of CuS-P nanoparticles

Figure 4.6. displays the emission spectra of the CuS-P nanoparticles. The nanoparticles emission maxima are 323.5, 302.5 and 306.3 nm, as compared to the absorption maxima, 289.0, 287.0 and 285.0 nm, for CuS-P at 120°C, 180°C and 220°C respectively. The emission peaks have shifted to the higher wavelengths compared to those of absorption.

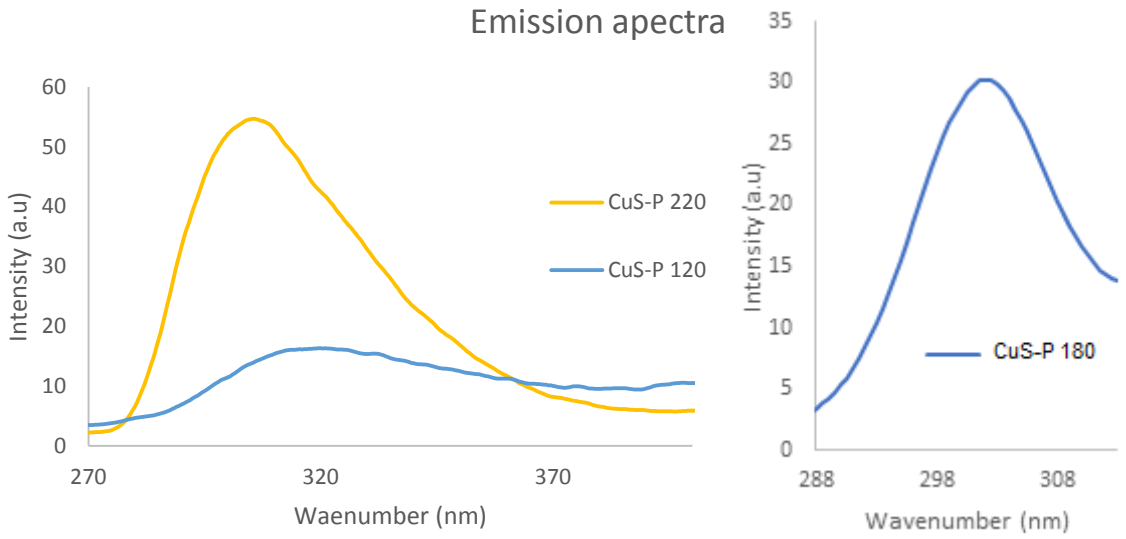

Figure 4. 6 Overlay Fluorescence spectra of CuS-Pnanoparticles synthesized at 120°C, 180°C and 220°C

4.3.2. Structural and optical studies of CuS-M nanoparticles synthesized from copper(II) morpholine DTC complex

4.3.2.1. Powder X-ray diffraction patterns of CuS-M nanoparticles

The overlay patterns of the powder X-ray diffraction patterns of the CuS-M synthesized at three different temperatures are presented in Figure 4.7. The synthesized nanoparticles showed the diffraction peaks that corresponded to the digenite Cu_9S_5 or $Cu_{1.8}S$ crystallinity phase as shown by the JCPDS (95-005-3331) card. The peaks were then indexed with reference to JCPDS (47-1748) in the literature [19]. The diffraction patterns show that the nanoparticles synthesized at a lower temperature (120°C) are more crystalline than the nanoparticles synthesized at elevated temperatures as the peaks of CuS-M 120 are sharper. This may be due to the Ostwald ripening leading to bigger size of the nanoparticles.

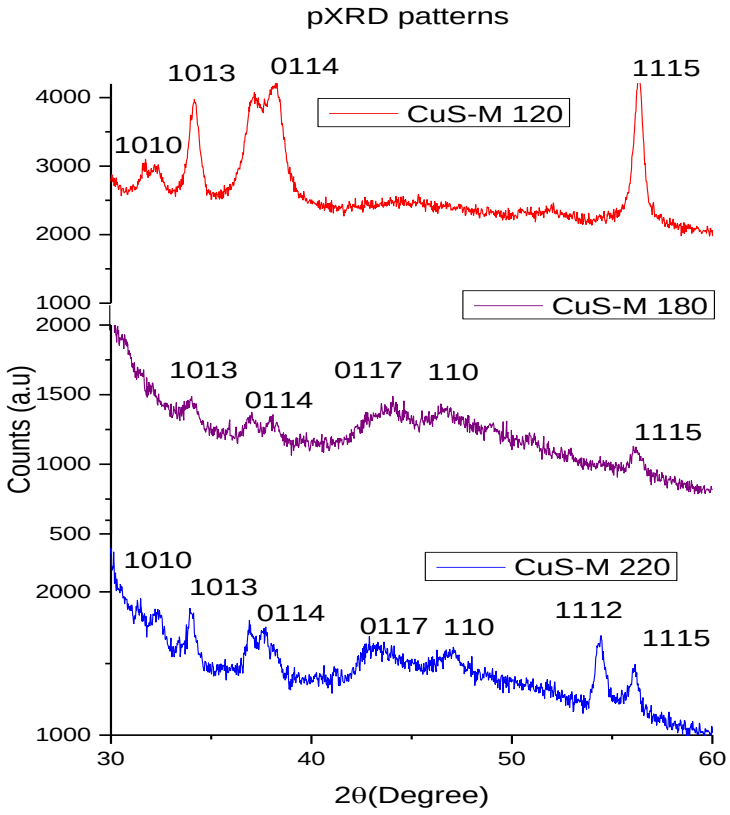

Figure 4. 7 pXRD patterns of CuS-M nanoparticles synthesized at 120°C, 180°C and 220°

4.3.2.2. Transmission electron microscopy studies of CuS-M nanoparticles.

Figure 4.8 shows the TEM images of the CuS-M nanoparticles synthesized at 120°C, 180°C and 220°C from [Cu(Morph)$_2$] complex. CuS-M synthesized at 220°C have the size ranging from 41.86 to 71.21 nm with mixed hexagonal and cubic shapes. The nanoparticles exhibit less agglomeration as compared to the nanoparticles synthesized at 180°C. When the precursor was thermolyzed at 180°C, the shapes of nanoparticles changed to square and semi-spherical shapes with a size range from 15.99 – 26.39 nm. When the thermolysis was done at 120°C the nanoparticles showed wide range of sizes from 12.92 nm to 54.47 nm and there was no trace of agglomeration. The shapes changed to mixture of spherical and hexagonal. The precursor seems to have behaved like the others and gave smaller particles at lower the temperature.

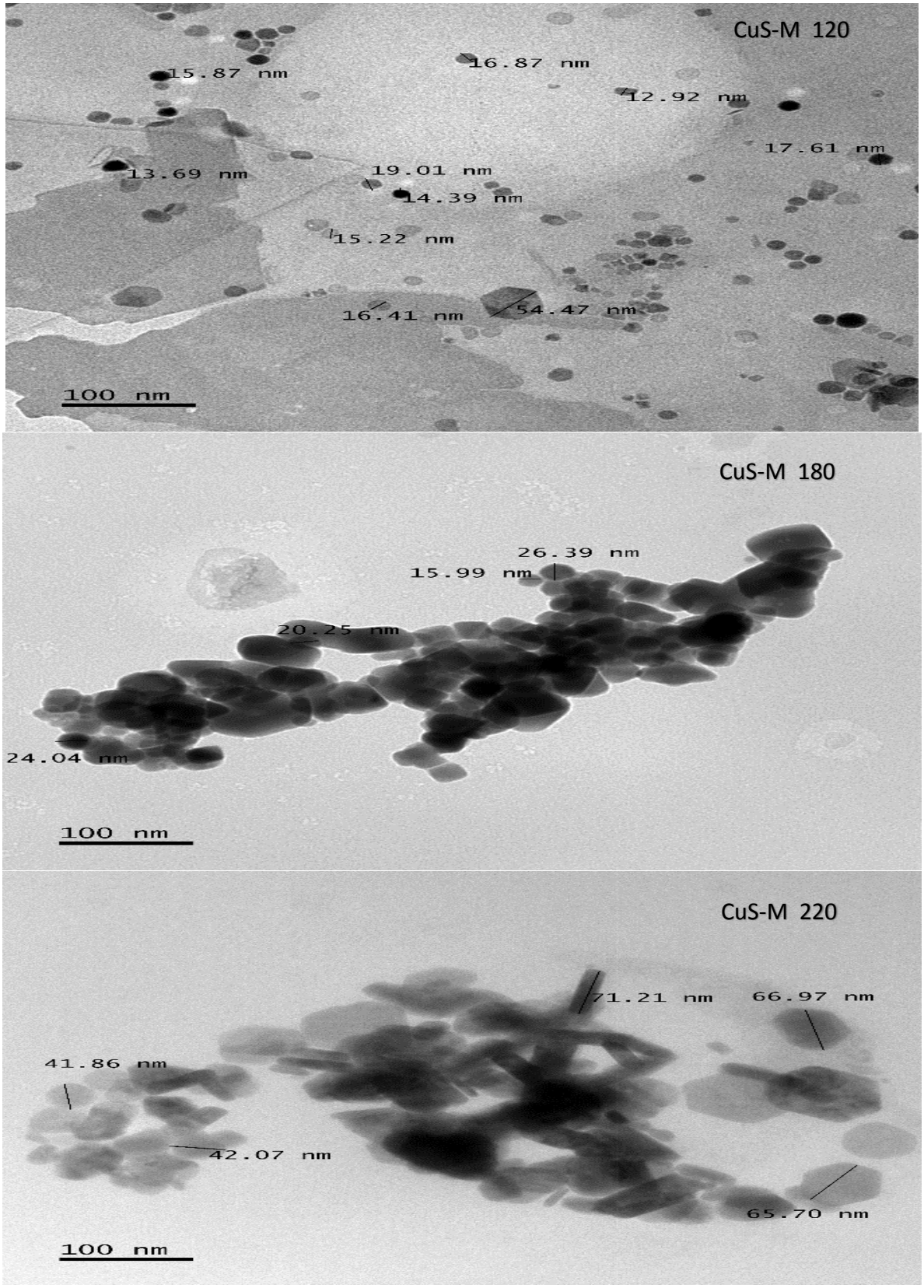

Figure 4. 8 TEM images of CuS-M nanoparticles synthesized at 120°C, 180°C and 220°C

4.3.2.3. Scanning electron microscope studies of CuS-M nanoparticles

The CuS-M micrographs as shown in Figure 4.9 display the same rough surface morphologies for the nanoparticles synthesized at 220°C and 120°C. Whereas, the CuS-M nanoparticles synthesized at 180°C shows a surface with smooth layers. The EDX spectra of all the nanoparticles confirmed the presence of copper and sulphur in the nanoparticles.

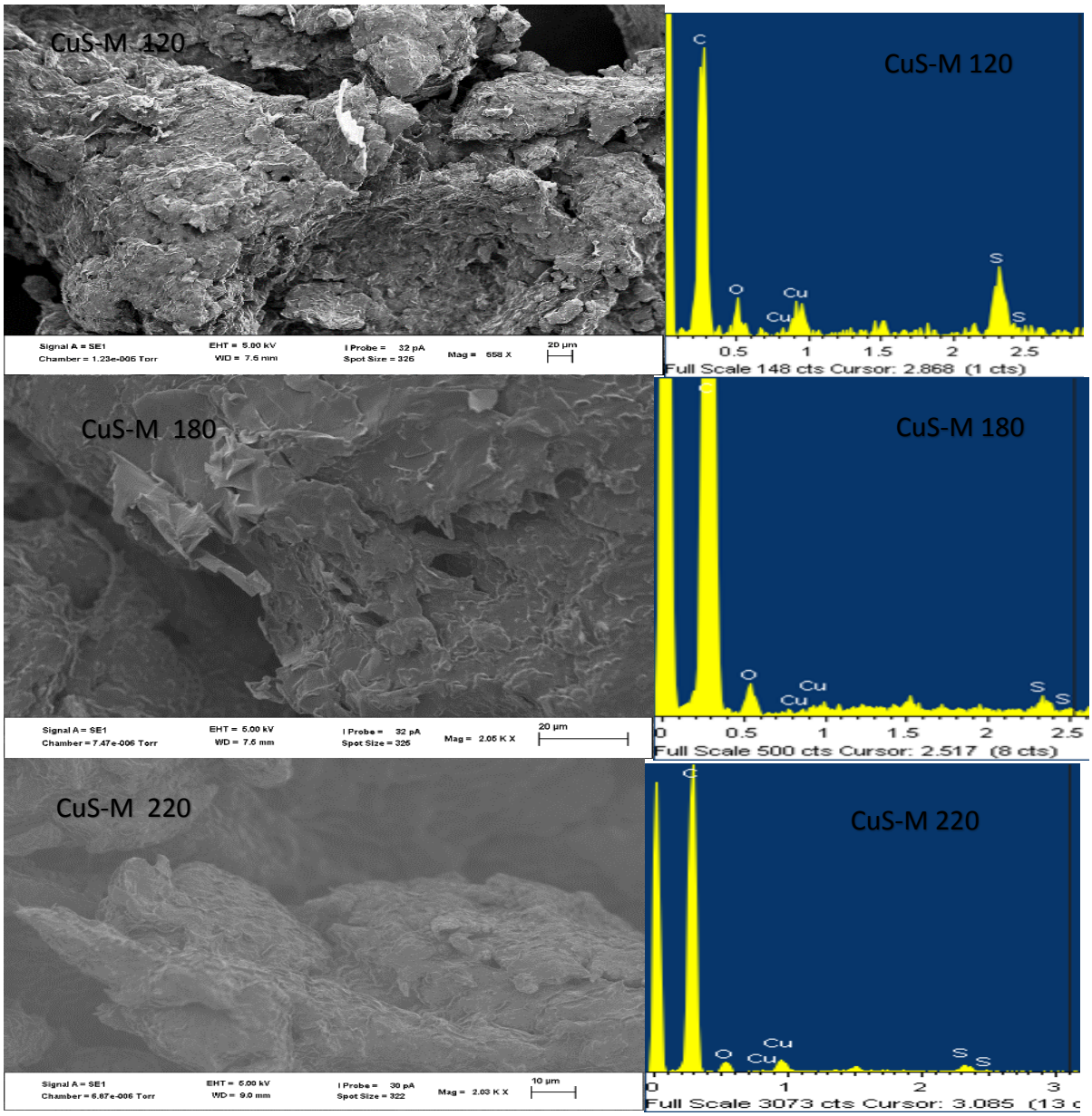

Figure 4. 9 SEM micrographs and EDX spectra of CuS-M nanoparticles synthesized at 120°C, 180°C and 220°C

4.3.2.4. Fourier-transform infrared spectroscopy studies of CuS-M nanoparticles

The overlay FTIR spectra of the CuS nanoparticles synthesized from copper(II) morpholine dithiocarbamate complex at 120°C, 180°C and 220°C is showed in Figure 4.10. The spectra clearly show that the bands of the pure oleic acid appeared in the spectra of the nanoparticles. The C=O stretching mode observed at 1750 cm^{-1} in the oleic acid spectrum was observed at 1650 cm^{-1} in all the spectra of the nanoparticles. The carboxylate stretching mode was observed at 1550 cm^{-1} for all the nanoparticles and the oleic acid. The O-H stretching mode expected around 3000 cm^{-1} was observed at 2950 cm^{-1} for all the nanoparticles [16].

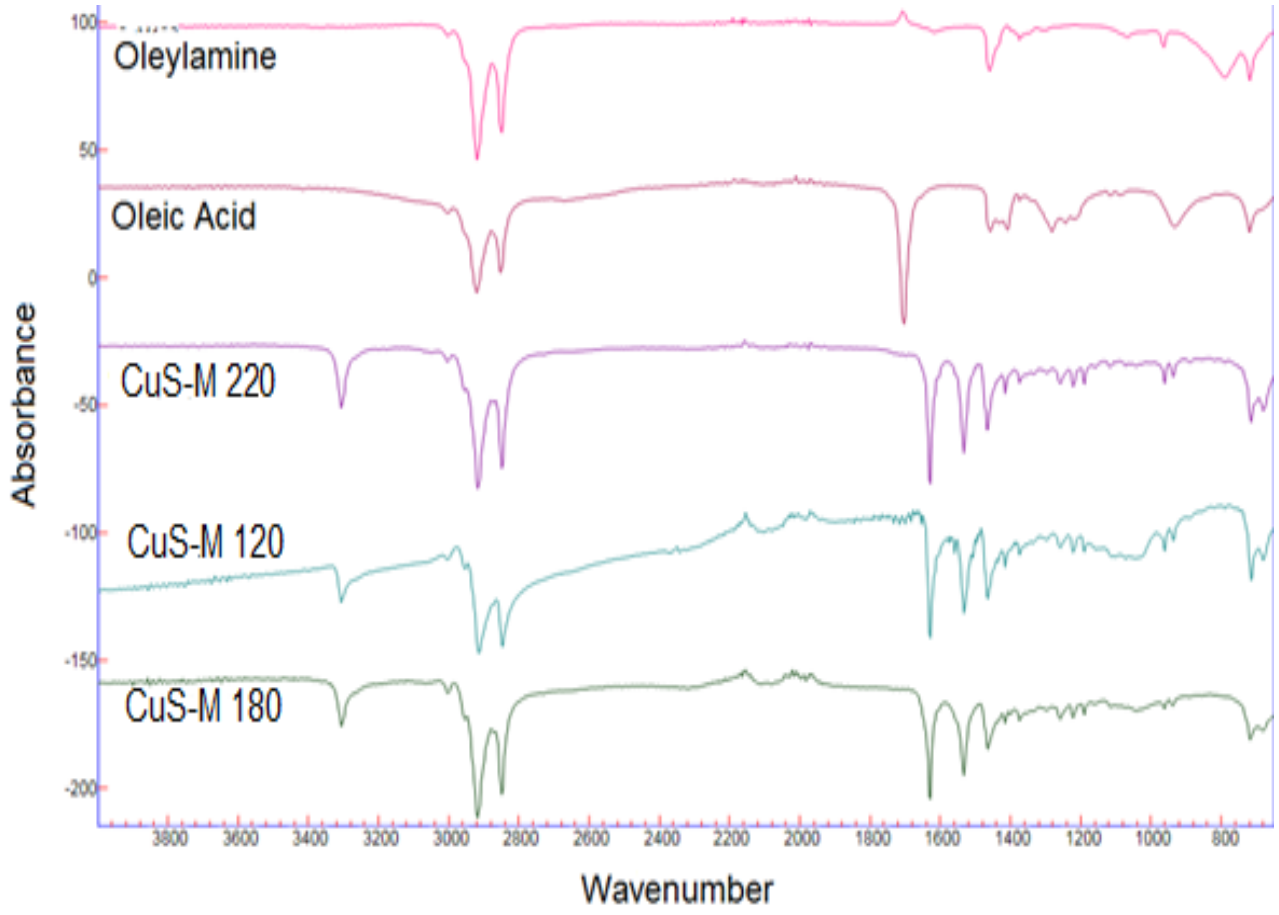

Figure 4. 10 Overlay FTIR spectra of CuS-M nanoparticles synthesized at 120°C, 180°C and 220°C

4.3.2.5. Absorption spectra studies of CuS-M nanoparticles

The recorded spectra from the UV-Visible are displayed in Figure 4.11. The spectra were used to estimate the band gap energy values of the synthesized nanoparticles. Tauc plot displayed below was used to estimate the band gap energy. The estimated bandgaps were as follows, 3.51eV, 3.45eV, 2.65eV for CuS-M nanoparticles synthesized at 120°C, 180°C and 220°C respectively. These values were compared to the band gap energy value of the bulk from the literature [17] which is 1.2 eV and they are greater and that is due to the decrease in the size of the particles.

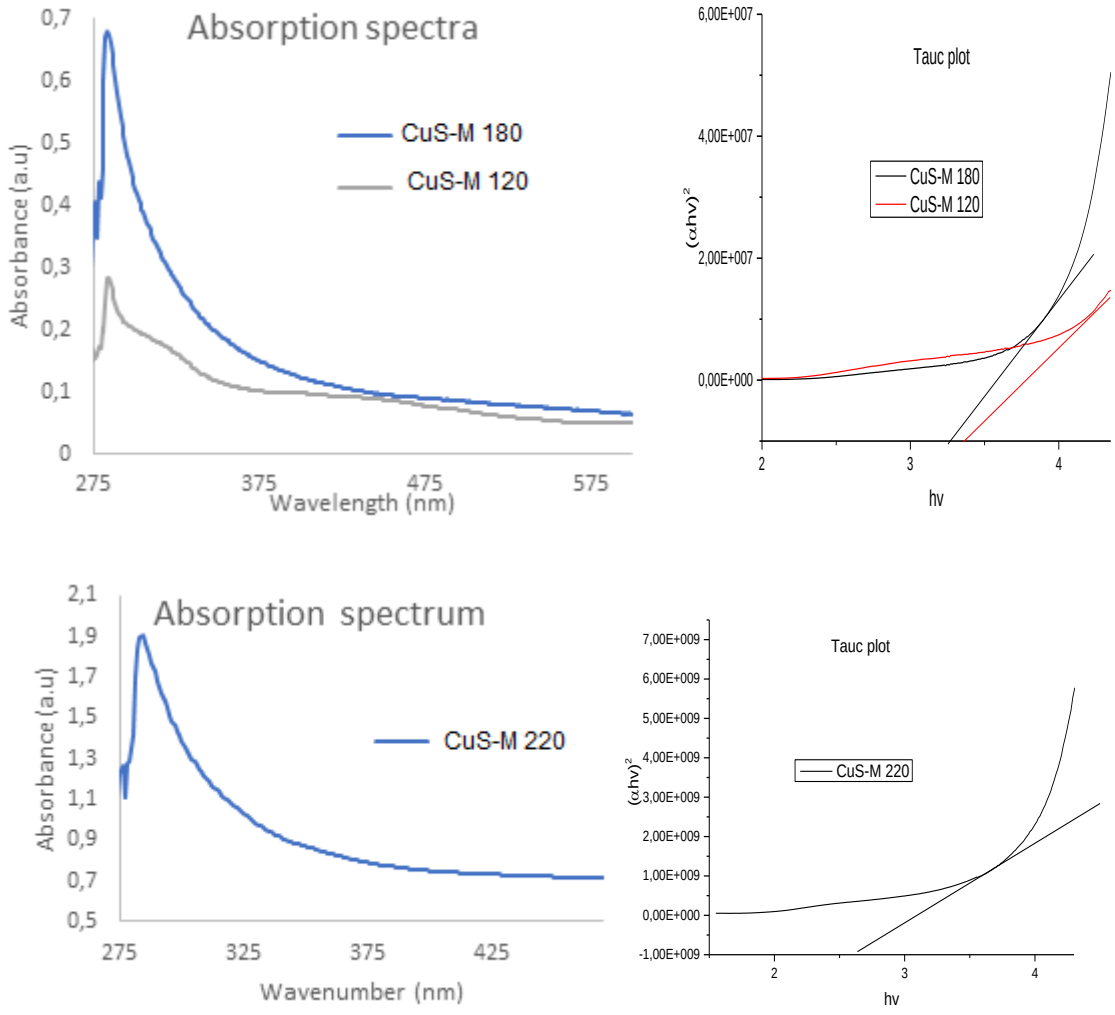

Figure 4. 11 Overlay UV-Vis spectra and Tauc plot of CuS-M nanoparticles synthesized at 120°C, 180°C and 220°C.

4.3.2.6. Emission studies of CuS-M nanoparticles

The photoluminescence spectra of CuS-M nanoparticles synthesized 120°C, 180°C and 220°C are displayed in Figure 4.12. The wavelength of the emission maxima was compared to the wavelength of the absorption maxima of the nanoparticles. The nanoparticles showed maximum absorption at 285, 284 and 284 nm and emitted at 308, 421, 325 nm when the thermolysis was done at 120°C, 180°C and 220°C temperatures respectively. The emission wavelength maxima are red shifted with respect to the absorption wavelength.

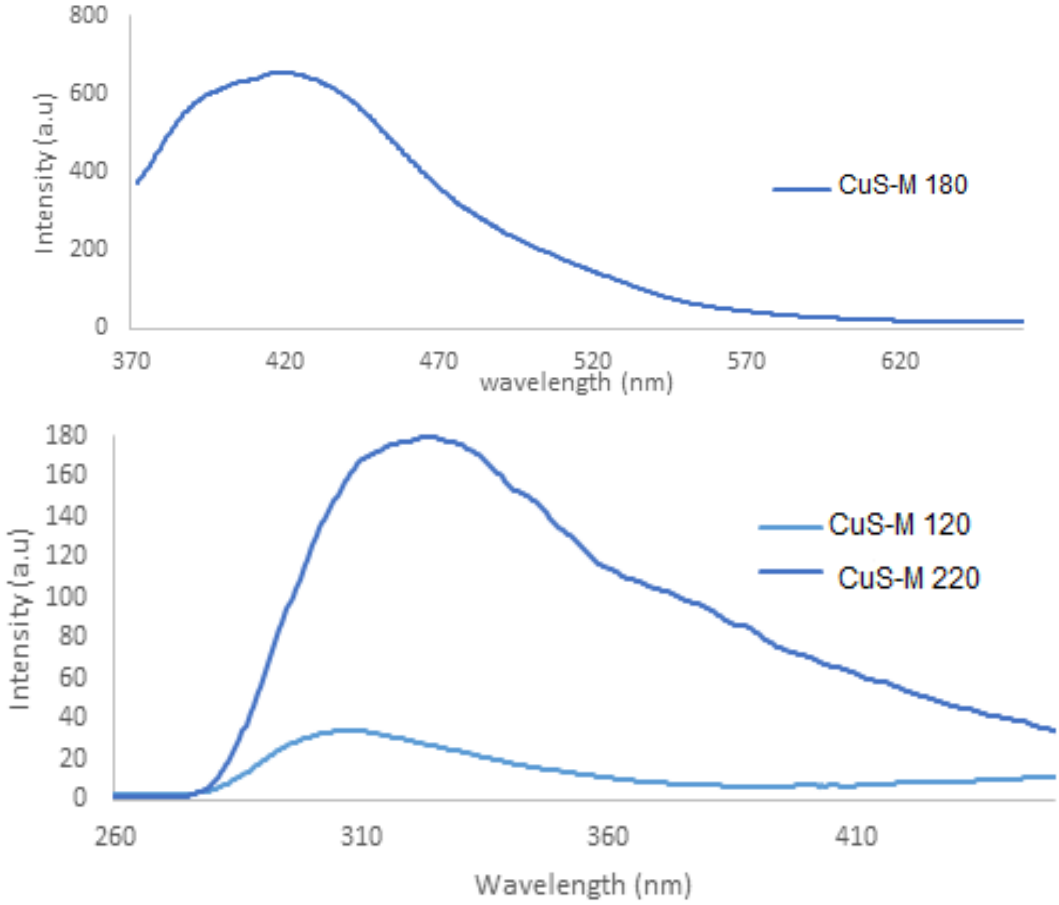

Figure 4. 12 Overlay emission studies of CuS-M nanoparticles synthesized at 120°C, 180°C and 220°C

4.3.3. Structural and optical studies of CuS-NEA nanoparticles synthesized from copper(II) N-ethyl aniline DTC complex

4.3.3.1. Powder X-ray diffraction patterns of CuS-NEA nanoparticles

Figure 4.13 displays the powder X-Ray diffraction patterns of the CuS-NEA nanoparticles. The nanoparticles obtained at 120°C gave diffraction peaks at 2θ = 32°, 34°, 35°, 47°, 54° and 57° that were indexed to 1010, 1013, 0114, 1112 and 1115 according to JCPDS (47-1748). In the literature [14], the particle crystalline phase was identified to be digenite $Cu_{1.8}S$ by JCPDS (95-005-3331) card data. However CuS-NEA 220 and CUS-NEA 180 showed the covellite phase diffraction peaks at 2θ = 37° and 42° showing the mixture of phases present. CuS-NEA 120 showed sharp narrow diffraction peaks showing the crystallinity of the particles [20].

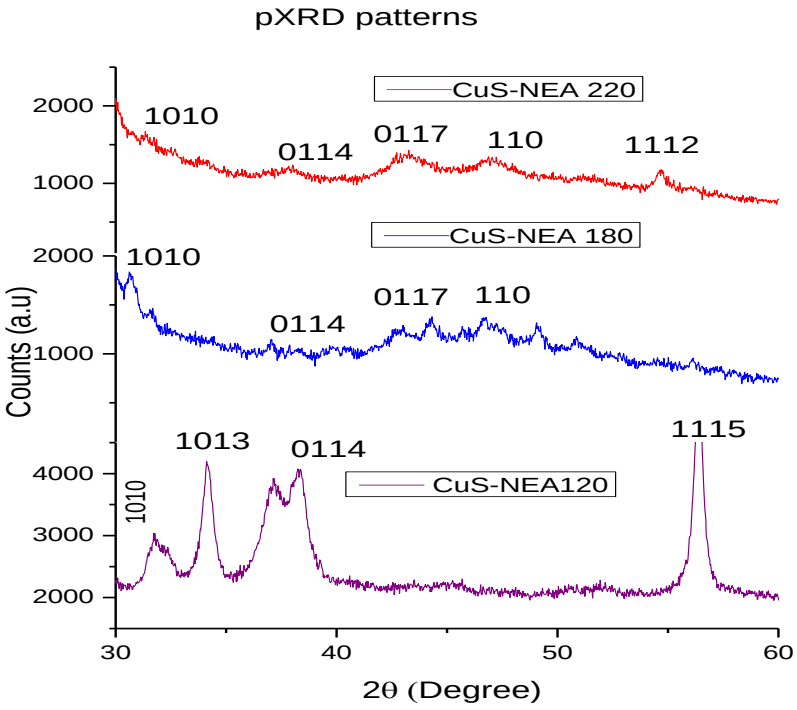

Figure 4. 13 P-XRD patterns of CuS-NEA nanoparticles synthesized at 120°C, 180°C and 220°C

4.3.3.2. Transmission electron microscopy studies of copper sulphide nanoparticles synthesized from copper(II)N-ethyl aniline DTC complex

TEM images of the copper sulphide nanoparticles synthesized from copper N-ethyl aniline DTC complex are displayed in Figure 4.14. The TEM image of CuS-NEA nanoparticles synthesized at 120°C exhibit nanoparticles size in the range of 6.40 - 48.15 nm with hexagonal shape. When the thermolysis was done at 180°C, the image showed the nanoparticles with wide particle size distribution in the range 10.73 - 55.20 nm that are hexagonal in shape. TEM image of CuS-NEA synthesized at 220°C showed agglomerated particles with three different shapes: spherical, triangular and mostly square shape. The crystallite size of the nanoparticles are in the range 47.51 to 73.01 nm.

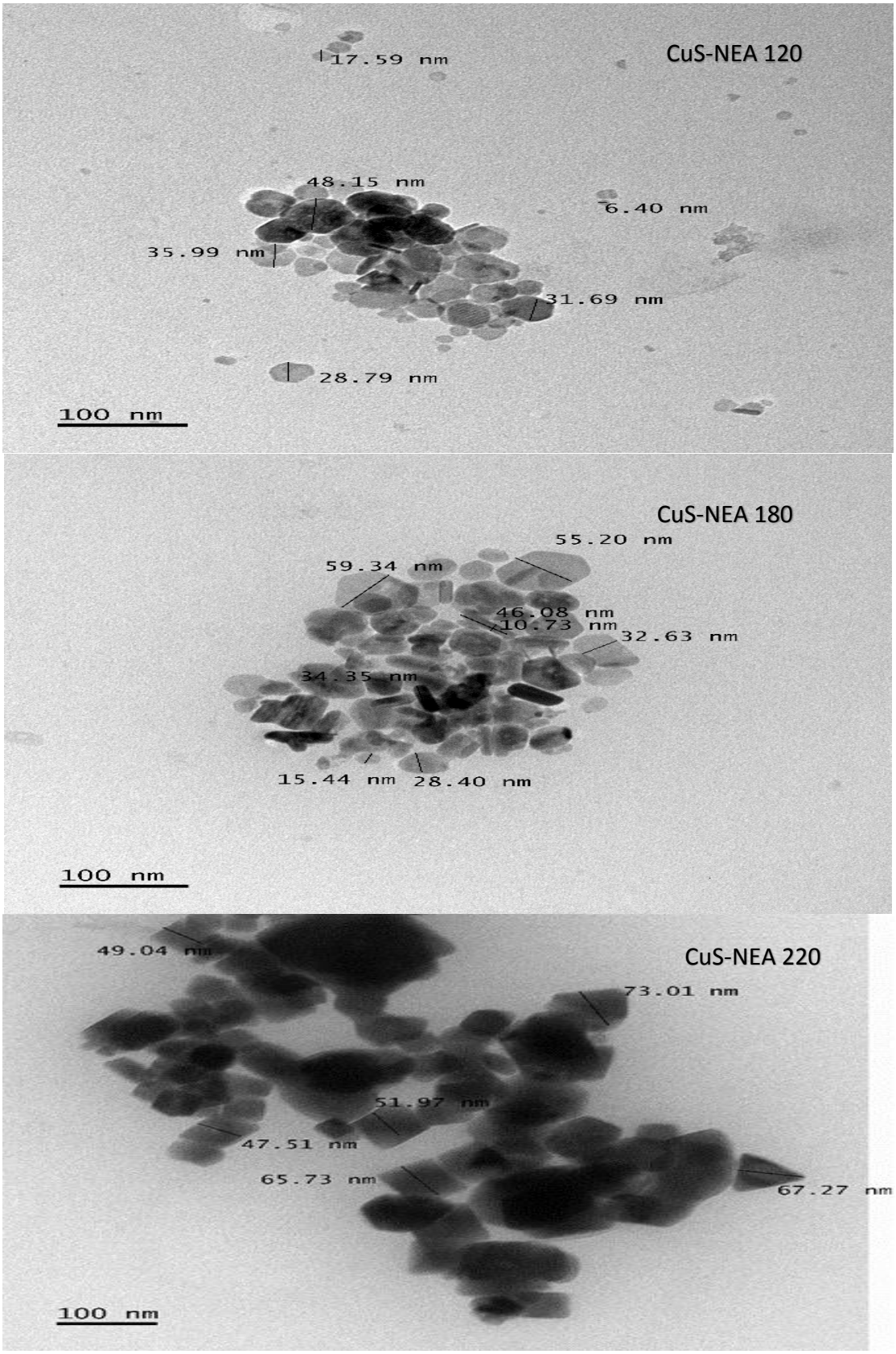

Figure 4. 14 TEM images of CuS-NEA nanoparticles synthesized at 120°C, 180°C and 220°C

4.3.3.3. Scanning electron microscope studies CuS-NEA nanoparticles

Figure 4.15 shows the CuS-NEA nanoparticle micrographs and their respective EDX. The images were taken to study the surface morphology of the nanoparticles. The Cu(II)NEA complex was thermolyzed at three different temperatures, 120°C, 180°C and 220°, three different surface morphologies, leaves like layers, irregular surface and clustered micro fibres respectively were observed. The EDX spectra confirmed the presence of copper and sulphur in the nanoparticles. However, the spectra also showed carbon and oxygen peaks due to the capping agent on the surface of the nanoparticles.

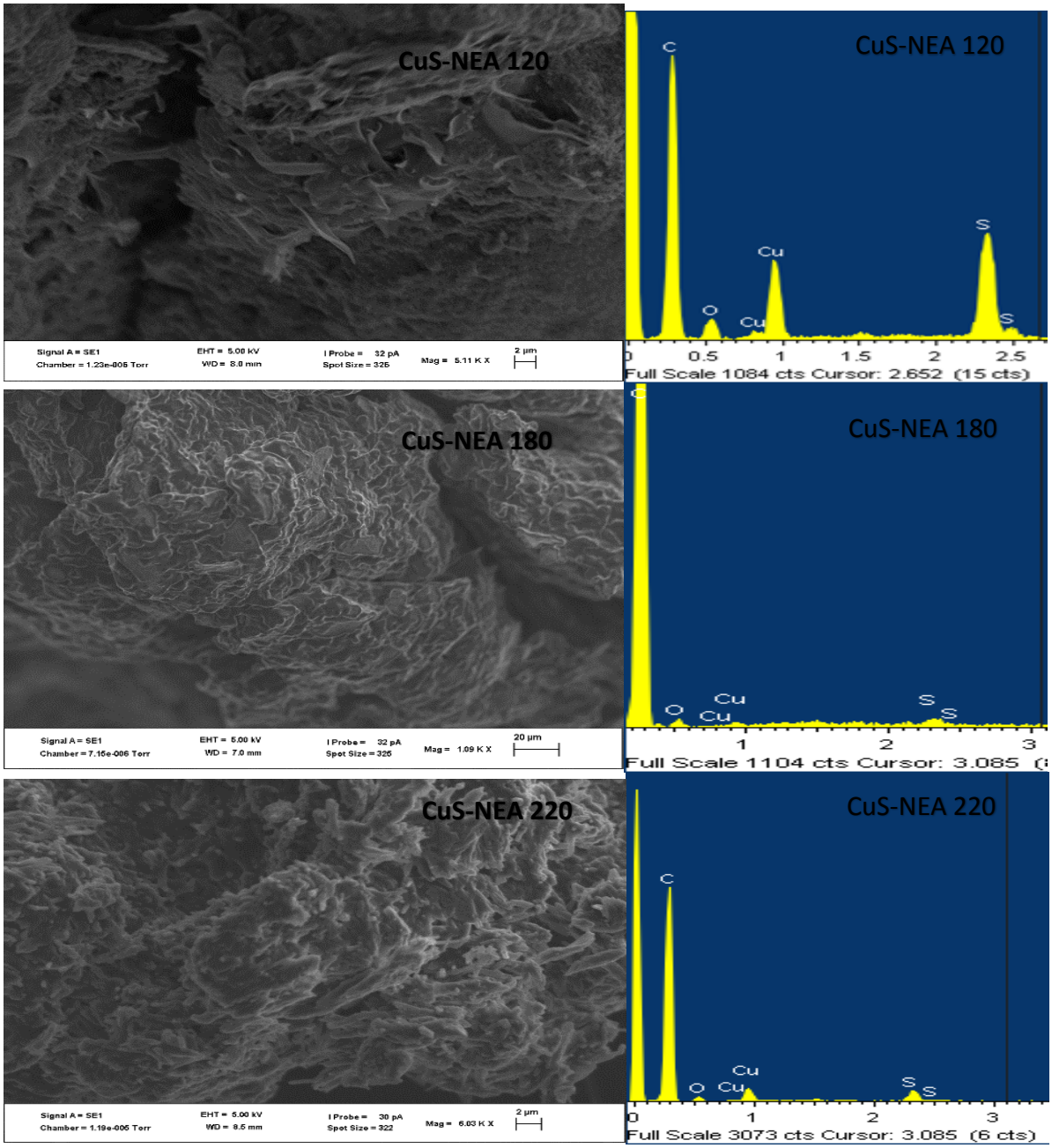

Figure 4. 15 SEM micrographs and EDX spectra of CuS-NEA nanoparticles synthesized at 120°C, 180°C and 220°C.

4.3.3.4. Fourier transform infrared spectroscopy studies of CuS-NEA nanoparticles

The FTIR spectra of the synthesized copper sulphide nanoparticles from copper(II) N-ethyl aniline DTC complex and the capping agents used in the synthesis of the nanoparticles are presented in Figure 4.16. The spectra showed strong C=O stretching modes around 1700 cm^{-1}. This frequency are attributed to the carboxylic group in the oleic acid [16]. The presence of these bands on the nanoparticle spectra confirmed the presence of only oleic acid on the surface of the copper sulphide nanoparticles.

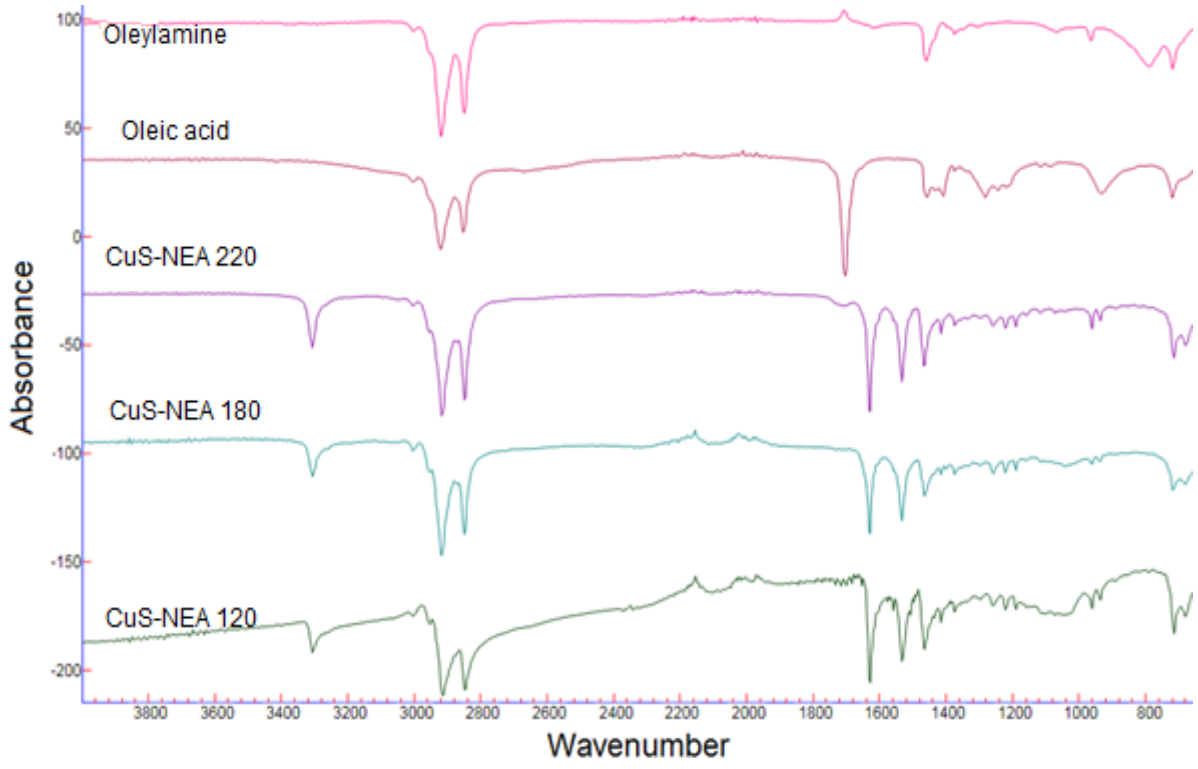

Figure 4. 16 overlay FTIR spectra of CuS-NEA nanoparticles synthesized at 120°C, 180°C and 220°C.

4.3.3.5. Absorption studies of CuS-NEA nanoparticles

The absorption spectra and the respective Tauc plots for CuS-NEA nanoparticles are displayed in Figure 4.17. The Tauc plots were used to estimate the energy band gap for the nanoparticles synthesized. The band gap energy was found to be 3.48 eV, 3.22 eV and 2.51 eV for the nanoparticles synthesized at 120°C, 180°C and 220°C respectively. The observed energy values were compared to the energy band gap of the bulk from the literature and the values were found to be greater. This shows the quantum confinement effects that are due to the decrease in the size of the particles.

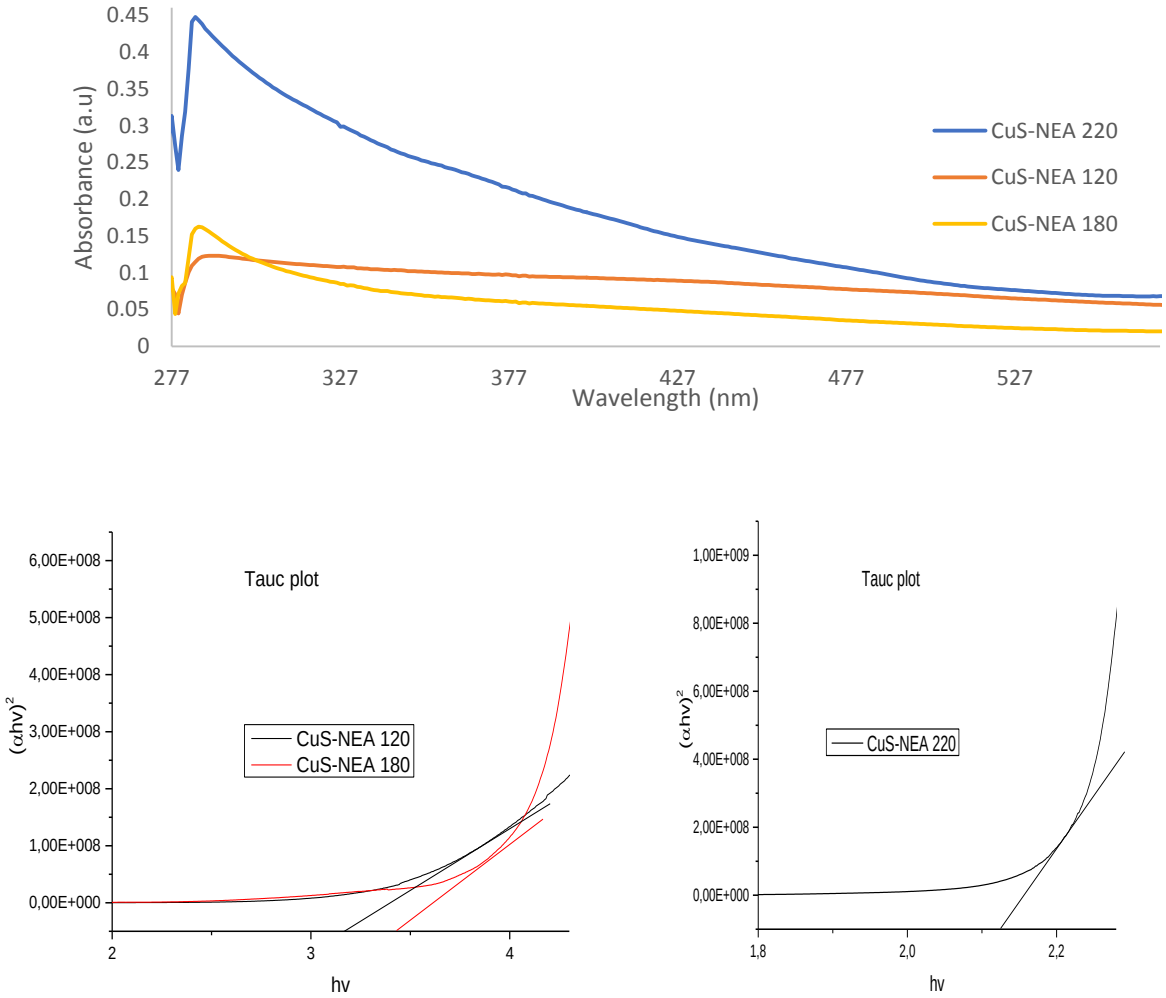

Figure 4. 17 Overlay UV-Vis spectra and Tauc plot of the CuS-NEA nanoparticles synthesized at 120°C, 180°C and 220°C.

4.3.3.6. Emission studies of CuS-NEA nanoparticles

The overlay of the emission spectra of the nanoparticles synthesized at 120°C, 180°C and 220°C from copper(II) N-ethyl aniline DTC complex are displayed in Figure 4.18. The nanoparticles synthesized at 180°C showed broad emission maxima in comparison to the nanoparticles synthesized at 120°C and 220°C. The broadening of the emission is likely due to the wide size range of the nanoparticles. The emission maxima wavelengths in comparison to the absorption band edges of the particles indicates that they are red shifted. The emission wavelengths have shifted to higher band edges as the absorption wavelengths are 285 nm for all the particles and the emission wavelengths are 307, 360 and 328 nm for CuS-NEA 120, CuS-NEA 180 and CUS-NEA 220 nanoparticles obtained at 120°C, 180°C and 220°C respectively.

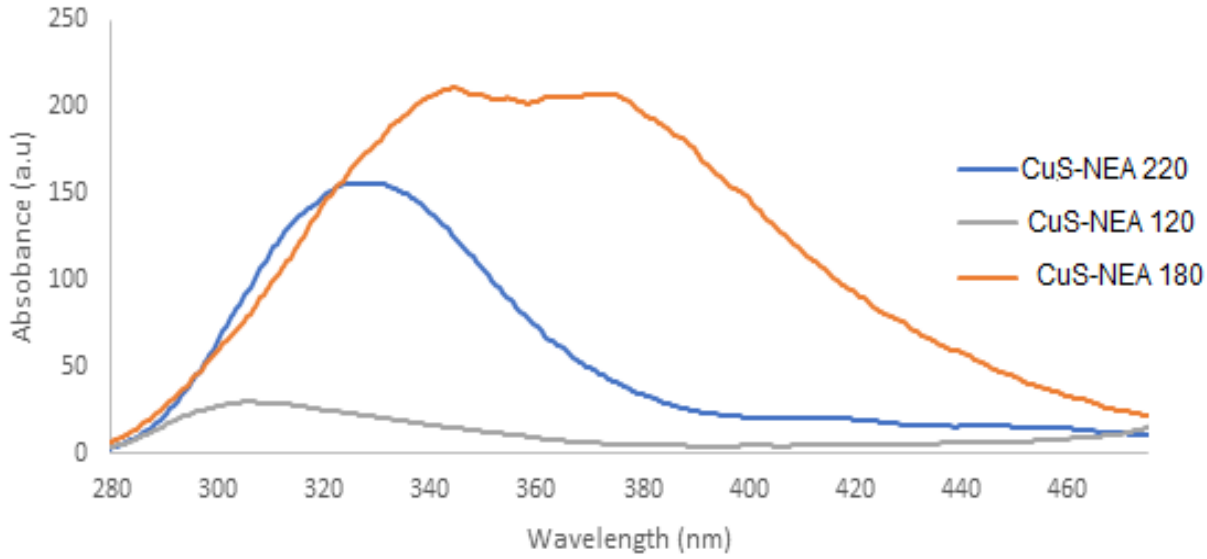

Figure 4. 18 Overlay fluorescence spectra of CuS-NEA nanoparticles synthesized at 120°C, 180°C and 220°C

4.3.4. Structural and optical studies of CuS-BA nanoparticles synthesized from copper(II) butyl amine DTC complex

4.3.4.1. Powder X-ray diffraction patterns of CuS-BA nanoparticles

Figure 4.19 represent the powder X-ray diffraction patterns of the synthesized nanoparticles from copper(II)butyl amine dithiocarbamate complex at three different temperatures. The nanoparticle peaks showed that the nanoparticles are getting more crystalline as the reaction temperature decreases hence the sharp diffraction peaks and they get more amorphous as the reaction temperature increases resulting to broad diffraction peaks. The phase of the nanoparticles was identified to be digenite $Cu_{1.8}S$ using JCPDS (95-005-3331) data card. The peaks were indexed with reference to the literature [14].

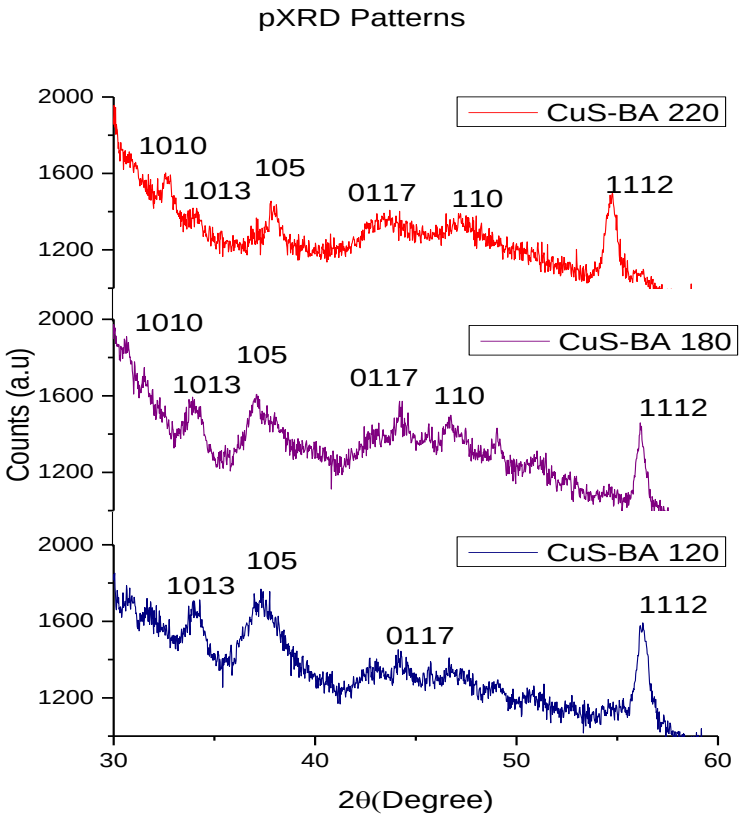

Figure 4. 19 Overlay pXRD patterns of CuS-BA nanoparticles synthesized at 120°C, 180°C and 220°C.

4.3.4.2. Transmission electron microscopy studies CuS-BA nanoparticles

Figure 4.20 displays the TEM images of CuS-BA nanoparticles. The TEM image of CuS-BA synthesized at 120°C displayed the triangular shaped nanoparticles with no trace of agglomeration. The nanoparticle crystallite size ranged between 7.88 - 15.17 nm. The CuS-BA nanoparticles synthesized at 180°C shows less agglomeration and the image consists of the mixture of spherical shape particles and rods. The uniform spherically shapes particles have narrow size distributions from 20.79 - 22.31 nm. The rod shaped particles were measured to be in the range 54.08 to 111.32 nm long in length. The TEM image of CuS-BA nanoparticles synthesized at 220°C indicates the nanoparticles have crystallite size ranging from 48 to 72 nm. The nanoparticles seem to have strong agglomeration effect. In this precursor the thermolysis temperature seems to have affected the particle size and shape and has an effect also on agglomeration.

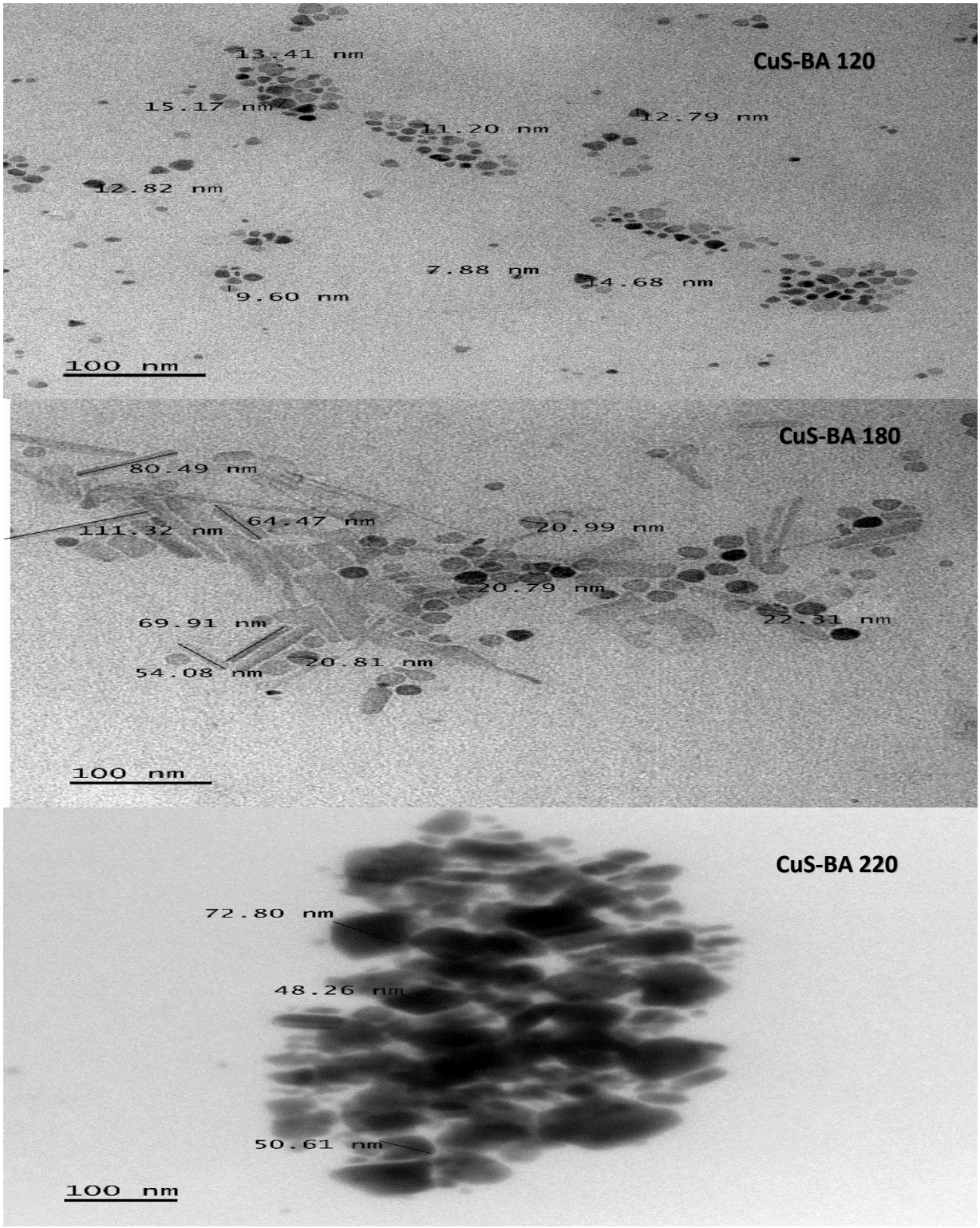

Figure 4. 20 TEM images of CuS-BA nanoparticles synthesized at 120°C, 180°C and 220°C.

4.3.4.3. Scanning electron microscopy studies of CuS-BA nanoparticles

The SEM micrographs of copper sulphide nanoparticles synthesized at three different temperatures from copper(II) butyl amine DTC complex are shown in Figure 4.21. The CuS-BA nanoparticles synthesized at 220°C and at 180°C shows rough surfaces with patches. However, when the same precursor was thermolyzed at 120°C the nanoparticles exhibit a smooth surface morphology with layers. The corresponding EDX spectra are displayed below confirming the presence of copper and sulphur in the nanoparticles synthesized.

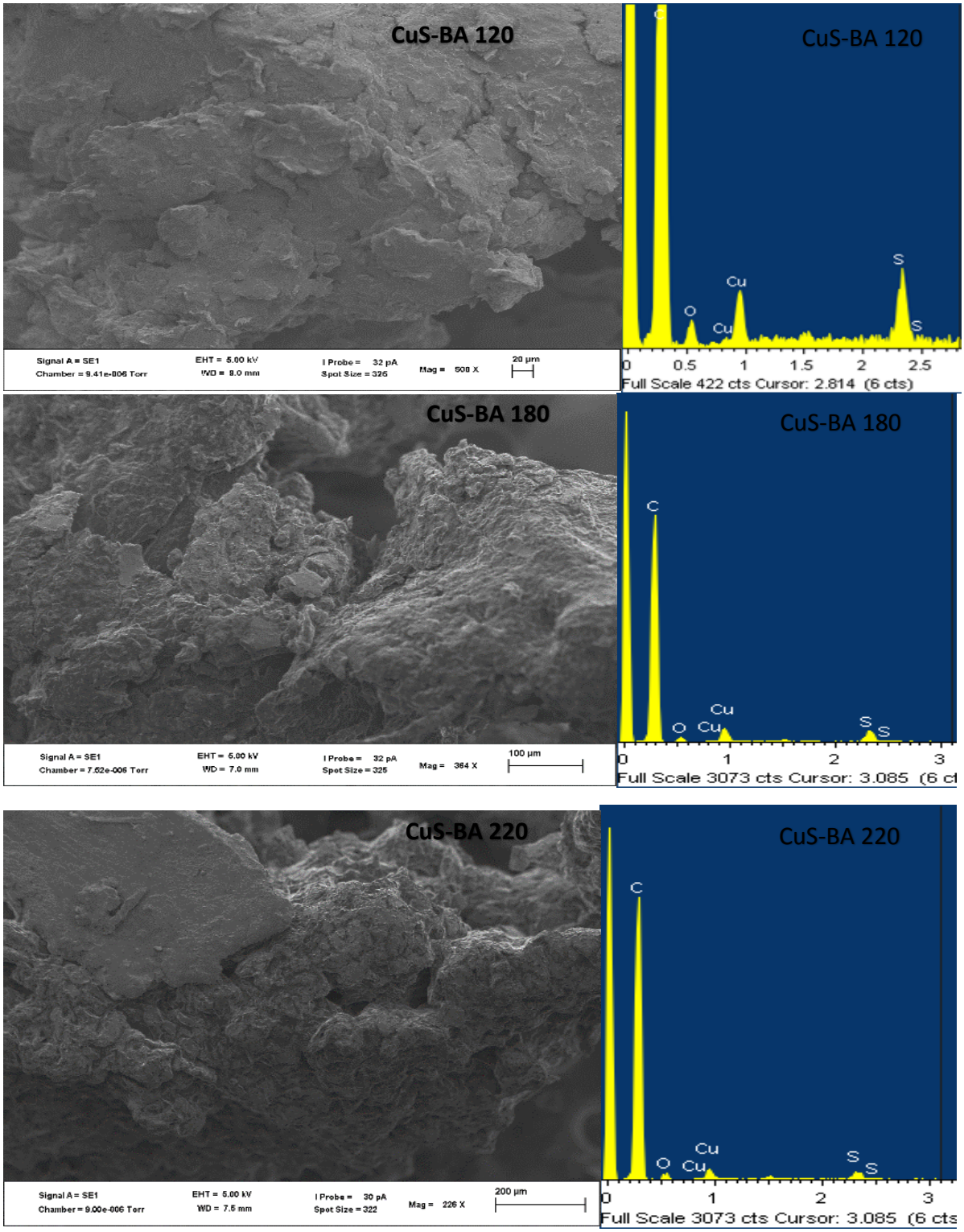

Figure 4. 21 SEM images and EDX spectra of CuS-BA nanoparticles synthesized at 120°C, 180°C and 220°C.

4.3.4.4. Fourier transform infrared spectroscopy studies of CuS-BA nanoparticles

The CuS nanoparticles synthesized from Copper(II) butyl amine DTC complex at 120°C, 180°C and 220°C were also characterized with FTIR to confirm the presence of the capping agent on the surface of the nanoparticles. The overlay spectra of the nanoparticles and the spectra of oleic acid and oleylamine are presented in Figure 4.22. From the spectra, it is observed that oleic acid has coordinated to the surface of the particles. As the particles adapted the bands observed in oleic acid spectra. All the nanoparticles spectrums show the presence of the carboxylic group by the C=O and O-H stretching modes appearing at 1750 cm^{-1} and 2950 cm^{-1} respectively. It can clearly be seen that the bands of the pure oleic acid appear also in the spectra of the nanoparticles [16].

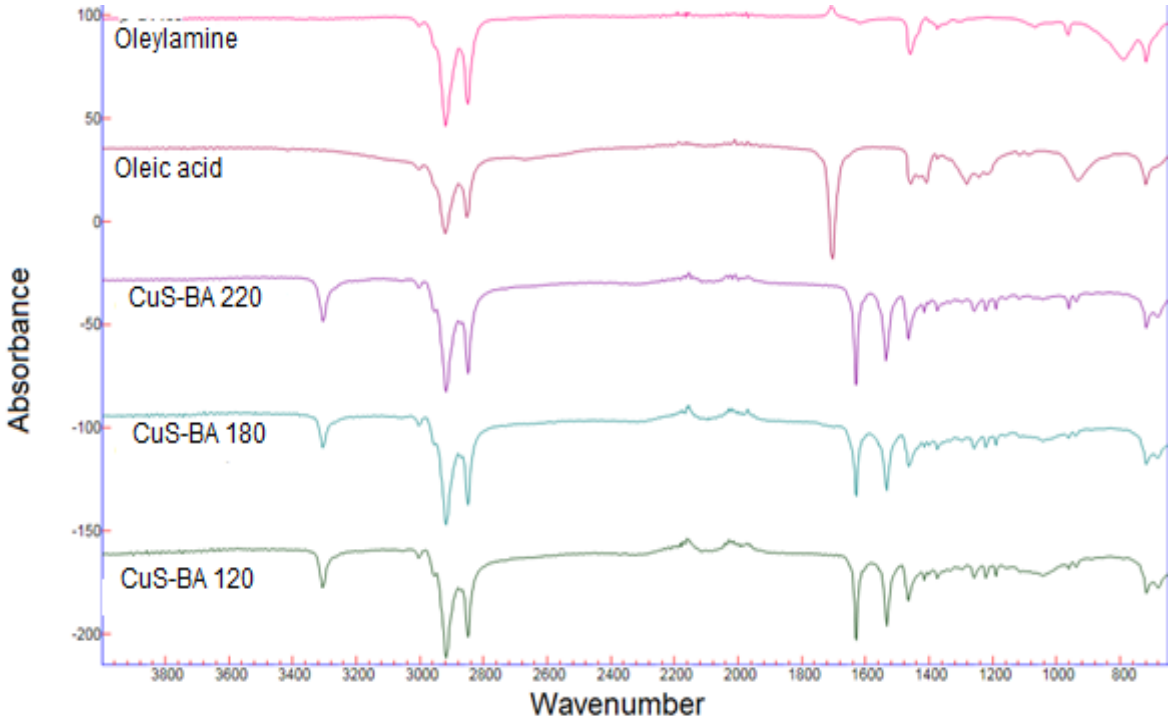

Figure 4. 22 Overlay FTIR spectra of CuS-BA synthesized at 120°C, 180°C and 220°C.

4.3.4.5. Absorption studies of CuS-BA nanoparticles

Figure 4.23 shows the UV-Vis spectra of the nanoparticles and the Tauc plots. The absorption spectra were directly used to estimate the band gap energy of the particles using Tauc's equation [12]. The nanoparticles showed band gap energy values of 3.59 eV, 3.04 eV and 3.29 eV for the CuS-BA nanoparticles synthesized at 120°C, 180°C and 220°C temperatures respectively. The spectra were blue shifted when the band gap values were compared to that of the bulk reported in the literature [17]. The blue shift of these values is usually because of the decrease in the particle sizes.

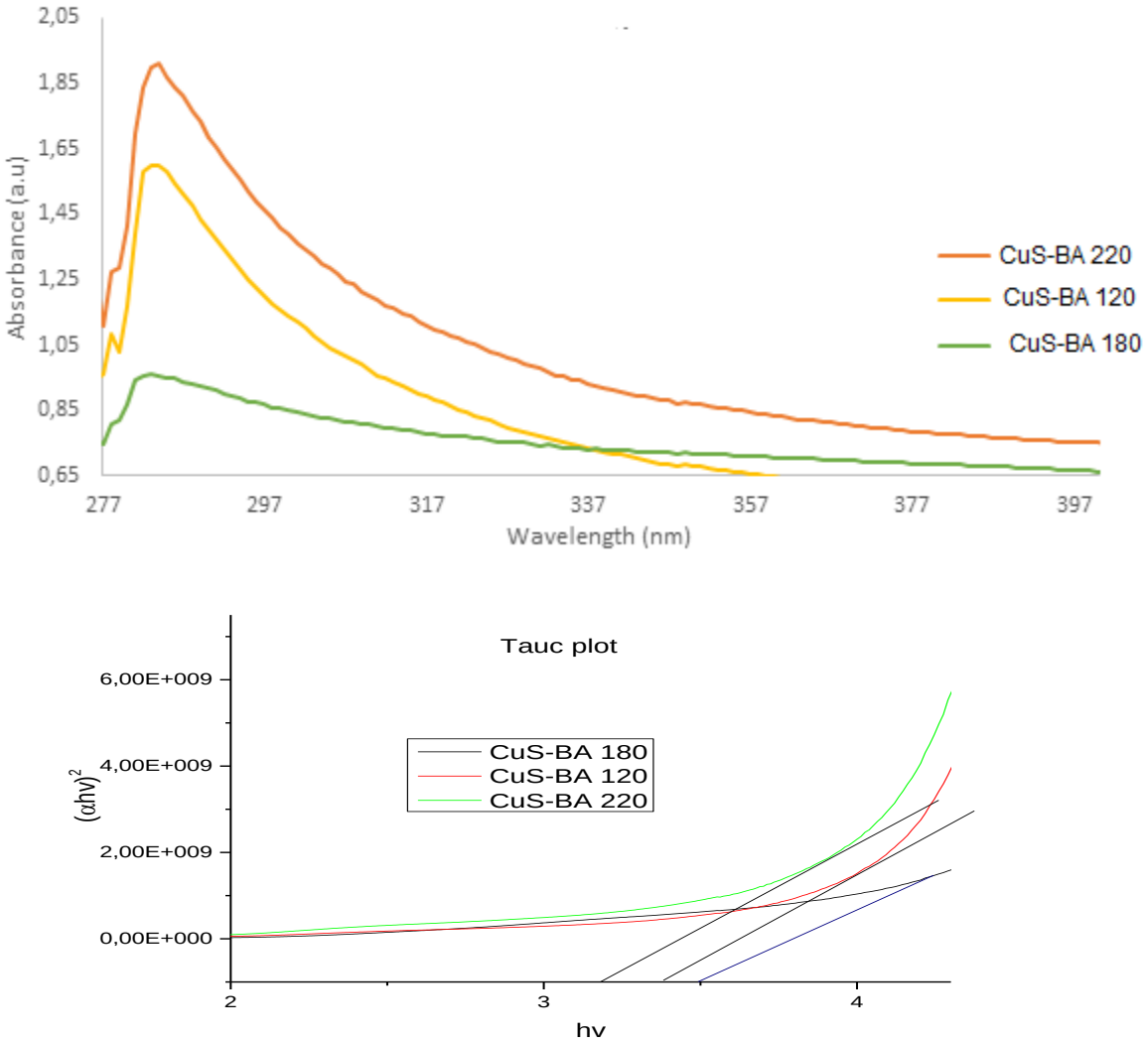

Figure 4. 23 Overlay UV-Vis spectra and Tauc plots of the CuS-BA nanoparticles synthesized at 120°C, 180°C and 220°C.

4.3.4.6. Emission studies of CuS-BA nanoparticles

The emission spectra of CuS-BA nanoparticles are presented in Figure 4.24. The emission spectra are generally broad with emission maxima at 307, 306 and 325 nm for the nanoparticles synthesized at 120°C, 180°C and 220°C respectively. These emission maxima were observed to have red shifted in comparison to the absorption edges at 284 nm for CuS-BA prepared at both 120°C and 220°C, 282 nm for CuS-BA synthesized at 180°C,

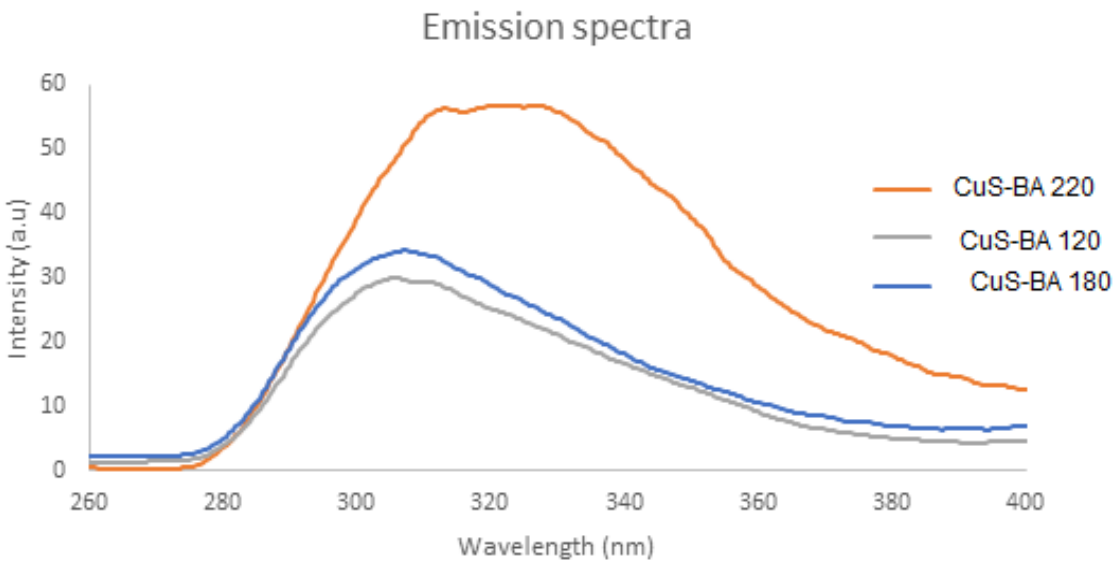

Figure 4. 24 Overlay Fluorescence spectra of CuS-BA synthesized at 120°C, 180°C and 220°C.

4.3.5. Structural and optical studies of copper sulphide nanoparticle synthesized from different precursors at 220°C (CuS-DBA, CuS-NMB, CuS-DA, CuS-PP)

4.3.5.1. Powder X-ray diffraction patterns of CuS-DBA, CuS-NMB, CuS-DA, CuS-PP nanoparticles

The powder X-ray diffraction patterns of the synthesized copper sulphide nanoparticles are displayed in Figure 4.25. The peaks were indexed with reference to JCPDS (47-1748) in the literature. Whereby, 2θ = 55°, 46°, 42°, 37° and 32° corresponds to (1112), (110), (0117), (0114) and (1010) [40]. The digenite $Cu_{1.8}S$ crystallinity phase of the nanoparticles were identified when the patterns were compared to the JCPDS (95-005-3331). The $Cu_{1.8}S$ major peaks at 2θ = 32°, 46° and the $Cu_{1.8}S$ minor peak at 2θ = 55° are clear in the XRD patterns [21]. The strong diffraction peaks that appeared in the patterns suggest that the synthesized copper sulphide nanoparticles are well crystalline in nature [19].

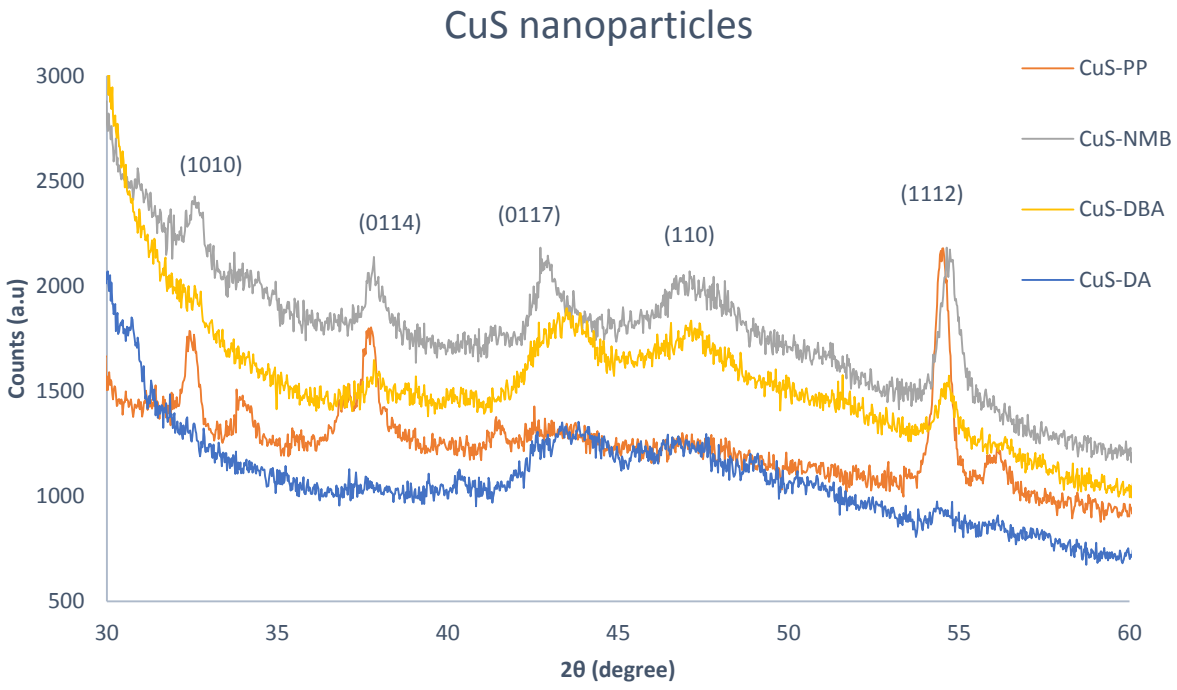

Figure 4. 25 P-XRD patterns of copper sulphide nanoparticles synthesized at 220°C

4.3.5.2. Transmission electron microscopy studies of CuS-DBA, CuS-NMB, CuS-DA, CuS-PP nanoparticles

The TEM images of the as prepared copper sulphide nanoparticles are shown in Figure 4.26. All the copper sulphide nanoparticles were dispersed in hexane and they were sonicated for 15 minutes before the images were recorded. CuS-NMB image shows the particles consists of mixtures of semi spherical and rod-like shapes. The size of the nanoparticles ranges from 19 - 56 nm. The image also shows the agglomeration of the particles. The CuS-DA images shows prominent agglomeration in comparison to others. These particles appeared as spherical and semi-spherical in shapes. Their size ranges between 40 and 70 nm. CuS-DBA image also shows agglomerated nanoparticles with size range of 13.50 to 36.90 nm with square and semi spherical shapes. However, CuS-PP seems to have different properties. The crystallite size range of the CuS-PP nanoparticles ranges from 5.29 to 12.21 nm with a uniform spherical shape with less agglomeration.

The SAED patterns of CuS-DA, CuS-DBA and CuS-PP were taken and are also presented to their TEM images in Figure 4.25. CuS-DA and CuS-PP SAED patterns (Figure 4.26 A and D) shows visible rings and bright spots proving the crystallinity of the particles synthesized. CuS-DBA SAED patterns (Figure 4.26 B) shows dim spots which means that the CuS-DBA particles are amorphous. The lattice fringes d-spacing of CuS-DBA (Figure 4.26 C) and CuS-PP (Figure 4.26 E) were measured and were found to be different in different areas. For CuS-DBA d = 0.26 nm and 0.3 nm then for CuS-PP d = 0.32 nm and 0.34 nm. However, the measurements are within the parameters of the d-spacing found for the nanoparticles of digenite copper sulphide phase [22, 23].

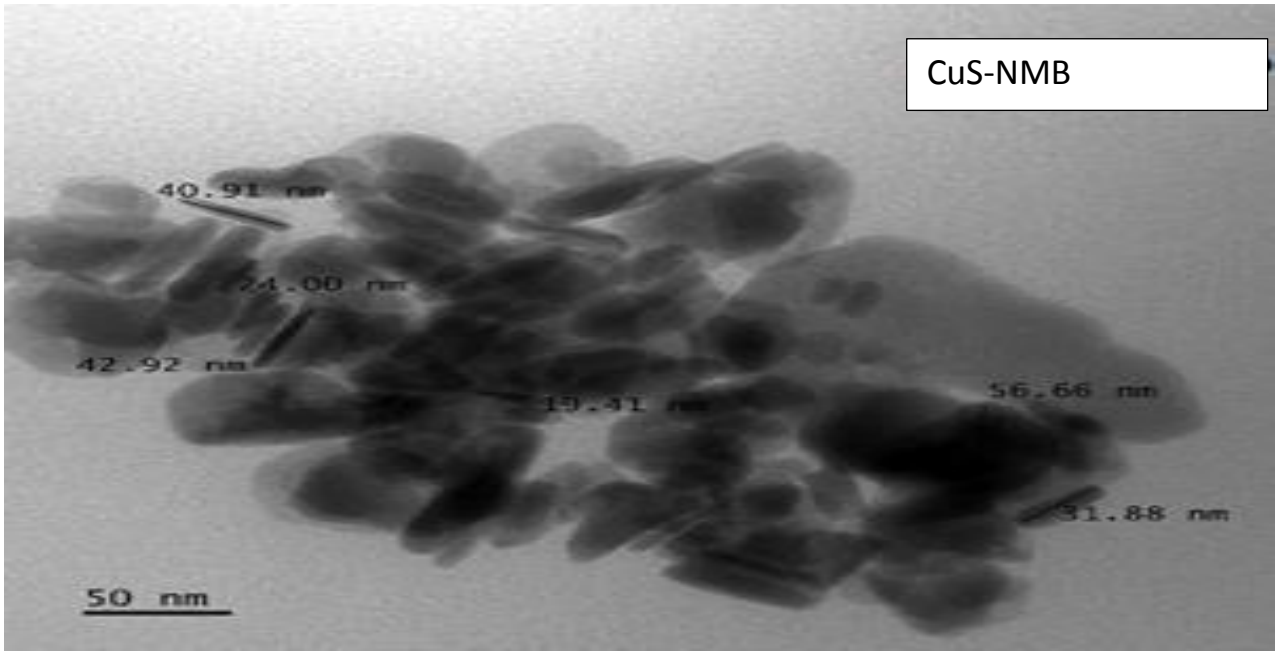
CuS-NMB
40.91 nm
24.00 nm
42.92 nm
19.41 nm
56.66 nm
31.88 nm
50 nm

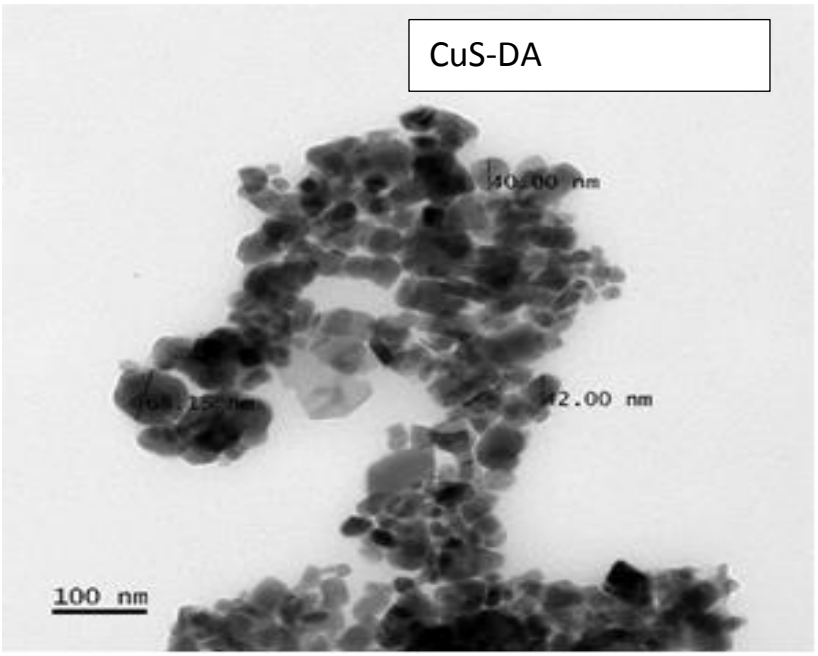
CuS-DA
42.00 nm
100 nm

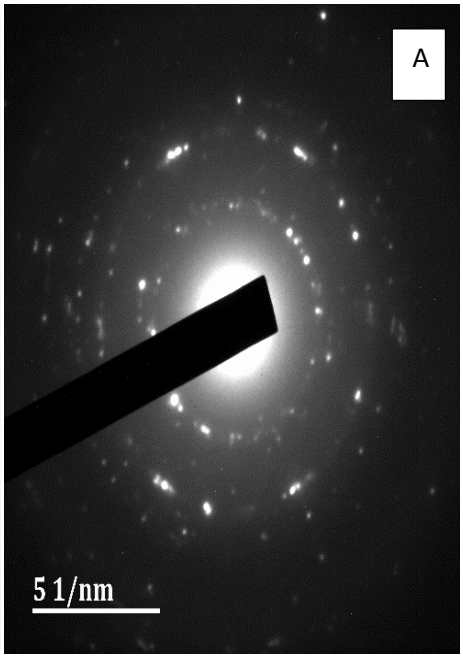
A
5 1/nm

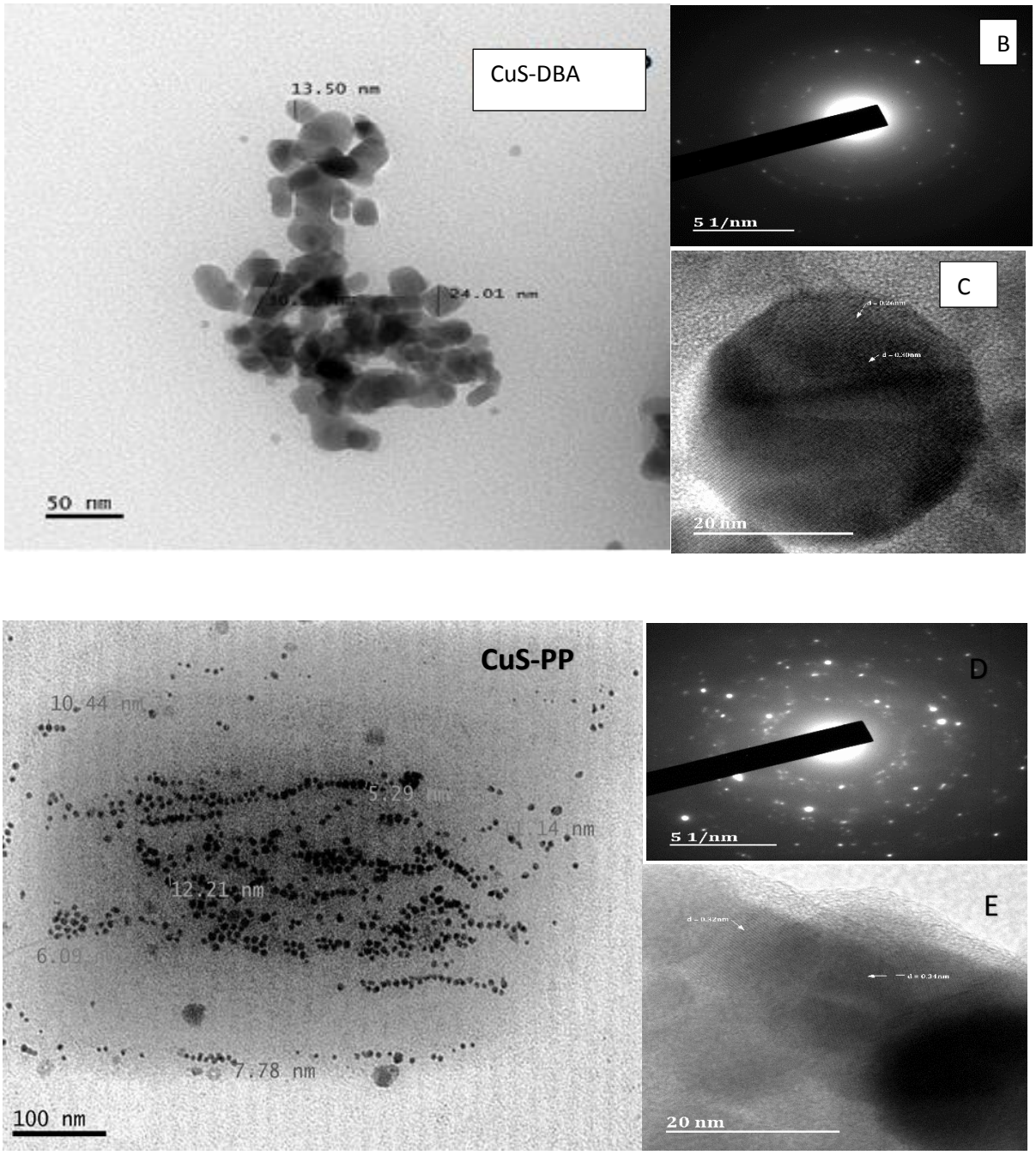

Figure 4. 26. TEM images and A. CuS-DA SAED, B. CuS-DBA SAED, C. CuS-DBA lattice fringes, D. CuS-PP SAED and E. CuS-PP lattice fringes of copper sulphide nanoparticles synthesized at 220°C

4.3.5.3. Scanning electron microscope and Energy-dispersive X-ray spectroscopy studies of CuS-DBA, CuS-NMB, CuS-DA, CuS-PP nanoparticles

Figure 4.27 shows the SEM images of the nanoparticles and the EDX spectra showing the elemental composition of the synthesized nanoparticles. The SEM images shows different morphologies for the nanoparticles which could mean that the morphology depends on the precursor used. CuS-NMB image shows a rough surface morphology while very smooth surface is observed for the CuS-DBA nanoparticles. However, CuS-DA and CuS-PP exhibit flaky surfaces. All the EDX spectra confirmed the presence of copper and sulphur with carbon and oxygen that are assumed to be due to the capping agents used.

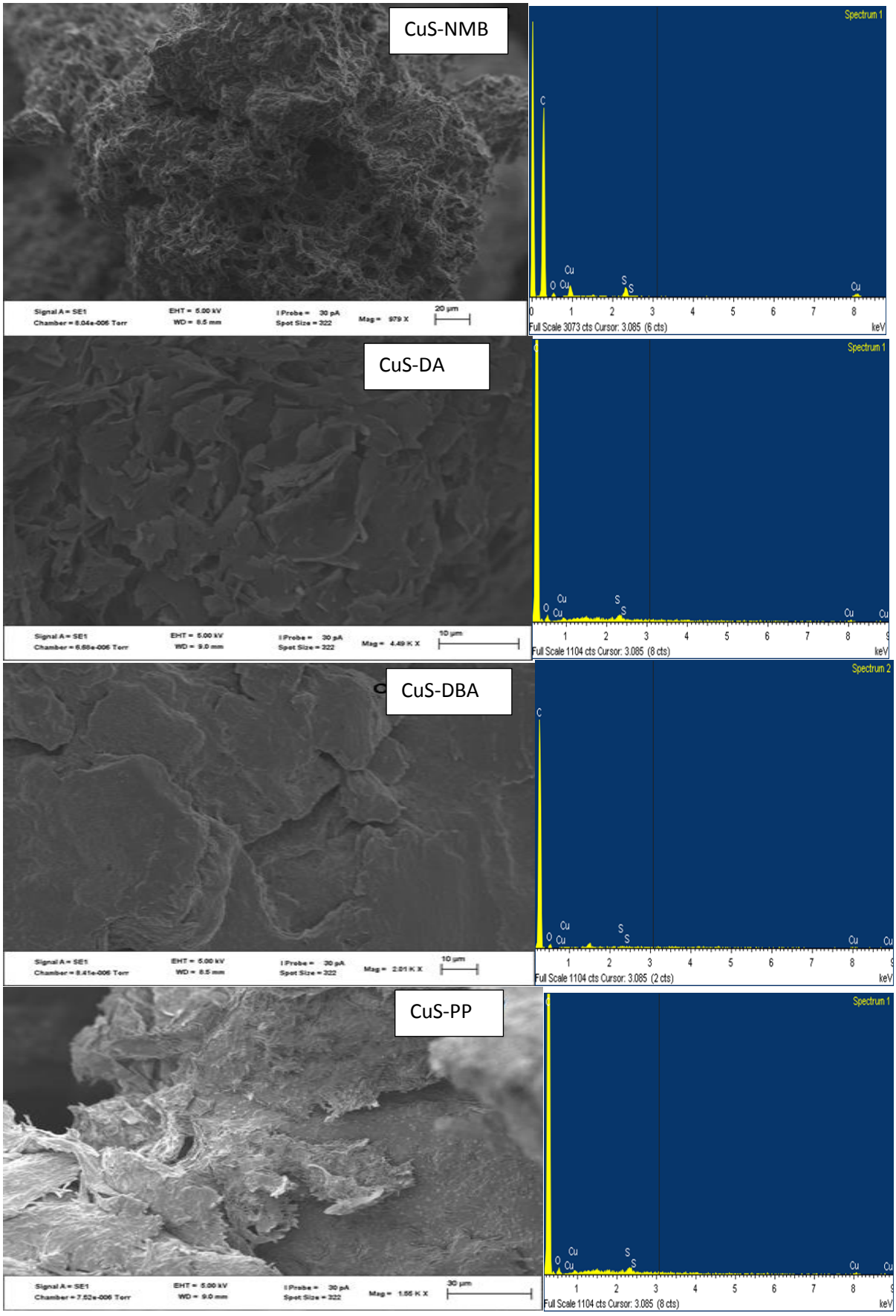

Figure 4.27 SEM images and EDX spectra of the copper sulphide nanoparticles synthesized at 220°C from four different precursors

4.3.5.4. Fourier-transform infrared spectroscopy studies of CuS-DBA, CuS-NMB, CuS-DA, CuS-PP nanoparticles

Figure 4.28 shows the overlay FTIR spectra of the nanoparticles synthesized and the surfactants used for the synthesis of the nanoparticles, oleic acid and oleylamine. The FTIR spectra of the nanoparticles shows the peaks in the oleic acid, the strong band at around 1700 cm^{-1} in the oleic acid spectra resonating to the C=O in the carboxylic acid appeared at 1650 cm^{-1} in the spectra of the nanoparticles, and the antisymmetric and symmetric C-H vibrations of the CH_2 in the oleic acid also appeared on the spectra of all the nanoparticles confirming the presence of the long chain on the nanoparticles surface [24].

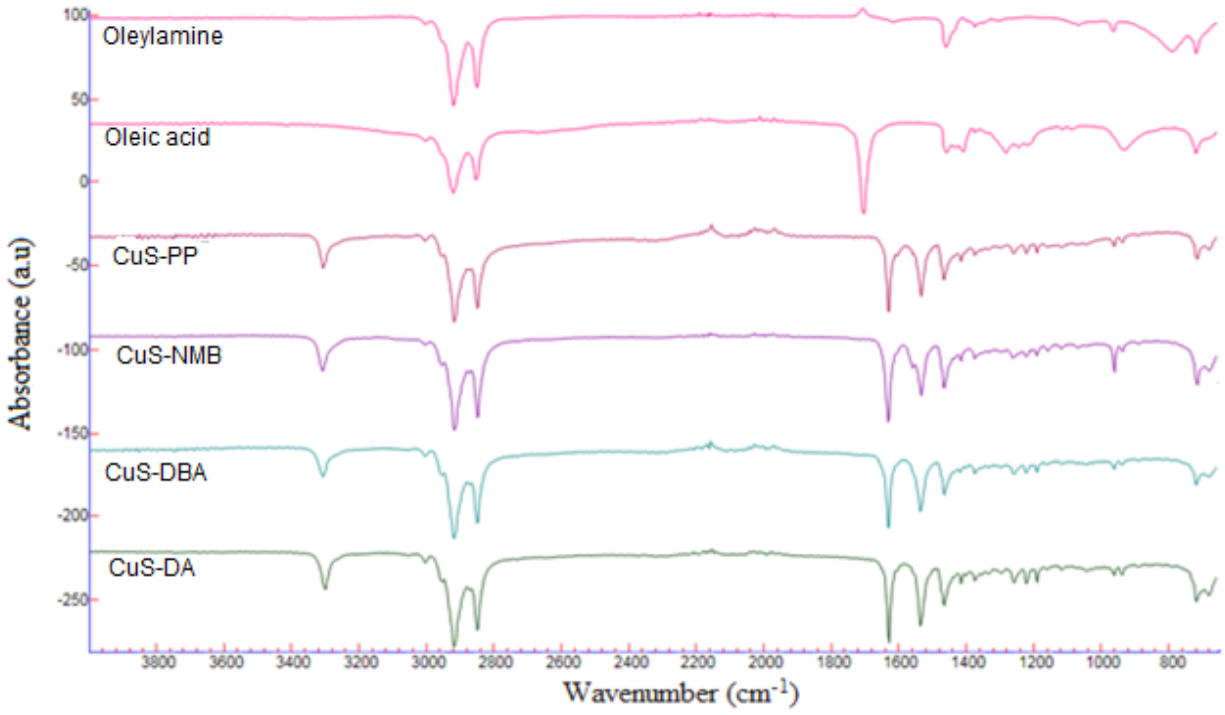

Figure 4. 28 Overlay FTIR spectra of copper sulphide nanoparticles synthesized at 220°C from four different precursors

4.3.5.5. Absorption studies of CuS-DBA, CuS-NMB, CuS-DA, CuS-PP nanoparticles

The absorption spectra of the copper sulphide nanoparticles synthesized and their Tauc plots are shown Figure 4.29. The Tauc plots were used to estimate the energy band gaps of the nanoparticles. The estimated energy band gaps are 3.44, 3.93, 4.04 and 3.94 eV for CuS-PP, CuS-DBA, CuS-NMB and CuS-DA respectively. The estimated band gaps of the copper sulphide nanoparticles are much higher when compared to the copper sulphide band gap energy of the bulk which is 1.2 eV as reported [25]. These band gap energies are higher due to the shift of the absorbance peak to a smaller wavelength leading to an increase in the confinement energy caused by an increase in the energy band gap of the nanoparticles showing the decrease in the size of these particles [26].

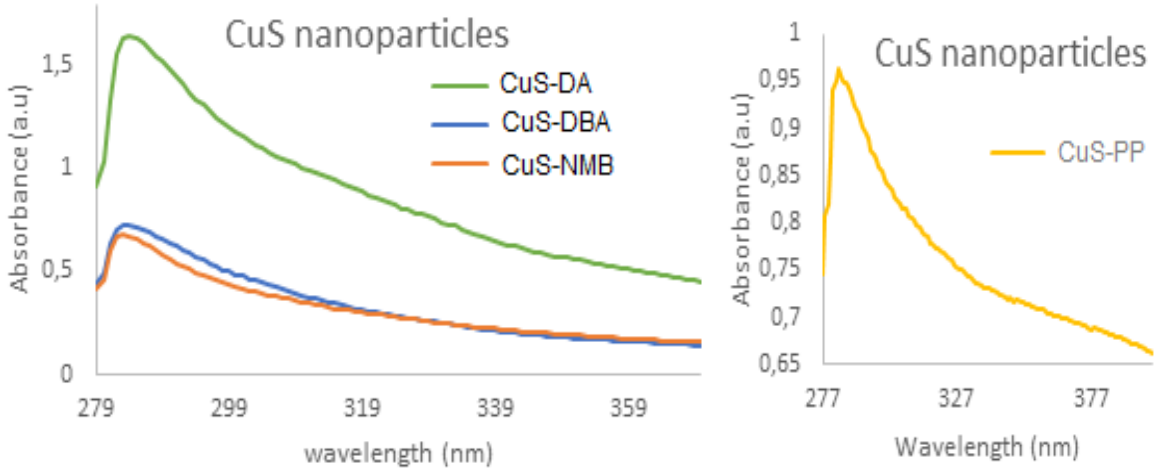

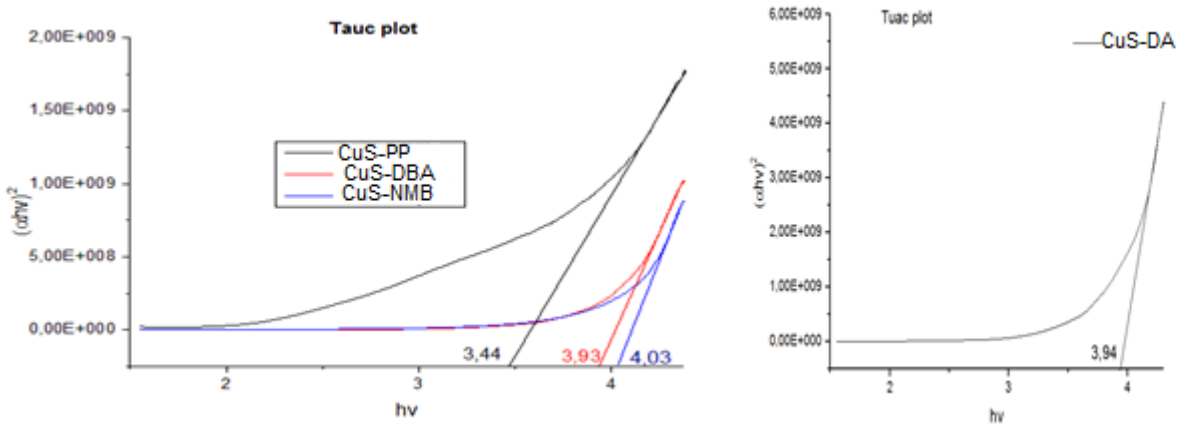

Figure 4. 29 Overlay UV-Vis spectra and Tauc plot of the copper sulphide nanoparticles synthesized at 220°C from four different precursors

4.3.5.6. Emission studies of CuS-DBA, CuS-NMB, CuS-DA, CuS-PP nanoparticles

Figure 4.30 shows the fluorescence spectra of the copper sulphide nanoparticles. The spectra show the broad emissions with the emission maxima at 370, 377, 386 and 382 nm for CuS-PP, CuS-DBA, CuS-DA and CuS-NMB respectively. The emission bands have shifted to higher wavelengths as compared to the absorption bands, at 284 nm for all the four nanoparticles. Which may correspond to the intermolecular charge transfer of the molecule [27].

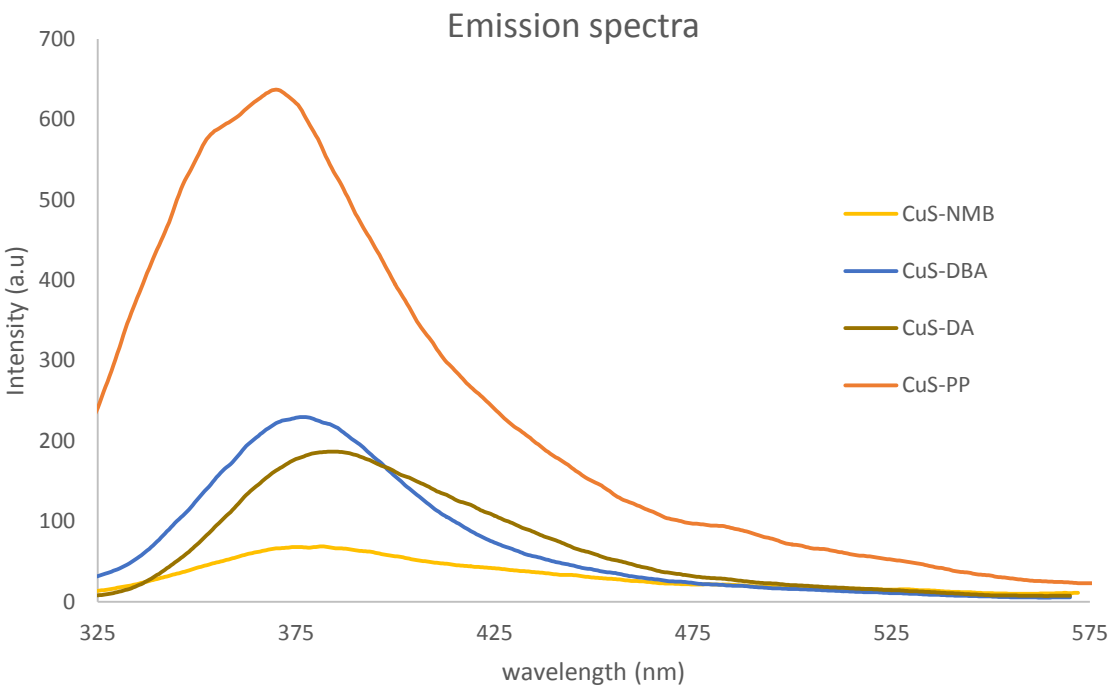

Figure 4. 30 Overlay Fluorescence spectra of the copper sulphide nanoparticles synthesized at 220°C from four different precursors.

4.4. Structural and optical studies of silver sulphide nanoparticle synthesized at 120, 180 and 220°C

4.4.1. Structural and optical studies of AgS-P nanoparticles synthesized from silver(I) piperidine DTC complex

4.4.1.1. Powder X-ray diffraction patterns of AgS-P nanoparticles

Figure 4.31 shows the overlay p-XRD patterns of the AgS-P 120, AgS-P 180 and AgS-P 220 synthesized from silver(I) piperidine dithiocarbamate complex at 120°C, 180°C and 220°C respectively. When the precursor was thermolyzed at 120°C, sharp diffraction peaks correspond to (-121), (013), (-104), (031), (-202), (023), (-214) and (-224) were observed. These sharp peaks suggest the nanoparticles to be crystalline. When the synthesis was done at 220°C and at 180°C the patterns gave the same peaks at the same angles that were indexed in the literature [36]. Their broad peaks were indexed to (-121), (013), (-104), (031), (-202), (023), (-214) and (224) showing the nanoparticles to be crystalline. The phase of these nanoparticles was found to be acanthite $Ag_{1.93}S$ [32, 33].

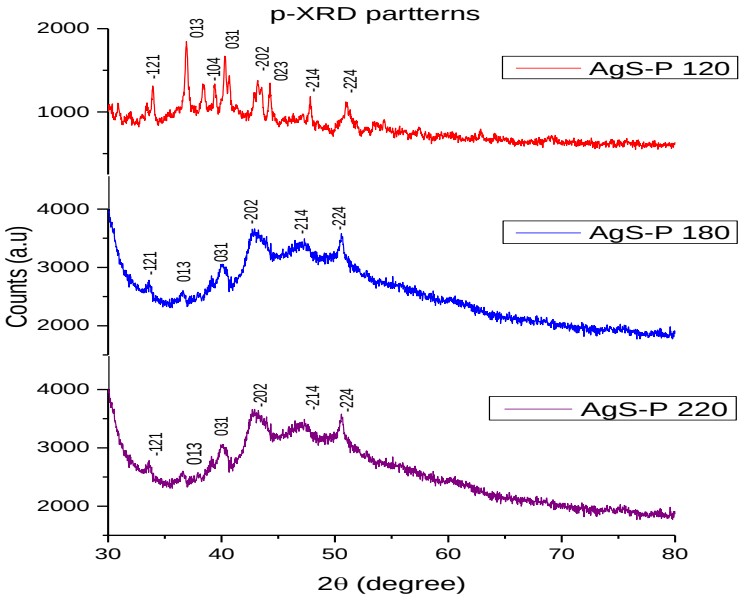

Figure 4. 31 P-XRD patterns of AgS-P nanoparticles synthesized at 120°C, 180°C and 220°C

4.4.1.2. Transmission electron microscopy studies of AgS-P nanoparticles

The TEM images of the silver sulphide nanoparticles (AgS-P) synthesized at different temperatures from silver(I) piperidine DTC complex as the precursor are shown in Figure 4.32. AgS-P synthesized at 220°C and 120°C gave narrow size ranges from 8.78 to 14.63 nm and 7.73 to 23.86 nm respectively whereas, AgS-P synthesized at 180°C gave a very wide range of size from the minimum size of 4.86 nm to the maximum size of 71.18 nm. The images show monodispersed nanoparticles with uniform shapes irrespective of the thermolysis temperature. No agglomeration is observed in all the three images.

The SAED patterns of AgS-P at 220°C and the HRTEM image with d-spacing measurements are presented besides the TEM images of AgS-P 220. The SAED patterns shows three visible rings with bright spots confirming the crystallinity of these nanoparticles. The measured distance from the lattice fringes is 0.24 nm which corresponds with the d-spacing found in the literature [28].

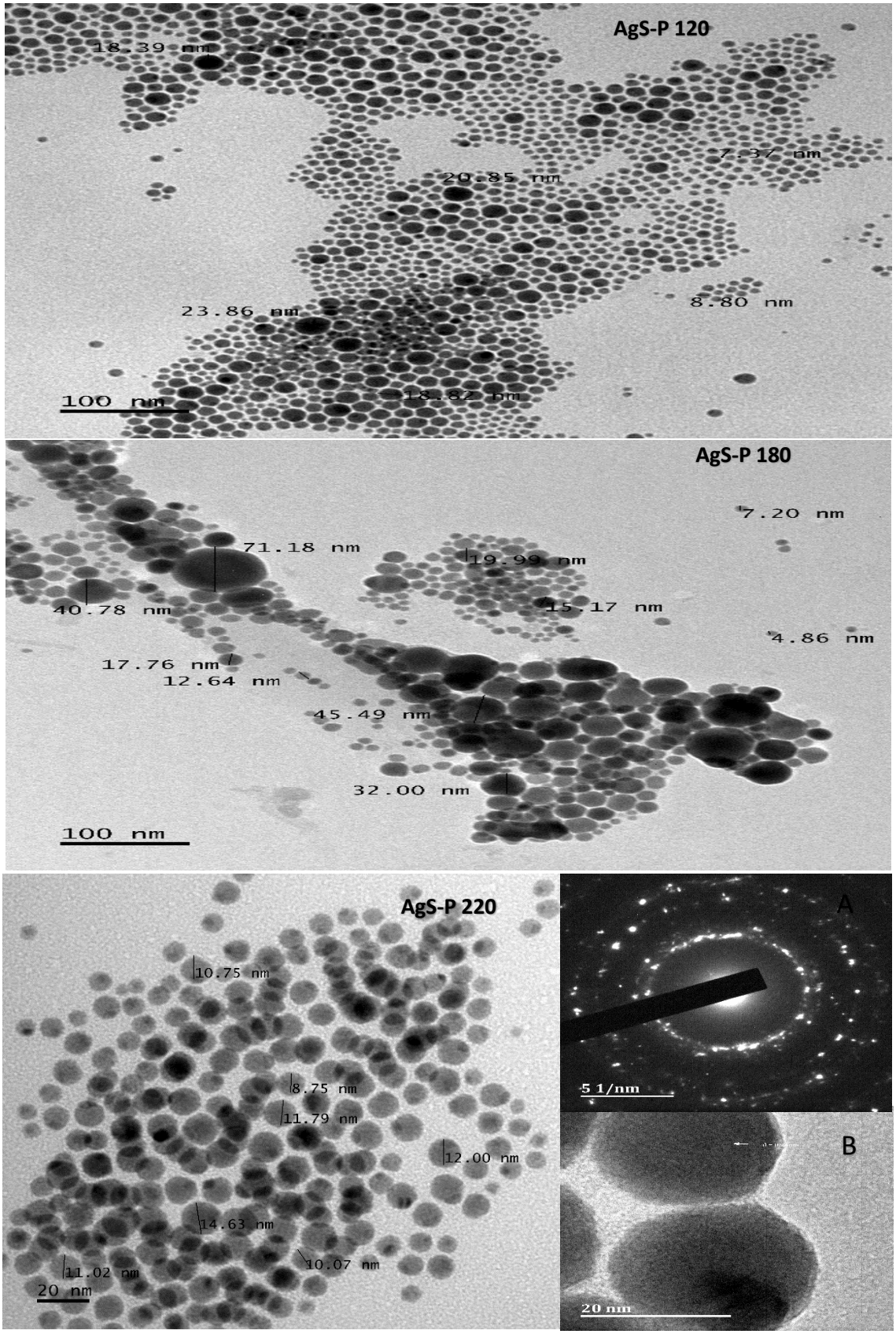

Figure 4. 32 TEM images of AgS-P nanoparticles synthesized at 120, 180 and 220°C and A. SAED and B. lattice fringes of AgS-P 220.

4.4.1.3. Scanning electron microscope studies of AgS-P nanoparticles

Figure 4.33 displays the SEM micrographs of the silver sulphide nanoparticles synthesized at 120, 180 and 220°C from silver(I) piperidine DTC complex (AgS-P). The SEM image of the nanoparticles surface when the precursor was thermolyzed at 120°C shows a surface morphology with disorganised rods. However, when the temperature was increased to 180°C the surface morphology changed to solid layers while the SEM images of the nanoparticles when thermolysis of precursor was done at 220°C showed fibre like surface morphology.

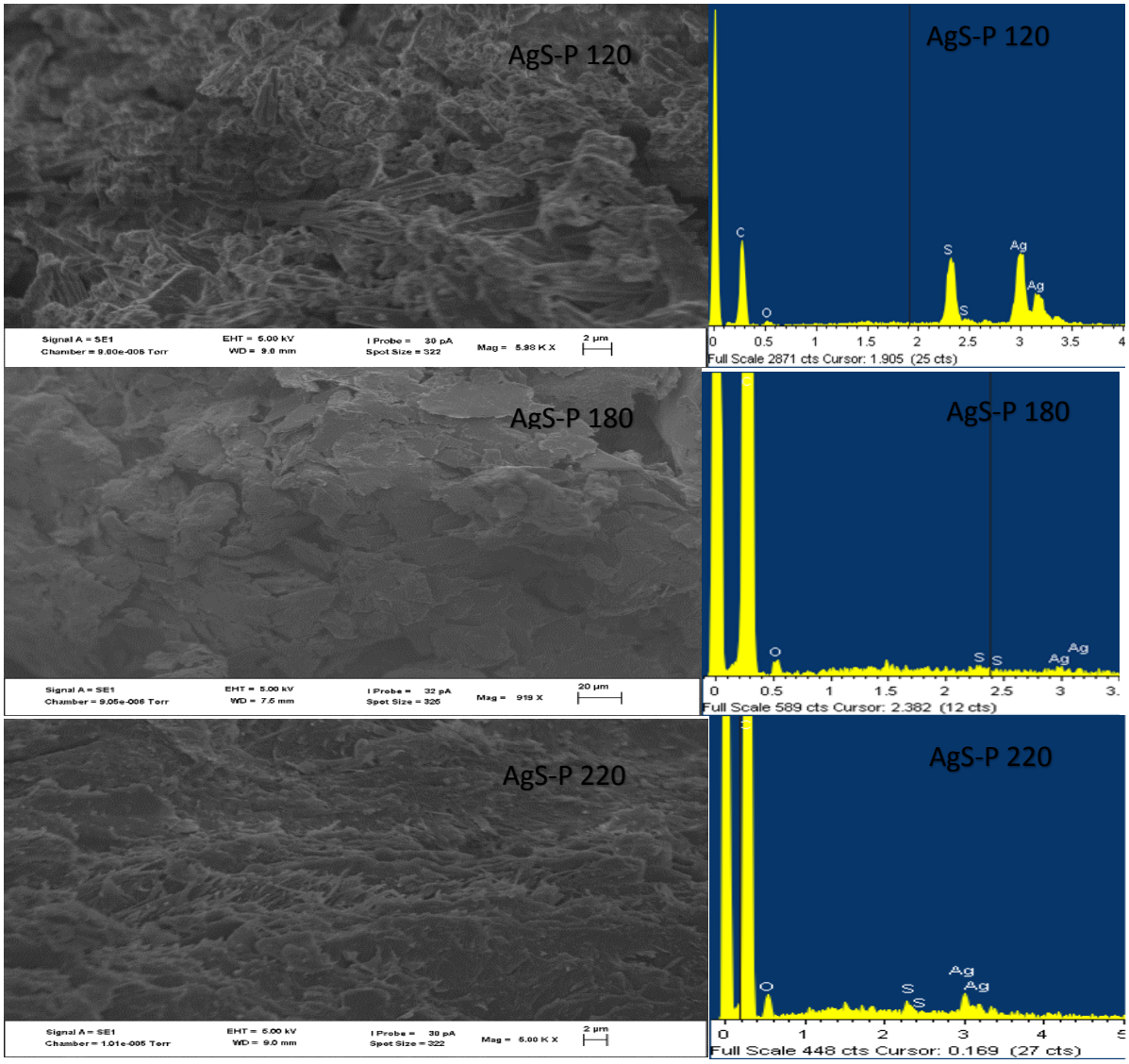

Figure 4. 33 SEM micrographs and EDX spectra of AgS-P nanoparticles synthesized at 120°C, 180°C and 220°C.

4.4.1.4. FTIR spectra of silver sulphide nanoparticles synthesized from silver(I) piperidine DTC complex

The over lay spectra of the silver sulphide nanoparticles synthesized at 120°C, 180°C and 220°C and the stabilizers used are displayed in Figure 4.34. The spectra of the nanoparticles are compared with the spectra of both the oleylamine and oleic acid that were used in the synthesis. The spectra of the nanoparticles showed all the peaks observed in the spectra of the pure oleic acid thereby confirming the presence of the oleic acid on the surface of the particles synthesized. The nanoparticles also showed the C-H bending modes from 1600 cm^{-1} to 1400 cm^{-1} as the evidence of the alkyl chain from the oleic acid. The peak observed at around 1700 cm^{-1} is attributed to the carboxylic acid (C=O) stretching mode in the oleic acid indicating the existence of oleic acid on the nanoparticles [17].

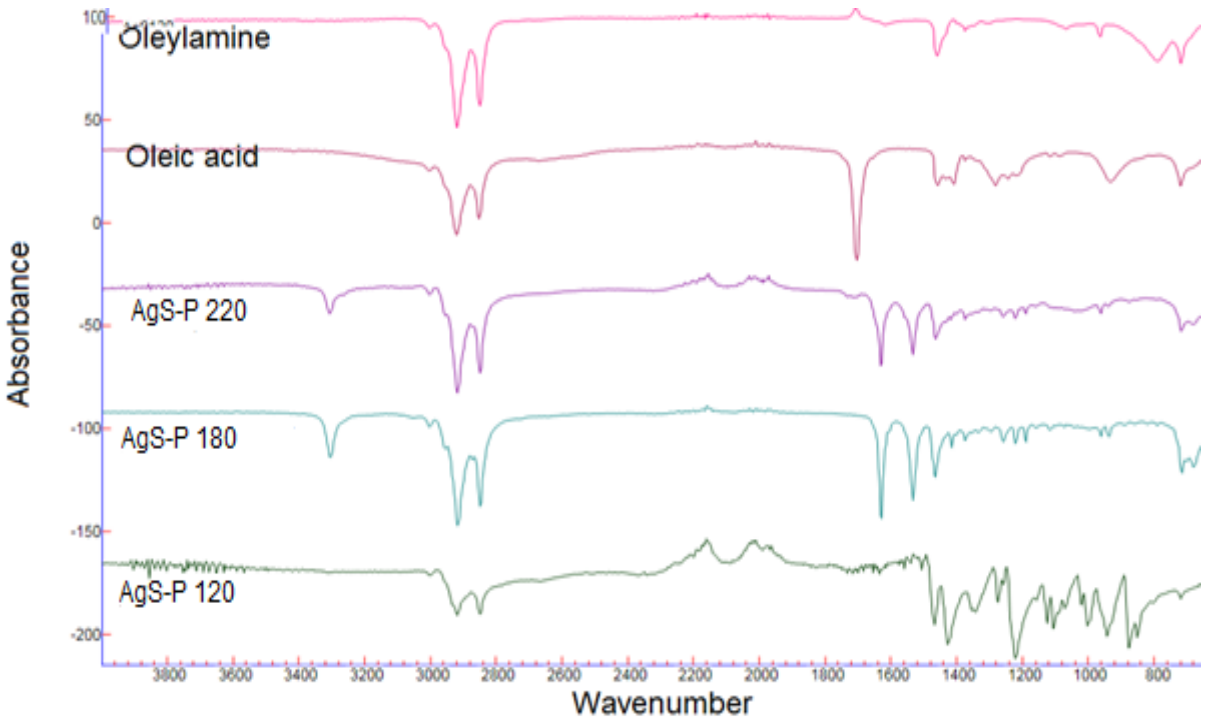

Figure 4. 34 Overlay FTIR spectra of AgS-P nanoparticles synthesized 120°C, 180°C and 220°C.

4.4.1.5. Absorption studies of AgS-P nanoparticles

The overlay spectra of the UV-Visible spectra of the nanoparticles prepared at different temperatures from silver(I)piperidine DTC complex as a precursor are displayed in Figure 4.35 with the corresponding Tauc plots obtained from the absorption spectra. The Tauc's equation was used to determine the energy band gap of the silver sulphide nanoparticles directly from the absorption spectra. The absorption spectra of AgS-P nanoparticles synthesized at 120, 180 and 220°C gave band energy gap values 3.48, 3.22 and 2.51 eV from the Tauc plots respectively. When these values were compared to the bulk band gap energy of 0.9 eV as reported in the literature [29], they showed blueshift which is attributed to the small size of the nanoparticle.

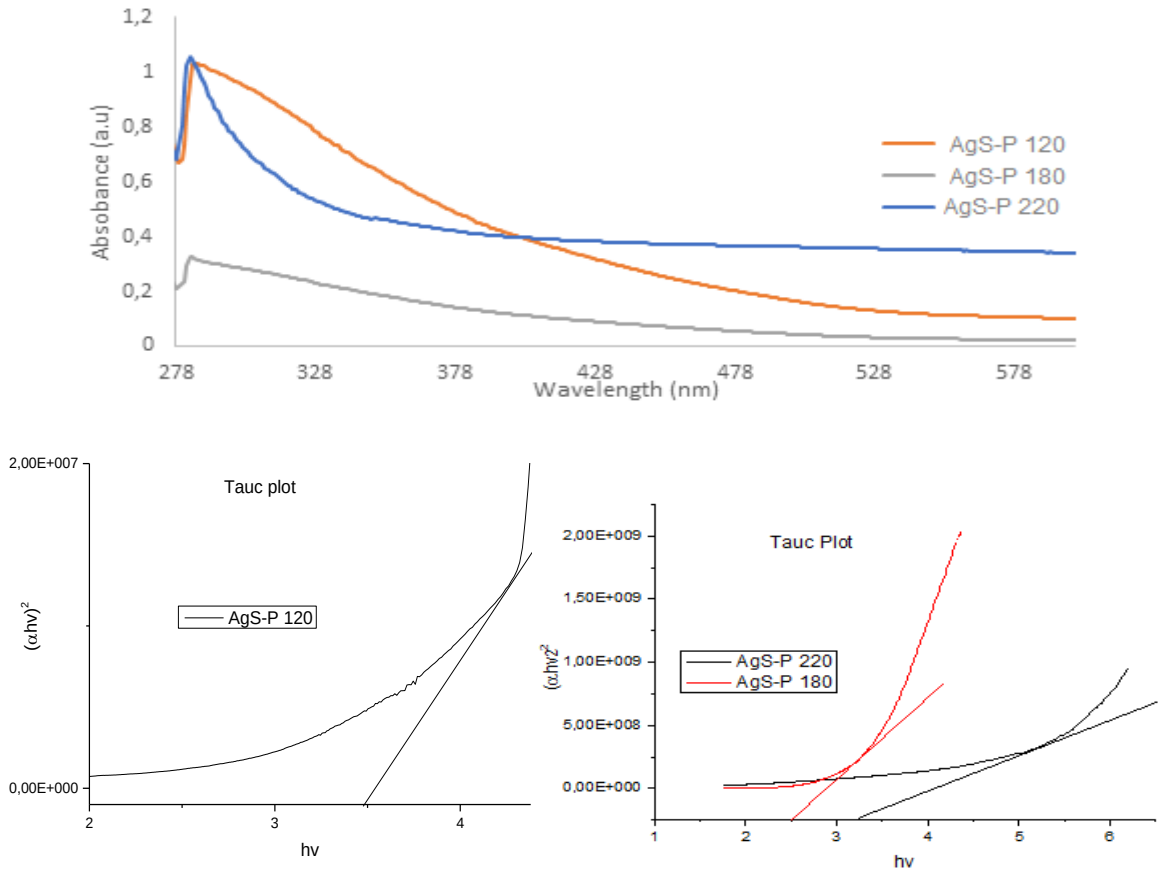

Figure 4. 35 overlay UV-Vis spectra and Tauc plots of AgS-P nanoparticles synthesized at 120°C, 180°C and 220°C

4.4.1.6. Emission studies of AgS-P nanoparticles

The Emission spectra of AgS-P synthesized at different temperatures are presented in Figure 4.36. The emission maxima of the nanoparticles were compared to the absorption wavelength from the UV-Vis absorption spectra in Figure 4.34. The nanoparticles AgS-P 120, AgS-P 180 and AgS-P 220 emitted at 445, 310 and 380 nm wavelengths and absorbed at 286, 285 and 285 nm respectively. This showed the red shift of the emission maxima wavelengths in comparison to the absorption wavelengths.

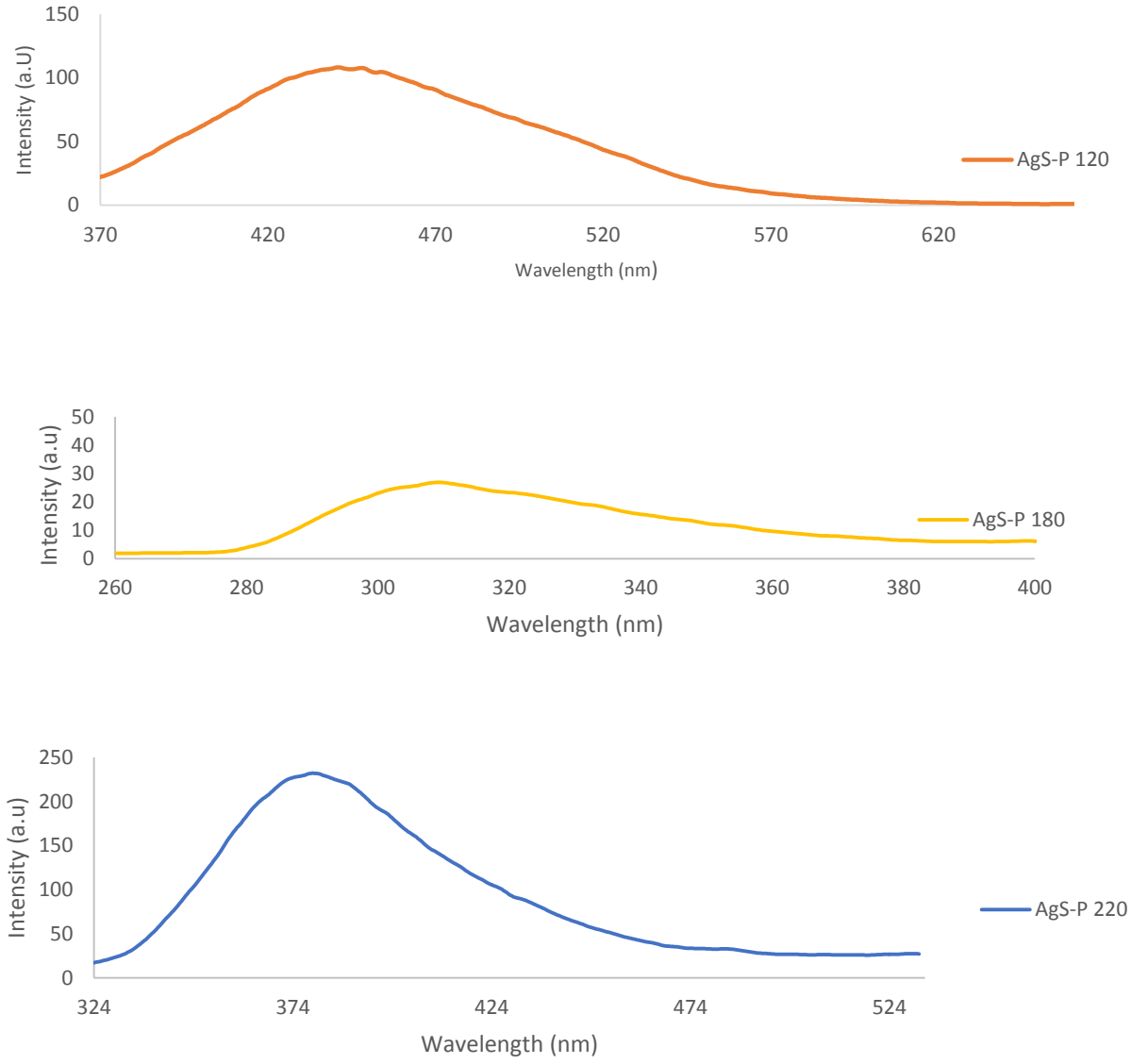

Figure 4. 36 Photoluminescence spectra of AgS-P synthesized at 120°C, 180°C and 220°C.

4.4.2. Structural and optical studies of AgS-M synthesized from silver(I) morpholine DTC complex

4.4.2.1. Powder X-Ray diffraction patterns of AgS-M nanoparticles

The overlay XRD patterns of the AgS-M synthesized at three different temperatures is displayed in Figure 4.37. The nanoparticles synthesized at 220°C and at 120°C gave similar patterns with the same angles that were indexed to literature values. Their peaks were indexed to (-121), (013), (-104), (031), (-202), (-212), (-214), (014), (224), (-142), (-135), (133) and (-227). When the precursor was thermolyzed at 180°C the patterns gave peaks that corresponded to (-121), (013), (031), (-202), (-214) and (014). AgS-M 220 and AgS-M 120 showed to be more crystalline as the patterns gave sharp peaks. However, the AgS-M 180 nanoparticles to be amorphous. The phase of these nanoparticles was found to be acanthite $Ag_{1.93}S$ [32, 33].

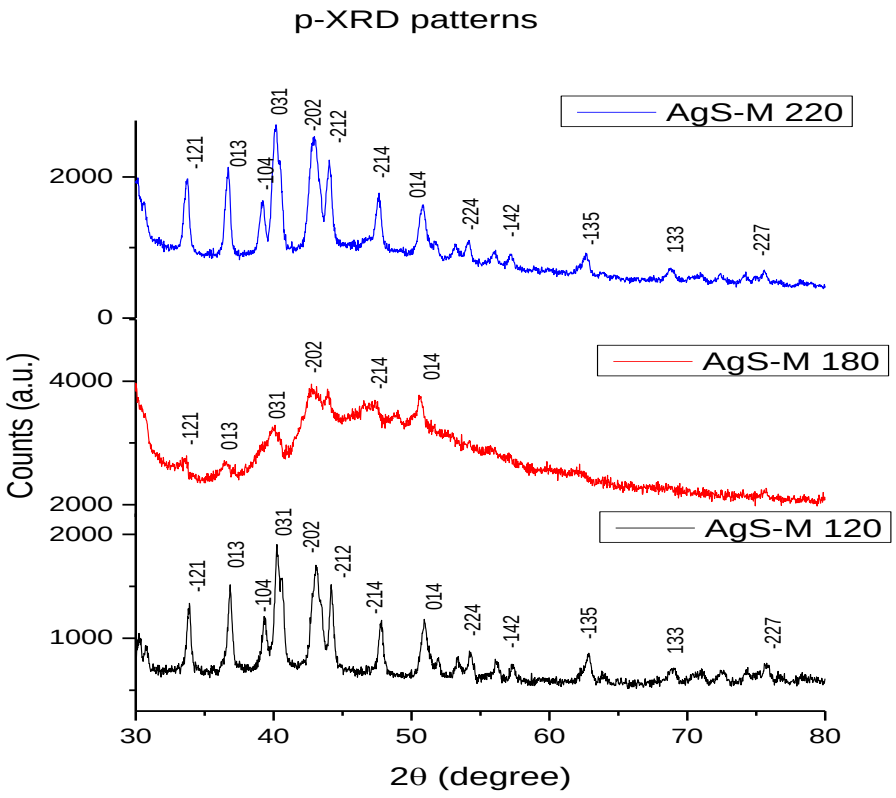

Figure 4. 37. p-XRD patterns of AgS-M nanoparticles synthesized at 120, 180 and 220°C.

4.4.2.2. Transmission electron microscopy studies of AgS-M nanoparticles

According to the TEM images of AgS-M shown in Figure 4.38, when the precursor was thermolyzed at 120°C the size of the nanoparticles ranged from 16.33 - 24.79 nm. At 220°C and 180°C, the nanoparticles seemed to have wide size distribution range as they gave nanoparticles with the size ranging from 12.43 to 61.09 nm and 24.79 to 89.62 nm respectively. They all showed the same uniform spherical shapes with no agglomeration. SAED patterns of AgS-M 220 shows that the nanoparticles are crystalline by the bright ring spots. The lattice fringes d- spacing is within 0.22 - 0.24 nm.

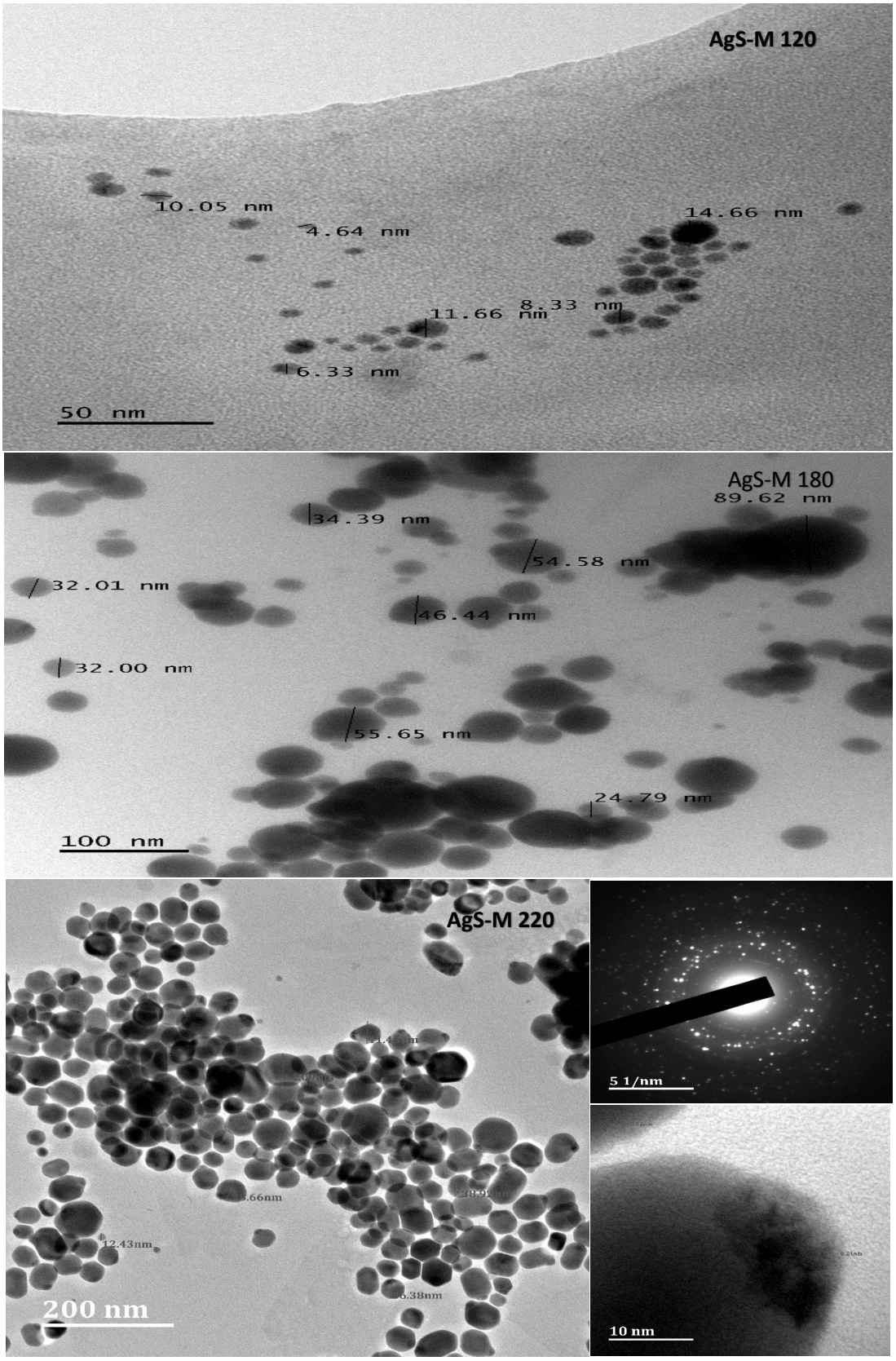

Figure 4. 38 TEM images of AgS-M nanoparticles synthesized at 120, 180 and 220°C. SAED and d-lattice of AgS-M 220.

4.4.2.3. Scanning electron microscope studies of AgS-M nanoparticles

The SEM micrographs taken for the AgS-M nanoparticles synthesized at 120, 180 and 220°C and the EDX analysis on their selected areas are shown in Figure 4.39. The images showed the surface of the nanoparticles to be rough. When the precursor was thermolyzed at 220°C the image exhibits solid rough surface and when thermolyzed at 180°C shows a very rough surface with cracks on it. Whereas, at 120, the surface made up of micro layers. The EDX spectra shows the presence of silver and sulphur in the nanoparticles.

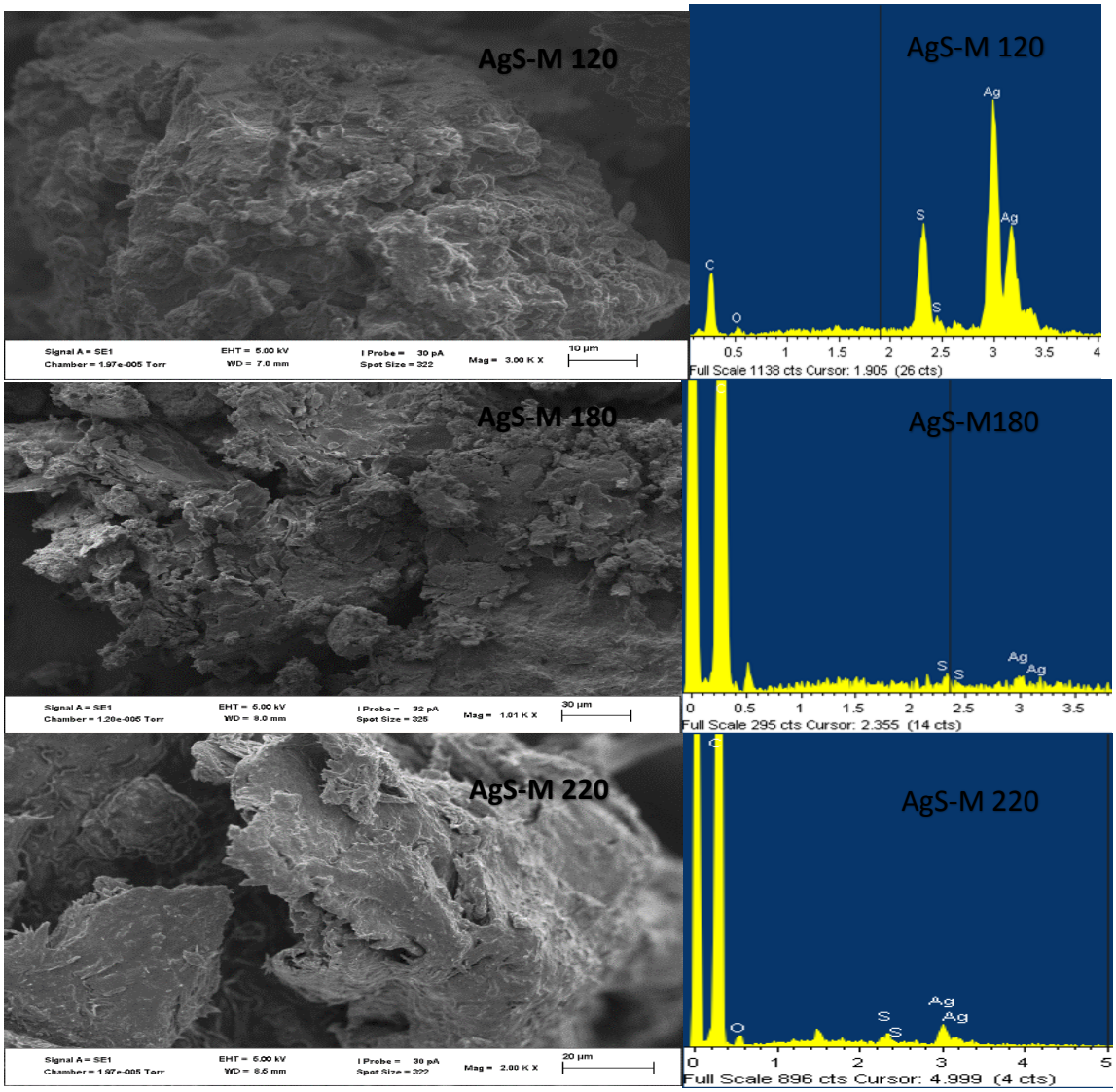

Figure 4. 39 SEM micrographs and EDX spectra of the AgS-M nanoparticles synthesized at 120, 180 and 220°C.

4.4.2.4. Fourier transform infrared spectroscopy studies of AgS-M nanoparticles

The overlay spectra of the AgS-M nanoparticles synthesized from silver(I) morpholine DTC complex at 120, 180 and 220°C and the capping agents used for their synthesis are displayed in Figure 4.40. Comparing the spectra of the nanoparticles with the spectra of both the capping agents, the spectra of the AgS nanoparticles showed all the peaks that are found in the spectrum of the pure oleic acid suggesting the interaction of the oleic acid with the surface of the nanoparticles synthesized. The nanoparticles showed the C-H bending modes in the range 1600 to 1400 cm^{-1} signifying the presence of the oleic acid alky chain. The C=O stretching mode is observed around 1700 cm^{-1} corresponding to the carboxylic acid in the oleic acid [17]. Even though the peaks are not that visible in the spectra of AgS synthesized at 120°C they are there but with very low intensity.

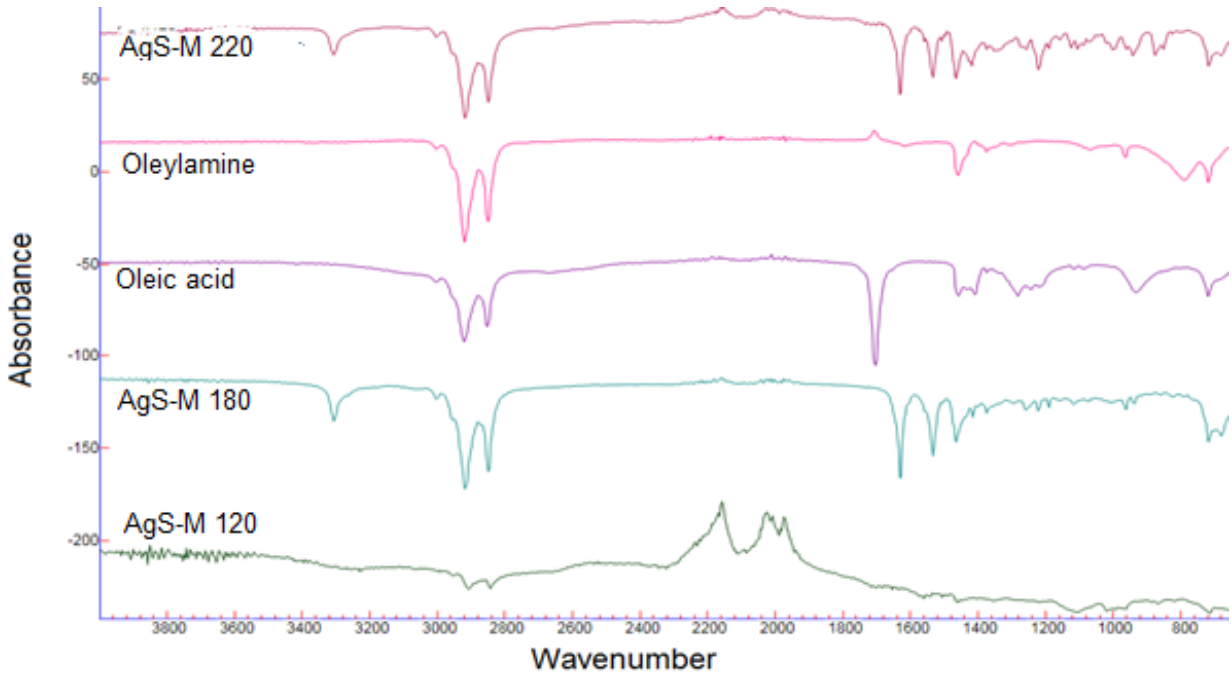

Figure 4. 40 Overlay FTIR spectra of AgS-M nanoparticles synthesized at 120, 180 and 220°C.

4.4.2.5. Absorption studies of AgS-M nanoparticles

The overlay UV-Visible absorption spectra of AgS-M at 120, 180 and 220°C is presented in Figure 4.41 with their respective Tauc plots. The UV-Vis spectra were used to estimate band gap energy from the Tauc plots. The estimated band gap energy of AgS-M nanoparticles are 2.4, 2.3 and 2.6 eV for the particles synthesized at 120, 180 and 220°C respectively. The band gap energies were therefore compared to the band gap energy of AgS bulk which is 0.9 eV. The obtained values were greater than that of the bulk and that shows the energy band gap of the nanoparticles are blue shifted with respect to the bulk which may be due to the exciton confinement [30].

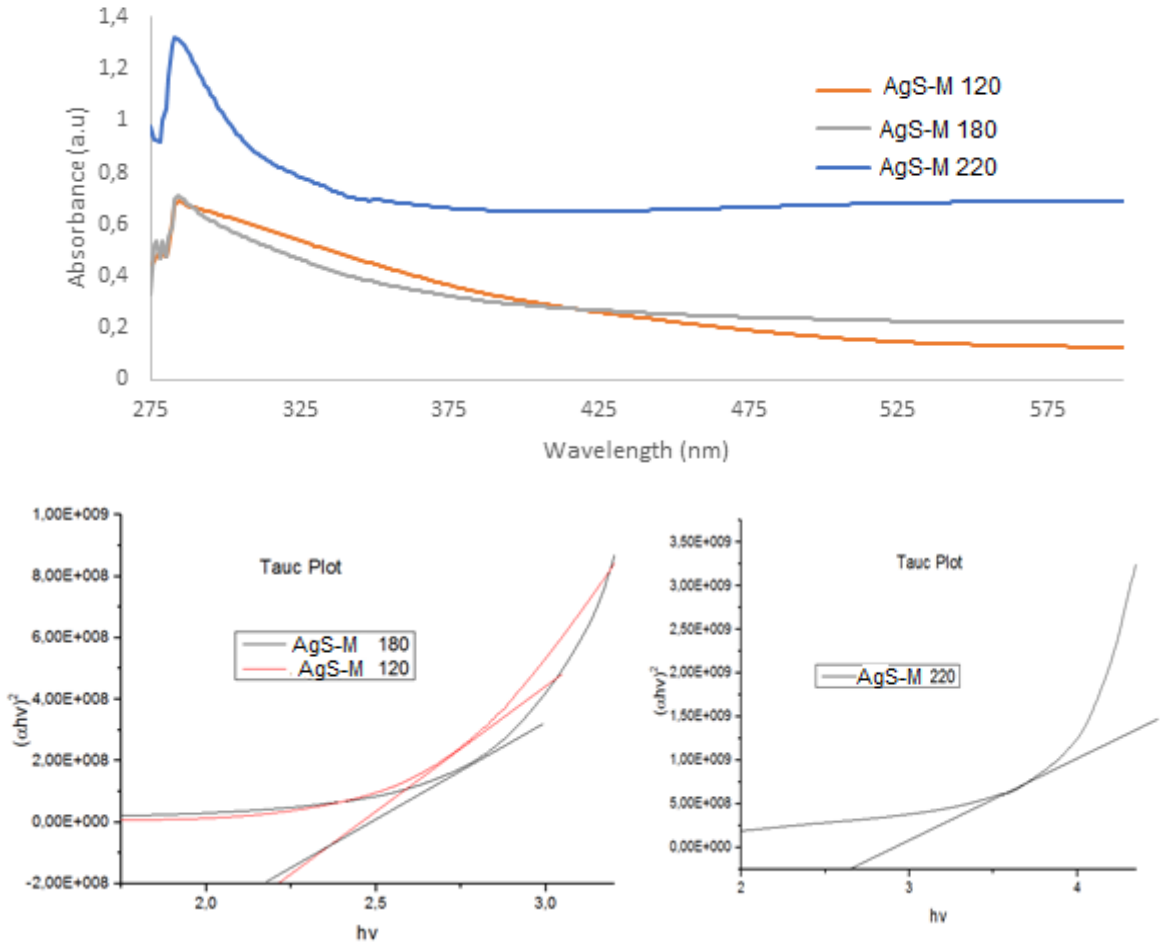

Figure 4. 41 Overlay UV-Vis spectra and Tauc plots of AgS-M synthesized 120, 180 and 220°C.

4.4.2.6. Emission studies of AgS-M nanoparticles

Figure 4.42 shows the emission spectra of AgS-M synthesized at 120, 180 and 220°C. The spectra shows broad emission maxima with wide size distributions. It was observed that the emission spectra became wider as the temperature increases. The emission maxima for the nanoparticles are observed at 380, 312 and 489 nm for the nanoparticles synthesized at 120, 180 and 220°C respectively. The emission maxima were to be red shifted when compared to the absorption band edges.

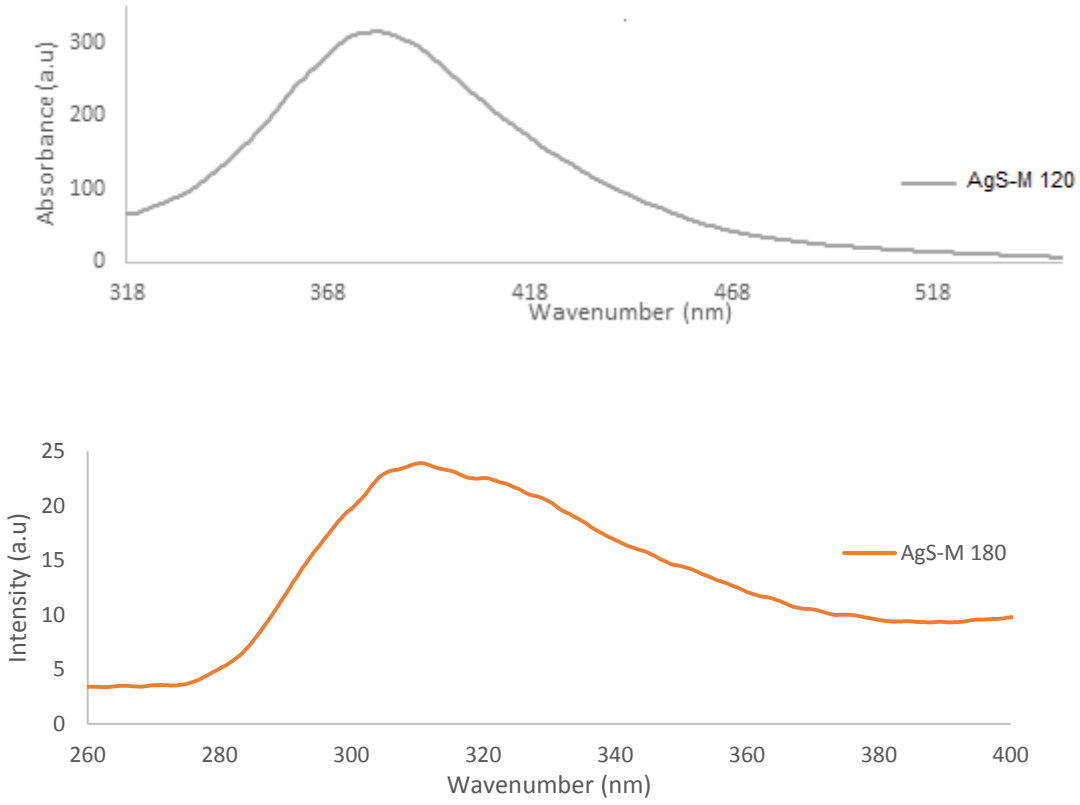

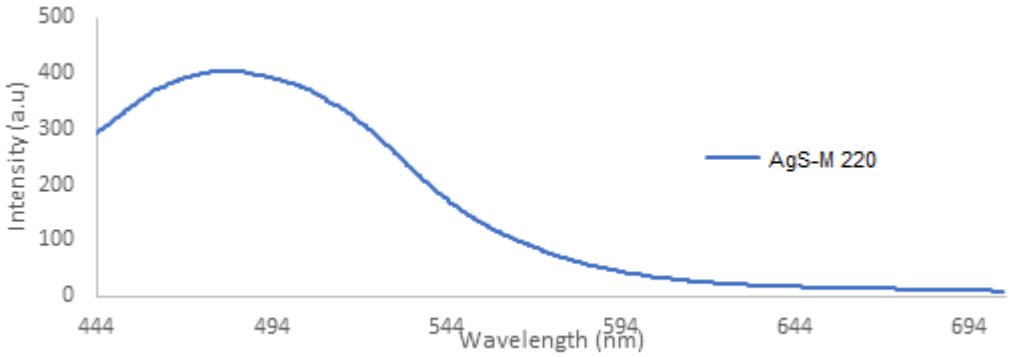

Figure 4. 42 Photoluminescence spectra of AgS-M nanoparticles synthesized at 120, 180 and 220°C.

4.4.3. Structural and optical studies of AgS-NEA synthesized from silver(I) N-ethyl aniline DTC complex

4.4.3.1. Powder X-ray diffraction patterns of AgS-NEA nanoparticles

Figure 4.43 shows the overlay spectra of the powder X-ray diffraction patterns of the silver sulphide nanoparticles synthesized at three different temperatures. The XRD pattern peaks were indexed according to the literature [36]. The nanoparticles synthesized at 120°C corresponded to (-121), (013), (031), (-202), (-214) and (-224) miller indices. The peaks of the nanoparticles synthesized at 180 and 220°C corresponded to (202), (214), (224) and (013), (031), (224) miller indices respectively. The phase of the particles was determined to be Acanthite $Ag_{1.93}S$ crystalline phase with the space group $P2_1/c$ [32, 33].

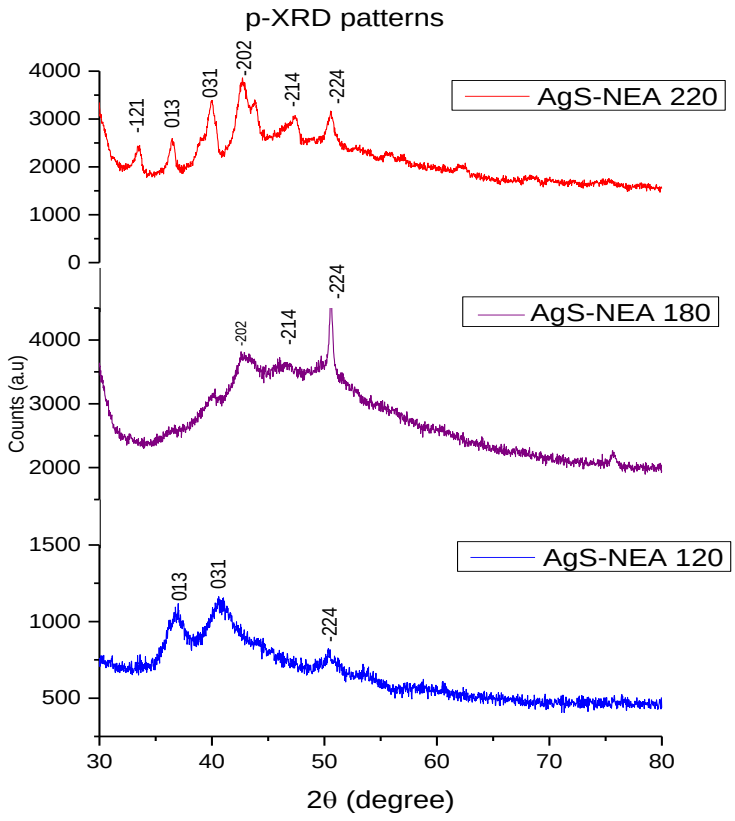

Figure 4. 43. p-XRD patterns of AgS-NEA nanoparticles synthesized at 120, 180 and 220°C.

4.4.3.2. Transmission electron microscopy studies of AgS-NEA nanoparticles

AgS-NEA TEM images shows nanoparticles that are below 20 nm in size irrespective of thermolysis temperature of the reaction. At the highest temperature, 220°C, their size ranged from 11.93 to 19.10 nm. Nanoparticles of diameters ranging from 5.6 to 16.87 nm and 2.43 to 7.40 nm were obtained at 180 and 120°C. It was observed that the lower the temperature the smaller the particle sizes. All TEM images showed monodispersed nanoparticles with uniform spherical shapes with no trace of agglomeration is observed. The SAED patterns recorded for the AgS-NEA 220 nanoparticles shows tiny ring spots obscured by amorphous materials probably from the capping agents. The AgS-NEA 220 lattice fringes also were 0.22 - 0.24 nm.

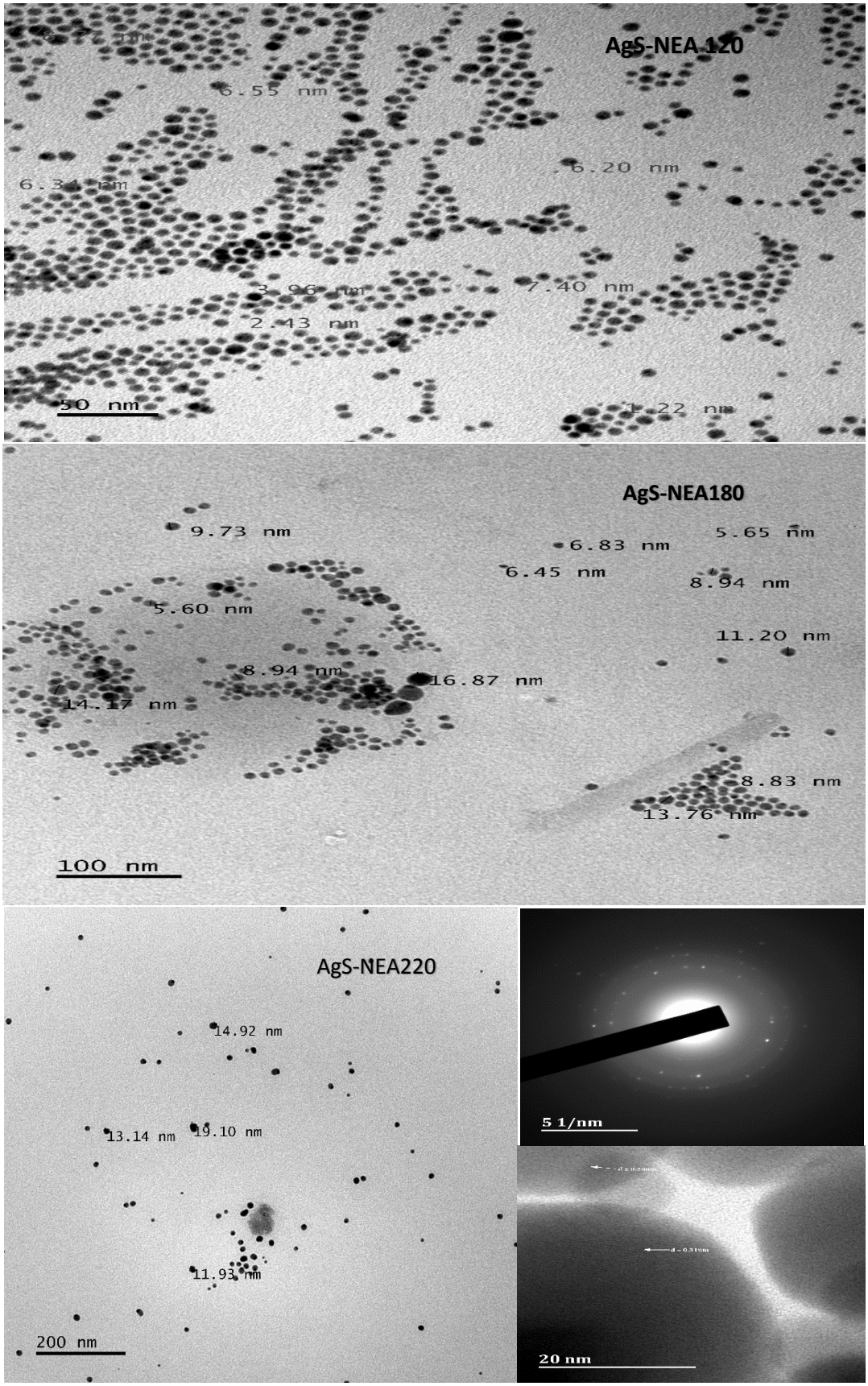

Figure 4. 44 TEM images of AgS-NEA nanoparticles synthesized at 120, 180 and 220°C. SAED and d-lattice of AgS-NEA 220.

4.4.3.3. Scanning electron microscope studies of AgS-NEA nanoparticles

The SEM micrographs of AgS-NEA used to study the surface morphology of the nanoparticles are presented in Figure 4.45. When the synthesis was done at 120°C, the image showed the particles to have a very smooth surface morphology. However, when the nanoparticles were obtained at 180°C, the nanoparticles exhibited peeling off like surface. Surface morphology made up of fibres packed into layers was observed from the AgS-NEA synthesized at 220°C. The observations confirm the influence of temperature of the reaction on the surface morphology of the as-prepared nanoparticles. The EDX spectra showed the presence of silver and sulphur in the nanoparticles.

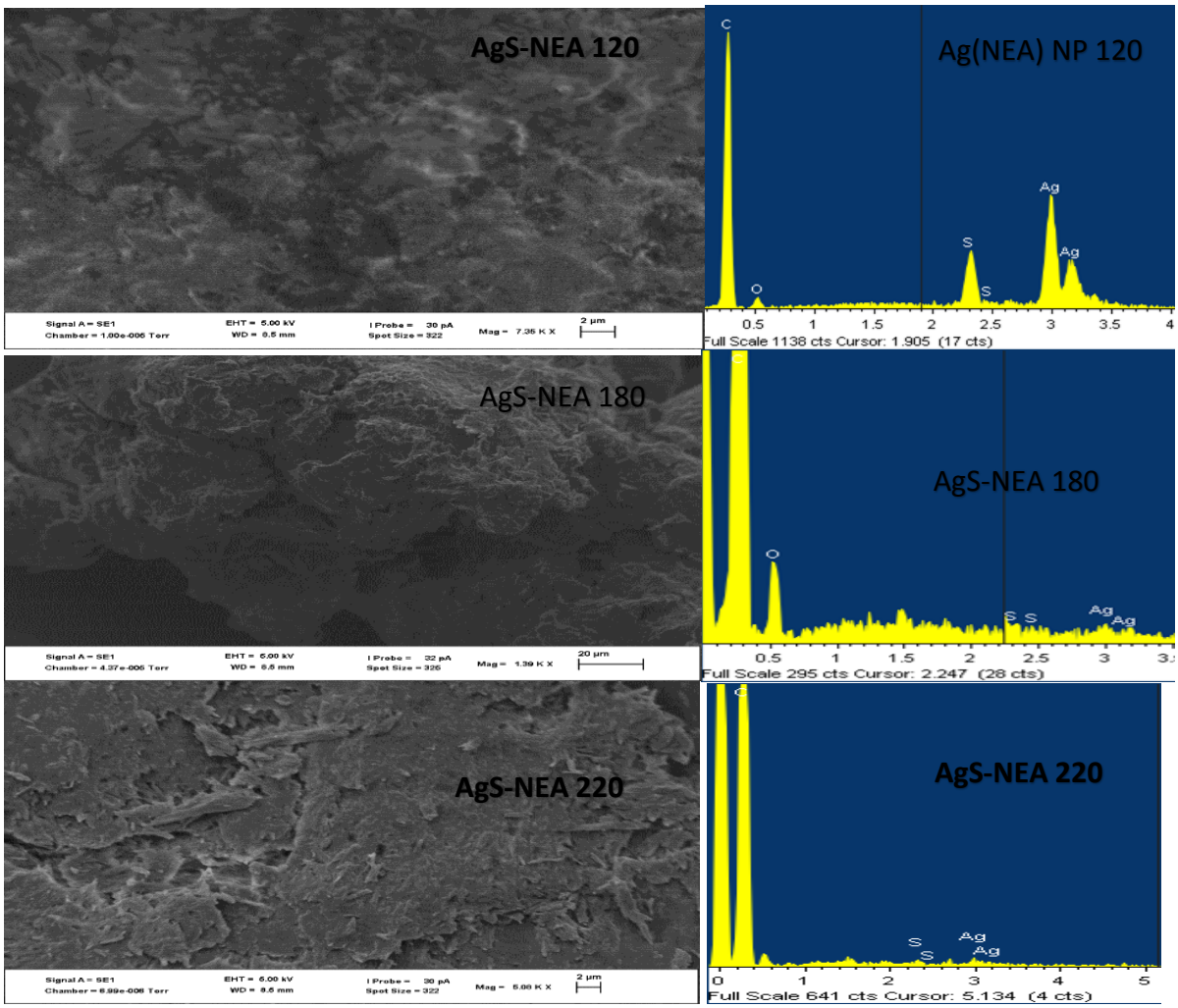

Figure 4. 45 SEM micrographs and EDX spectra of AgS-NEA nanoparticles synthesized at 120, 180 and 220°C.

4.4.3.4. FTIR spectra of AgS-NEA nanoparticles synthesized from silver(I) N-ethyl aniline DTC complex

Figure 4.46 shows the FTIR spectra of the nanoparticles synthesized from silver(I)N-ethyl aniline DTC complex. The spectra of the nanoparticles compared with the spectra of the capping agents used for the synthesis of the nanoparticles. The spectra of pure oleic acid show the C-H and C=H bending modes from 1600 to 1400 cm^{-1} of the alkyl chain and C=O stretching mode at 1700 cm^{-1} from the carboxylic acid [17]. These vibrations were all observed also in the spectra of the nanoparticles. Therefore, Oleic acid has bonded to the nanoparticles surface.

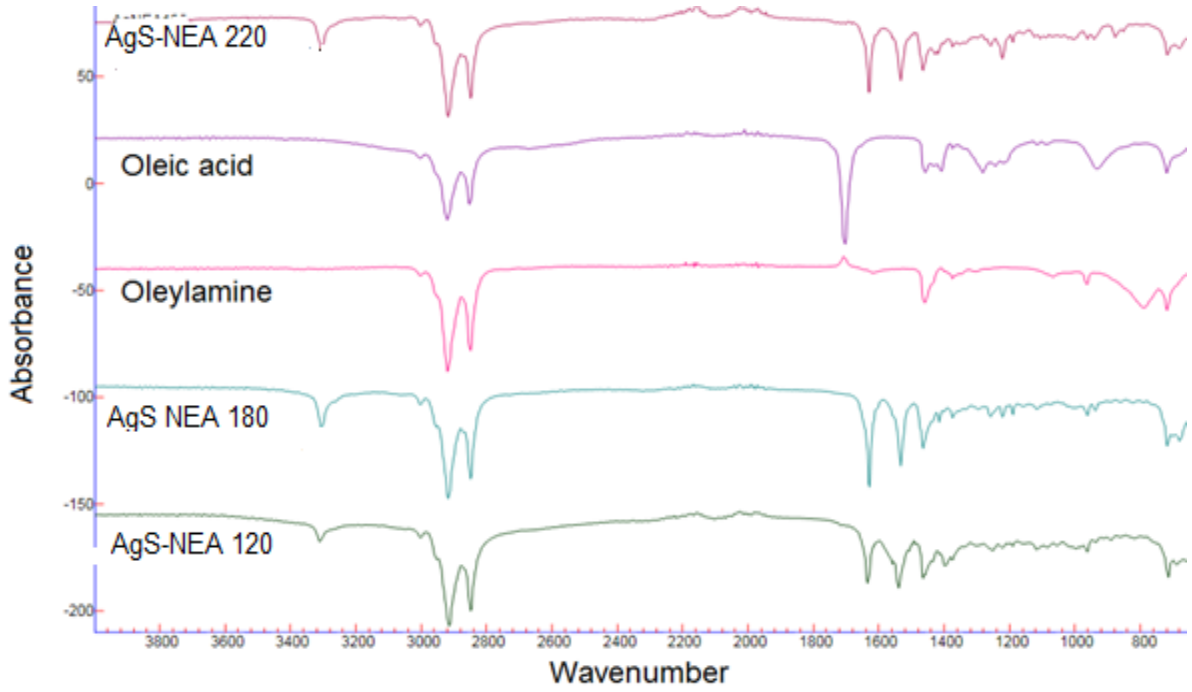

Figure 4. 46 Overlay FTIR spectra of AgS-NEA nanoparticles synthesized at 120, 180 and 220°C.

4.4.3.5. Absorption studies of AgS-NEA nanoparticles

The absorption spectra of the AgS-NEA nanoparticles are displayed in Figure 4.47 with their respective Tauc plots. The Tauc plot was used to estimate the band gap energies of the nanoparticles. The band gap energies for AgS-NEA 120, AgS-NEA 180 and AgS-NEA 220 were found to be 2.0, 2.3 and 3.23 eV respectively, which are greater than 0.9 eV band gap energy of the bulk. The estimated band gap energies showed considerable blue shift which is attributed to the smaller sized nanoparticles.

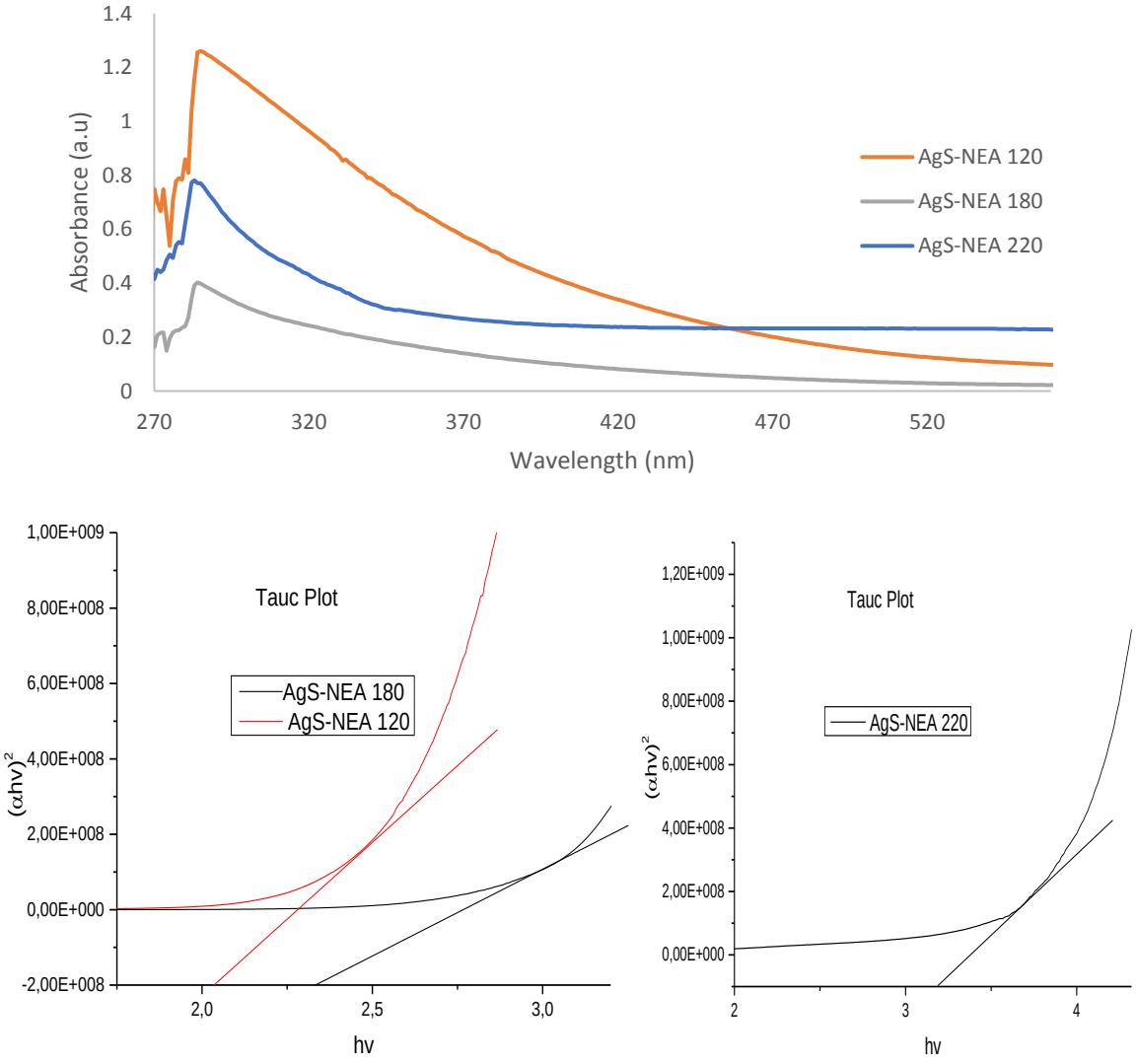

Figure 4. 47 Overlay UV-Vis spectra and Tauc plot of AgS-NEA nanoparticles synthesized at 120, 180 and 220°C.

4.4.3.6. Emission studies of AgS-NEA nanoparticles

Figure 4.48 shows the emission spectra of AgS-NEA nanoparticles synthesized at 120, 180 and 220°C. The emission maxima were compared to the absorption band edges. The emission wavelengths have shifted from 287, 286 and 284 nm absorption wavelengths to 341, 311 and 379 nm wavelengths for AgS-NEA 120, AgS-NEA 180 and AgS-NEA 220 respectively. The spectra showed intense red-shift that could be attributed to the trap related electron-hole recombination [31].

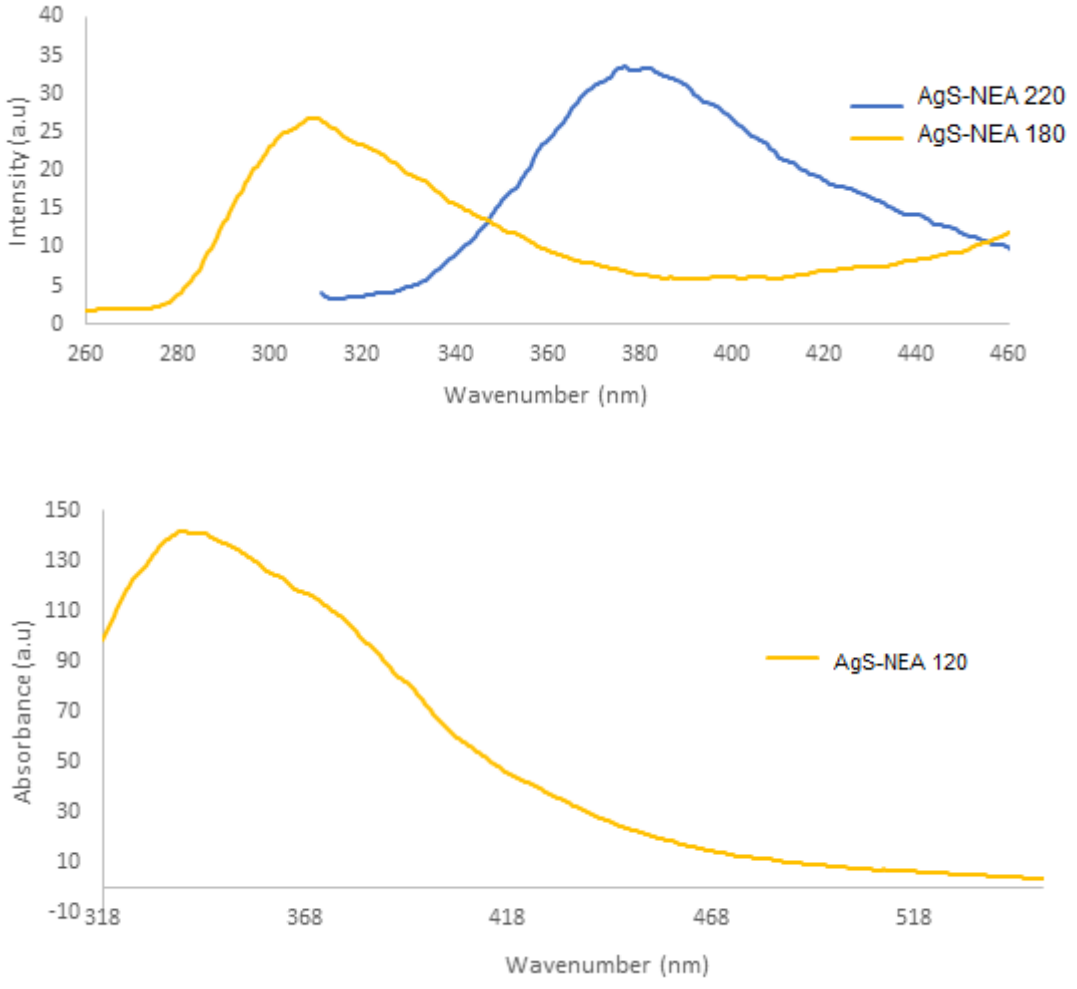

Figure 4. 48 Overlay photoluminescence spectra of AgS-NEA nanoparticles synthesized at 120, 180 and 220°C.

4.4.4. Structural and optical studies of AgS-BA synthesized from silver(I) butyl amine DTC complex

4.4.4.1. Powder X-Ray diffraction patterns of AgS-BA nanoparticles

The overlay spectra of the powder X-ray diffraction patterns of the silver sulphide nanoparticles synthesized from silver(I) butyl amine dithiocarbamate complex at three different temperatures are displayed in Figure 4.49. The peaks were indexed to (-121), (013), (031), (-202), (-212), (-214), (-224) and (-135) for nanoparticles synthesized at 120°C, (013), (031), (-202) and (-224) for the nanoparticles synthesized at 180°C and (013), (031), (-202), (-212), (-214), (-224) and (-135) for nanoparticles synthesized at 220°C respectively according to the literature [36]. The patterns were analysed by comparing them to the literature data. Acanthite $Ag_{1.93}S$ crystalline phase with the space group $P2_1/c$ was identified [32, 33].

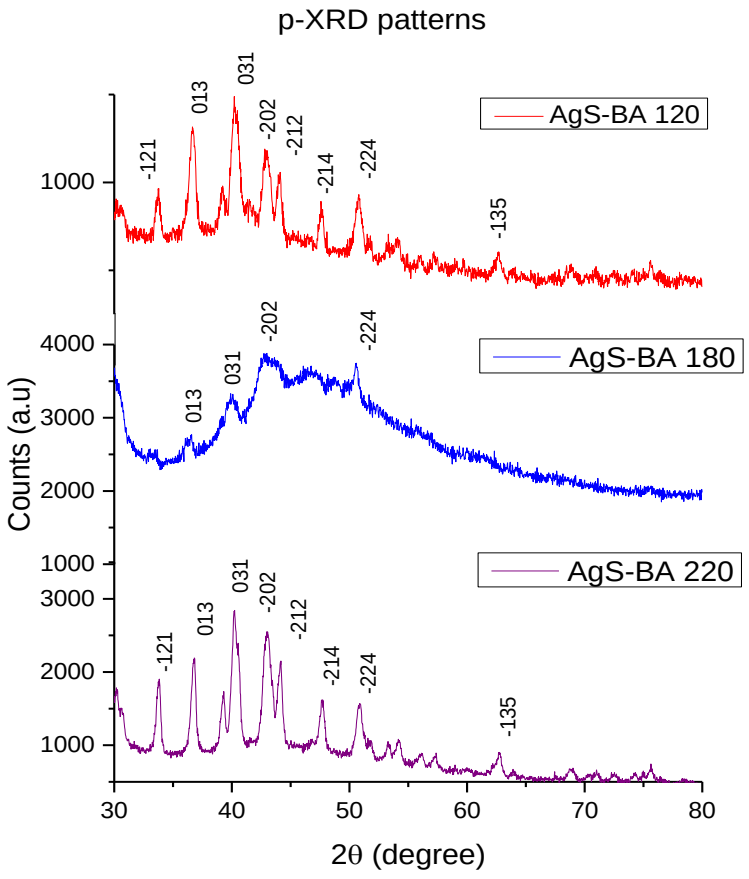

Figure 4. 49. p-XRD patterns of AgS-BA nanoparticles synthesized at 120, 180 and 220°C.

4.4.4.2. Transmission electron microscope studies of AgS-BA nanoparticles

Figure 4.50 shows the TEM images of AgS-BA nanoparticles synthesized at 120, 180 and 220°C. All the images showed uniform spherical shapes as well as size distribution. The TEM image of the nanoparticles synthesized at 120°C have crystallite size that ranged from 7.92 to 20.79 nm. However, when the synthesis was done at 180°C the size increased and ranged from 9.60 to 32.87 nm. The size range increased more when the precursor was thermolyzed at 220°C from 40.05 to 78.53 nm. SAED patterns were recorded for the AgS-BA 220°C, and showed the nanoparticles to be amorphous and not crystalline as there was no bright spots in the image except diffuse rings. The measured lattice fringes d-spacing is 0.24 nm.

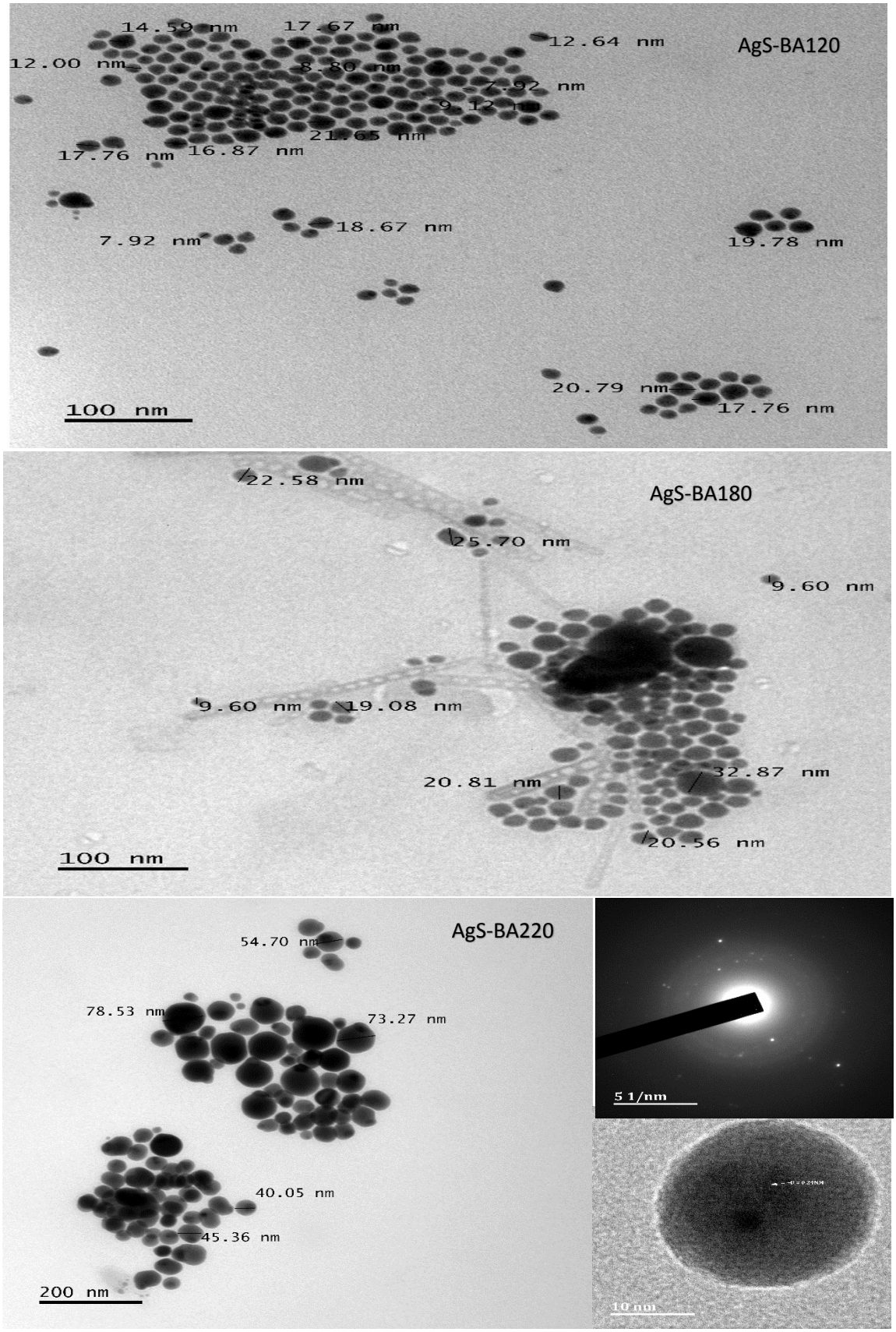

Figure 4. 50 TEM images of AgS-BA nanoparticles synthesized at 120, 180 and 220°C. SAED and d-lattice of AgS-BA 220

4.4.4.3. Scanning electron microscope studies of AgS-BA nanoparticles

The SEM micrographs of the silver sulphide nanoparticles synthesized and the EDX spectra showing elemental composition of the nanoparticles are shown in Figure 4.51. The nanoparticles images showed that thermolysis temperature influences the surface morphologies of the nanoparticles. AgS-BA gave nanoparticles with surface with clustered fibres when it was thermolyzed at 220°C. When this precursor was thermolyzed at 180°C the nanoparticles showed a flaky surface morphology. However, when synthesized at a low temperature of 120°C, the surface appeared out smooth. The EDX spectra of the nanoparticles showed that silver and sulphur are present in the nanoparticles.

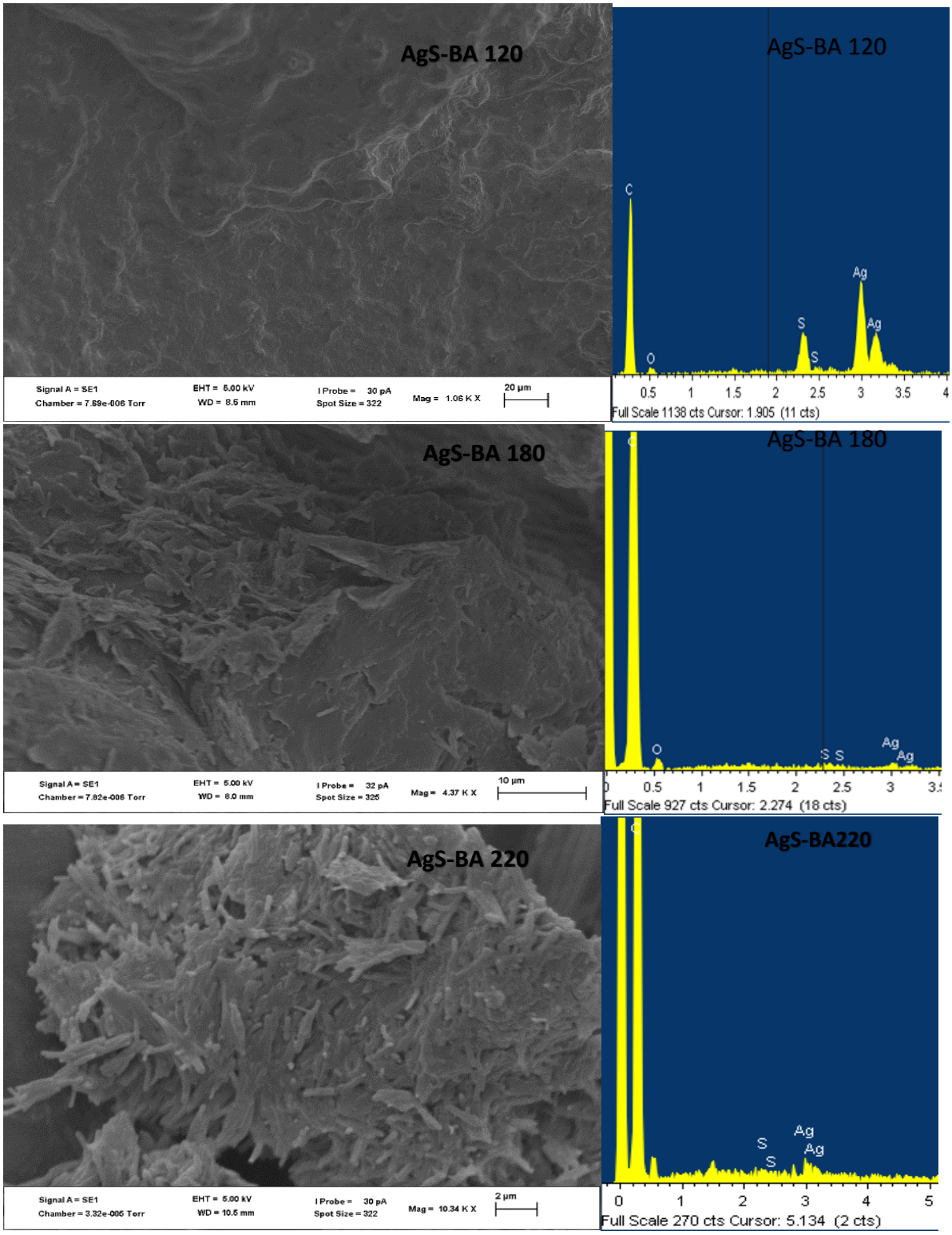

Figure 4. 51 SEM micrographs and EDX spectra of the AgS-BA nanoparticles synthesized at 120, 180 and 220°C.

4.4.4.4. Fourier transform infrared spectroscopy studies of AgS-BA nanoparticles

The overlay spectra of AgS-BA nanoparticles synthesized at three different temperatures and the capping agents used are displayed in Figure 4.52. When the spectra of the nanoparticles were compared with the spectra of both capping agents used in the synthesis, it was observed that the nanoparticles and the oleic acid showed similar vibration frequencies. The C=O stretching mode which appeared at 1700 cm^{-1} in the Oleic acid spectrum, however, moved to a lower wavenumber 1650 cm^{-1} in the nanoparticle spectra. The nanoparticles also showed the C-H bending modes from 1600 to 1400 cm^{-1} as the evidence of the alkyl chain from the oleic acid [17].

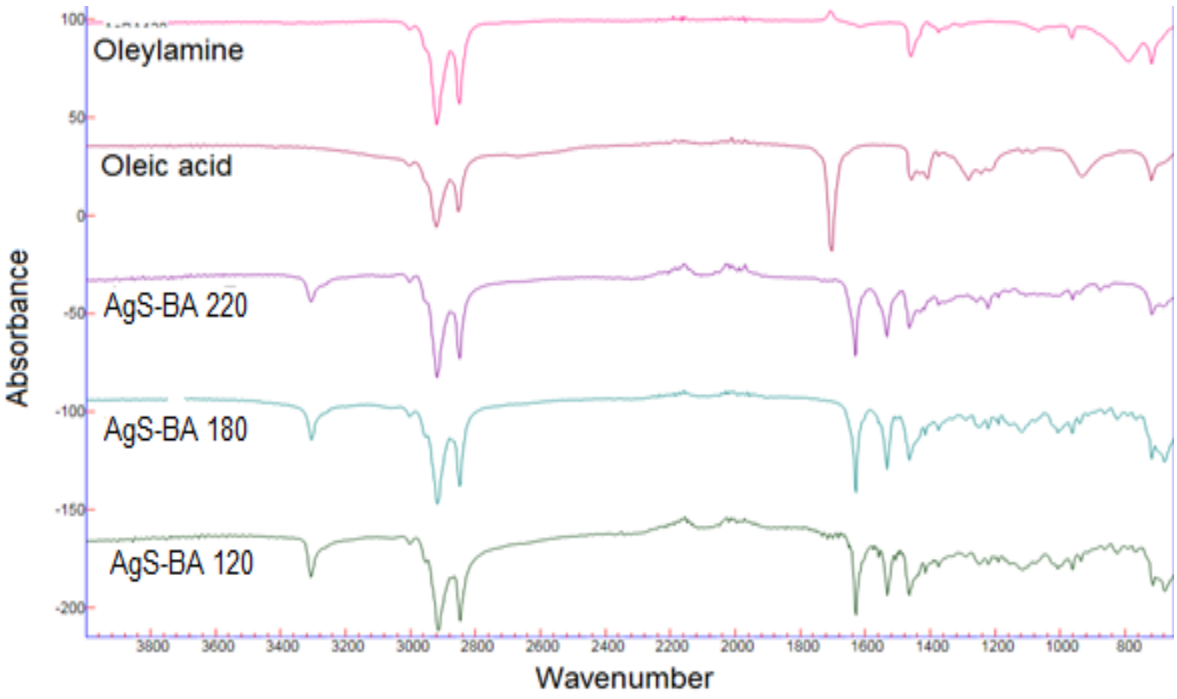

Figure 4. 52 Overlay FTIR spectra of AgS-BA nanoparticles synthesized at 120, 180 and 220°C.

4.4.4.5. Absorption studies of AgS-BA nanoparticles

The UV-Vis spectra of the AgS-BA nanoparticles synthesized at 120, 180 and 220°C are displayed in Figure 4.53. The spectra were used to calculate the band gap energy from the Tauc plots. The Tauc plot shows the estimated band gap energies of the nanoparticles to be 3.0, 2.4 and 2.3 eV for AgS-BA 220, AgS-BA 180 and AgS-BA 120 respectively. The band gap energies obtained were compared to the band gap energy of the bulk AgS which is 0.9 [29]. These band gaps are blue shifted which is attributed to the quantum confinement of the as-prepared silver sulphide nanoparticles due to their small crystallite sizes [28].

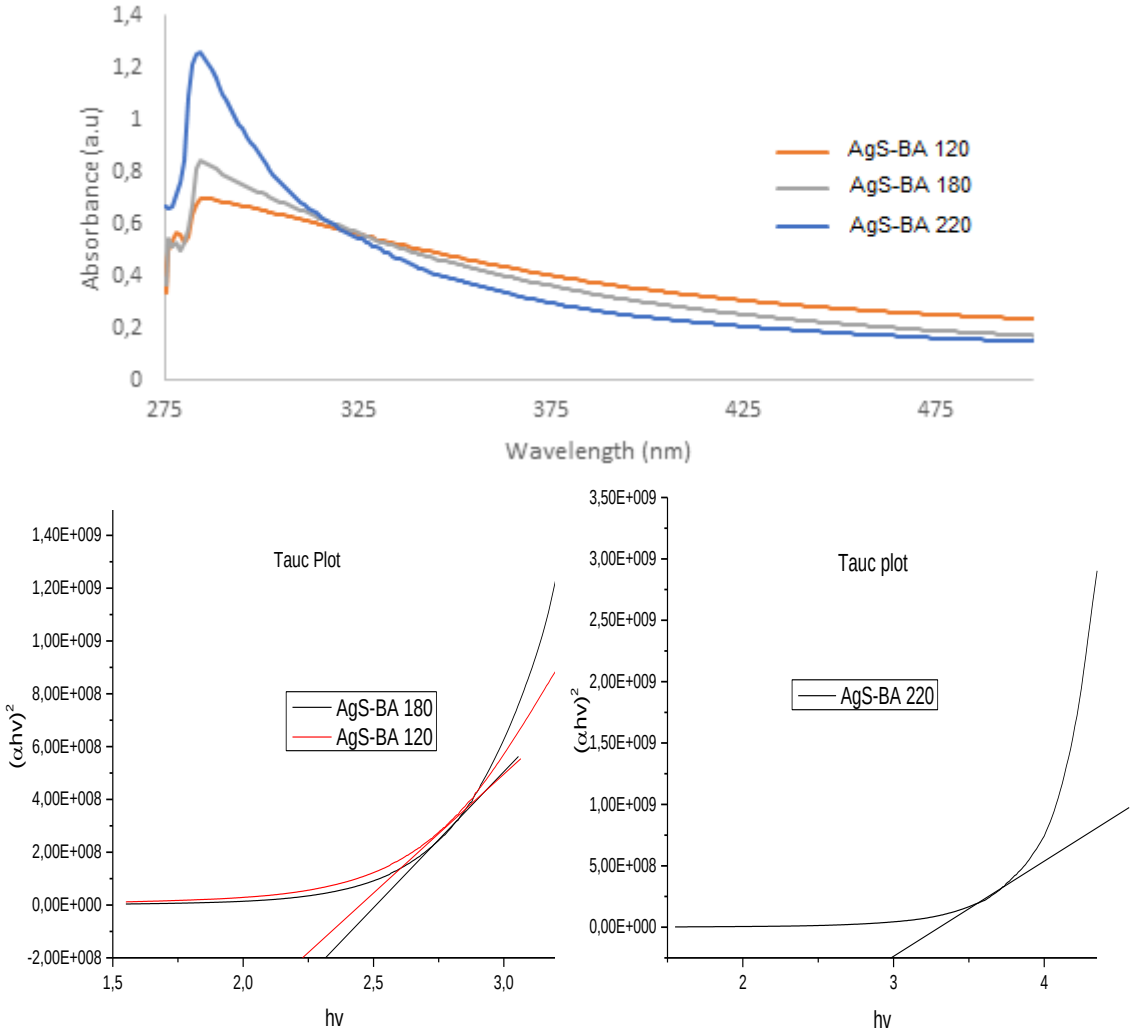

Figure 4. 53 Overlay UV-Vis spectra and Tauc lot of AgS-BA nanoparticles synthesized at three different temperatures.

4.4.4.6. Emission studies of AgS-BA nanoparticles

Figure 4.54 displays the emission spectra of the AgS-BA nanoparticles synthesized at 120, 180 and 220°C. The emission maxima were compared to the absorption band edges of the nanoparticles. The emission maxima are red shifted to higher wavelengths of 380, 307 and 386 nm in comparison to the absorption band edges at 285, 286 and 286 nm for AgS-BA 220, AgS-BA 180 and AgS-BA 120.

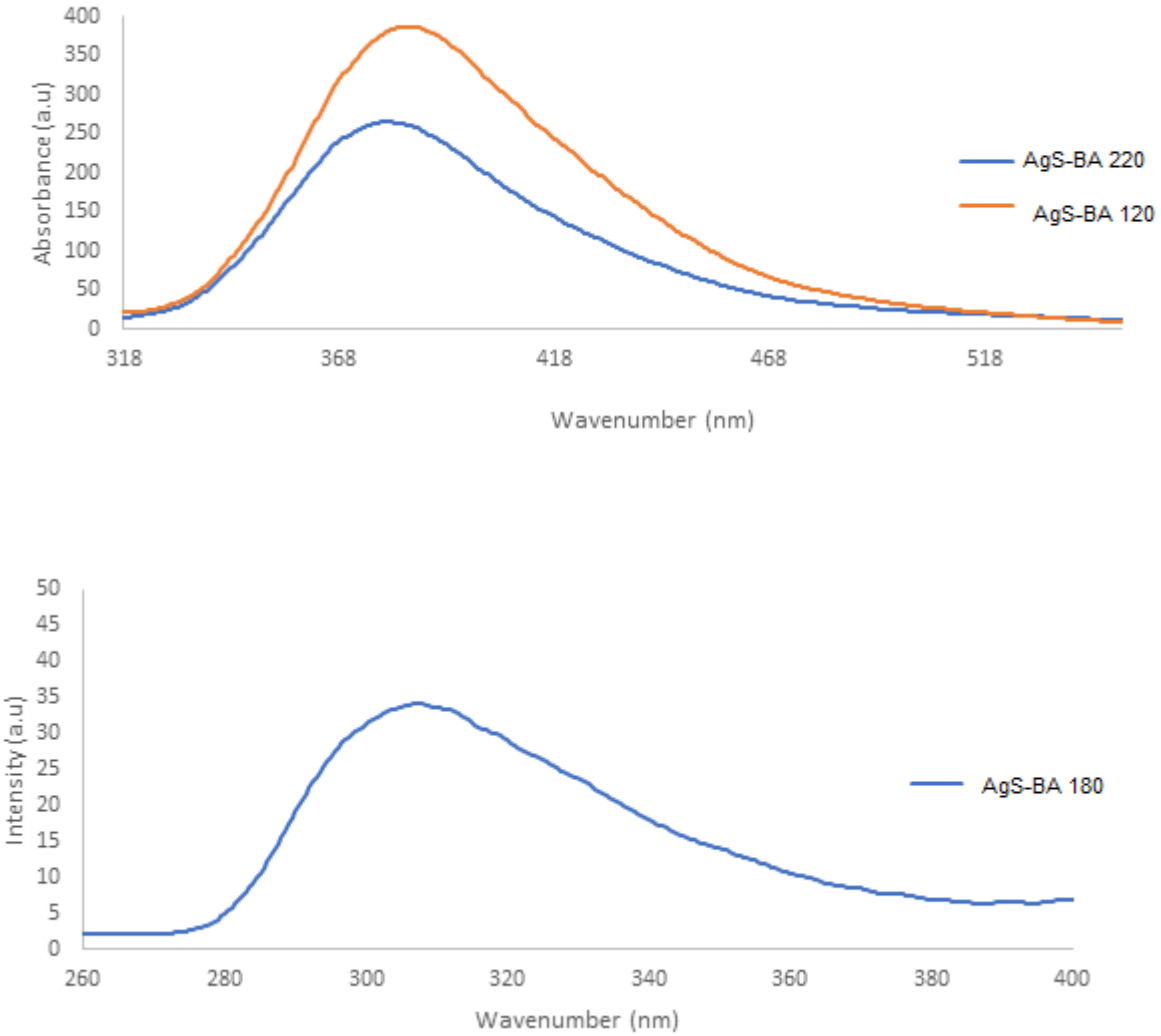

Figure 4. 54 Overlay photoluminescence spectra of AgS-BA nanoparticles synthesized at 120, 180 and 220°C.

4.4.5. Structural and optical studies of silver sulphide nanoparticle synthesized at 220°C (AgS-DBA, AgS-NMB, AgS-DA, AgS-PP)

4.4.5.1. Powder X-ray diffraction patterns of AgS-DBA, AgS-NMB, AgS-DA, AgS-PP nanoparticles

The overlay spectra of the powder X-ray diffraction patterns of the silver sulphide nanoparticles [AgS-PP 220, AgS-NMB 220, AgS-DBA 220 and AgS-DA 220] synthesized are displayed in Figure 4.55. The peaks were indexed to (-121), (013), (-104), (031), (-202), (-212), (-214), (-014), (-224), (-142), (-135), (133) and (-227) miller indices according to the literature [36]. The patterns were analysed by comparing them to literature data. Acanthite $Ag_{1.93}S$ crystalline phase with the space group $P2_1/c$ was identified [32, 33].

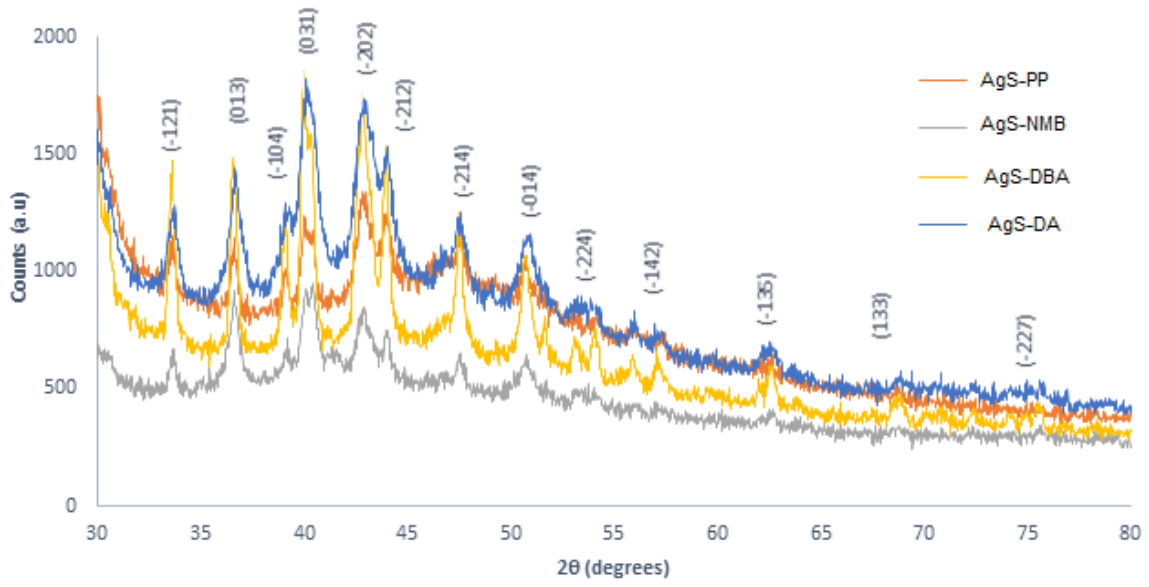

Figure 4. 55. Powder XRD patterns of the prepared silver sulphide nanoparticles synthesized at 220°C from four different precursors

4.4.5.2. Transmission electron microscopy studies of AgS-DBA, AgS-NMB, AgS-DA, AgS-PP nanoparticles

Figure 4.56 shows the TEM images of the synthesized silver sulphide nanoparticles. These four images show that the nanoparticles were not affected by the thermolysis temperature used for their synthesis as they show no trace of agglomeration. The TEM image of the AgS-DA shows that the nanoparticles are spherical in shape. Their sizes appear to be below 20 nm as they range in between 7 and 13 nm. The AgS-DBA TEM image shows that the nanoparticles are spherical in shape with the size range which seems to be also below 30 nm as they are between 11 and 27 nm with no agglomeration. The Ag(NMB) nanoparticles exhibit two different shapes which are semi spherical and spherical shape with the size ranging from 14.70 to 48.04 nm. The AgS-PP image showed the spherical shape nanoparticles with the size range of 36.19 to 29.22 nm.

The SAED patterns of the silver sulphide nanoparticles and their d-spacing lattice fringes were also recorded and are shown next to their corresponding TEM images. AgS-DA, AgS-DBA and AgS-NMB SAED patterns shows bright spots which indicates that the nanoparticles are crystalline even though the rings are diffused but AgS-NMB seems to be more crystalline as the spots are brighter. AgS-PP SAED patterns shows the particles to be amorphous as it is not showing any visible rings. The lattice fringes measured are in the same range which proves that all the nanoparticles have the same phase. For AgS-DBA d= 0.25 and 0.30 nm, for AgS-PP 0.27 and 0.34 nm while for AgS-DA and AgS-NMB d=0.24 and 0.30 nm respectively.

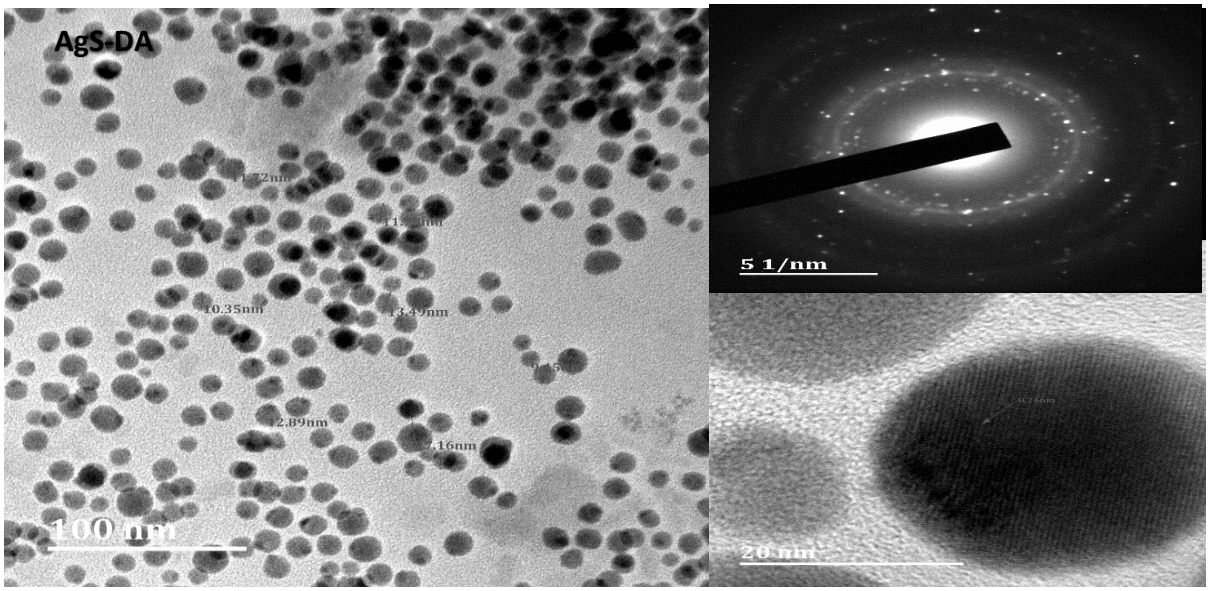
AgS-DA
10.35nm
13.49nm
12.89nm
100 nm
5 1/nm
20 nm

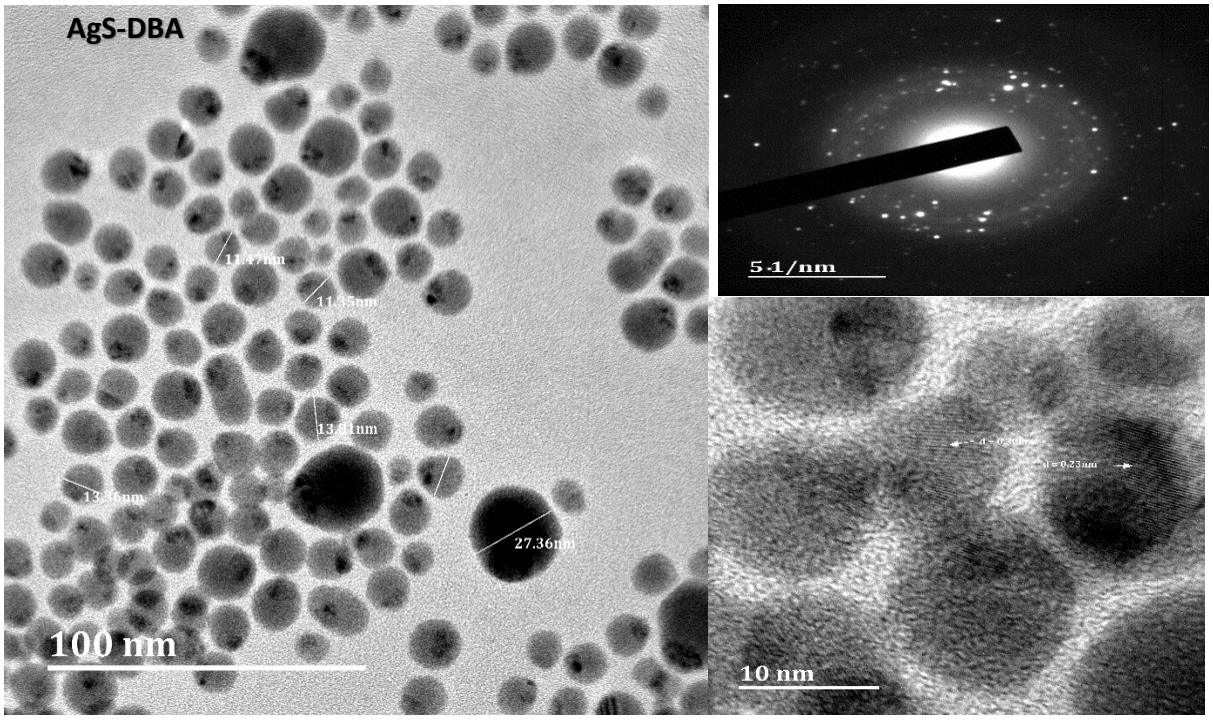
AgS-DBA
11.47nm
11.45nm
27.36nm
100 nm
5 1/nm
10 nm

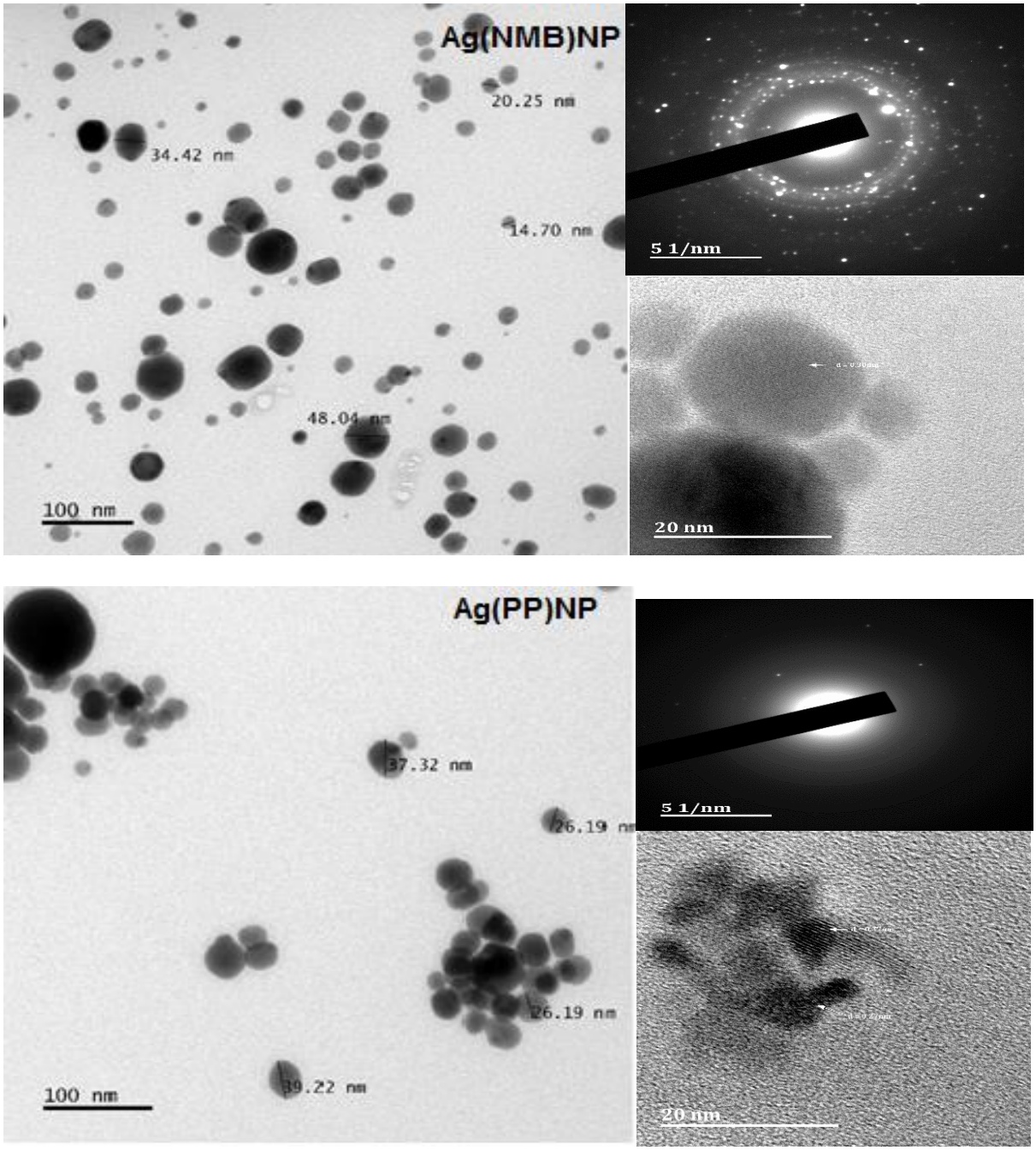

Figure 4. 56 TEM/HRTEM images, lattice fringes and SAED of silver sulphide nanoparticles synthesized at 220°C from four different precursors.

4.4.5.3. Scanning electron microscope and Energy-dispersive X-ray spectroscopy of AgS-DBA, AgS-NMB, AgS-DA, AgS-PP nanoparticles

SEM micrographs displayed in Figure 4.57 were taken to study the surface morphology of the synthesized silver sulphide nanoparticles. The images clearly show that the nanoparticles synthesized from different precursors have different surface morphologies. The image of AgS-NMB shows the nanoparticles have smooth with micro holes morphology. AgS-DBA nanoparticles have the surface made up of packed fibres. AgS-DA have rough solid surface that looks like arranged patches. While AgS-PP image exhibit a surface with disorganised layers making the surface a bit rough. The EDX spectra displayed in Figure 4.57 shows the elemental composition of the silver sulphide nanoparticles and confirms the presence of silver and sulphur in the silver sulphide nanoparticles.

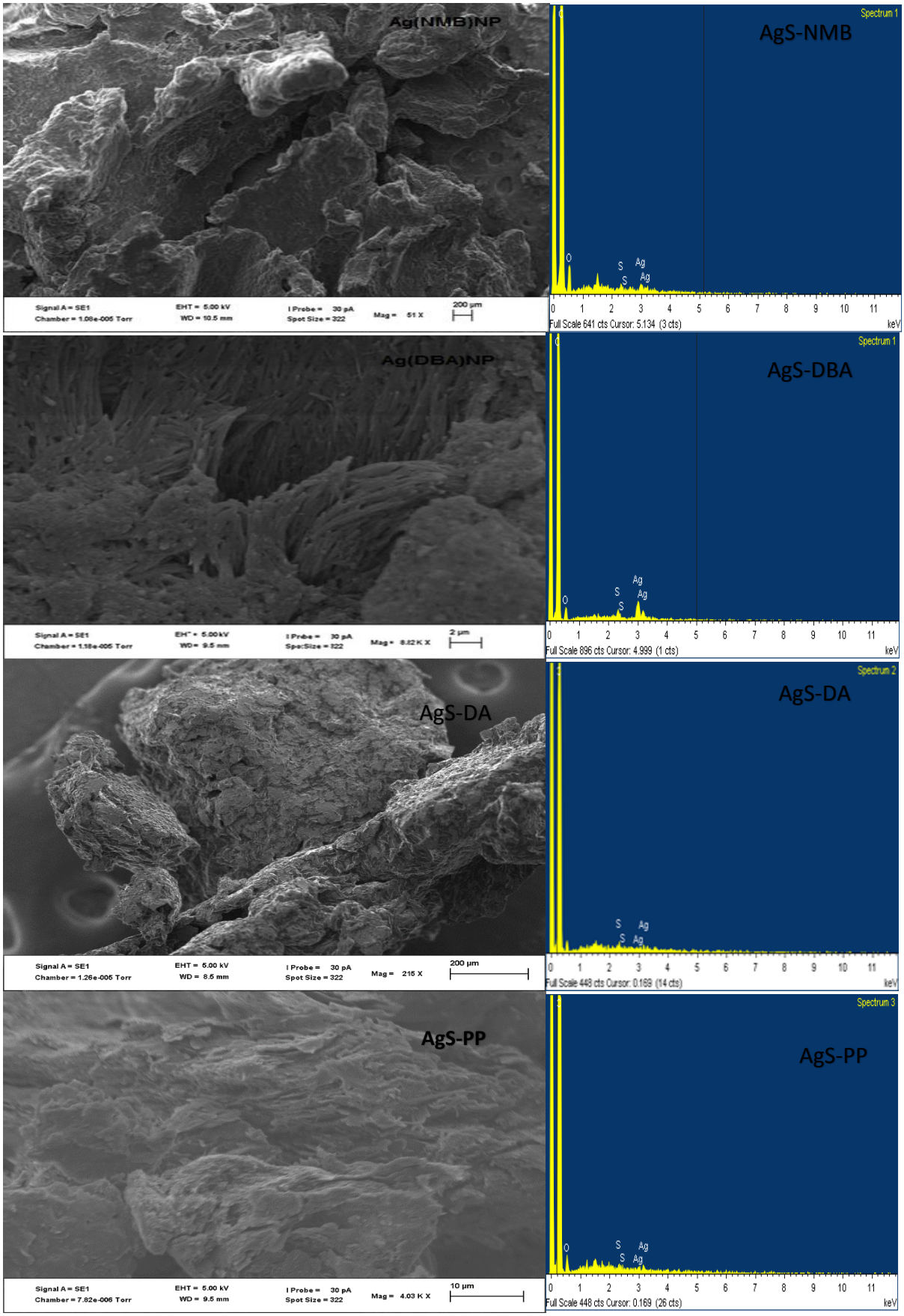

Figure 4. 57. SEM images and EDX spectra of the prepared silver sulphide nanoparticles synthesized at 220°C from four different precursors

4.4.5.4. Fourier-transform infrared spectroscopy studies of AgS-DBA, AgS-NMB, AgS-DA, AgS-PP nanoparticles

To confirm the capping agent that capped the nanoparticles, FTIR spectra of the nanoparticles and the surfactants used were recorded and are shown in Figure 4.58. The nanoparticle spectra show traces of oleic acid. They all portray the C-H asymmetric and C-H symmetric stretching modes around 3000 cm^{-1} and the C=O stretching mode around 1750 cm^{-1} which are attributed to the carboxylic acid in the oleic acid. This confirms the nanoparticles are capped with oleic acid but not oleyl amine as the expected N-H wagging mode between 700 and 800 cm^{-1} is not on the nanoparticles spectra [34].

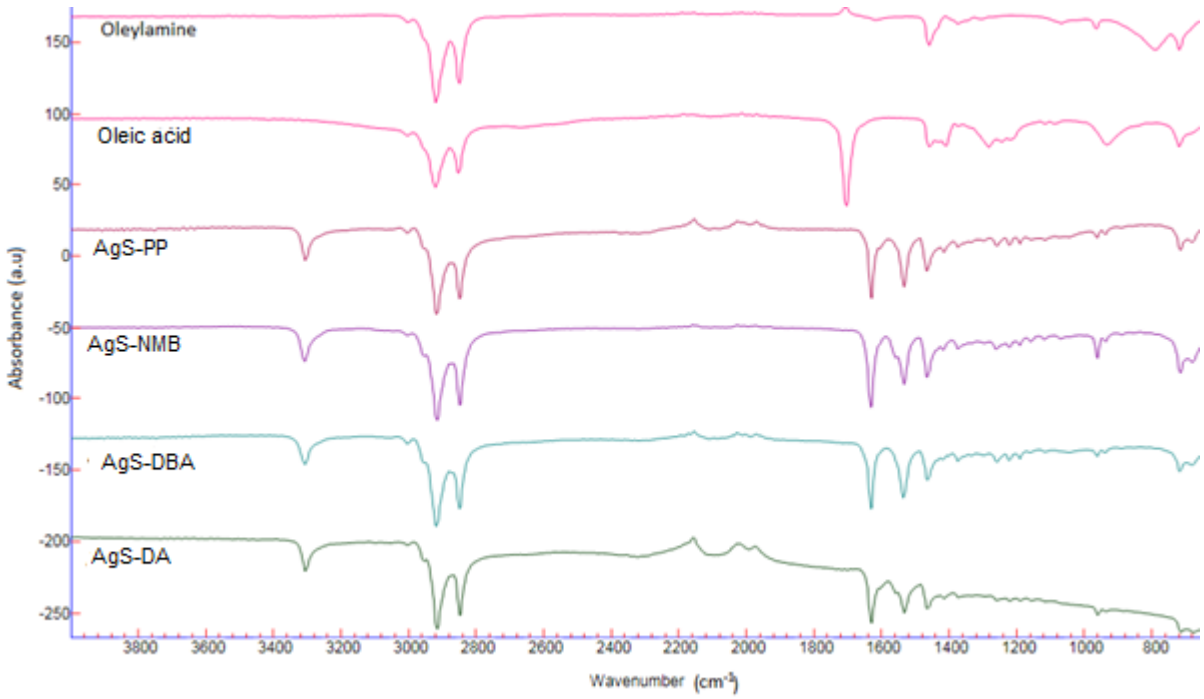

Figure 4. 58. Overlay FTIR spectra of the prepared silver sulphide nanoparticles synthesized at 220°C from four different precursors

4.4.5.5. Absorption studies of AgS-DBA, AgS-NMB, AgS-DA, AgS-PP nanoparticles

The band gap energies of the nanoparticles were calculated directly from the UV-Visible absorption spectra using the Tauc's equation. The band gap energies were determined by plotting $(\alpha hv)^2$ against (hv) and extrapolation of the linear part of the curve to the energy axis, the Tauc plot spectra are shown in Figure 4.59 with the estimated energy band gap of 4.05, 3.96 , 3.96 and 3.79 eV for AgS-DBA, AgS-NMB, AgS-PP and AgS-DA respectively. All these band gap energies are higher when compared to the silver sulphide band gap energy of the bulk which is around 0.9 eV as reported [28]. This shows that the absorption maxima shift observed resulted to the higher band gap energies, However, leading to an increase in the confinement energy showing the decrease in the size of these particles [26].

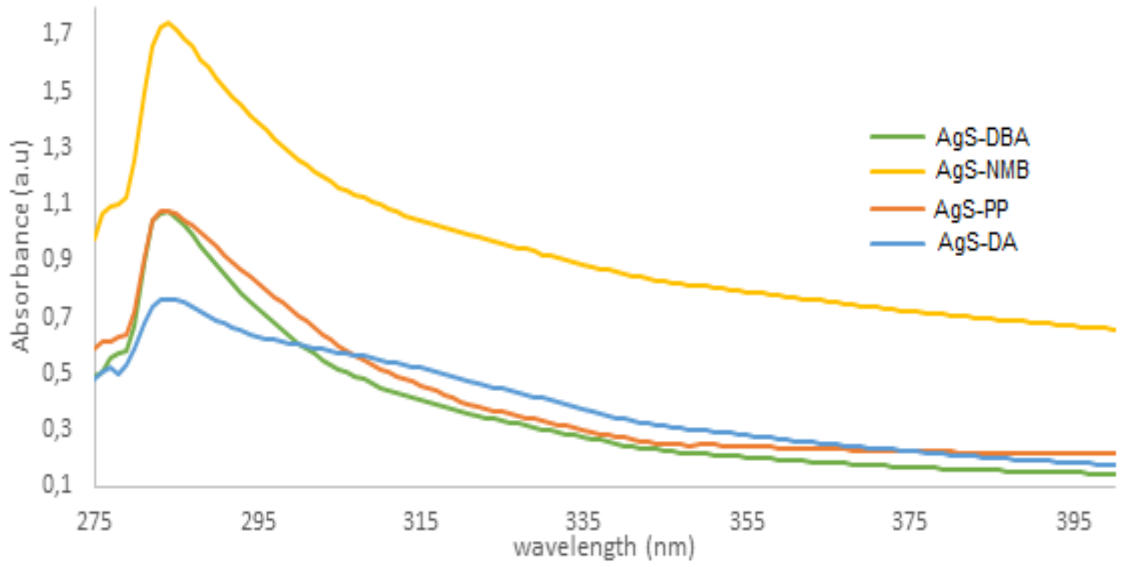

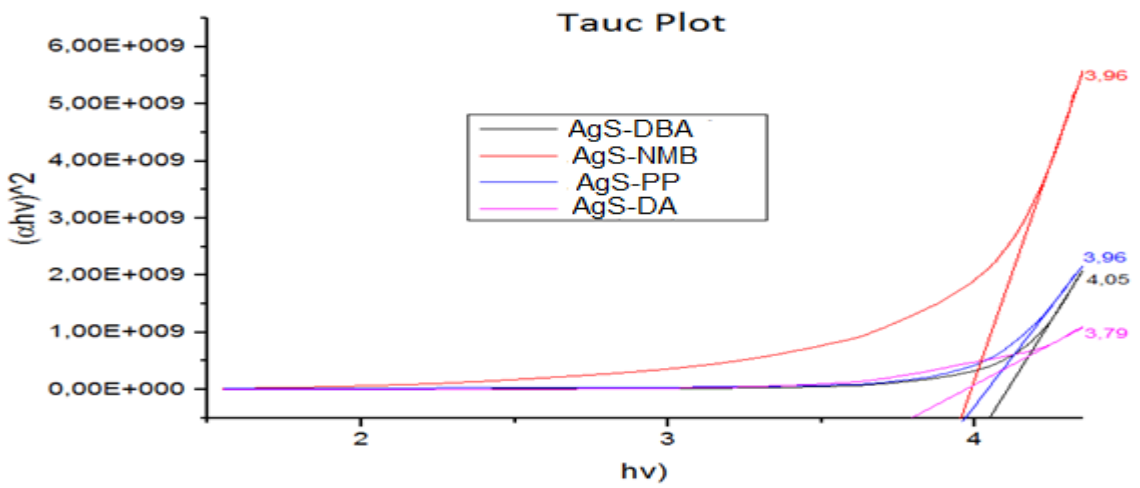

Figure 4. 59. UV-Vis spectra and Tauc plot of the prepared silver sulphide nanoparticles synthesized at 220°C from four different precursors

4.4.5.6. Emission studies of AgS-DBA, AgS-NMB, AgS-DA, AgS-PP nanoparticles

Figure 4.60 shows the emission spectra of the silver sulphide nanoparticles recorded from the fluorescence spectroscopy. The spectra showed broad emission bands with the emission maxima for AgS-DBA and AgS-NMB at 378 and 361 nm respectively while AgS-PP and AgS-DA emission maxima occurred at 383 nm. The broad width of the peaks is associated with the wide size distribution of the particles [35]. The emission wavelengths were compared with the absorption wavelengths as shown by absorption spectra of these nanoparticles to be at 282 nm for AgS-DBA and 284 nm for AgS-DA, AgS-PP and AgS-NMB. The emission bands were found to be red shifted in comparison to the absorption band edges.

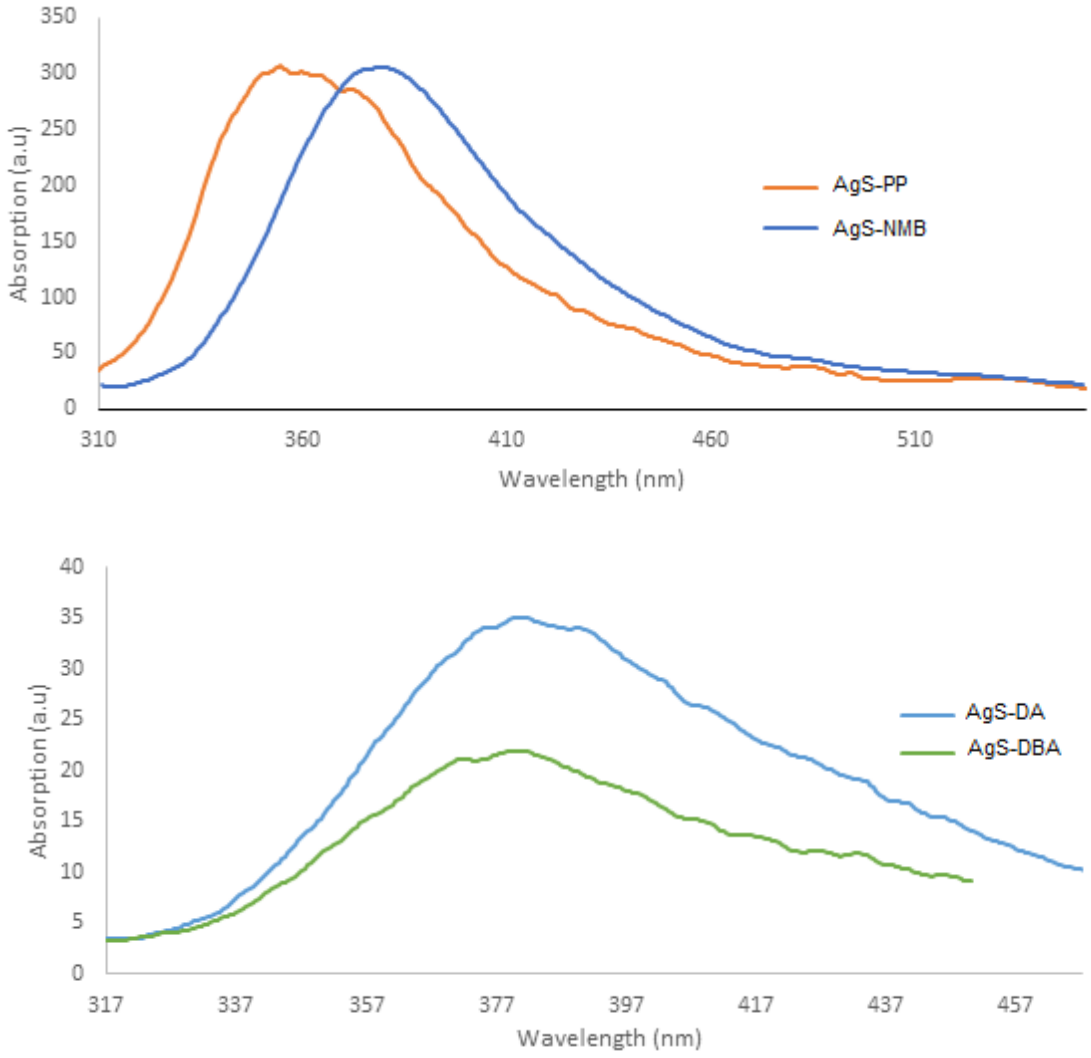

Figure 4. 60. Fluorescence spectra of the prepared silver sulphide nanoparticles synthesized at 220°C from four different precursors

4.5. References

[1] Andrew, F. P.; Ajibade, P. A. Metal complexes of alkyl-aryl dithiocarbamates: Structural studies, anticancer potentials and applications as precursors for semiconductor nanocrystals. *J. Mol. Struct*. **2018**, 1155, 843-855.

[2] Sun, J.; Buhro, W. E. The use of single-source precursors for the solution–liquid–solid growth of metal sulfide semiconductor nanowires. *Angew. Chem*. **2008**, 120, 3259 –3262.

[3] Ajibade, P. A.; Botha, N. L. Synthesis and structural studies of copper sulfide nanocrystals. *Results in Physics,* **2016**, 6, 581-589.

[4] Mbese, J. Z.; Ajibade, P. A. Synthesis, structural and optical properties of ZnS, CdS and HgS nanoparticles from dithiocarbamato single molecule precursors, *J. Sulfur Chem*. **2014**, 35(4), 438–449.

[5] Nqombolo, A; Ajibade. P. A. Synthesis and spectral studies of Ni(II) dithiocarbamate complexes and their use as precursor for nickel sulphide nanocrystals. *J. Chem*. **2016**, 2016, 1-9.

[6] Chintso, T.; Ajibade, P. A. Synthesis and structural studies of hexadecylamine capped lead sulphide nanoparticles from dithiocarbamate complexes single source precursors. *Mater. Lett*. **2015**, 141, 1-6.

[7] Botha, N. L.; Ajibade, P. A. Effect of temperature on crystallite sizes of copper sulfide nanocrystals prepared from copper(II)dithiocarbamate single source precursor. *Mater. Sci. Semicond. Process.* **2016**, 43, 149–154.

[8] Moloto, N.; Revaprasadu, N; Musetha, P. L.; Moloto. The effect of precursor concentration, temperature and capping group on the morphology of CdS nanoparticles. *J. Nanosci. Nanotech*. **2009**, 1 – 23.

[9] Wang, Z.; Chen, Y.; Zeng, D.; Zhang, Q.; Peng, D. L. Solution synthesis of triangular and hexagonal nickel nanosheets with the aid of tungsten hexacarbonyl. *Cryst. Eng. Commun*. **2016**, 8, 1295–1301.

[10] Mubiayi, K.P.; Revaprasadu, N.; Garje, S. S.; Moloto, M. J. Designing the morphology of PbS nanoparticles through a single source precursor method. *J. Saudi Chem. Soc*. **2017**, 21, 593–598.

[11] Gharibshahi, L.; Saion, E.: Gharibshahi, E.; Shaari, A. H.; Matori, K. A. Structural and optical properties of Ag nanoparticles synthesized by thermal treatment method. *Materials*, **2017**, 10, 402. 1-13.

[12] Samanta, P. K.; Saha, A.; Kamilya, T. Chemical synthesis and optical properties of ZnO nanoparticles. *J. Nano- Electr*. **2014**, 6, 4, 1-2.

[13] Zhang, Y.; Du, Y.; Xu, H.; Wang, Q. Diverse-shaped iron sulphide nanostructures synthesized from a single source precursor approach. *Cryst. Eng. Comm*. **2010**, 12, 3658–3663.

[14] Kumar, P.; Gusain, M.; Nagarajan, R. Synthesis of $Cu_{1.8}S$ and CuS from copper-thiourea containing precursors; Anionic (Cl^-, NO_3, SO_4^{2-}) influence on the product stoichiometry. *Inorg. Chem*. **2011**, 50, 3065–3070.

[15] Abdelhady, A. L.; Ramasamy, K.; Malik, M. A.; O'Brien, P.; Haigh, S. J.; Raftery, J. New routes to copper sulfide nanostructures and thin films. *J. Mater. Chem*. **2011**, 21, 17888–17895.

[16] Wang, C. Y.; Hong, J. M.; Chen, G.; Zhang, Y.; Gu, N. Facile method to synthesize oleic acid-capped magnetite nanoparticles. *Chinese Chem. Lett*. **2010**, 21, 179–182.

[17] Wu, Y.; Wadia, C.; Ma, W.; Sadtler, B.; Alivisatos, A. P. Synthesis and photovoltaic application of copper(I) sulfide nanocrystals. *Nano Lett*. **2008**, 8, 2551-2555.

[18] Cattley, C. A.; Stavrinadis, A.; Beal, R.; Moghal, J.; Cook, A. G.; Grant, P. S.; Smith, J. S.; Assender, H.; Watt. A. A. R. Colloidal synthesis of lead oxide nanocrystals for photovoltaics. *Chem. Commun*. **2010**, 46, 2802–2804.

[19] Saranya, M.; Santhosh, C.; Ramachandran, R.; Kollu, P.; Saravanan, P.; Vinoba, M.; Jeong, S. K.; Grace, A. N. Hydrothermal growth of CuS nanostructures and its photocatalytic properties. *Powder Technol*. **2014**, 252, 25–32.

[20] Sharma, R.; Bisen, D. P.; Shukla, U.; Sharma, B. G. X-ray diffraction: A powerful method of characterizing nanomaterials. *Recent Res. Sci. Technol.* **2012**, 4(8), 77-79.

[21] Zhao, Y.; Pan, H.; Lou, Y.; Qiu, X.; Zhu, J.; Burda, C. Plasmonic $Cu_{2-x}S$ nanocrystals: Optical and structural properties of copper-deficient copper(I) sulfides. *J. Am. Chem. Soc*. **2009**, 131, 4253–4261.

[22] Reich, M.; Chryssoulis, S. L.; Deditius, A.; Palacios, C.; Zuniga, A.; Weldt, M.; Alvear, M. "Invisible" silver and gold in supergene digenite ($Cu_{1.8}S$). *Geochim Cosmochim. Acta*., **2010**, 74, 6157–6173.

[23] Liu, L.; Zhong, H.; Bai, Z.; Zhang, T.; Fu, W.; hi, L. S.; Xie, H.; Deng, L.; Zou, B. Controllable transformation from rhombohedral $Cu_{1.8}S$ nanocrystals to hexagonal CuS clusters: Phase- and composition dependent plasmonic properties. *Chem. Mater*. **2013**, 25, 4828−4834.

[24] Chena, S.; Liu, W. Oleic acid capped PbS nanoparticles: Synthesis, characterization and tribological properties. *Mater. Chem. Phys*. **2006**, 98, 183–189.

[25] van der Stam, W.; Gudjonsdottir, S.; Evers, W. H.; Houtepen, A. J. Switching between plasmonic and fluorescent copper sulfide nanocrystals. *J. Am. Chem. Soc.* **2017**, 139, 13208−13217.

[26] Anitha, A.; Usha, J; Sajeevan, J. P.; Christy, C.; Varughese, A. characterization, thermal effect on optical band gap energy and photoluminescence in wurtzite ZnO:Er Nanocrystallites. *Mater. Proceedings*, **2016**, 3, 145-151.

[27] C. Mastrodonato, C.; Pagano, P.; Daniel, J.; Vaultier, M.; Blanchard-Desce, M. *Molecules*, **2016**, 21, 1227.

[28] Rui Chen, R.; Nuhfer, N. T.; Moussa, L.; Morris, H. R.; Whitmore, P. M. Silver sulfide nanoparticle assembly obtained by reacting an assembled silver nanoparticle template with hydrogen sulfide gas. *Nanotechnology*, **2008**, 19, 455604, 1-11.

[29] Ekpekpo, A.; Chukwuka, D. D. Synthesis and characterization of silver sulphide quantum dots by uv-ava spectroscopy. *Int. J. Applied Phys. Math*. **2014**, 4(4), 263-266.

[30] Koole, R.; Groeneveld, E.; Vanmaekelbergh, D.; Meijerink, A.; de Mello Donegá, C. Size Effects on Semiconductor Nanoparticles. *Nanoparticles*, **2014**, 13-51.

[31] Slimane, A. B.; Najar, A.; Elafandy, R.; San-Román-Alerigi, D. P.; Anjum, D.; Ng, T. K.; Boon Ooi, B. S. On the phenomenon of large photoluminescence red shift in GaN nanoparticles. *Nanos. Res. Lett.* **2013**, 8, 342, 1 - 6.

[32] Gusev, A I.; Sadovnikov, S. I. Acanthite–Argentite transformation in nanocrystalline silver sulfide and the Ag_2S/Ag nanoheterostructure. *Semiconductors*, **2016**, 50, 5, 682–687.

[33] Sadovnikov, S. I.; Gusev, A. I.; Rempel, A. A. An in situ high-temperature scanning electron microscopy study of acanthite–argentite phase transformation in nanocrystalline silver sulfide powder. *Phys. Chem. Chem. Phys*. **2015**, 17, 20495—20501.

[34] Stavrinadis, A.; Smith, J. M.; Cattley, C. A.; Cook, A. G.; GrantP. S.; Watt, A. A. R. SnS/PbS nanocrystal heterojunction photovoltaics. *Nanotechnology*, **2010**, 21, 185202, 1-7.

[35] Reynolds, R. A.; Stramski, D.; Wright, V. M.; Woźniak, S. B. Measurements and characterization of particle size distributions in coastal waters. *J. Geophys. Res*. **2010**, 115, C08024.

[36] Sadovnikov, S. I.; Gusev, A. I.; Rempela, A. A.; Nonstoichiometry of nanocrystalline monoclinic silver sulfide. *Phys. Chem. Chem. Phys*. **2015**, 17, 12466-12471.

[37] Cheng, G.; Walker, A. R. H. Transmission electron microscopy characterization of colloidal copper nanoparticles and their chemical reactivity. *Anal. Bioanal. Chem.* **2010**, 396, 1057–1069.

CHAPTER FIVE

5.1. Summary of results, conclusion and future prospects

5.1.1. Summary of results

This study is based on the synthesis and spectroscopic characterization of copper(II) dithiocarbamate complexes and silver(I) dithiocarbamate complexes and their use as single source precursors to synthesize copper sulphide and silver sulphide nanoparticles. The first chapter of this thesis describes the types of nanomaterials and their applications. The chapter describes the methods that have been used to synthesize nanomaterials. The challenges in their synthesis and their properties. The complexes that have been used to synthesize these materials were also described. The chapter then gives the aim and the objectives of the study. Chapter two describes all the experimental methods used in this study to synthesize sodium dithiocarbamate ligands and copper(II) and silver(I) dithiocarbamate complexes. The chapter also contains detailed characterization techniques used to characterize the synthesized compounds and also the materials used in all the reactions. The schemes showing all the reactions starting with the synthesis of dithiocarbamates (N-ethyl aniline DTC, N-methyl benzyl amine DTC, piperidine DTC, morpholine DTC, phenyl piperazine DTC, Dibenzyl amine DTC, Butyl amine DTC and Diallylamine DTC) and the corresponding copper(II) and silver(I) dithiocarbamate complexes were also detailed in this chapter.

Chapter three focuses on the spectroscopy characterization of the ligands and complexes. The chapter first describes the physical properties of the synthesized compounds. This is followed by the table summarizing the FTIR results of the ligands and their respective metal complexes.

The FTIR results of the ligands showed the C – S, C = S and C – N vibrations corresponding to the dithio- moiety that were expected. In the complexes, the C – S and C = S frequency gave one vibration confirming the coordination of the metals to the ligands. The ligands were also characterized using the ^{1}H NMR spectroscopy and all the ligands showed all the expected resonances. The carbon-13 NMR confirmed the formation of the dithiocarbamates by showing the peak at around 210 ppm ascribed to the C – SS environment. UV-Vis analysis carried out on the ligands showed two shoulder in ultra violet region corresponding to $\pi - \pi^*$ and $n - \pi^*$ attributed by N–C=S and S–C=S groups. The UV-Vis spectra of the copper complexes confirmed the square planar coordination geometry of the copper ion to the ligand. The complexes showed two bands at the visible region confirming the square planar geometry. The X-ray crystallography of the four complexes isolated (silver(I)N-ethyl aniline, silver(I) dibenzyl amine dithiocarbamate, copper(II) piperidine dithiocarbamate and copper(II) dibenzyl amine dithiocarbamate complexes) showed the silver(I) dithiocarbamate complexes to be metal clusters and the copper(II) complexes to have coordinated in square planar geometry.

Chapter four started with a brief introduction on the method used to synthesized metal sulphide nanoparticles and dwelled on the temperature effect on nanomaterial synthesis using this method. The method used to synthesize copper sulphide and silver sulphide nanoparticles was also presented including the material used and the techniques used to characterize the nanomaterials. The nanomaterials were characterized using p-XRD, TEM/HRTEM, SEM and FTIR. Their optical properties were investigated with UV-Visible spectroscopy and fluorescence spectroscopy. The p-XRD patterns were used to determine the crystallinity phases of the copper sulphide and silver sulphide nanoparticles. The patterns suggested the copper sulphide nanoparticles to have $Cu_{1.8}S$ digenite phase irrespective of the temperature used in the synthesis. α-Ag_2S Acanthite phase was revealed for the Ag sulphide nanoparticles at all the

temperatures used. TEM images were used to determine the shapes and the sizes of these particles. The copper sulphide nanoparticles synthesized at 220°C gave sizes ranging from 41 - 125 nm, 180°C gave 10 – 55 nm and at 120°C the size ranged from 4 – 54 nm. The particles showed a mixture of spherical, square and hexagonal shapes. The silver sulphide nanoparticles all showed uniform spherical shape irrespective of reaction temperatures, but the size ranges were different. When the precursors were thermolyzed at 120°C the size ranged from 2 to 23 nm, at 180°C they ranged from 5 to 71 nm and 8 – 78 nm at 220°C.

SEM micrographs showed the metal sulphide nanoparticles have different surface morphologies with different precursors and different temperature used in the synthesis. The FTIR was used to confirm the coordination of the capping agent on the nanoparticles. UV-Vis spectra were used to estimate the energy band gaps of the particles by plotting the Tauc plot. The estimated energy band gaps of copper sulphide nanoparticles increased with decrease in the thermolysis temperature. That corresponds with the size of the particles obtained from the TEM images. However, that did not apply to all the precursors. The band gap energy of the silver sulphide nanoparticles showed no particular pattern. All the nanoparticles band gap energy were higher than that of the bulk which is 1.2 eV for copper sulphide and 0.9eV for silver sulphide semiconductor. This increase in the bandgap is observed as a blue shift in the absorption spectra.

5.1.2. Conclusion

The aim of this study was to synthesize and characterize copper(II) and silver(I) dithiocarbamate complexes, use them as single source precursors to synthesize metal sulphide nanoparticles and study the effect of the precursor and the reaction temperature on the properties of the synthesized nanoparticles. The eight sodium dithiocarbamate ligands, eight copper(II) and eight silver(I) dithiocarbamate complexes synthesized were characterized. The FTIR was used to confirm the C-S, C=S and N-C functional groups, UV-Vis was used to confirm the coordination of the metal ion to the ligand, TGA to study the thermal stability of the complexes and Single Crystal X-ray for some complexes. The ligands were further characterized with ^{13}C and ^{1}H NMR. According to the used characterization techniques the ligands and complexes were successfully synthesized. The NMR confirmed the formation of the ligands by showing the carbon resonance at around 200 ppm. FTIR studies indicated the formation of the complex as two peaks for C-S and C=S were observed in the ligand and only C-S frequency was observed in the complexes. UV-Vis confirmed the square planar coordination of the ligands to the copper(II) ion.

The sixteen metal complexes were used as single source precursors to synthesize thirty-two metal sulphide nanoparticles. Four single source precursors, for each metal were thermolyzed at 200℃ to study the effect of the precursor in the nanoparticle structural and optical properties. The other four precursors for each metal were thermolyzed at three different temperatures, 220, 180 and 120℃, to study the influence of the temperature to the structural and optical properties of the nanoparticles. Their optical properties were studied using Photoluminescence and UV-Visible. The nanoparticles were found to be quantum confined as the estimated band gap energies showed blue shift when compared to that of the bulk.

Their structural properties were characterized using TEM, SEM, FTIR and XRD. The temperature of the reaction and the precursor used to synthesize the nanoparticles were observed to have an influence on the size and shape of the nanoparticles. It was observed that the higher the temperature the bigger the sizes and the higher the agglomeration in CuS nanoparticles but all the AgS nanoparticles had a size range between 3 to 30 nm with uniform spherical shape.

Characterization of the nanoparticles synthesized proved that the temperature used in the synthesis has an effect on the properties of the nanoparticles produced from some precursors. The influence of this factor with the precursors and the metals. When the silver precursors were thermolyzed at different temperatures, the lower the temperature the smaller the size range as the temperature increases the wider the size range. However, irrespective of the temperature used the silver complexes gave the same shape and no effect of agglomeration.

Copper complexes showed a different pattern, the sizes of the particles increased as the temperature used for thermolysis increased. The degree of agglomeration also became higher at higher temperature. The shape of the particles differs with the precursors and the temperature used. This proved that the temperature used in the synthesis has an effect on the size of the particles which will affect the optical properties of the particles. However, this effect differs with the metal used. Silver dithiocarbamate complexes showed a potential in producing uniform shaped and mono dispersed nanoparticles using the single source precursor method with oleic acid and oleylamine as stabilizer and capping agents.

5.1.3. Future prospects

The future recommendations would be to look at other sulphur containing complexes using the same surfactant/capping agents and the same single source precursor method. Also the study of the same precursor with different capping agents especially for copper precursors will be valueable. Another aspect that needs to be investigated while using this method is the ratio of the precursor and capping agents used in the synthesis and also the effect of the reaction duration in the formation of the nanoparticles. In-depth understanding of the mechanism of the nucleation of the nanoparticles in this method is also very important. The nanoparticles can also be used to make nanocomposites with the possibility of looking at potential applications in biology and catalysis.

6. Appendix A: FTIR spectra of ligands and complexes

6.1. Appendix A1: FTIR spectra of butyl amine dithiocarbamate, copper(II) and silver(I) complex

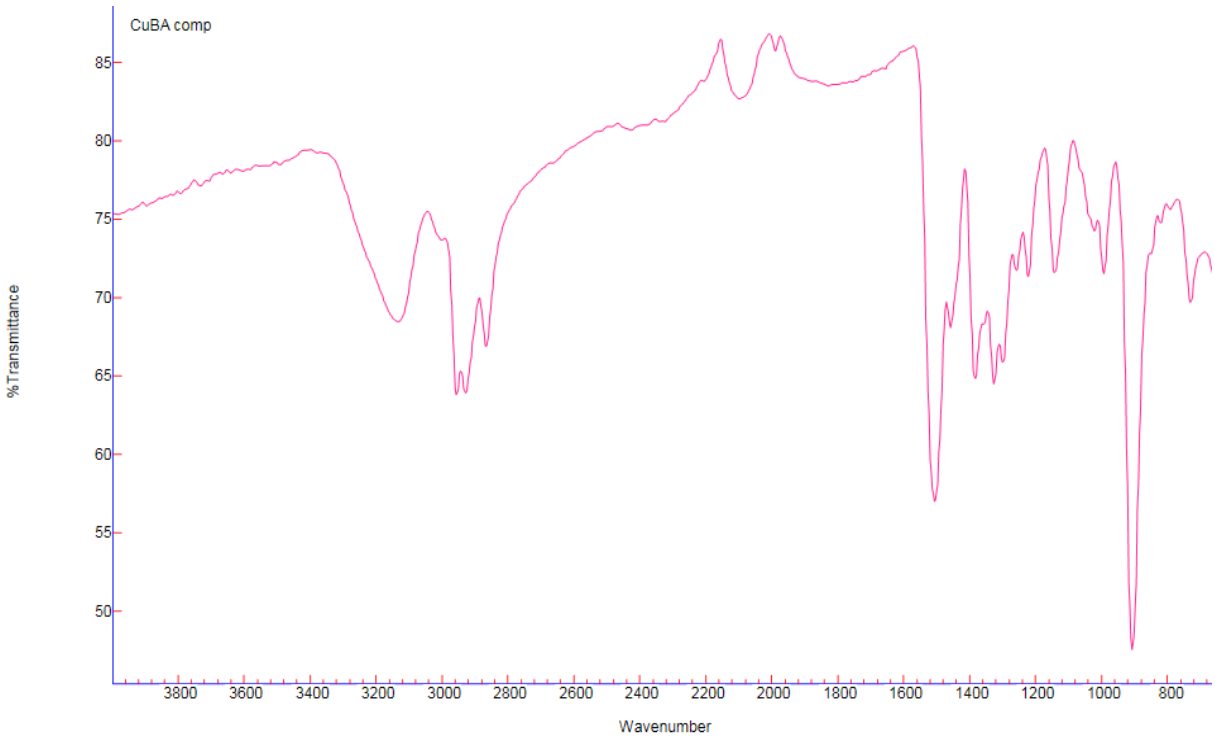

6.2. Appendix A2: FTIR spectra of diallyl amine DTC, copper(II) and silver(I) complex

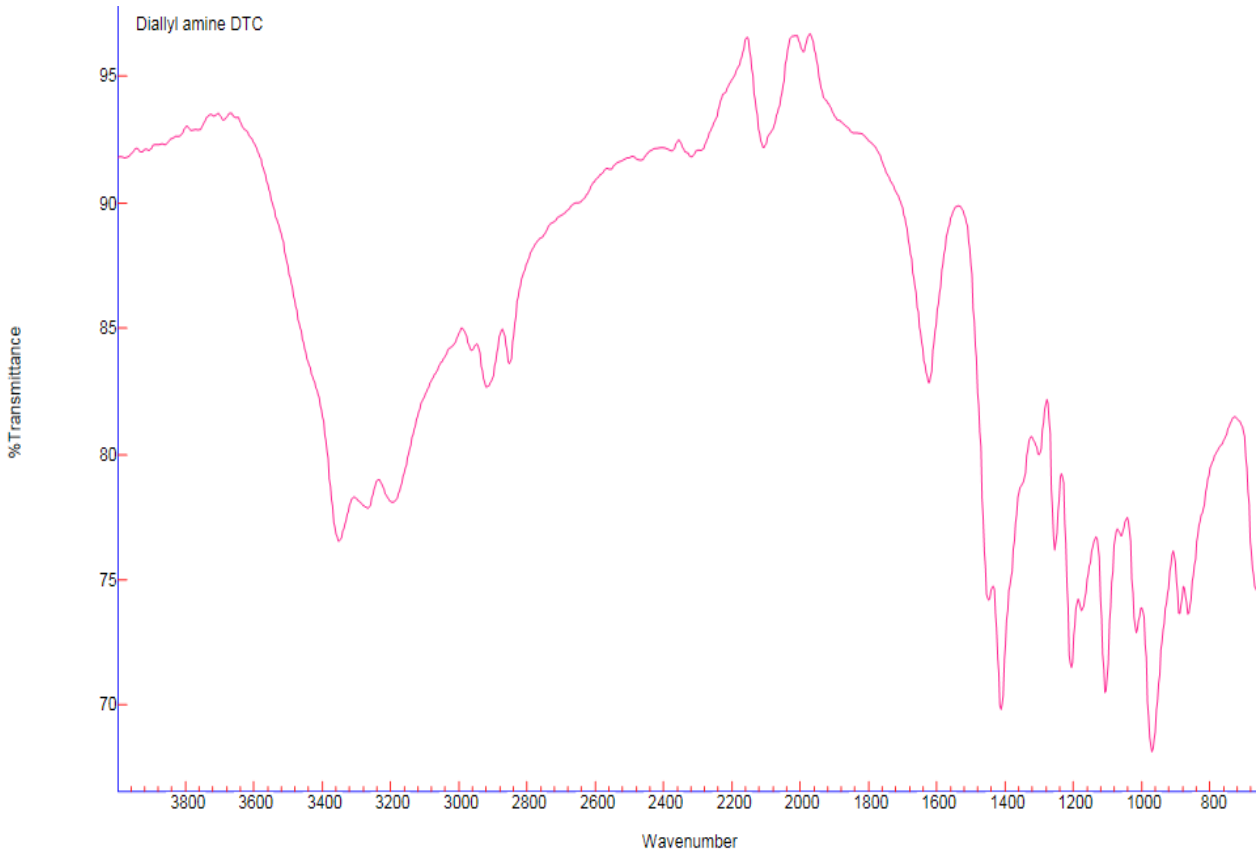


Cu DA compl
%Transmittance
85
80
75
70
65
60
55
50
45
40
35
3800
3600
3400
3200
3000
2800
2600
2400
2200
2000
1800
1600
1400
1200
1000
800
Wavenumber

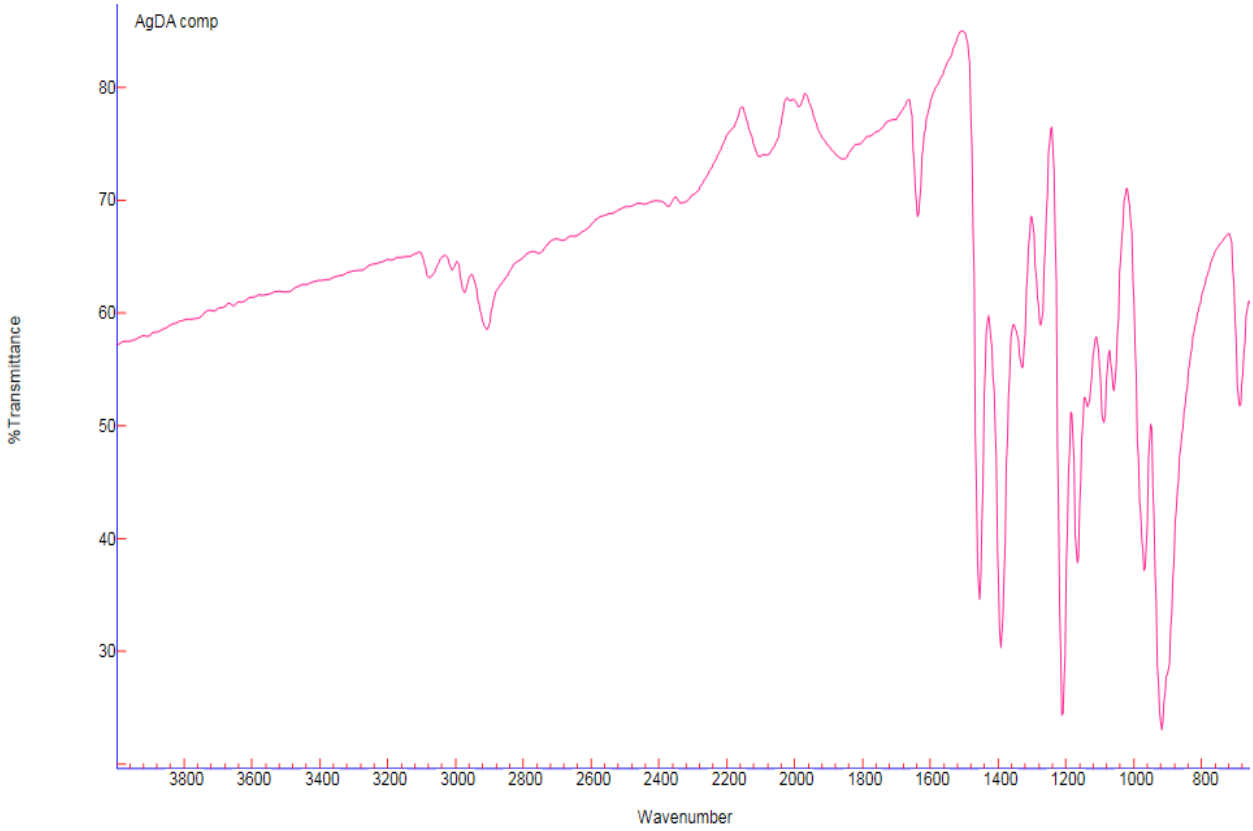
AgDA comp
%Transmittance
80
70
60
50
40
30
3800
3600
3400
3200
3000
2800
2600
2400
2200
2000
1800
1600
1400
1200
1000
800
Wavenumber

6.3. Appendix A3: FTIR spectra of dibenzyl amine DTC, copper(II) and silver(I) complex

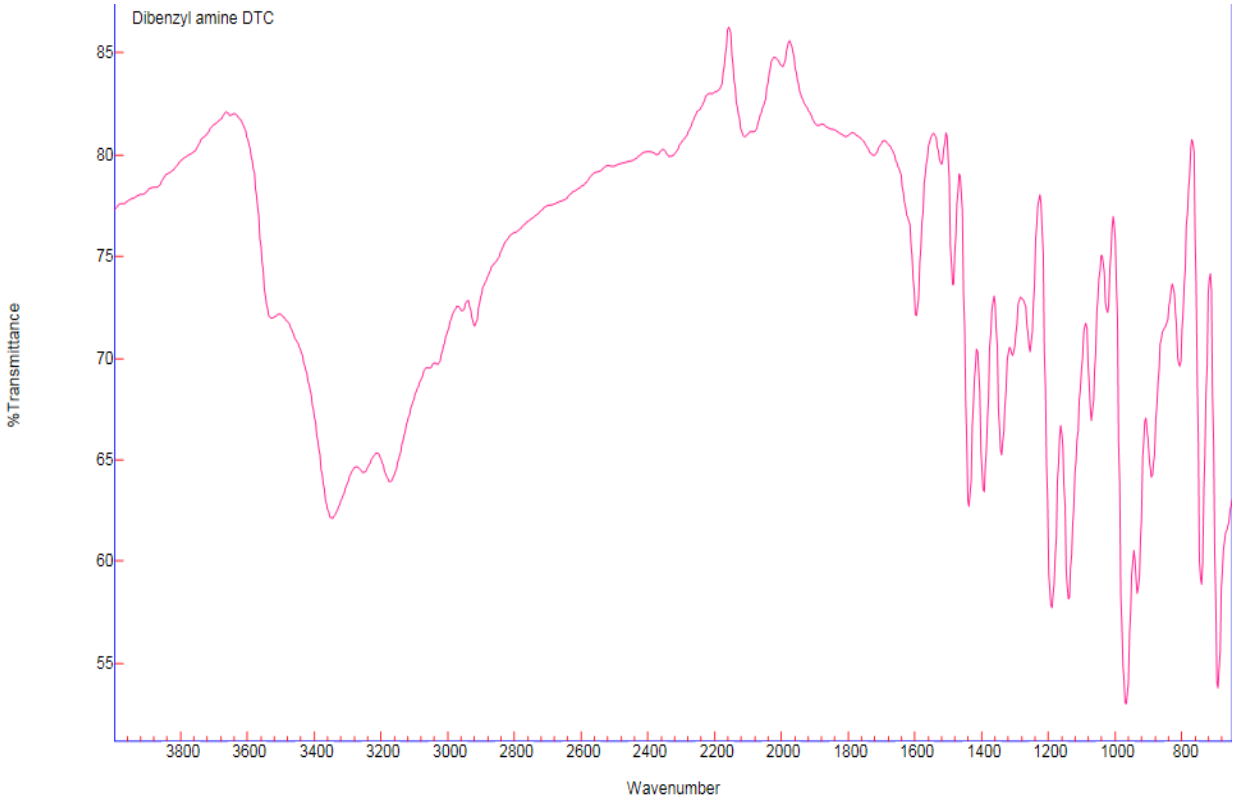

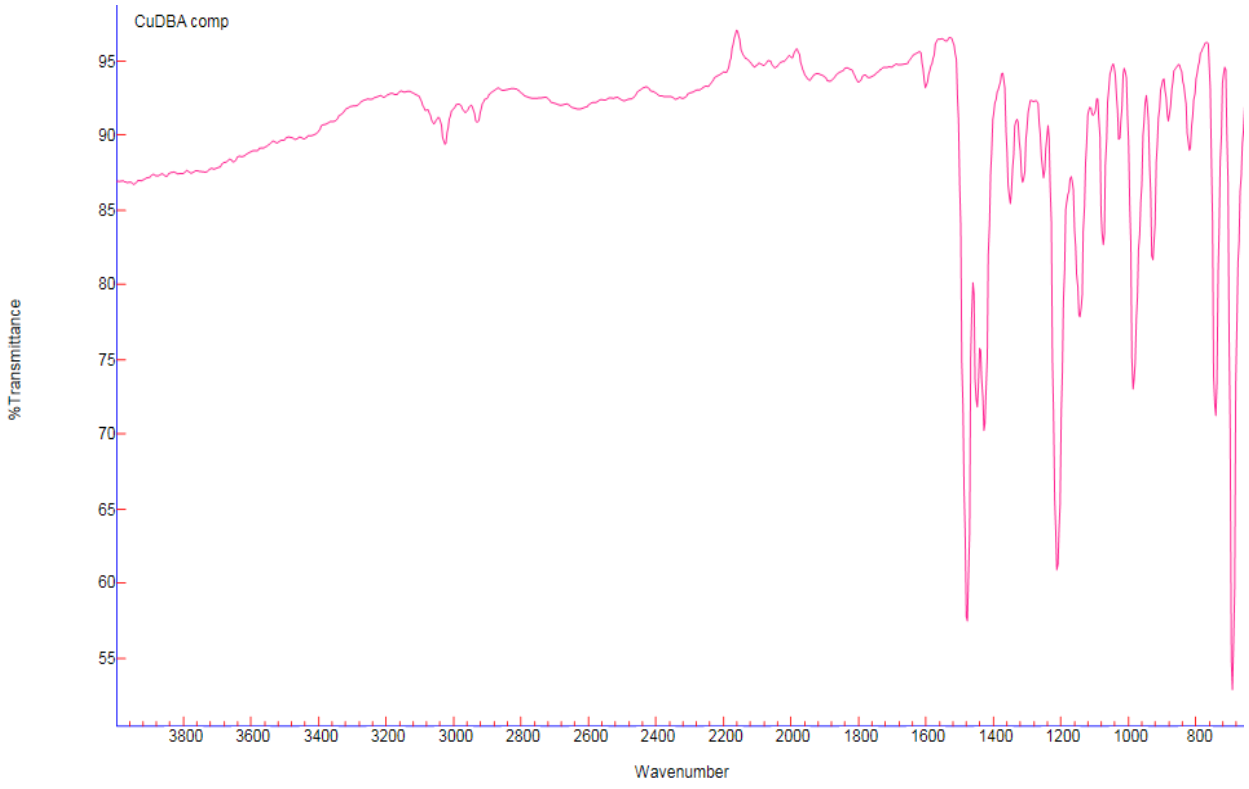

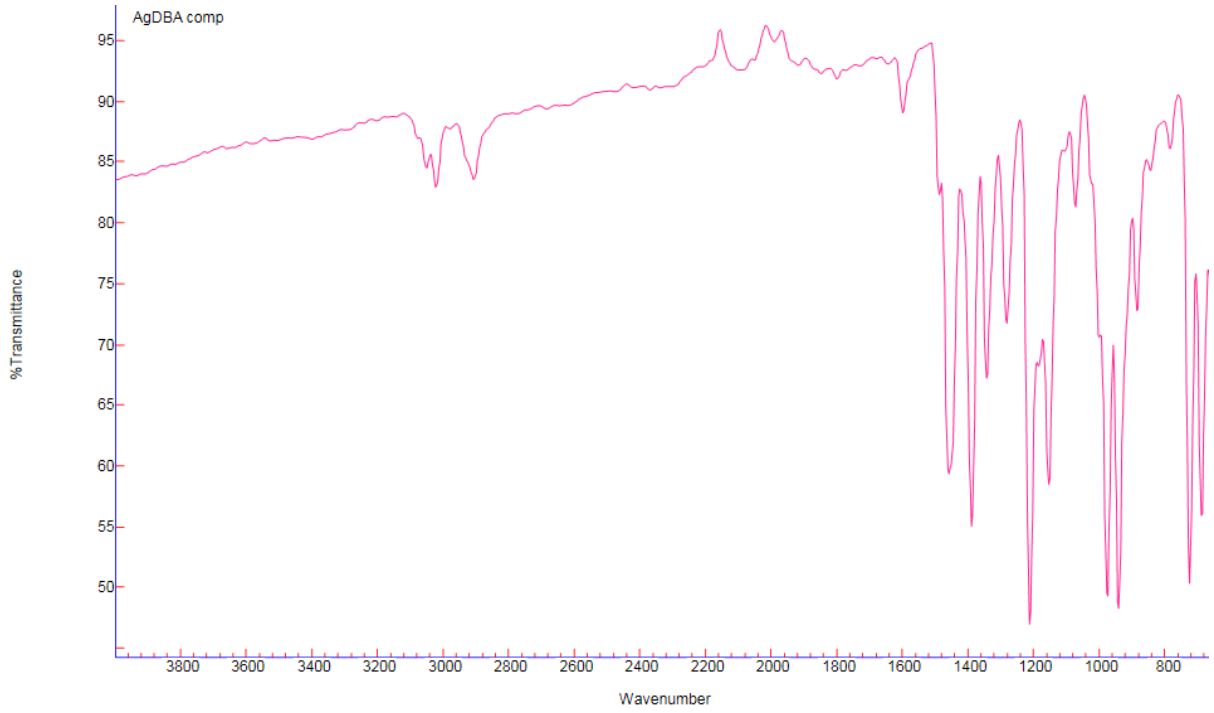

6.4. Appendix A4: FTIR spectra of N-methyl benzyl amine DTC, copper(II) and silver(I) complex

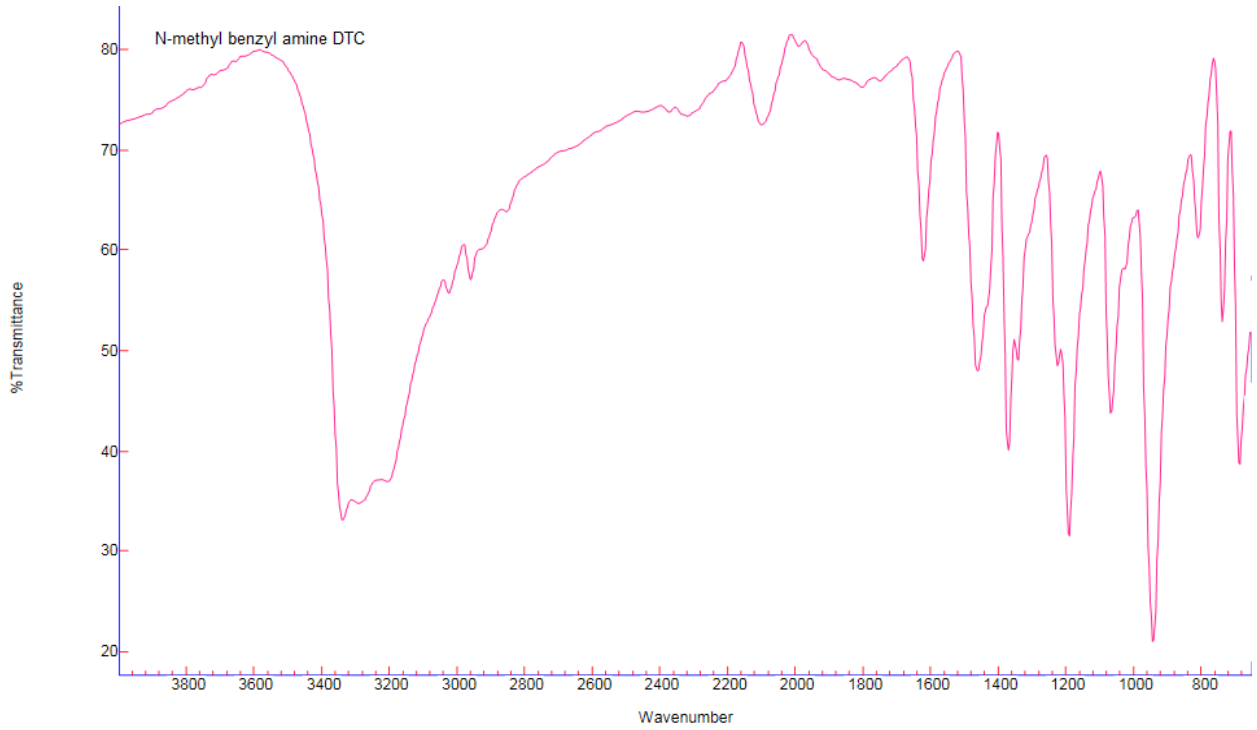

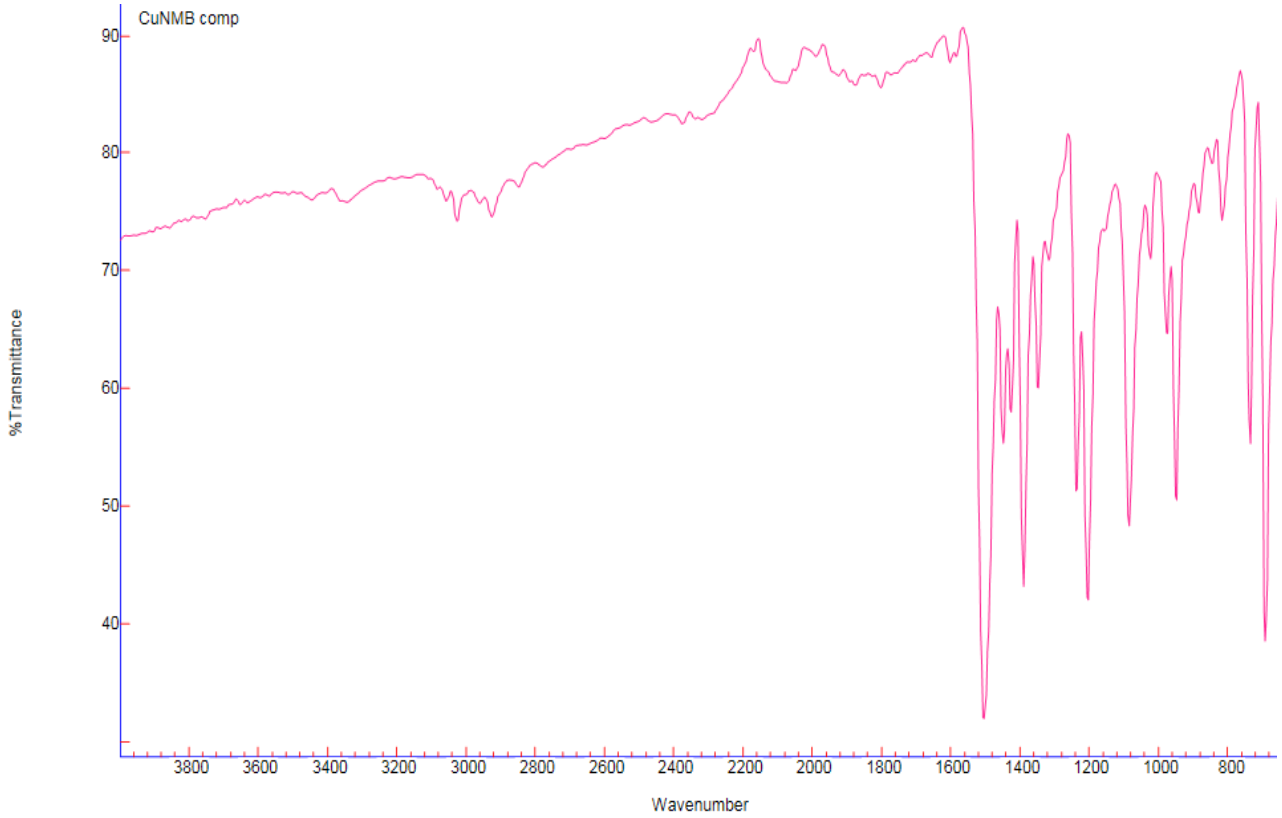
CuNMB comp
%Transmittance
90
80
70
60
50
40
3800
3600
3400
3200
3000
2800
2600
2400
2200
2000
1800
1600
1400
1200
1000
800
Wavenumber

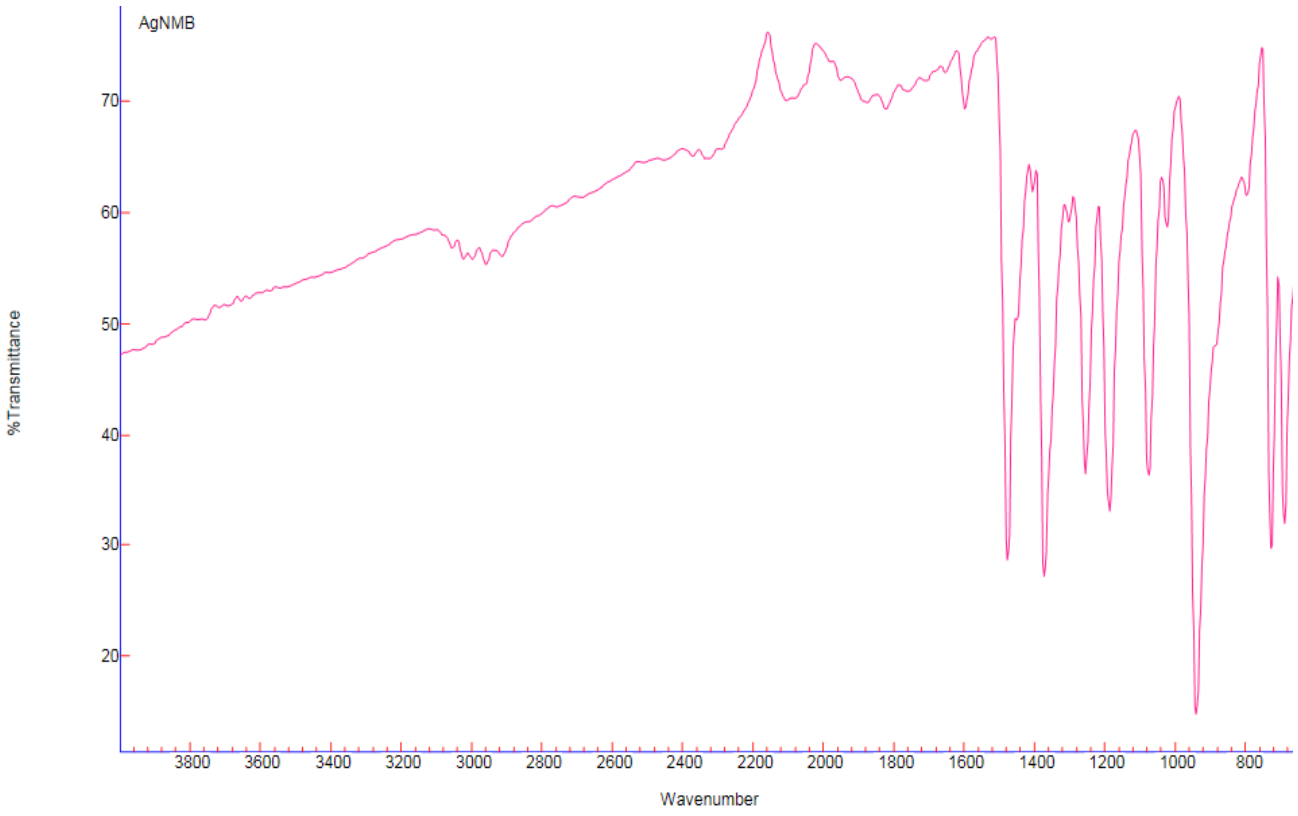
AgNMB
%Transmittance
70
60
50
40
30
20
3800
3600
3400
3200
3000
2800
2600
2400
2200
2000
1800
1600
1400
1200
1000
800
Wavenumber

6.5. Appendix A5: FTIR spectra of N-ethyl aniline DTC, copper(II) and silver(I) complex

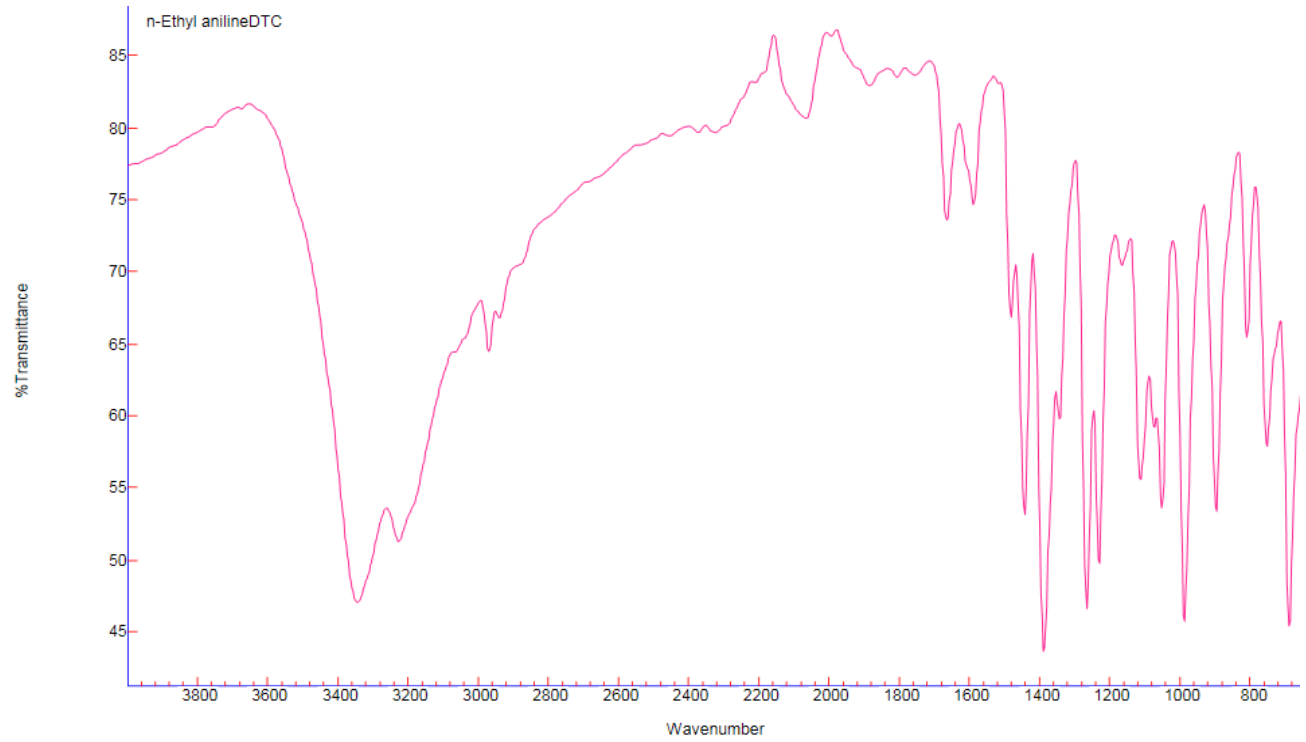

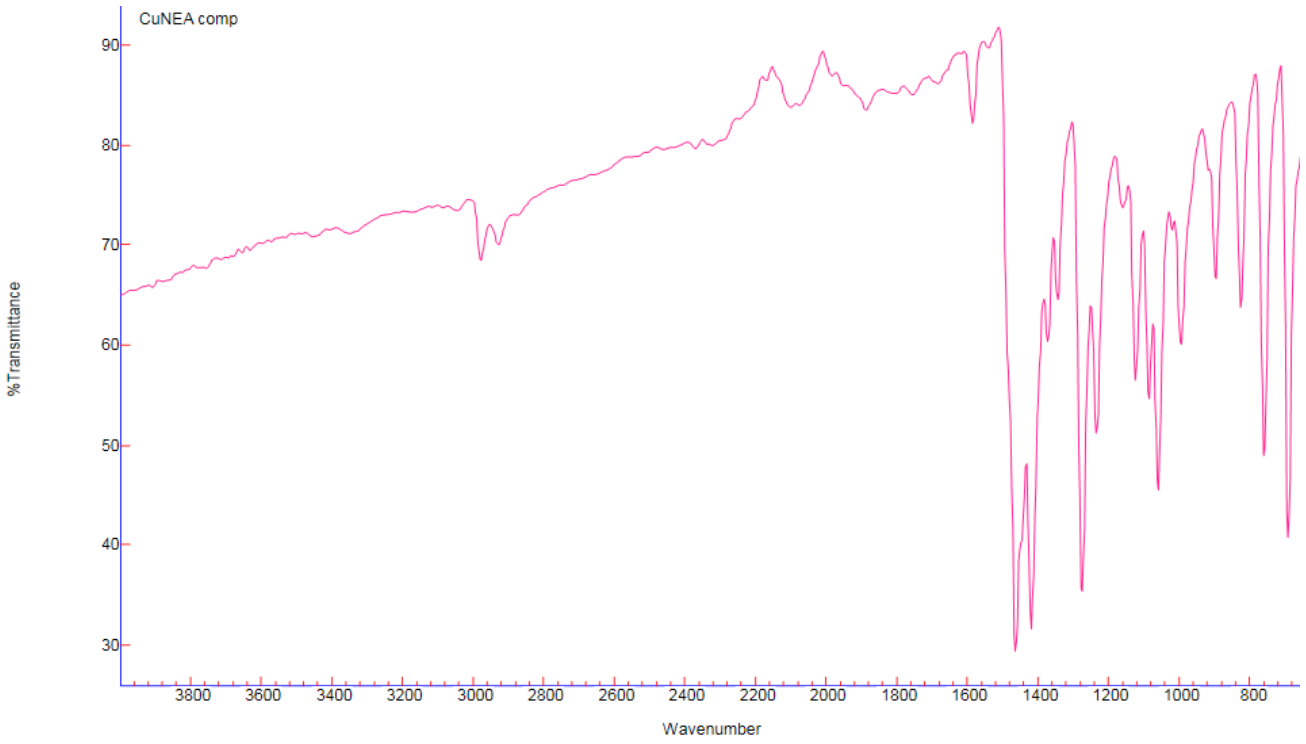

6.6.Appendix A6: FTIR spectra of phenyl piperizine DTC, copper(II) and silver(I) complex

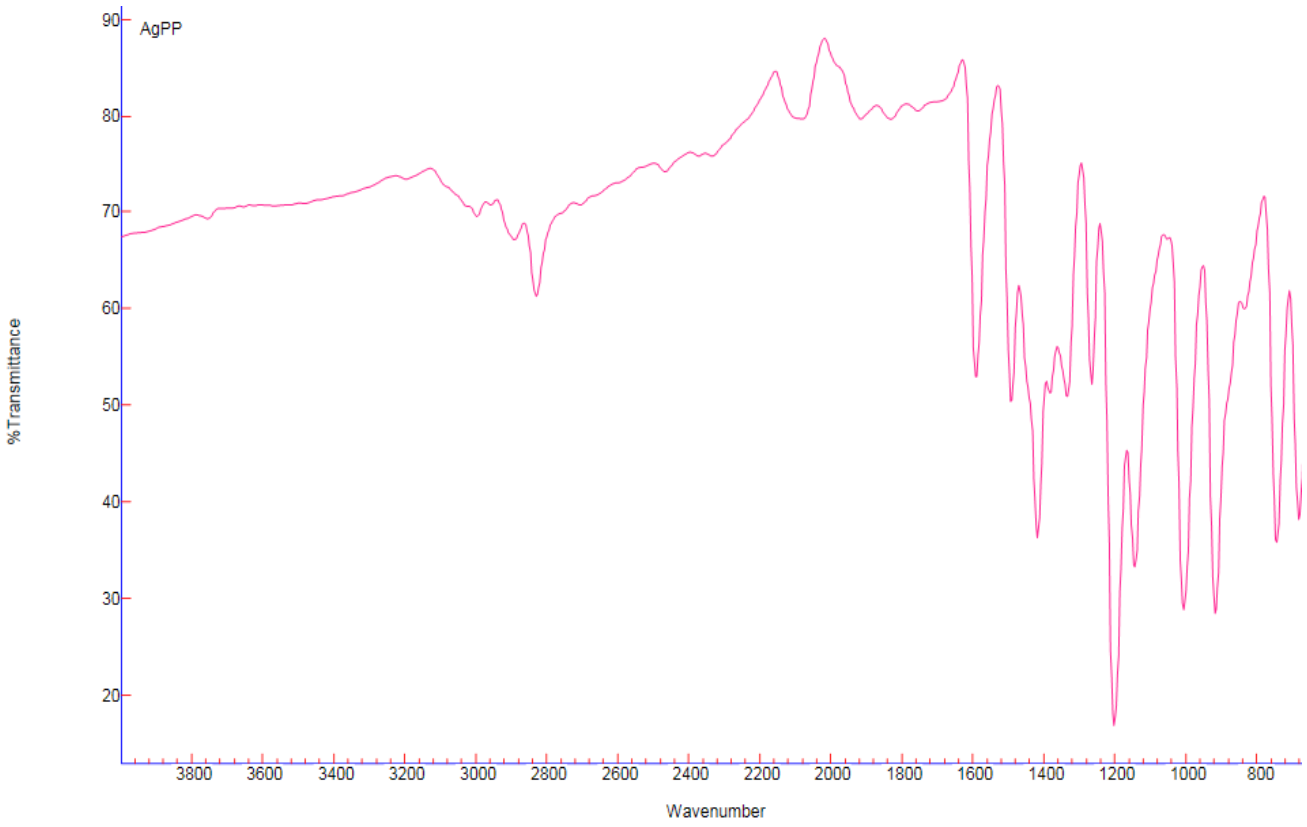

6.7. Appendix A7: FTIR spectra of morpholine DTC, copper(II) and silver(I) complex


CuM comp
%Transmittance
90
80
70
60
50
40
30
20
3800
3600
3400
3200
3000
2800
2600
2400
2200
2000
1800
1600
1400
1200
1000
800
Wavenumber

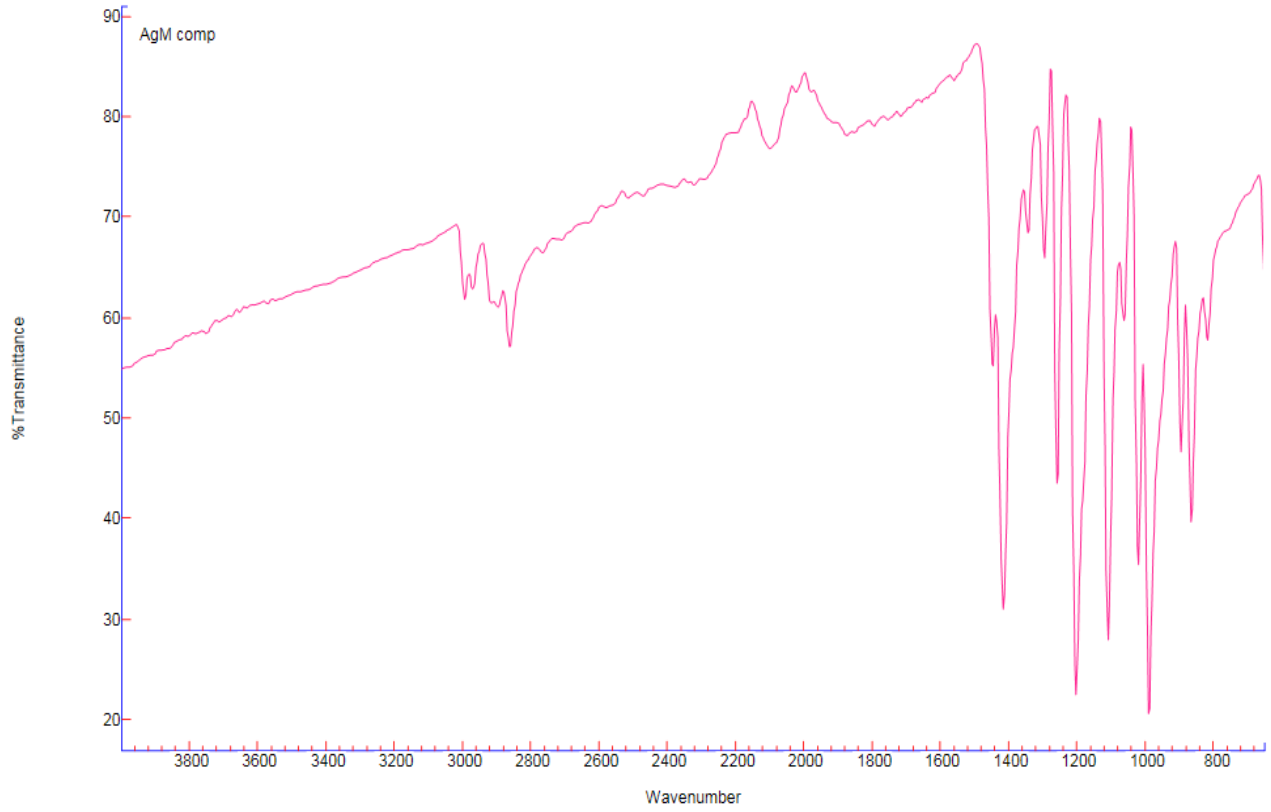
AgM comp
%Transmittance
90
80
70
60
50
40
30
20
3800
3600
3400
3200
3000
2800
2600
2400
2200
2000
1800
1600
1400
1200
1000
800
Wavenumber

6.8.Appendix A8: FTIR spectra of piperidine DTC, copper(II) and silver(I) complex


AgP comp
%Transmittance
90
80
70
60
50
40
3800
3600
3400
3200
3000
2800
2600
2400
2200
2000
1800
1600
1400
1200
1000
800
Wavenumber

7. Appendix B: Crystal structure details of the metal dithiocarbamate complexes

Table 1: Data of the crystals

Compound	**$[Ag_6(DBA\text{-}DTC)_6]$**	**$[Ag_4(NEA\text{-}DTC)_4]$**	**$[Cu(P\text{-}DTC)_2]$**	**$[Cu(DBA\text{-}DTC)_2]$**
Formula	$C_{92}H_{86}Ag_6Cl_6N_6S_{12}$	C36H40Ag4N4S8	C12H20CuN2S4	$C_{30}H_{28}CuN_2S_4$
$D_{calc.}$/ g cm^{-3}	1.778	1.993	1.645	1.464
μ/mm^{-1}	1.709	2.349	1.933	1.117
Formula Weight	2520.30	1216.68	384.08	608.32
Colour	green	yellow	green	red
Shape	block	block	block	block
Size/mm^3	0.31×0.23×0.14	0.31×0.17×0.12	0.33×0.19×0.13	0.34×0.23×0.11
T/K	100(2)	100(2)	100(2)	100(2)
Crystal System	triclinic	tetragonal	monoclinic	triclinic
Space Group	*P*-1	I41/a	P21/c	*P*-1
	11.0126(6)	18.9394(7)	6.0792(4)	13.7098(9)
	14.4254(8)	18.9394(7)	8.4270(6)	14.3201(10)
	16.2955(10)	11.3026(5)	15.2231(10)	16.2979(11)
	78.343(3)	90	90	64.916(4)
	73.321(2)	90	95.995(3)	72.302(3)
	73.2140(10)	90	90	82.774(2)
V/Å^3	2354.0(2)	4054.3(3)	775.61(9)	2760.8(3)
Z	1	4	2	4
Z'	0.5	0.25	0.5	2
Wavelength/Å	0.71073	0.71073	0.71073	0.71073
Radiation type	MoK□	MoK□	MoK□	MoK□
	1.316	2.098	2.691	1.437
	26.500	27.441	27.432	27.597
Measured Refl.	35157	32065	12560	39434
Independent Refl.	9209	2319	1752	11444
Reflections with I > 2(I)	7745	2305	1675	7950
R_{int}	0.0326	0.0328	0.0294	0.0485
Parameters	550	119	88	667
Restraints	0	0	0	0
Largest Peak	1.717	1.043	0.442	0.558
Deepest Hole	-1.023	-0.352	-0.283	-0.956
GooF	1.044	1.263	1.233	1.070
wR_2 (all data)	0.1006	0.0511	0.0617	0.1034
wR_2	0.0937	0.0509	0.0611	0.0914
R_1 (all data)	0.0502	0.0234	0.0293	0.0774
R_1	0.0388	0.0231	0.0277	0.0446

Table 2: $[Ag_6(DBA\text{-}DTC)_6]$ bond lengths

Atom	Atom	Length/Å
Ag1	Ag2	3.0374(5)
Ag1	Ag3	2.9198(5)
Ag1	S5	2.5135(10)
Ag1	S1	2.4421(11)
Ag1	S4	2.5161(11)
Ag2	Ag3	3.3210(5)
Ag2	$Ag3^1$	3.3465(5)
Ag2	S2	2.5402(11)
Ag2	$S5^1$	2.5171(12)
Ag2	S3	2.5161(11)
Ag3	S2	2.4813(10)
Ag3	S6	2.4642(11)
Ag3	$S4^1$	2.5476(12)
S2	C15	1.755(4)
S5	C30	1.752(4)
S6	C30	1.708(4)
S1	C15	1.707(5)
S4	C45	1.750(4)
S3	C45	1.707(5)

Table 3: $[Ag_6(DBA\text{-}DTC)_6]$ bond angles

Atom	Atom	Atom	Angle/°
Ag3	Ag1	Ag2	67.729(12)
S5	Ag1	Ag2	121.04(3)
S5	Ag1	Ag3	78.04(3)
S5	Ag1	S4	91.95(3)
S1	Ag1	Ag2	92.34(3)
S1	Ag1	Ag3	90.27(3)
S1	Ag1	S5	135.35(4)
S1	Ag1	S4	129.72(4)
S4	Ag1	Ag2	69.08(3)
S4	Ag1	Ag3	120.91(3)
Ag1	Ag2	$Ag3^1$	83.324(13)
Ag1	Ag2	Ag3	54.450(11)
Ag3	Ag2	$Ag3^1$	98.875(12)
S2	Ag2	Ag1	75.62(3)
S2	Ag2	Ag3	47.84(2)
S2	Ag2	$Ag3^1$	146.70(3)
$S5^1$	Ag2	Ag1	143.12(3)
$S5^1$	Ag2	$Ag3^1$	70.10(3)
$S5^1$	Ag2	Ag3	103.90(2)
$S5^1$	Ag2	S2	113.79(4)
S3	Ag2	Ag1	85.73(3)
S3	Ag2	$Ag3^1$	88.73(3)
S3	Ag2	Ag3	137.72(3)
S3	Ag2	S2	114.64(4)
S3	Ag2	$S5^1$	117.67(4)
Ag1	Ag3	Ag2	57.822(11)
Ag1	Ag3	$Ag2^1$	72.757(12)
Ag2	Ag3	$Ag2^1$	81.126(12)
S2	Ag3	Ag1	78.72(3)
S2	Ag3	$Ag2^1$	130.48(3)
S2	Ag3	Ag2	49.36(2)
S2	Ag3	$S4^1$	104.99(4)
S6	Ag3	Ag1	91.71(3)
S6	Ag3	$Ag2^1$	83.75(3)
S6	Ag3	Ag2	148.86(3)
S6	Ag3	S2	137.30(4)
S6	Ag3	$S4^1$	114.29(4)
$S4^1$	Ag3	Ag1	124.74(3)
$S4^1$	Ag3	Ag2	82.69(3)

Table 4: $[Ag_4(NEA\text{-}DTC)_4]$ bond angles

Atom	Atom	Atom	Angle/°
Ag11	Ag1	Ag12	62.888(8)
Ag12	Ag1	Ag13	58.557(4)
Ag11	Ag1	Ag13	58.557(4)
S13	Ag1	Ag11	146.166(17)
S13	Ag1	Ag13	88.065(17)
S13	Ag1	Ag12	96.465(17)
S13	Ag1	S22	109.12(2)
S13	Ag1	S2	128.18(2)
S22	Ag1	Ag12	53.717(16)
S22	Ag1	Ag11	81.088(16)
S2	Ag1	Ag11	56.197(16)
S2	Ag1	Ag13	79.815(16)
S2	Ag1	Ag12	117.896(16)
S22	Ag1	Ag13	111.228(15)
S2	Ag1	S22	122.295(13)
C9	S1	Ag13	107.39(9)
Ag1	S2	Ag11	70.087(18)
C9	S2	Ag1	104.60(9)

Table 4: $[Ag_4(NEA\text{-}DTC)_4]$ bond Lengths

Atom	Atom	Length/Å
Ag1	Ag11	2.9115(3)
Ag1	Ag12	2.9115(3)
Ag1	Ag13	3.0376(4)
Ag1	S13	2.4490(7)
Ag1	S2	2.4962(7)
Ag1	S22	2.5732(7)
S1	C9	1.700(3)
S2	C9	1.758(3)
C9	N1	1.341(3)
N1	C1	1.449(3)

Table 6: [Cu(P-DTC)$_2$] bond angles

Atom	Atom	Atom	Angle/°
S1	Cu1	S11	180.00(2)
S11	Cu1	S21	77.83(2)
S1	Cu1	S2	77.83(2)
S1	Cu1	S21	102.17(2)
S11	Cu1	S2	102.17(2)
S21	Cu1	S2	180.0
C1	S1	Cu1	84.68(8)
C1	S2	Cu1	84.16(8)
S2	C1	S1	112.82(13)
N1	C1	S1	123.50(17)
N1	C1	S2	123.66(17)

Table 7: [Cu(P-DTC)2] bond lengths

Atom	Atom	Length/Å
Cu1	S1	2.2894(6)
Cu1	S11	2.2894(6)
Cu1	S21	2.3105(6)
Cu1	S2	2.3105(6)
S1	C1	1.737(2)
S2	C1	1.731(2)
C1	N1	1.312(3)
N1	C2	1.479(3)

Table 8: [Cu(DBA-DTC)$_2$] bond lengths

Atom	Atom	Length/Å
Cu1	S1	2.2971(9)
Cu1	S2	2.2969(8)
Cu1	S3	2.3036(8)
Cu1	S4	2.2924(9)
Cu2	S5	2.2733(10)
Cu2	S6	2.3123(8)
Cu2	S7	2.2968(10)
Cu2	S8	2.3231(8)
S1	C1	1.724(3)
S2	C1	1.729(3)
S3	C16	1.727(3)
S4	C16	1.721(3)
S5	C31	1.720(3)
S6	C31	1.728(3)
S7	C46	1.723(3)
S8	C46	1.722(3)
N1	C1	1.321(4)
N1	C2	1.469(3)
N1	C9	1.479(3)
N2	C16	1.319(4)
N2	C17	1.487(3)
N2	C24	1.476(3)
N3	C31	1.327(4)
N3	C32	1.476(3)
N3	C39	1.471(4)
N4	C46	1.338(4)
N4	C47	1.468(4)
N4	C54	1.466(3)
C2	C3	1.516(4)
C3	C4	1.386(4)
C3	C8	1.388(4)
C4	C5	1.392(4)
C5	C6	1.372(5)
C6	C7	1.394(5)
C7	C8	1.388(4)
C9	C10	1.506(4)
C10	C11	1.385(4)
C10	C15	1.389(4)
C11	C12	1.392(4)
C12	C13	1.383(4)
C13	C14	1.389(5)
C14	C15	1.381(5)

Table 9: [Cu(DBA-DTC)$_2$] bond angles

Atom	Atom	Atom	Angle/°
S1	Cu1	S3	102.35(3)
S2	Cu1	S1	77.84(3)
S2	Cu1	S3	179.73(3)
S4	Cu1	S1	179.16(4)
S4	Cu1	S2	101.79(3)
S4	Cu1	S3	78.02(3)
S5	Cu2	S6	77.89(3)
S5	Cu2	S7	178.26(3)
S5	Cu2	S8	101.67(3)
S6	Cu2	S8	169.28(3)
S7	Cu2	S6	103.23(3)
S7	Cu2	S8	77.48(3)
C1	S1	Cu1	84.25(11)
C1	S2	Cu1	84.14(10)
C16	S3	Cu1	83.71(10)
C16	S4	Cu1	84.17(11)
C31	S5	Cu2	84.98(11)
C31	S6	Cu2	83.58(10)
C46	S7	Cu2	84.58(11)
C46	S8	Cu2	83.79(10)
C1	N1	C2	123.1(2)

Atom	Atom	Atom	Angle/°
C1	N1	C9	122.4(2)
C2	N1	C9	114.5(2)
C16	N2	C17	122.7(2)
C16	N2	C24	122.4(2)
C24	N2	C17	114.7(2)
C31	N3	C32	122.6(3)
C31	N3	C39	121.6(2)
C39	N3	C32	115.7(2)
C46	N4	C47	122.3(2)
C46	N4	C54	121.6(3)
C54	N4	C47	116.1(2)
S1	C1	S2	113.39(18)
N1	C1	S1	123.3(2)